Efficient Terahertz-Range Beam Control Using Flat Optics

by

Daniel Headland

B Eng (Electrical and Electronic Engineering, 1st class Honours),
The University of Adelaide, Australia, 2012

Thesis submitted for the degree of

Doctor of Philosophy

in

Electrical and Electronic Engineering
University of Adelaide

2017

THE UNIVERSITY
of ADELAIDE

Contents

Abstract

The terahertz range, which spans 0.1 to 10 THz of the electromagnetic spectrum, has significant potential for numerous diverse uses including high-volume short-range communications, non-invasive and non-destructive sub-dermal medical imaging, and safe imaging of personnel and postal items for security applications. These capabilities are identified due to the unique properties of terahertz radiation; terahertz waves are of high carrier frequency relative to conventional wireless communications, are able to transmit through dry, non-polar substances, and yet are non-ionising. However, owing to factors including a lack of available power and significant atmospheric attenuation, it is challenging to maintain sufficient signal power over a realistic propagation distance for terahertz waves. For this reason, the terahertz range is presently lacking in practical applications, and hence it occupies an under-utilised portion of the electromagnetic spectrum. As unused spectrum is a valuable resource, the development of technologies to exploit the terahertz range is a highly desirable goal.

Beam-control techniques—the capacity to shape and steer electromagnetic radiation—can prevent radiated power from being lost to undesired directions. Thus, techniques of this variety have the capacity to address the aforementioned obstacles to the realisation of practical terahertz technologies. This thesis is therefore centred around the development of terahertz beam-control devices that satisfy two criteria. Firstly, the beam manipulation operation must be highly efficient, as much of the motivation of this work is to mitigate the constraints upon power. Secondly, planar devices are preferable, as this is a requirement for compact systems. With these restrictions in mind, various techniques are explored for their viability in future applications of terahertz technology, including various forms of metallic and dielectric resonators, 3D printing, and composite materials with effective properties. The advantages and drawbacks of each approach are evaluated.

Statement of Originality

I certify that this work contains no material which has been accepted for the award of any other degree or diploma in my name, in any university or other tertiary institution and, to the best of my knowledge and belief, contains no material previously published or written by another person, except where due reference has been made in the text. In addition, I certify that no part of this work will, in the future, be used in a submission in my name, for any other degree or diploma in any university or other tertiary institution without the prior approval of the University of Adelaide and where applicable, any partner institution responsible for the joint-award of this degree.

I give consent to this copy of my thesis when deposited in the University Library, being made available for loan and photocopying, subject to the provisions of the Copyright Act 1968.

I acknowledge that copyright of published works contained within this thesis resides with the copyright holder(s) of those works.

I also give permission for the digital version of my thesis to be made available on the web, via the University's digital research repository, the Library Search and also through web search engines, unless permission has been granted by the University to restrict access for a period of time.

15/05/2017

Signed

Date

Acknowledgments

To my wonderful wife, Véra Daye, I am extremely grateful for your support. Without it, this would not have been possible.

I would like to thank my parents, Michael Headland and Meera Verma, for supporting and educating me throughout my formative years, and well beyond. That they both hold higher degrees has no doubt inspired my pursuit of a PhD. My older brother, Matthew Headland, also played a large role in fostering my interest in engineering in particular, as well as shaping my values and world-view.

I would like to thank all of my supervisors personally—Prof. Derek Abbott, Dr Withawat Withayachumnankul, and Prof Michael Webb, for each contributing much-needed guidance, direction, and support in their own way. I am also very appreciative of Prof. Christophe Fumeaux for choosing to involve me in one of his terahertz-range projects.

I am very fortunate to have had the opportunity to work with international collaborators throughout my doctoral program. I would like to thank Dr Hou-Tong Chen and Dr Chun-Chieh Chang of Los Alamos National Laboratory, Los Alamos, USA, for hosting and working with me as a visiting scholar, as well as the anonymous donor for providing the funding that made that visit possible. I would like to thank Dr Eduardo Carrasco Yepez of the Institute for Technology in Society in Zurich, Switzerland, for generously collaborating with me. I am also grateful to have shared a collaboration with Prof. Julien Perruisseau-Carrier of the École Polytechnique Fédérale de Lausanne in Lausanne, Switzerland, which was sadly cut short by his untimely passing on June 6th, 2014.

I would like to thank all of my national collaborators; Assoc. Prof. Sharath Sriram, Assoc. Prof. Madhu Bhaskaran, Ms Shruti Nirantar, Dr Philipp Gutruf, Mr Daniel Stavrevski, Mr James Schwarz, and Ms Aditi Upadhyay of RMIT University, Melbourne; and Prof. Andre Luiten and Prof. Heike Ebendorff-Heidepriem of the Institute of Photonics and Sensing in Adelaide.

I would like to thank Mr Wing-Hang "Henry" Ho for his reliable and invaluable assistance in conducting terahertz time-domain spectroscopy experiments. I would like to thank Mr Luis Lima-Marquez and Mr Lijesh Thomas for conducting 3D printing. I

would also like to thank Mr Ian Linke, Mr Brad Pullen, and Mr Hayden Tronnolone for constructing high-quality custom equipment, often at little notice, with minimal specification.

I would like to thank the members of the committee of examiners for reviewing my doctoral thesis. I find it highly flattering that anyone would choose to read my work at all, let alone a $\sim$270-page volume of it.

Lastly, I would like to extend my gratitude to The University of Adelaide for providing The George Fraser Scholarship, which has supported me throughout this endeavour.

Conventions

Typesetting

This thesis it typeset using the LaTeX2e software. Vim build 7.4 was used as an effective interface to LaTeX.

Referencing

Harvard style is employed for referencing and citation in this thesis.

System of units

The units comply with the international system of units recommended in an Australian standard: AS ISO 1000-1998 (Standards Australia Committee ME/71, Quantities, Units and Conversions 1998).

Spelling

Australian English spelling is adopted, as defined by the Macquarie English Dictionary (Delbridge 2001).

Terminology

Where applicable, recent terminology is employed for this thesis, in accordance with that which is seen to be used most frequently in the interested academic community. For instance, the frequency range in which these investigations are undertaken could validly be classified as either the sub-mm or the terahertz range, but most recent work at similar frequencies employs the latter terminology, and hence this is adopted for this thesis.

Publications

Journal publications

Chang-C.-C.,* **Headland-D.**,* Abbott-D., Withayachumnankul-W., and Chen-H.-T. (2017). Demonstration of a highly efficient terahertz flat lens employing tri-layer metasurfaces, *Optics Letters*, **42**(9) pp. 1867–1870.
*These authors contributed equally to this work.

DH performed unit-cell modelling, array-level design and modelling, experimentation, and lead the writing and publication of the manuscript.

Headland-D., Niu-T., Carrasco-E., Abbott-D., Sriram-S., Bhaskaran-M., Fumeaux-C., and Withayachumnankul-W. (2017). Terahertz reflectarrays and nonuniform metasurfaces (**Invited for special issue on Terahertz Photonics**), *IEEE Journal of Selected Topics in Quantum Electronics*, **23**(4), art. no. 8500918.

DH lead the writing of the manuscript of this review article.

Headland-D., Withayachumnankul-W., Webb-M., Ebendorff-Heidepriem-H., Luiten-A., and Abbott-D. (2016). Analysis of 3D-printed metal for rapid-prototyped reflective terahertz optics, *Optics Express*, **24**(15), pp. 17384–17396.

DH performed design and modelling of the devices in this work, conducted all experiments and analysis, and lead the writing of the article.

Headland-D., Carrasco-E., Nirantar-S., Withayachumnankul-W., Gutruf-P., Schwarz-J., Abbott-D., Bhaskaran-M., Sriram-S., Perruisseau-Carrier-J., and Fumeaux-C. (2016). Dielectric resonator reflectarray as high-efficiency nonuniform terahertz metasurface, *ACS Photonics*, **3**(6), pp. 1019–1026.

DH performed modelling of the device presented in this work, conducted all experiments and analysis, and lead the writing of the article.

Headland-D., Nirantar-S., Withayachumnankul-W., Gutruf-P., Abbott-D., Bhaskaran-M., Fumeaux-C., and Sriram-S. (2015). Terahertz magnetic mirror realized with dielectric resonator antennas, *Advanced Materials*, **27**(44), pp. 7137–7144.

DH performed modelling of the device presented in this work, conducted all experiments and analysis, and lead the writing of the article.

Headland-D., Thurgood-P., Stavrevski-D., Withayachumnankul-W., Abbott-D., Bhaskaran-M., and Sriram-S. (2015). Doped polymer for low-loss dielectric material in the terahertz range, *Optical Materials Express*, **5**(6), pp. 1373–1380.

DH conducted all experiments and analysis, and lead the writing of the article.

Cheng-Y. Z., Withayachumnankul-W., Upadhyay-A., **Headland-D.**, Nie-Y., Gong-R. Z., Bhaskaran-M., Sriram-S., and Abbott-D. (2015). Ultrabroadband plasmonic absorber for terahertz waves, *Advanced Optical Materials*, **3**(3), pp. 376–380.

DH performed modelling and analysis.

Niu-T., Upadhyay-A., Withayachumnankul-W., **Headland-D.**, Abbott-D., Bhaskaran-M., Sriram-S., and Fumeaux-C. (2015). Polarization-dependent thin-film wire-grid reflectarray for terahertz waves, *Applied Physics Letters*, **107**(3), art. no. 031111.

DH conducted experiments.

Cheng-Y. Z., Withayachumnankul-W., Upadhyay-A., **Headland-D.**, Nie-Y., Gong-R. Z., Bhaskaran-M., Sriram-S., and Abbott-D. (2014). Ultrabroadband reflective polarization convertor for terahertz waves, *Applied Physics Letters*, **105**(18), art. no. 181111.

DH conducted experiments.

Conference publications

Carrasco-E., **Headland-D.**, Nirantar-S., Withayachumnankul-W., Gutruf-P., Schwarz-J., Abbott-D., Bhaskaran-M., Sriram-S., and Fumeaux-C. (2017). Demonstration of a high-efficiency reflectarray antenna at 1 THz based on dielectric resonators (**Finalist for a best paper award**), *11th European Conference on Antennas and Propagations*, Paris, France, pp. 3335–3337.

Headland-D., Carrasco-E., Nirantar-S., Gutruf-P., Schwarz-J., Abbott-D., Bhaskaran-M., Sriram-S., Perruisseau-Carrier-J., Fumeaux-C., and Withayachumnankul-W. (2016). Efficient terahertz reflectarray based on dielectric resonator antennas, *41st International Conference on Infrared, Millimeter, and Terahertz Waves*, Copenhagen, Denmark.

Headland-D., Nirantar-S., Gutruf-P., Abbott-D., Bhaskaran-M., Fumeaux-C., Sriram-S., and Withayachumnankul-W. (2016). Fabrication of micro-scale single-crystal silicon structures for efficient terahertz magnetic mirror, *41st International Conference on Infrared, Millimeter, and Terahertz Waves*, Copenhagen, Denmark, DOI: 10.1109/IRMMW-THz.2016.7758654.

Headland-D., Withayachumnankul-W., Webb-M., Ebendorff-Heidepriem-H., and Luiten-A. (2016). Reflective terahertz optics using 3D-printed metals, *41st International Conference on Infrared, Millimeter, and Terahertz Waves*, Copenhagen, Denmark, DOI: 10.1109/IRMMW-THz.2016.7758632.

Fumeaux-C., Zou-C., **Headland-D.**, Nirantar-N., Gutruf-P., Zou-L., Bhaskaran-M., Sriram-S., and Withayachumnankul-W. (2016). Terahertz and optical dielectric resonator antennas: Potential and challenges for efficient designs (**Invited**), *10th European Conference on Antennas and Propagations*, Davos, Switzerland, DOI: 10.1109/EuCAP.2016.7481118.

Withayachumnankul-W., **Headland-D.**, Sriram-S., Bhaskaran-M., and Fumeaux-C. (2016). Silicon terahertz resonators, *2nd Australian Microwave Symposium*, Adelaide, Australia, pp. 27–28, DOI: 10.1109/AUSMS.2016.7593477.

HEADLAND-D., WITHAYACHUMNANKUL-W., NIRANTAR-S., BHASKARAN-M., SRIRAM-S., AND FUMEAUX-C. (2016). High-efficiency dielectric resonator antennas in the terahertz range (**Invited**), *IEEE MTT-S International Microwave Workshop Series on Advanced Materials and Processes for RF and THz Applications*, Chengdu, China, DOI: 10.1109/IMWS-AMP.2016.7588409.

HEADLAND-D., TAHA-M., GUTRUF-P., WITHAYACHUMNANKUL-W., BHASKARAN-M., FUMEAUX-C., ABBOTT-D., AND SRIRAM-S. (2015). Passive electric monopole array for terahertz surface wave launcher, *40th International Conference on Infrared, Millimeter, and Terahertz Waves*, Hong Kong, DOI: 10.1109/IRMMW-THz.2015.7327543.

HEADLAND-D., THURGOOD-P., STAVREVSKI-D., WITHAYACHUMNANKUL-W., ABBOTT-D., BHASKARAN-M., AND SRIRAM-S. (2015). Modified elastomeric polymers for loss reduction in the terahertz range, *40th International Conference on Infrared, Millimeter, and Terahertz waves*, Hong Kong, DOI: 10.1109/IRMMW-THz.2015.7327610.

HEADLAND-D., WITHAYACHUMNANKUL-W., WEBB-M., UPADHYAY-A., BHASKARAN-M., SRIRAM-S., AND ABBOTT-D. (2014). Dielectric hole lattice for terahertz diffractive optics with high transmission, *39th International Conference on Infrared, Millimeter, and Terahertz Waves*, Tucson, USA, DOI: 10.1109/IRMMW-THz.2014.6956000.

CHENG-Y. Z., WITHAYACHUMNANKUL-W., UPADHYAY-A., **HEADLAND-D.**, NIE-Y., GONG-R. Z., BHASKARAN-M., SRIRAM-S., AND ABBOTT-D. (2014). Broadband terahertz reflective linear polarization convertor, *39th International Conference on Infrared, Millimeter, and Terahertz Waves*, Tucson, USA, DOI: 10.1109/IRMMW-THz.2014.6956188.

HEADLAND-D., WITHAYACHUMNANKUL-W., WEBB-M., AND ABBOTT-D. (2013). Beam deflection lens at terahertz frequencies using a hole lattice metamaterial, *38th International Conference on Infrared, Millimeter and Terahertz Waves*, Mainz, Germany, DOI: 10.1109/IRMMW-THz.2013.6665703.

List of Figures

For images taken from published work, the appropriate reference is included in each case. In cases in which no such reference is provided, the illustration is by the author.

List of Tables

PART I

Context

Chapter 1

Introduction

THE terahertz range is a portion of the electromagnetic spectrum with significant potential for applications including communications, medical imaging, security screening, and pharmaceutical quality control. However, this range is presently under-exploited due to practical challenges. This introductory chapter offers a brief definition of the terahertz range, and discusses unique properties, prospective applications, and associated challenges. The research focus of this doctoral program is defined, and a summary of the motivations for pursuing this topic is given. Additionally, an outline of the thesis structure is provided.

1.1 Terahertz range

This doctoral thesis is concerned chiefly with the manipulation of terahertz radiation, and hence a definition of this frequency range must come foremost. In terms of classification, the terahertz range is loosely defined as the frequencies from 0.1 to 10 THz (Abbott and Zhang 2007). As shown in Figure 1.1, this frequency range is situated between the microwave and infrared ranges of the electromagnetic spectrum, with some overlap. At the lower-frequency end, there is overlap with the millimetre wave and sub-millimetre-wave ranges, which span from 0.03 to 0.3 THz, and from 0.3 to 3 THz, respectively (Wiltse 1984). At the higher-frequency end, the terahertz range overlaps with the far infrared, which is typically defined as ranging from 3 to 20 THz (Vatansever and Hamblin 2012). Despite this overlap, the terahertz range as a whole is considered a distinct field of study. This "terahertz" paradigm has stemmed both from sub-millimetre-wave and far-infrared study. Whilst these ranges are typically accessed with technologies that employ incoherent emission and detection, much of the progress in the terahertz range is due to the advent of terahertz time-domain spectroscopy (THz-TDS) (Cheung and Auston 1986, Van Exter *et al.* 1989b,

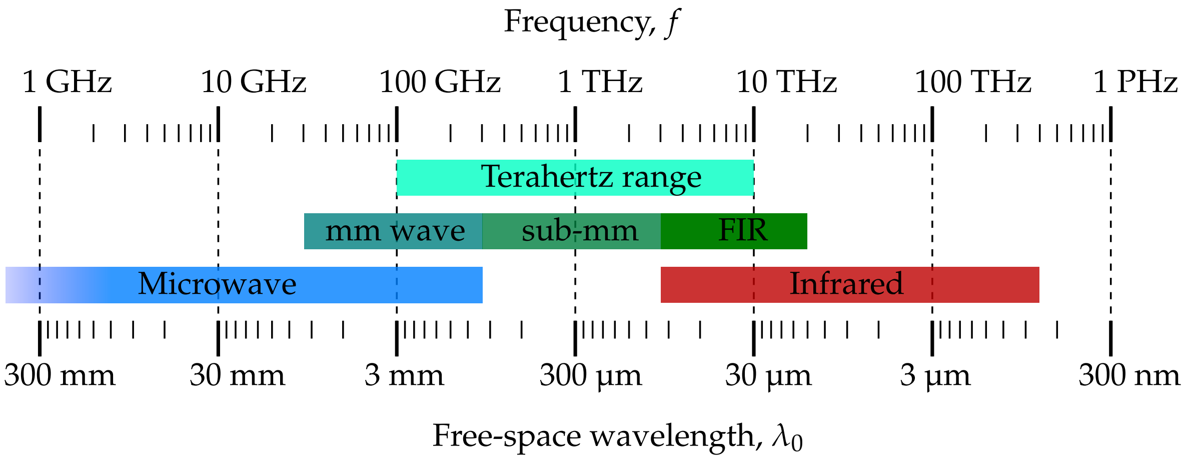

Figure 1.1. Electromagnetic spectrum. The terahertz range in the electromagnetic spectrum, showing overlap with microwave and infrared frequencies. The sub-millimetre-wave range, a subset of terahertz frequencies, is also shown. Overlap of this sort in designations of the electromagnetic spectrum is not unique to the terahertz range, as there is a similar overlap between the X-ray and γ-ray bands, at higher frequencies.

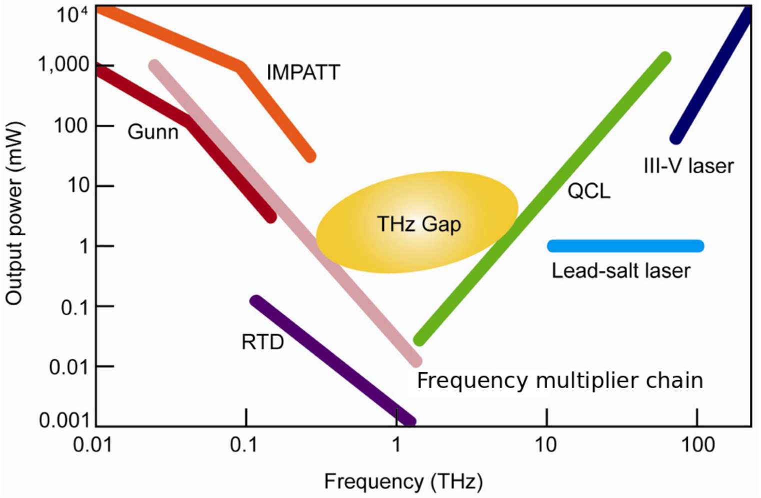

Figure 1.2. Overview of sources. Illustration of the issue of low available power in the terahertz range, in terms of the output power of various forms of radiation source. After Moloney *et al.* (2011).

Grischkowsky *et al.* 1990, Withayachumnankul and Naftaly 2014), which is both coherent[1] and broadband. The unique properties of electromagnetic radiation in this range, as well as particular challenges associated, will be discussed in this chapter.

1.1.1 Terahertz gap

The terahertz range is noteworthy for being one of the least-utilised portions of the electromagnetic spectrum, despite close to a century of scientific interest (Nichols and Tear 1925, Siegel 2002). Indeed, in the late 19th century it was identified that, whilst light and radio waves exist as phenomena on the same spectrum, there is a technology gap that separates them (Rubens and Nichols 1897, Chamberlain 2004). However, the development of terahertz technology had not been intensively studied until recent decades, and the level of attention that the terahertz range receives at present is driving rapid progress.

---

[1] The term "coherent" can be used to refer to different properties of a signal, depending on the context. In some cases, this means a signal has a high degree of uniformity in frequency and phase, i.e. it is very narrow-band. In this case, however, coherence refers to the ability to measure both the amplitude and phase of a broadband signal, rather than just amplitude, which is an attractive feature of THz-TDS.

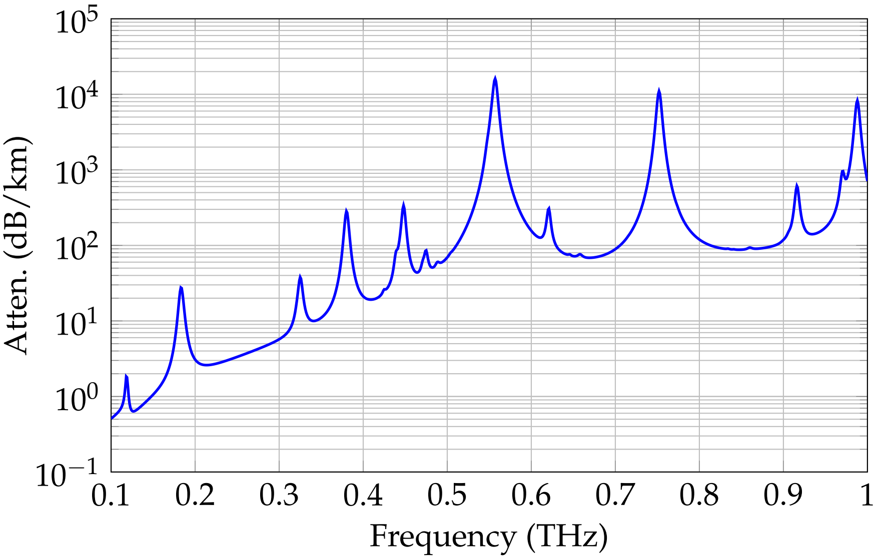

Figure 1.3. Atmospheric absorption. Attenuation of electromagnetic radiation by atmospheric gases. After ITU-R (2013).

A key challenge in the terahertz range is the development of sources capable of generating adequate terahertz power. At frequencies below the terahertz range, electronics-oriented techniques are most commonly employed to generate power, such as two- and three-terminal semiconductor devices (Huang *et al.* 1997, Eisele and Haddad 1998). However, such approaches are increasingly ineffective at higher frequencies, due to the parasitic reactances inherent to electronic devices, and the tendency for such reactances to produce a low-pass response (Sedra and Smith 2004). Additionally, typical semiconductor response times are not well-suited for operation in the terahertz range. Therefore, electronics-oriented devices experience a gradual decrease in output power with respect to increase in frequency, to the point where they are typically unusable at moderate terahertz frequencies. At frequencies above the terahertz range, lasers are well-established as a power source. However such devices require gain media with the appropriate energy level transitions, and media with energy level transitions corresponding to terahertz frequencies become thermalised (Williams 2007, Abbott and Zhang 2007). Due to limitations such as these, it is notoriously challenging to generate a significant amount of power in the terahertz range, as illustrated in Figure 1.2 (Moloney *et al.* 2011).

To compound issues arising from the absence of sufficient available power, terahertz radiation attenuates rapidly in the atmosphere. As shown in Figure 1.3, atmospheric attenuation of terahertz radiation can exceed several thousands of dB/km (ITU-R 2013), thereby making it challenging to maintain adequate signal strength over any reasonable propagation distance. This extreme attenuation is partly due to the fact that several key molecules such as water resonate in the terahertz range, and hence humid and rainy environments are particularly problematic. However, Figure 1.3 also shows several absorption windows, most notably at ∼250 GHz, ∼650 GHz, and ∼850 GHz. Whilst the atmospheric attenuation is still strong in these windows, it is significantly lower than the absorption peaks. Therefore, any practical terahertz application will need to be informed by knowledge of these windows.

Jointly, the issues of low power and high attenuation have inhibited the development of practical technologies that exploit terahertz frequencies. Thus, the terahertz range is often termed the "terahertz gap," and has remained near-exclusively in the realm of research for decades.

1.1.2 Applications of terahertz waves

Whilst practical applications of the terahertz range are presently limited, its unique properties make it attractive for numerous potential uses. Therefore, if the key challenges discussed in Section 1.1.1 were to be successfully addressed, it would constitute a veritable breakthrough, with numerous benefits for human society at large.

Terahertz radiation is non-ionising, in that individual terahertz photons do not possess sufficient energy to liberate electrons from their atoms. Additionally, in soft materials (eg. dermal tissue, plastic foams, etc.) where X-rays provide poor contrast, terahertz techniques provide a complementary capability. The wavelength of terahertz radiation is less than a millimetre, which is sufficient to produce images of adequate resolution for a number of applications. Therefore, terahertz radiation has been demonstrated in applications in safe medical imaging (Reid *et al.* 2010, Yu *et al.* 2012, Suen and Padilla 2016), security screening (Luukanen *et al.* 2013), and non-destructive investigations of priceless artefacts and art (Jackson *et al.* 2011, Walker *et al.* 2013), as shown in Figure 1.4.

Many substances of interest exhibit molecular resonance in the terahertz range, including water, explosives, and many proteins and drugs (Taday *et al.* 2003, Xu *et al.* 2006, Davies *et al.* 2008). Owing to these spectral features, the terahertz range presents a valuable opportunity to study a broad variety of substances. Terahertz spectroscopy has therefore been successfully employed in investigations of materials (Naftaly and Miles 2007, George and Markelz 2012), pharmaceutical quality control (Zeitler *et al.*

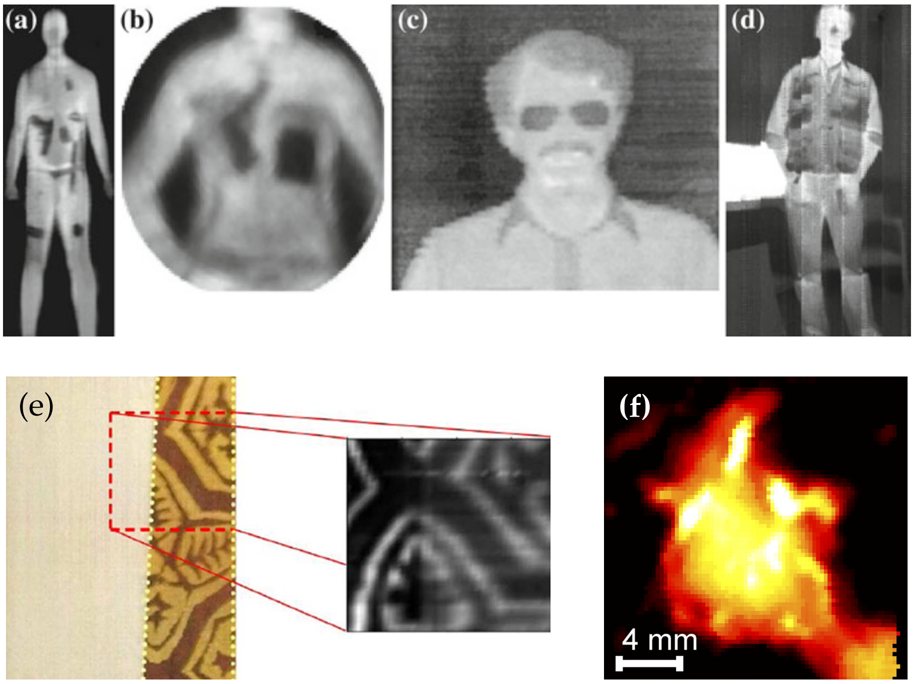

Figure 1.4. Terahertz applications. Some demonstrations of potential imaging applications in terahertz range (a-d) detection of hidden weapons for security screening at 94 GHz, 350 GHz, 600 GHz, and in a broadband 0.2–1.0 THz range respectively, after Luukanen *et al.* (2013). (e) Sub-surface imaging at 150 GHz of partly covered gold leaf pattern in artwork, after Gallerano *et al.* (2009), and (f) imaging of breast tumor tissue, employing a pulsed system with 0.1–3.0 THz bandwidth, after Fitzgerald *et al.* (2006).

2007, Shen 2011), and probing water content of samples (Banerjee *et al.* 2008, Balakrishnan *et al.* 2009).

Lastly, the terahertz range has been identified as having potential for communications applications (Song and Nagatsuma 2011, Kleine-Ostmann and Nagatsuma 2011, Nagatsuma *et al.* 2016a). It is well known that data traffic increases exponentially. Indeed, worldwide mobile data traffic is expected to grow to 30.6 exabytes by the year 2020, which is an eightfold increase over 2015 levels, as shown in Figure 1.5 (Cisco 2016). In order to support this growth, the raw bandwidth offered by the air-interface technologies of future communications links is of crucial importance. Given that the frequencies typically allocated to terrestrial mobile data services are both saturated, and stringently regulated, it is difficult to provide suffficient bandwidth with the carrier frequencies available for current technologies.

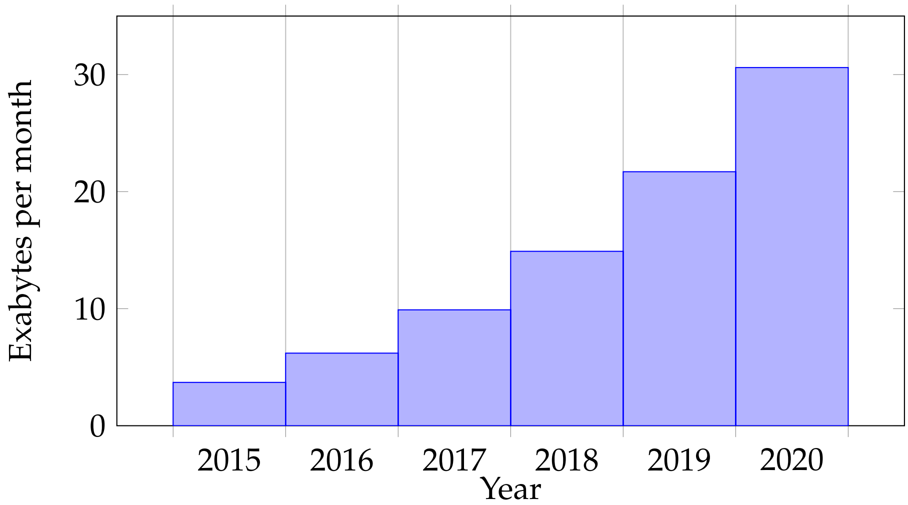

Figure 1.5. Cisco forecast. Projection of global mobile data traffic growth from 2015 to 2020 After Cisco (2016).

Whilst the use of higher carrier frequencies entails practical challenges, it is naturally suited to higher bandwidth, and hence higher data-rates. For instance, a theoretical terahertz communications link using a carrier frequency of 1 THz, with 1% bandwidth, occupies 10 GHz of spectrum in total. This absolute Hertz-value is greater than the carrier frequencies of all commonly employed mobile telephony technologies in the world (Fernandes 2015a, Fernandes 2015b, Sundberg 2015), and is therefore far in excess of the spectral bandwidth provided by such carrier frequencies. A wireless link with such a spectral bandwidth is, in principle, capable of data rates comparable to fibre-optics. Thus, if coupled directly to a fibre-optic connection, a terahertz link will provide the last portion of an end-to-end multi-Gbps internet connection. Terahertz frequencies are therefore envisioned for high-volume, short-range communications.

To-date, most noteworthy demonstrations of terahertz communications links have been limited to carrier frequencies at or below 0.4 THz, achieving reliable transmission with data rates of several tens of Gbps (Nagatsuma *et al.* 2009, Song *et al.* 2012, Koenig *et al.* 2013, Song *et al.* 2014, Nagatsuma *et al.* 2016a). Additionally, higher carrier frequencies have been demonstrated (Ishigaki *et al.* 2012, Kitagawa *et al.* 2016), and with advances in source technology, as well as multi-level modulation schemes, it is anticipated that carrier frequencies up to and beyond 1 THz will become viable for high-volume communications links.

Note that frequencies higher than the terahertz range are also envisioned for high-data-rate communications over relatively short distances. This follows naturally from the aforementioned consideration that available bandwidth is relative to carrier frequency; why not bypass the terahertz range altogether, and aim for carrier frequencies that are higher still? A significant amount effort has been dedicated to the optical frequency range to serve this purpose, including both infrared (Barry 2012) and visible light ranges (Armstrong 2009, Arnon 2015). Furthermore, optical frequencies are not hampered by the transmit-power and atmospheric-absorption constraints discussed in Section 1.1.1.

In order to generate transmit power for optical communications, the most popular options are light emitting diodes (LED) and lasers, which are both mature technologies. Note that LED-based lighting fixtures are already extremely common, and hence ambient lighting fixtures can be adapted to serve both illumination and communications applications simultaneously. In such cases, the modulating signal is not perceived visually as flicker, as the frequencies involved are far too great to be perceived by human eyes. However, an individual LED-based communications channel provides data rates that are limited to tens to a few hundreds of Mbps. This is because the modulation rate of LEDs is constrained by factors including power-bandwidth trade-off and parasitic impedances in LED packaging (Jovicic *et al.* 2013). Furthermore, LED light is incoherent by nature, which precludes sophisticated modulation schemes (Rajagopal *et al.* 2012). By combining channels using multiple-input multiple-output (MIMO) techniques, greater data rates in the order of ~1 Gbps are achievable, but this comes at the cost of increased complexity (Pathak *et al.* 2015, Azhar *et al.* 2013). Considering that modern mobile telephony standards (including LTE and WiMAX) can provide data rates up to 1 Gbps over a longer distance (Chang *et al.* 2010), the advantage provided by LED-based optical wireless communication is not clear.

On the other hand, lasers will in-general provide coherence, higher power, and faster modulation rates than LEDs. Thus, high-volume communications employing laser sources have previously been demonstrated, with single links carrying tens of Gbps being combined into Tbps links (Wang *et al.* 2012). However, such systems require well-defined beams that are more sensitive to alignment than terahertz communications. Additionally, whilst lasers can provide significant transmit power, in practice there are restrictions imposed by safety considerations; excessively-high optical power is not eye-safe, and this is particularly true for infrared beams, as humans are unprotected by aversion response. Lastly, atmospheric effects such as turbulence, fog, and smoke affect optical communications more significantly than terahertz, and hence terahertz links are likely to be preferred in short-range outdoor environments in which such effects cannot easily be controlled (Federici and Moeller 2010).

Ultimately, there are advantages and disadvantages to both frequency ranges. The option that sees widespread adoption in practical applications will depend on how well current and future technological challenges are addressed, as well as deliverable data rates, reliability, and cost. Furthermore, devices utilising these different frequency ranges will not mutually interfere, and can therefore be seen as supplementary to each other. In the future, we may find terahertz and optical communications links working in tandem to deliver high-volume data over short distances, and finding synergy between the strengths of both options.

1.2 Motivation for efficient beam control

Due to the previously-discussed constraints of low available power and high atmospheric attenuation, practical terahertz communications links must waste as little radiated power as possible. It is therefore crucial to minimise the amount of power that is projected into directions in which it will not be received. This is typically achieved with high-gain antennas, which concentrate the radiated power into a given desired direction, with little angular distribution, and hence have high directivity. In general, employing more directive antennas will result in higher received power, provided proper alignment is observed. This illustrates the need for high-gain antennas in terahertz communications links. Link-budget analysis of terahertz communications links at frequencies in the range from 300 to 900 GHz show that, if adequately-high-gain antennas are employed, data rates of several tens of Gbps are achievable over distances of up to 1 km (Schneider *et al.* 2012).

A crucial concern to achieving high antenna gain is antenna aperture. This is defined as the total projected area, with normal vector in the direction of propagation, which intercepts the same amount of power as the receiving antenna. It is well-known that antenna gain is directly proportional to antenna aperture (Balanis 2016), which is closely related to physical antenna size. For this reason, highly directive radio and microwave range antennas are commonly implemented with devices such as reflector dish-based antennas, which occupy a large area. A typical reflector dish antenna consists of a curved, reflective dish, and a primary feed that illuminates the dish with a divergent beam. The curvature of the dish re-directs the divergent beam such that all reflected

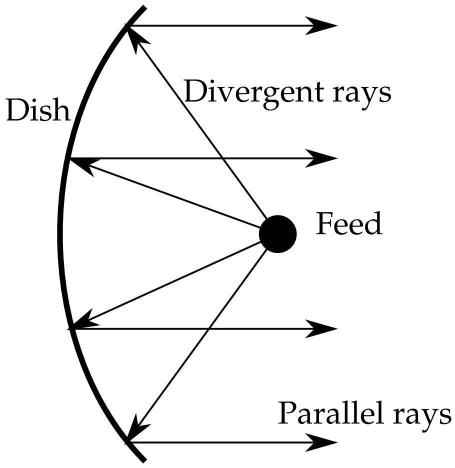

Figure 1.6. Dish antenna. High-directivity dish antenna concept.

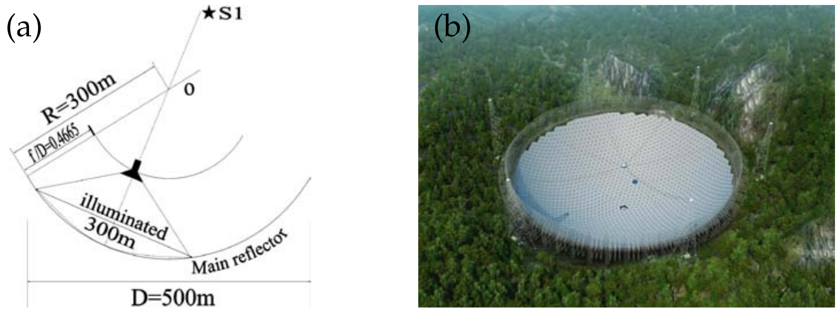

Figure 1.7. FAST radio telescope. Example of a large-aperture radio telescope, showing (a) basic geometry, and (b) a 3D graphic of the yet-to-be completed structure. After Nan *et al.* (2011).

rays are collimated, and hence the antenna has high directivity, as illustrated in Figure 1.6. An example of such an antenna is the under-construction Five-hundred-metre Aperture Spherical radio Telescope (FAST), with a range from 70 MHz to 3 GHz, and a 300 m spherical reflector radius, shown in Figure 1.7. This antenna is intended for a radio-astronomy application, and hence it requires high directivity to survey a specific portion of the sky.

The dish portion of the dish antenna is an example of a beam-shaping, or beam-control, device. In general such devices collect, manipulate, and re-radiate a given beam, and this is most often performed to enhance overall gain. A beam-shaping approach presents significantly greater design freedom than a primary radiator alone, and hence this approach has high versatility and customisability. For this reason, beam-shaping techniques are favoured for the realisation of high-gain terahertz antennas, and are crucial to the realisation of practical terahertz communications links.

In the terahertz range, the wavelength is several orders of magnitude smaller than in radio frequencies, and hence a large electrical aperture is achievable with relatively-small physical size. For instance, if an antenna with equivalent directivity to the aforementioned FAST radio telescope were theoretically scaled to terahertz frequencies, with a range from 100 GHz to 4 THz, its reflector radius would be $\sim$21 cm. This is a consequence of the fact that all physical dimensions of electromagnetic devices are relative to the size of a wavelength, and hence by scaling up the frequency, the wavelength and device dimensions are proportionally scaled down. Therefore, a key advantage of the terahertz range is the ability to achieve high-gain antennas of modest physical dimensions. Additionally, the scale of a terahertz wavelength is such that strong interaction is possible with structures of sizes accessible to microfabrication techniques.

In order to be deployed in a practical terahertz communications link, a beam-shaping device must meet certain key requirements. Firstly, it is crucial that the beam-shaping operation is highly efficient. This is because the main motivations for investigating terahertz beam control pertain to difficulties in generating and transmitting significant power, and hence an inefficient beam control mechanism defeats the purpose. Secondly, compact devices are generally preferable for communications applications, and hence flat-profile beam shapers are desirable. Additional to these concerns, it is also of interest to produce devices of reasonable bandwidth, as this is required for high-volume communications. Lastly, whilst this is not a strict requirement, it is attractive to have polarisation-sensitive devices, in order to increase the overall throughput of a given terahertz beam-shaping device.

1.3 Application concepts

In the terahertz range, the paradigm of “coverage” is dissimilar to radio frequencies, as terahertz radiation propagates in narrow beams. A consequence is that, whilst a point-to-point link may be established, terahertz radiation is not capable of generally-available service over a broad area, like wi-fi and mobile telephony coverage. This drawback is significant, but it is compensated by the high available bandwidth. Terahertz communications links are therefore best suited to high-volume, on-demand applications, when a significant amount of data must be transmitted between two discrete devices in a short amount of time. Another drawback of terahertz radiation is that its range is limited, but this has hidden benefits. Firstly, interference from other transceivers is a significant challenge in mobile telephony, and hence emphasis is placed upon multiplexing schemes that mitigate this problem. In the terahertz range, however, radiation from different transceivers is unlikely to be of sufficient signal strength to cause interference. Secondly, terahertz communications links are inherently secure, as power will not travel sufficiently far to be intercepted by malicious parties. Owing to these facts, terahertz radiation provides an opportunity to employ relatively simple modulation schemes for communications, without much cause to encrypt the signal, or share bandwidth with other users, which further increases the achievable data rates. Bearing in mind the above properties and limitations of terahertz radiation, the following applications of terahertz communications are conceptualised.

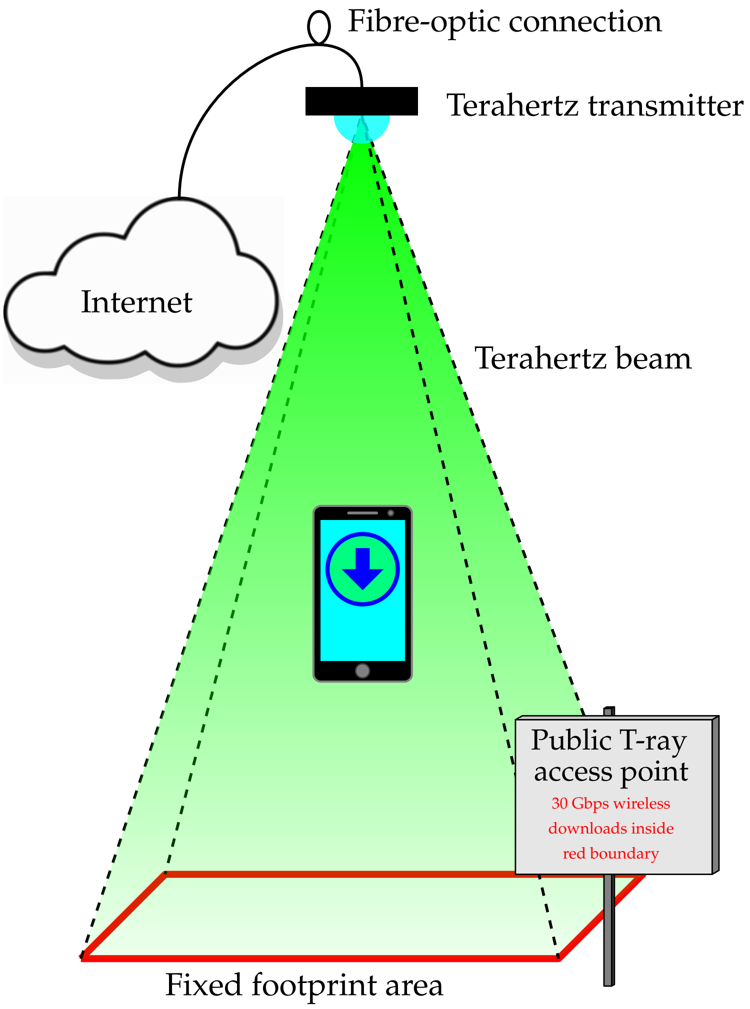

Figure 1.8. Public terahertz access point. Terahertz public data shower concept, to enable high-volume downloads to users within a limited, well-defined area.

1.3.1 Public data shower

Given the high market penetration of smartphones and other mobile, internet-accesible devices, the provision of data coverage in public spaces is becoming increasingly common, either in the form of mobile data service (eg. GPRS, UMTS, LTE), or wi-fi “hot spots” that are made accessible to the general public. However, such services are typically congested, as they are shared with a large number of users. Additionally, in the case of mobile data, usage of these services for large volumes of data can come at significant fiscal expense to the user. Therefore, such services are not amenable to rapid transmission of large-volume data traffic, and terahertz technology has the potential to address this absence.

In the “data shower” concept, a small area is designated for terahertz coverage, and a terahertz transmitter is installed above. Using beam-shaping technology, the radiation pattern of the terahertz transmitter can be engineered so as to provide a precise, well-defined footprint. The terahertz transmitter is fed directly by a fibre-optic cable, resulting in wireless internet access with download speeds of several tens of Gbps. Therefore, if a member of the public has need of a large-volume download, they can simply step into the footprint area, point their device to the transmitter, and download several GB of data in a matter of seconds. For instance, a standard (i.e. single-layer) Blu-ray disc contains around 25 GB of data (Blu-ray Disc Association 2012), and hence a link supplying ∼50 Gbps, as reported in Nagatsuma *et al.* (2016b), can transfer the entire contents of such a disc in ∼4 seconds. Note that in the aforementioned demonstration, the carrier frequency is 330 GHz, and the link distance is between 1 and 2 m, which is amenable to the data shower concept. This concept is illustrated in Figure 1.8. Terahertz radiation is both eye-safe and non-ionising, and the transmit power required for a short-range link such as this is well below that which can cause hazardous heating effects in the human body (Kristensen *et al.* 2010). Thus, such a service poses no health risks to the public, and can be installed in well-populated locations. Additionally, this concept can be implemented in outdoor areas, without the added complexity of background-subtraction techniques, where ambient light contributes significant interference to light-based communications links (Grobe *et al.* 2013).

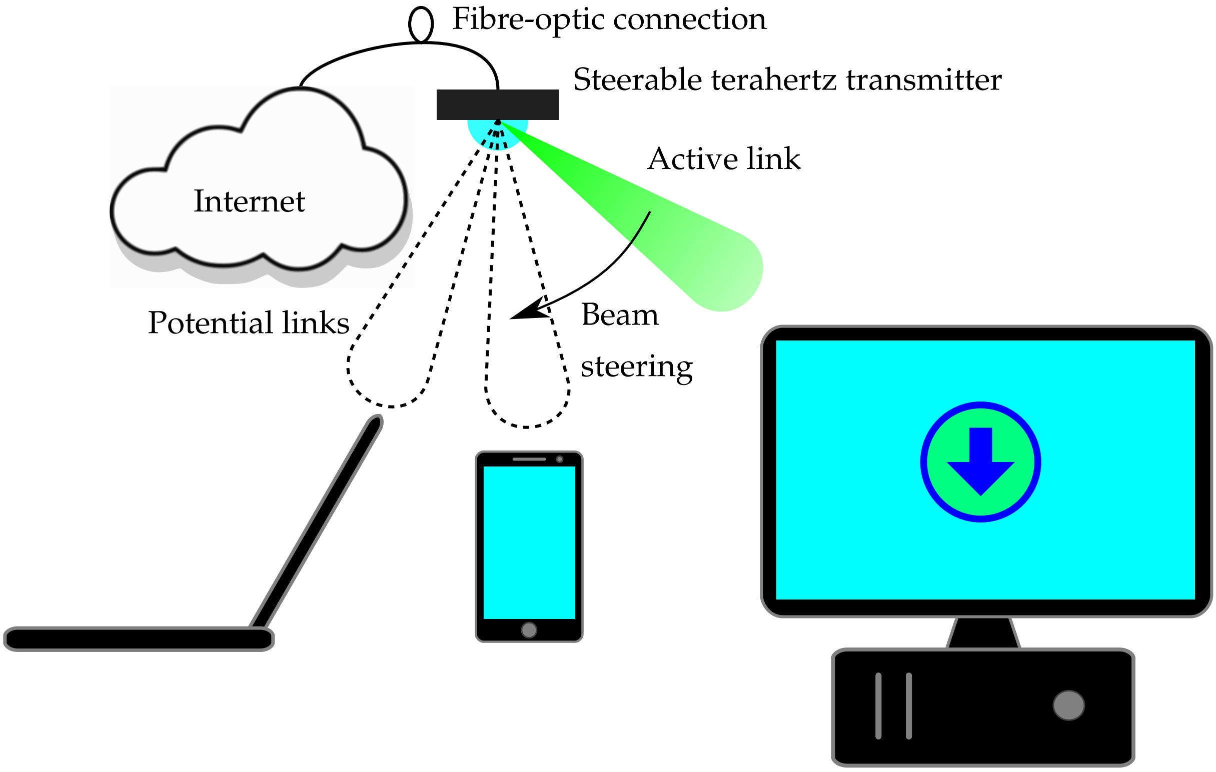

Figure 1.9. Terahertz indoor communications. Terahertz indoor communications link, covering several devices individually.

1.3.2 Indoor communications

If a terahertz transmitter is combined with a dynamically-scannable beam-control device, the directionality of the device can then be reconfigured in real-time. This potentially allows for on-the-fly adjustment of the alignment of a terahertz link. Therefore, such a device can possibly service multiple devices individually, as per immediate requirement. Feedback to the beam-scanning mechanism can potentially be provided over a more general, lower data rate technology such as wi-fi, in order to facilitate automated tracking. As with the data shower concept, the terahertz transmitter is fed by a direct fibre-optic link, resulting in wireless download speeds in excess of several tens of Gbps. One can visualise such a terahertz transmitter installed in the ceiling of an office environment, enabling on-demand, high-volume downloads to a variety of electronic devices, as illustrated in Figure 1.9. Furthermore, in an indoor office environment, atmospheric effects such as high humidity can be controlled, and more damaging effects such as rainfall are entirely non-existent. This results in overall lower attenuation, and hence higher signal to noise ratio and link reliability.

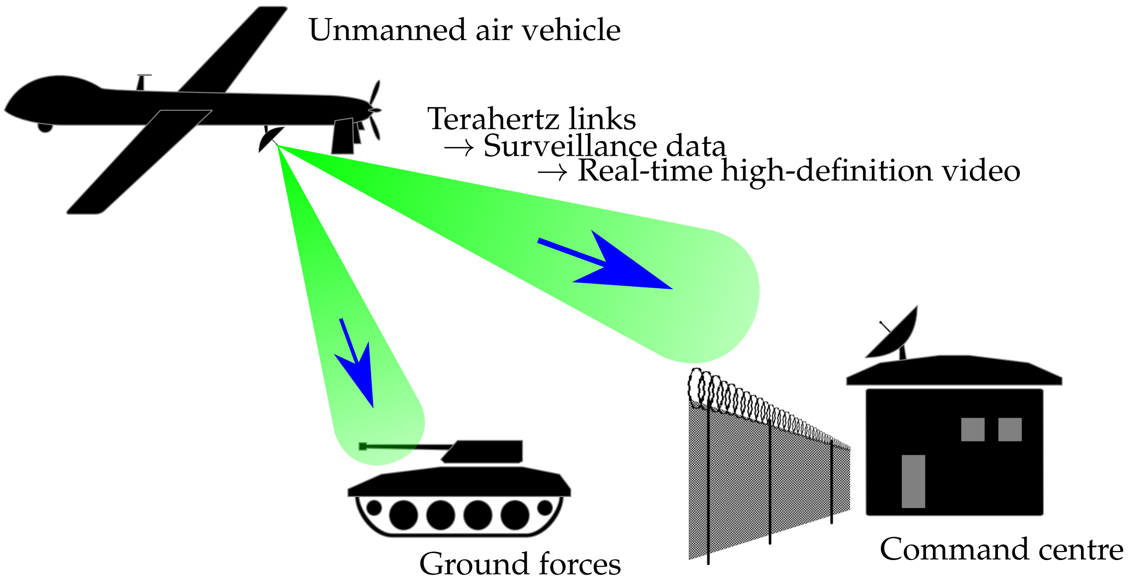

Figure 1.10. Terahertz VLPI communications. Potential for VLPI terahertz communications to be deployed in a battlefield environment.

1.3.3 Defence and secure communications

The inherent security of a terahertz communications link is advantageous in situations in which it is of critical importance that communications are not intercepted, such as in defence and diplomatic applications. Wireless communications at lower frequencies are inherently vulnerable to interception, as such frequencies are capable of penetrating walls, and travelling long distances. Additionally, antennas of moderate physical size at lower frequencies are not capable of providing a directive radiation pattern. These issues are typically mitigated at the modulation level, with schemes such as wide-band code-division multiplexing, such that the detection and decryption of a given signal is highly challenging for an unintended third-party recipient. Such techniques are termed low probability of intercept schemes (LPI) (Simon *et al.* 1994).

If wireless communications are only required over short distances, terahertz communications are a possible alternative to lower-frequency channels. Such communications links must employ extremely directive antennas, which concentrate radiated power in a narrow angle, and exhibit minimal sidelobes. Therefore, it is only possible to receive sufficient power in the direct path of the terahertz beam, making covert interception near-impossible. This additional information security is provided at the physical link level, which may be utilised in tandem with LPI modulation schemes, in order to realise very low probability of intercept communications (VLPI).

The requirement for a covert, strategic, ultra-high bandwidth communications link from an unmanned air vehicle (UAV) to a ground terminal, mobile or otherwise, highlights the benefits of a terahertz link to best effect. The UAV can potentially collect surveillance, tactical intelligence, and real-time video, and relay this information both to a nearby command centre, and also directly to ground forces. Due to the high data rate, minimal compression of transmitted data is required, which increases the usefulness of the gathered data, and reduces processor load of the UAV. Additionally, although the terahertz link is prone to intermittent fading, the high data rates associated may potentially ensure that an adequate mean data rate can be maintained. This concept is illustrated in Figure 1.10.

Note that, as this is a field environment, there are challenges that are not present in the previous two application concept examples, which pertain to indoor and domestic environments. Firstly, the distances associated with this type of environment are upwards of 1 km; significantly larger than indoor communications channels. Furthermore, detrimental effects such as atmospheric humidity cannot be controlled in such an outdoor environment. Thus, terahertz communications links employed in this way must exploit atmospheric transmission windows, such as those at $\sim$250 and $\sim$650 GHz, as shown in Figure 1.3.

1.4 Outline of thesis

This thesis is divided into four major parts, containing two to three chapters each, as well as a summary chapter, making ten chapters in total. This structure is outlined in Table 1.1.

Part I: Context The first three chapters provide the scientific context for this study. Chapter 1 provides definitions, and explains the motivations for pursuing beam control in the terahertz range. Chapter 2 gives a brief overview of relevant beam control theory, with a focus on techniques that are employed in this work. Chapter 3 is essentially a literature review of previous work in the field of beam control in the terahertz range, including limitations of each approach. Section 3.7 of Chapter 3 covers a particular body of work in more detail than all others, as this work was undertaken at The University of Adelaide, and hence the contributions of this thesis build directly thereupon.

Table 1.1. Thesis structure. Structure of thesis, with chapters grouped into two major sections, as well as a summary in the final chapter. Part I provides the research context for this study, including motivation, basic underlying principles, and related work reported in the literature. Part II provides any work pertaining to metallic resonator-based devices. Part III details devices based on of high-resistivity silicon on metal microstructures. Finally, Part IV covers path length-oriented devices.

Part I	Chapter 1	Introduction
	Chapter 2	Theory
	Chapter 3	Background
Part II	Chapter 4	Doped polymer for efficient metallic resonators
	Chapter 5	Polarisation-converting transmitarray for flat lens
Part III	Chapter 6	Fabrication and characterisation of dielectric resonator antennas
	Chapter 7	Dielectric-resonator-based reflectarray
Part IV	Chapter 8	Characterisation of 3D-printed metal for terahertz optics
	Chapter 9	Hole lattice zone plate
	Chapter 10	Thesis summary

Part II: Metallic resonators The overall objective of this part is to improve the efficiency of metallic resonator-based terahertz beam-control devices. Chapter 4 details efforts to modify the material properties of the polymer dielectric known as polydimethylsiloxane (PDMS) in order to reduce loss. In Chapter 5, an innovative metallic resonator-based transmissive structure that exhibits enhanced efficiency is devised and experimentally demonstrated.

Part III: Silicon-on-gold microstructures This part presents a lower-loss alternative to metallic resonators, namely dielectric resonator antennas. In Chapter 6, a homogeneous array of silicon-on-gold microstructures is fabricated and experimentally characterised. Subsequently, Chapter 7 makes use of dielectric resonators of the same sort in order to realise a reflectarray—a form of reflective terahertz beam-control device—with efficiency far greater than the transmitarray that is the subject of Chapter 5.

Part IV: Path-length techniques Previously-mentioned contributions have focused on resonator-oriented beam-control techniques. By contrast, this part of the thesis details contributions to efficient terahertz beam control that make use of no form of resonator, but rather employ optical path length to achieve beam control. In Chapter 8, 3D printing of metals is employed in order to realise a reflector device bearing a topology engineered for the manipulation of terahertz radiation. Chapter 9 presents an effective-medium approach with an all-silicon dielectric lattice design.

1.5 Summary of original contributions

This thesis contains several contributions to terahertz technology, in the form of new approaches to beam control and improvements upon existing techniques, as declared in this section.

Elastomeric polymers are useful materials for terahertz devices, but they are also quite lossy dielectrics in the terahertz range. Lower-loss dielectric materials are available, but are not directly amenable to microfabrication techniques such as spin-coating. A technique is presented to reduce the loss of a polymer dielectric in the terahertz range by doping with a lower-loss powder material (Headland *et al.* 2015c). Such a technique is intended to reduce the intrinsic loss of terahertz metallic resonators constructed using a polymer dielectric. In another contribution, polarisation-converting metallic resonators embedded in a polymer dielectric are employed to realise a flat lens that operates in the terahertz range (Chang *et al.* 2017). Whilst similar resonators have previously been demonstrated for beam deflection in the terahertz range (Grady *et al.* 2013), the flat lens device is more amenable to practical applications.

The most significant contribution of this doctoral thesis is the development of terahertz dielectric resonator antennas (DRAs), which provide a much-needed high-efficiency general-purpose terahertz resonator. Firstly, a technique to realise micro-scale single-crystal high-resistivity float-zone intrinsic silicon structures is developed, and employed for a homogeneous array of DRAs (Headland *et al.* 2015a). This device is demonstrated to function as an artificial magnetic conductor device, which has potential for applications in compact terahertz antennas. In a subsequent publication, a terahertz beam-shaping reflector device, or “reflectarray” is realised using DRAs of this type, which constitutes a highly efficient beam-control device with an operating frequency of 1 THz (Headland *et al.* 2016a).

Techniques to manipulate a terahertz beam by means of control over optical path length using structures of quasi-flat profile, rather than with resonators, are also explored. In one such study, the possibility of employing low-cost rapid-prototyping techniques for a beam-control application is investigated. A binary-phased focusing reflector device is realised in 3D-printed metal, and is subsequently characterised (Headland *et al.* 2016b). Additionally, the reflectivity of the build material is characterised in the terahertz range, in order to gain insight into the efficiency of the zone plate device. In another study, the possibility of employing an effective medium is explored, to exert local control over refractive index in a uniform-profile device. This particular effective medium is an array of subwavelength through-holes in a silicon slab (Headland *et al.* 2013, Headland *et al.* 2014).

These original contributions will serve to advance the sub-discipline of beam control in the terahertz range, which will subsequently serve as instrumental to the realisation of applications including terahertz communications as practical technologies.

Having expounded the motivations for this investigation into efficient beam control in this chapter, the following chapter will present aspects of theory that are relevant to the study.

Chapter 2

Theory

In this chapter, the basic theoretical principles of wavefront engineering are introduced. Broadly speaking, this is centred around the manipulation of field distribution in order to produce some desired propagating beam behaviour. Scalar diffraction theory and array theory are offered as tools to better understand and quantify the associated phenomena. Some commonly-employed techniques are briefly presented. Emphasis is placed upon methods of beam control that are relevant to this doctoral project.

2.1 Introduction

The aim of this chapter is to provide a sound foundation on the principles underlying beam control of terahertz radiation, as this forms the necessary basis for later chapters. Tools for understanding the propagating behaviour of electromagnetic radiation are provided in Section 2.2. General approaches to explicitly prescribing and controlling the behaviour of a given beam are subsequently presented in Section 2.3, and specific beam-control techniques are presented briefly, with a focus on those most relevant to this doctoral project, in Sections 2.4 and 2.5.

2.2 The Huygens-Fresnel principle of diffraction

This thesis is concerned with the manipulation of terahertz radiation, which was established in Section 1.1 as being a portion of the electromagnetic spectrum. It is therefore prudent to begin by developing an understanding of the behaviour of electromagnetic radiation as it propagates through space. The physical principles that govern this behaviour are the same across the entire electromagnetic spectrum, and hence frequency is treated abstractly for much of this chapter.

2.2.1 Historical background of scalar diffraction theory

The following historical background is taken from the book *Introduction to Fourier Optics* (Goodman 2005). Christiaan Huygens posited in 1678 that a given wavefront can be considered analogous to an array of infinitesimal secondary sources, which are now known as “Huygens’ point sources” or “Huygens’ source radiators,” where each outputs a spherical wave. The wavefront at a later instant can therefore be found by constructing the “envelope” of the secondary wavelets. The subsequent wavefront similarly generates the wavefront that follows, and so on, as the wave propagates through space. A two-dimensional representation of this concept is illustrated in Figure 2.1, showing plane wave propagation, refraction, and diffraction by a single slit. This theory is based on the wave-like behaviour of light, and hence it failed to gain traction throughout the 18th century, in which the field of optics was dominated by scientists such as Sir Isaac Newton who favoured the corpuscular theory of light. However, the 19th and 20th centuries saw a renewed interest in this wave-oriented paradigm, owed largely to James Clerk Maxwell’s phenomenal contributions to our understanding of

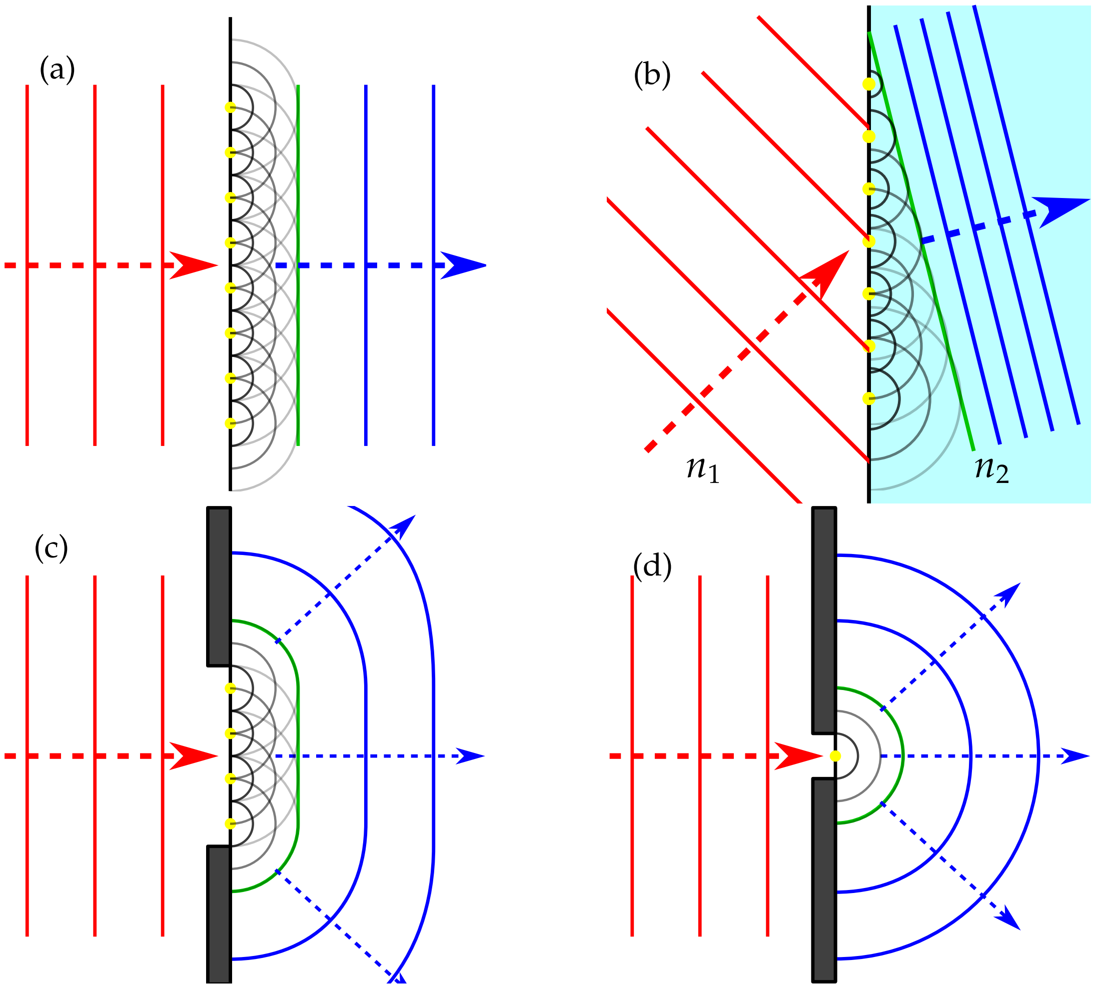

Figure 2.1. Phenomenology of Huygens-Fresnel principle. Illustration of the Huygens paradigm, showing the construction of subsequent wavefronts by the envelope of spherical wavelets, with four different cases (a) plane wave, (b) refraction, where $n_2 > n_1$, (c) diffraction by large slit, and (d) diffraction by small slit. Incident wavefronts are shown in red, secondary source centres are shown in yellow, wavelet envelope is shown in green, and subsequent wavefronts are shown in blue.

electromagnetic waves (Maxwell 1881). With contributions from distinguished scientists including Augustin Jean Fresnel and Gustav Kirchoff, this has resulted in a practical mathematical formulation of Huygens' aforementioned postulate that is given in the following section.

In Figures 2.1(c,d), the propagation direction appears to bend outward in response to the influence of the slit. This is not consistent with a straightforward ray-tracing paradigm, under which the rays that pass through the slit will simply carry on their set course from left to right, with no disturbance to their directionality. Incidentally, Sommerfeld (1964) defines diffraction as "any deviation of light rays from rectilinear paths which cannot be interpreted as reflection or refraction," which corresponds closely to the divergent fields emanating from the slit. Thus, Huygens' principle describes diffraction. Additionally, this paradigm treats electromagnetic waves as a scalar field. Strictly speaking, this is inconsistent with the vector nature of electromagnetic fields, but it can be interpreted as the assumption that the fields are of the same polarisation everywhere, and hence no particular polarisation vector need be specified. Combining these two attributes, this model employs a scalar-based approach to model diffractive behaviours, and hence it is often referred to as "scalar diffraction theory," but it is also often termed "the Huygens-Fresnel principle," or more simply, "Huygens' principle."

Note that methods are available that can provide a greater degree of accuracy than Huygens' principle. For instance, an equivalent vector diffraction theory is formulated by substituting the point sources for infinitesimal vector potentials, thereby preserving the vector nature of electromagnetic wave propagation (Marathay and McCalmont 2001). However, the formulation of scalar diffraction theory is more straightforward, and is of sufficient accuracy for the propagation distances and device sizes involved in this doctoral thesis.

2.2.2 Mathematical formulation

In the context of this work, it is most useful to consider the Huygens-Fresnel principle in rectangular coordinates. As shown in Figure 2.2, the diffracting aperture is in the (ξ, η)-plane, which is parallel to the (x, y)-plane, and situated at $z = 0$. Using the Huygens-Fresnel principle, it is possible to evaluate the distribution of the complex electric field amplitude, A, at a given point in Cartesian space, $P = (x, y, z)$, using the

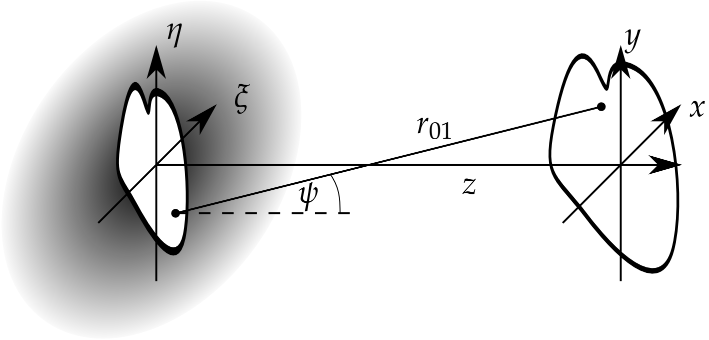

Figure 2.2. Huygens-Fresnel formulation. Illustration of the mapping from the (ξ, η) plane, in which the diffracting aperture resides, to the (x, y) plane, for which the field distribution is to be computed. These planes are separated by distance z.

following expression (Goodman 2005),

$$A(x,y,z) = \frac{1}{j\lambda} \iint\limits_{\Sigma} A(\xi,\eta,0)^* \, \frac{\exp(jkr_{01}) \cos\psi}{r_{01}} \mathrm{d}\xi \mathrm{d}\eta, \tag{2.1}$$

where it is assumed that propagation is along the z-axis, the distance from $(\xi,\eta,0)$ to (x,y,z) is $r_{01} = \sqrt{(x-\xi)^2 + (y-\eta)^2 + z^2}$, ψ is the angle that a line connecting these two points makes with the z-axis, and k is the wavenumber in the relevant medium. This carries the assumption that $r_{01} \gg \lambda$; that the observation distance is many wavelengths from the diffracting aperture. This approach is extremely powerful, as it can predict the behaviour of any given propagating beam based on the field distribution of its radiating aperture, and quantitatively determine the quantity of power that is delivered to a given region of space. Lastly, the double-integral can be expressed as a Riemann sum,

$$A(x,y,z) = \frac{1}{j\lambda} \sum_{\xi} \sum_{\eta} A(\xi,\eta,0)^* \, \frac{\exp(jkr_{01}) \cos\psi}{r_{01}} \Delta\xi \Delta\eta, \tag{2.2}$$

which is amenable to computer-oriented numerical techniques. This means that, if an arbitrary aperture distribution is known, the field at distance z from the aperture can be evaluated numerically. Note that the validity of this Riemann sum hinges upon the assumption that the steps over the summation area (i.e. $\Delta\xi$ and $\Delta\eta$) are subwavelength, in order to provide an adequate approximation of a function that is defined over a continuous domain. However, whilst it is a requirement that spacing is less than a wavelength, the precise requirements of a given case may vary with diffraction distance, aperture size, and the gradient with which the field distribution varies across the aperture. There is therefore no explicitly-clear consensus on the required value of step size for this purpose. Lastly, it is important to note that, whilst this expression is derived for a given beam output by a radiating aperture, the result is general. If the complex field distribution of a given beam can be known explicitly in a transverse plane (i.e. transverse to the optical axis), it is possible to evaluate the field distribution in another such transverse plane, providing the two are separated by a sufficient distance.

2.2.3 Relevance to array theory

Conceptually, the Huygens-Fresnel principle is directly analogous to the notion of "array factor," which is a useful approach to understanding the behaviour of array antennas. Both seek to express overall field as a linear superposition of fields from smaller sources. The difference is that, in the case of the Huygens-Fresnel principle, these sources are virtual and infinitesimal, whereas in the case of array theory the sources are the actual and finitely-sized antenna elements that make up the array. Another difference is that the Huygens-Fresnel principle seeks to determine field projected to a point in Cartesian space, a finite distance away from the radiating aperture, whereas array theory aims to determine the electric field projected into a given direction in spherical coordinates, in the far field.

A general expression for the array factor of a rectangular planar array, with spacing d_x and d_y, where a given element has complex amplitude A, is given in Equation 2.3 (Johnson and Jasik 1984),

$$\mathrm{AF}(\theta,\phi) = \sum_{\chi}\sum_{m} A_{\chi m}\mathrm{exp}(jk(\chi d_x \mathrm{sin}\theta\mathrm{cos}\phi + m d_y \mathrm{sin}\theta\mathrm{sin}\phi)). \tag{2.3}$$

For an array of identical radiators, this expression is multiplied by the radiation pattern of the individual element in order to derive the overall radiation pattern. However, it is

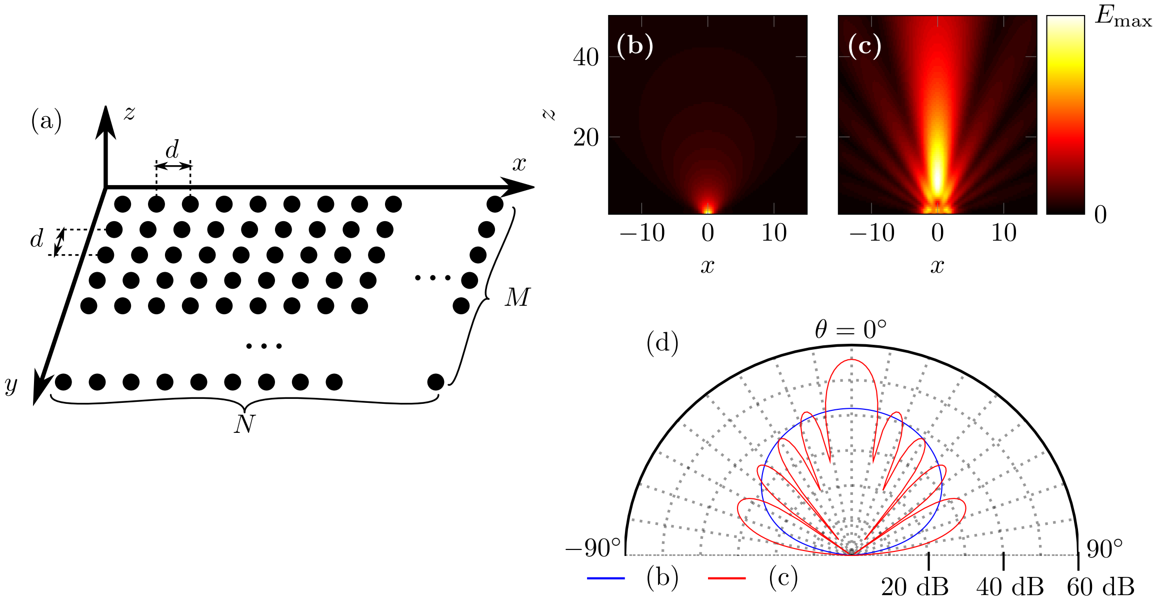

Figure 2.3. Array theory's equivalence to scalar diffraction theory. (a) A rectangular array of elements, representing either isotropic radiators in an array theory paradigm, or sampling points of an aperture distribution for scalar diffraction theory. The output near field distribution is calculated using scalar diffraction theory, for apertures of area (b) $1\lambda \times 1\lambda$, and (c) $5\lambda \times 5\lambda$, noting that these heatmaps are in linear scale and are normalised against their own respective maxima, with (d) corresponding far field radiation patterns.

often desirable to know the array factor in isolation, especially when the beam-shaping properties of the array are of greatest interest.

The equivalence of the Huygens-Fresnel principle to array theory is illustrated in Figure 2.3. In this example, an array of generic elements is given in Figure 2.3(a), which represent isotropic radiators in an array theory paradigm, and field sampling points in a scalar diffraction theory paradigm. The spacing of the elements is in a regular, square grid, i.e. $d_x = d_y = d$, and $\Delta\xi = \Delta\eta = d$. In this example, $d = \lambda/5$, $M = N$, and all elements are of uniform magnitude and phase. This is equivalent to either a uniformly-distributed aperture, or a planar array of uniform-excitation radiators. Two different aperture side-lengths are investigated, namely one and five wavelengths across, resulting in the field distributions is given in Figures 2.3(b) and (c) respectively. Corresponding array factors are given in Fig 2.3(d). The equivalence between the near field beam and the array factor can clearly be seen; the smaller aperture produces a single, highly divergent beam, whereas the larger aperture produces a more directive mainlobe, with several sidelobes.

Due to differences in physical scale, and the requirements of different applications, a far-field approach is generally most relevant at radio and microwave frequencies. However, at higher frequencies a beam-oriented paradigm is most relevant, and hence techniques such as the Huygens-Fresnel principle are preferred. Therefore, the choice of paradigm is informed by choice of operating frequency.

2.3 Wavefront engineering

Section 2.2.2 argues that the behaviour of a beam can be determined by its field distribution over a given transverse plane. Therefore, by careful manipulation of the aperture distribution, a degree of control may be exerted over the ensuing propagating beam. This correspondence between field distribution and the subsequent behaviour of the propagating beam is the basis for what is known as wavefront engineering. For simplicity, field distribution will be considered abstractly in this section, without providing an explanation of how such a field distribution is achieved. This is to better communicate the core concepts of wavefront engineering, free of obfuscatory practicalities.

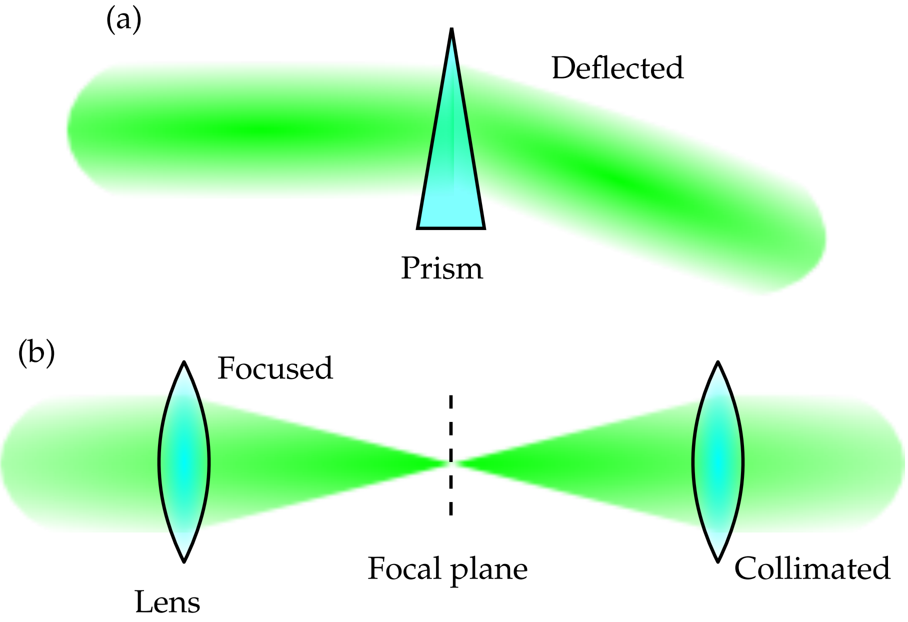

Figure 2.4. Beam operations. Basic beam operations with elementary optical components, showing (a) deflection using a prism, and (b) Focusing and collimating using lenses.

Two relatively straightforward beam-control operations will be considered as core example cases. The first operation is beam deflection, or beam steering, which is essentially the re-definition of the propagation direction of a beam by means of a transformation of field distribution. The second beam-manipulation operation to be considered is termed "lensing" in the context of this thesis. Lensing is the process of transforming a divergent beam into a collimated beam, i.e. one with minimal wavefront curvature, and sufficient lateral extent to mitigate strong diffraction. By reciprocity, such a device can also transform a collimated beam into a focused beam, which in-turn becomes a divergent beam after it passes through its focus. Both of these beam-control operations are illustrated in Figure 2.4, as performed by traditional optics. Both magnitude and phase-oriented control will both be considered and contrasted as means to achieve these operations.

2.3.1 Magnitude-based beam control

As previously mentioned, magnitude-based beam control is possible. This makes use of a particular field amplitude distribution in order to manipulate the shape and directionality of a propagating beam. However, it is noted that such techniques are not a particularly popular choice for most applications requiring beam control. One reason for this is that a specific magnitude distribution is typically achieved by blocking specific portions of an input beam, by either absorbing or reflecting radiation. Thus, a drawback of amplitude-blocking devices is that they are inefficient by nature, as they discard approximately half of the available power. This is not generally desirable, but it is particularly concerning in the terahertz range due to the power constraints detailed in Section 1.1.1. Additional to that, magnitude-based beam control exhibits a tendency to produce numerous undesired diffraction orders. Magnitude-based beam-control techniques are therefore most popular in the X-ray region, as the physical scale of a wavelength is extremely small, and radiation is ionising, which precludes the use of more sophisticated beam-control techniques.

Magnitude-deflection

One example of magnitude-based beam control is the amplitude-blocking diffraction grating. At its most simple, this device consists of a periodic arrangement of alternating blocking and non-blocking stripes. If the grating period is greater than a single wavelength, there will be energy diffracted into sidelobes, which are essentially higher diffraction orders, at angles θ_s (Kirz *et al.* 1986),

$$\sin\theta_s = \frac{s\lambda}{D} - \sin\theta_\mathrm{i}, \quad s = 0, \pm1, \pm2, \pm3, ..., \tag{2.4}$$

where D is the grating period, and θ_i is the angle of incidence. The reason for maxima in these angles in particular is that the field emanating from the non-blocking stripes will constructively interfere in these directions. In the absence of the blocking stripes, these field maxima are cancelled out by the field that would be output by the now-blocked regions, resulting in plane-wave forward propagation. Additionally, the grating equation shows that angle is frequency-dependent, and hence diffraction gratings can be employed to separate a broadband signal into constituent colours.

The amplitude-blocking diffraction grating concept is illustrated in Figure 2.5(a,b), showing two different values of grating period. Using Equation 2.3, the associated far-field array factors are computed, and are given in Figure 2.5(e). The field distribution is discretised into steps of $\lambda/5$ for this purpose. It can be seen that the energy is scattered into multiple directions, corresponding to the various grating orders.

Magnitude-based lensing

The concept of a diffraction grating can be extended to perform lensing operations by employing a non-periodic arrangement. If the period of a diffraction grating decreases

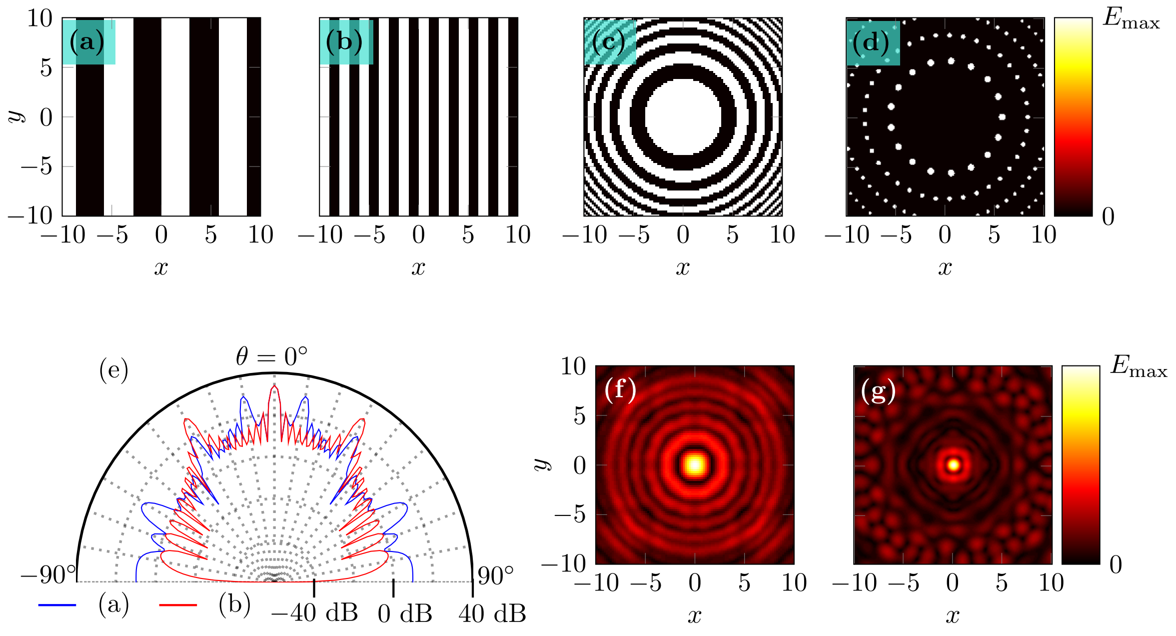

Figure 2.5. Magnitude-based beamforming. Illustration of the principles of magnitude-based wavefront engineering, showing (a-d) magnitude distributions required to produce various beam-control operations. The field distributions shown in (a) and (b) are diffraction gratings, with first-order diffraction angles of 10° and 30° respectively, producing the far-field radiation patterns shown in (e). The field distributions in (c) and (d) are for lensing operations, both with focal lengths of 15 λ, producing focal spots shown in (f) and (g) respectively.

progressively with respect to distance from the optical axis (i.e. it is chirped), then the diffraction angle will increase as a consequence. By varying the deflection angle such that all deflected rays are directed through the same point along the optical axis, constructive interference at that point will result. Lastly, by rotating this structure about the optical axis, a series of concentric zones are realised, alternating between blocking and non-blocking, with switching radii r_m (Kirz *et al.* 1986),

$$r_m = \sqrt{m\lambda F + \frac{m^2\lambda^2}{4}}, \quad m = 1, 2, 3, \ldots \tag{2.5}$$

This device is known as an amplitude-blocking zone plate. Constructive interference will occur along the optical axis, at a focal length F away from the zone plate device, producing a focal spot. Thus, this zone plate device is performing a lensing operation, and can both focus and collimate radiation, by the principle of reciprocity. A focusing zone plate is illustrated in Figure 2.5(c,f). Note that the field magnitude distribution of the focal spot is calculated using Equation 2.2, for which the field distribution is discretised into steps of $\lambda/5$. Much like the sidelobes of the diffraction grating shown in Figure 2.5(e), there are concentric field maxima surrounding the focal spot. This detracts from power delivered to the focus, and hence is an undesirable effect.

The concentric maxima produced by the zone plate can be diminished by employing a photon sieve arrangement (Kipp *et al.* 2001), as shown in Figure 2.5(d,g). This has the added benefit of producing a finer focus, which is beneficial for many applications. This device follows a zone arrangement that is closely related to that of the zone plate, but each concentric zone has been replaced with a annular array of small, circular apertures. A consequence of this is that the photon sieve device discards considerably more power than the zone plate, and is therefore less efficient. Note that, as with the previously-presented amplitude-blocking zone plate, the field distribution of the focal spot is computed using Equation 2.2. In this instance, however, a higher resolution of $\lambda/10$ is employed, in order to produce clearly-defined circular apertures.

2.3.2 Phase-based beam control

Phase-based beam control is, in general, more versatile and efficient than magnitude-based beam control, and it provides a greater degree of control. This will be seen in the following examples, as comparisons are provided in each case. Thus, phase-based techniques are preferred wherever possible, and will be the focus of the thesis.

Phase-based deflection

A linear-ramp phase distribution results in beam steering off to a non-normal angle in the far field. Phenomenologically, this can be explained with the retardation of the wavefront on one side of the array with respect to the other, resulting in a tilt of the subsequent wavefront, and hence in steering of the propagating wave. In order to achieve steering towards angle θ_s with respect to the normal in the xz-plane, the following phase distribution is required,

$$\varphi(x,y) = k_0 x \sin(-\theta_s), \tag{2.6}$$

where k_0 is the free-space wavenumber. Note that, for a given frequency, phase is wrapped to a 360° cycle, which effectively translates the ramp into a sawtooth function, as shown in Figures 2.6(a,b). This is similar to conventional blazed diffraction gratings, as the periodicity of this sawtooth function corresponds to the periodicity of the grating equation given in Equation 2.4. However, the crucial distinction that separates this device from an amplitude-blocking diffraction grating is that deflection will be exclusively towards the first-order maximum (i.e. $s = +1$).

It is desirable to know the far-field behaviour produced by this phase distribution, and to this end, the phase distributions shown are discretised with a step size of $\lambda/5$, such that Equation 2.3 can be employed. The resulting array factors are shown in Figure 2.6(e), where it is noted that a Gaussian beam excitation provides a low-sidelobe illumination. It can be seen that the direction and gradient of the phase ramp determine the angle of the far-field radiation pattern maximum. Unlike the magnitude-based techniques presented in Figure 2.5(a,b,e), the radiation pattern is asymmetrical, and there is a single, clear main lobe towards the first-order diffraction direction. This is testament to the greater degree of control provided by phase-based beam control.

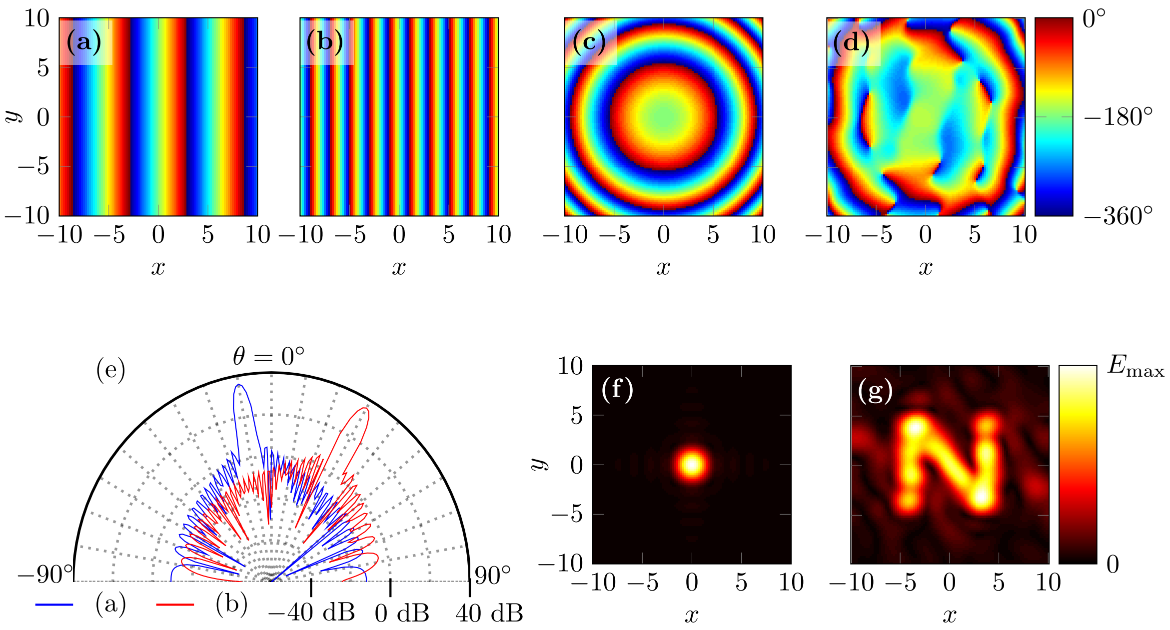

Figure 2.6. Phase-based beamforming. Illustration of the principles of phase-based wavefront engineering, showing (a-d) phase distributions required to produce various beam-control operations. Phase distributions (a) and (b) produce far-field beam steering shown in (e), phase distribution (c) produces the focal spot shown in (f), and phase distribution (d) produces a Gerchberg-Saxton hologram, representing the letter capital "N," in (g). All spatial dimensions are in units of wavelength, for generality. The propagation distance in both (f) and (g) is 30λ. In all cases, a 15λ-diameter Gaussian magnitude profile is employed in order to suppress sidelobes and fringing effects. After Headland *et al.* (2017).

More generally, shaped beams are achievable with similar phase-based beam-control techniques (Duan and Rahmat-Samii 1995, Villegas 2007), providing highly customisable far-field radiation patterns. For example, satellite communications employ such techniques in order to define a specific beam shape that corresponds to the contour of the geographical region to be serviced, and this minimises wasted power projected outside the bounds of the relevant region (Pozar *et al.* 1999, Encinar and Zornoza 2004, Encinar *et al.* 2006).

Phase-based lensing and related operations

The phase distribution required to achieve the lensing operation for a given focal length F is as follows,

$$\varphi(x,y) = k_0\left(\sqrt{F^2+(x^2+y^2)}-F\right)+\varphi_0, \tag{2.7}$$

with some arbitrary initial phase φ_0. An example of such a phase distribution is illustrated in Figure 2.6(c). The focal spot produced by this phase distribution is calculated using Equation 2.2, and results are shown in Figure 2.6(f). It can be seen that a well-defined focal spot is produced, without the undesired fringing maxima seen in Figure 2.5(f,g), and this illustrates the advantages of phase-based beam control over magnitude-based beam control. Note that the expected size of the focal spot is determined by the diameter of the Gaussian-distributed aperture, D, and focal length;

$$\frac{D}{2F} = \frac{\lambda_0}{\pi w_0}, \tag{2.8}$$

where w_0 is the $1/e$-radius of the focal spot (Saleh and Teich 2007).

More generally, with techniques such as the Gerchberg-Saxton phase retrieval algorithm (Gerchberg and Saxton 1972), it is possible to specify a near-arbitrary field amplitude distribution, and calculate the phase distribution required to produce it at a given propagation distance. To illustrate this concept, the phase distribution given in Figure 2.6(d) is calculated using a variant of the Gerchberg-Saxton phase retrieval algorithm that uses scalar diffraction theory rather than the two-dimensional fast Fourier transform. For this example, the required output field distribution is a representation of the capital letter “N.” Equation 2.2 is employed to determine its output field distribution, and this is shown in Figure 2.6(g). It is clearly visible that the bespoke capital letter has been reproduced with adequate fidelity.

Lastly, the phase distributions given in Equations 2.6 and 2.7 scale with respect to frequency. An alteration in frequency will therefore result in a change of steering angle, or focal length, respectively. This is an example of what is known as spatial dispersion.

Phase quantisation

Up to now, it has been taken for granted that a full phase cycle is always achievable. In practical cases, however, quite often only a finite number of phase levels can be implemented. That is to say, a 360° cycle is divided evenly into a certain number of steps. It is therefore worth considering how this phase quantisation impacts overall performance. This is illustrated in Figure 2.7. Phase distributions for deflection employing two and four evenly-spaced phase levels are presented in Figure 2.7(a) and (b), respectively. As before, the resulting far-field array factors are calculated using Equation 2.3, and the results are shown in Figure 2.7(c). The desired deflection angle corresponds to the deflector illustrated in Figures 2.6(b,e), which serves as an idealised case (i.e. un-quantised phase, or more accurately, quantisation into floating-point precision), for comparison purposes. It can be seen that the case with four phase levels has an increased sidelobe level relative to the idealised case, but still maintains a generous margin of around 20 dB between the mainlobe and the sidelobe. For binary phase (i.e. two phase levels), however, the phase distribution is symmetrical, and this is reflected in the total symmetry of the far-field pattern. This pattern of two lobes is an unavoidable (and most often undesirable) consequence of employing binary phase levels. However, the performance of this binary-phase grating still exceeds that of the magnitude-based grating given in Figures 2.5(b,e), both in terms of efficiency, and the suppression of higher-order diffraction modes.

Phase distributions for lensing that employ two, four, and eight phase levels are given in Figures 2.7 (d), (e), and (f), respectively. For comparison, an idealised case is presented in Figure 2.7(g). The corresponding focal spots are calculated with scalar diffraction theory, and are given in Figures 2.7(h-k). It can be seen that, predictably, the idealised case has the lowest fringing field effects. However, the fringing fields in the eight-level, and even the four-level case, are not particularly strong. Thus, a reasonably coarse degree of phase quantisation can still produce lensing with adequate performance. If binary phase levels are employed, as in Figure 2.7(d), then the alternating pattern of rings with 0° and 180° corresponds exactly to the zones of an amplitude-blocking zone plate. A device of this type is therefore known as a binary-phase zone

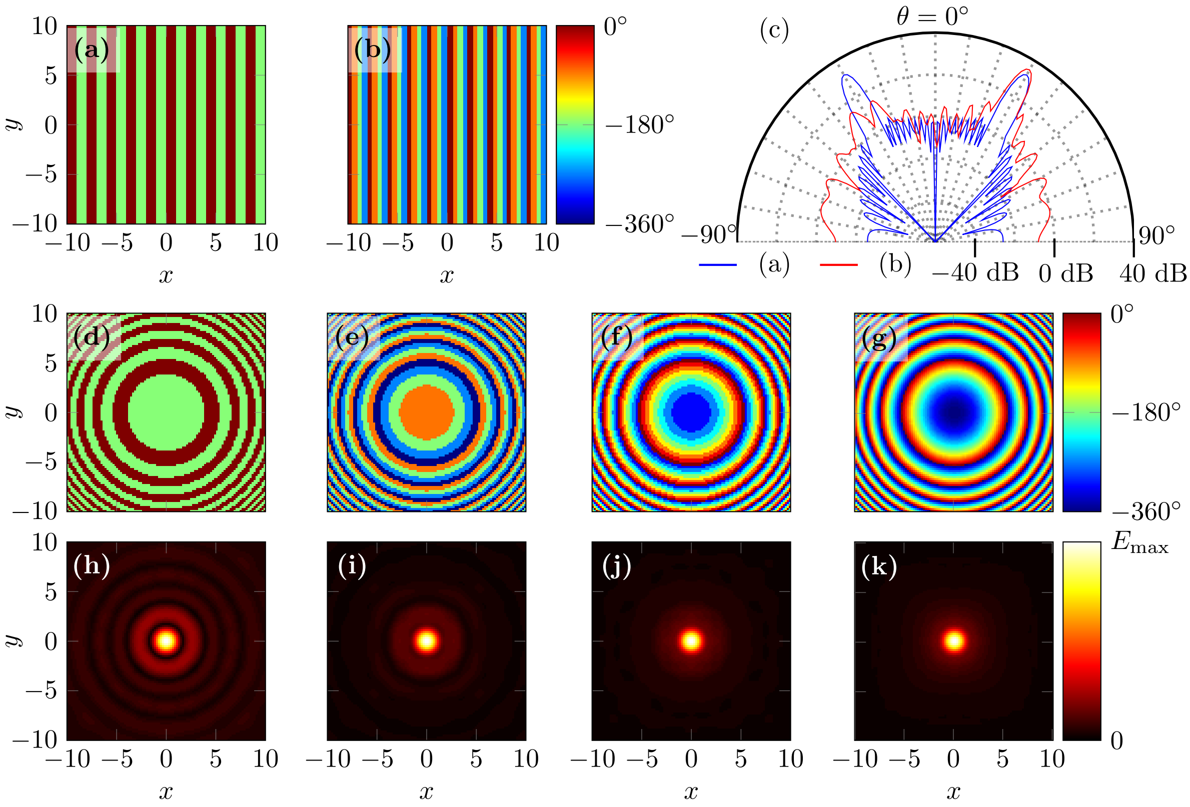

Figure 2.7. Effects of phase quantisation on beamforming. Illustration of the effects of phase quantisation on beam-control operations, showing (a) and (b) phase distributions for deflection to a 30° angle, with two and four phase levels, respectively, and (c) corresponding far-field array factors, (d-g) lensing phase distributions quantised into two, four and eight phase levels, with an un-quantised case for comparison, and (h-k) corresponding focal spots, normalised to their own respective maxima, after a propagation distance of 15 λ. In all cases, a 15λ-diameter Gaussian magnitude profile is employed as excitation in order to suppress sidelobes and fringing effects.

plate. It can be seen that the binary-phase zone plate exhibits the strongest fringing-field effects, as expected. This is analogous to the symmetrical deflection shown in Figure 2.7(c); for every ray that is deflected towards the focus, there is a ray of equal magnitude that is directed away. However, the the binary-phase zone plate still outperforms the magnitude-blocking zone plate, as its concentric maxima are less densely packed, and of lower power. The focal length in all cases presented here is 15 λ.

The efficiency penalty of quantisation can be quantified with the notion of diffraction efficiency, which is defined as the fraction of incident optical power that appears in a single diffraction order, usually the +1-order (Goodman 2005). Thus, a comparison of the maximum field intensity of the focal spots presented in Figure 2.7(h-k) provides some insight into the degree to which quantisation impairs diffraction efficiency. For two phase levels, the ratio is 47%; roughly half the energy is expressed in unwanted diffraction orders. For four, it is 83%, and for eight it is 95%. Reasonably-high diffraction efficiency is therefore accessible without large numbers of phase quantisation levels.

2.4 Techniques

Having expounded the relationship between phase and propagating beam behaviour, a few examples of popular techniques to achieve a given bespoke wavefront are introduced briefly. Phenomenological descriptions of the principles of operation are given, as this suffices to provide an overview. Later in the thesis, however, specific devices are to be introduced, and in such cases the relevant theory of operation will be provided in significantly more detail.

In this section, devices are grouped in terms of the level of technological sophistication required for implementation. In this case, the key question to consider is the specific mechanism that is exploited in order to achieve phase control, as well as the feeding architecture employed. However, it is worth noting that another author might quite validly examine the devices in question from a different perspective (eg. a more performance-oriented approach), and derive entirely dissimilar categories. Furthermore, demonstrations abound in the literature in which different principles are leveraged in tandem in order to achieve new functionality, thereby blurring the line further. This section is therefore categorised in accordance with the sensibilities of the author, and hence cannot be considered the final word.

2.4.1 Path-length techniques

As an un-guided wave travels through a medium, it acquires a phase delay that is proportional to the distance travelled, l, the index of the relevant medium, n, and the frequency of that wave,

$$\varphi_{\mathrm{PL}}(l) = -k_0 n l, \tag{2.9}$$

where k_0 is the free-space wavenumber. Thus, phase can be manipulated by controlling either the distance that a wave travels, or the refractive index of the relevant medium, or both. For instance, a wave passing through a dielectric (i.e. $n > 1$) slab experiences a delay relative to propagation in free space. By varying slab thickness as a function of lateral position, this effect can be exploited in order to achieve a given phase distribution, and in doing so, produce a desired beam-control operation. Perhaps the most widespread example of such a device is a traditional lens, such as the biconvex lens is illustrated in Figure 2.8(a). This is capable of focusing and collimating radiation, as the convex spherical curves that define its shape are closely related to the spherical phase characteristic described in Equation 2.7. Note, the operation of a lens is most commonly understood in terms of refraction, i.e. the curvature of the dielectric produces the bespoke lensing operation in accordance with Snell's law and ray-tracing optics. That said, both ray-tracing and phase delay paradigms of analysis will show the same lensing behaviour for the biconvex lens. However, one interesting result arises directly from the ray-tracing paradigm; Snell's law, which mathematically describes refraction at an index boundary, is independent upon frequency for a non-dispersive dielectric, and hence the directionality of individual rays transmitted through the lens device is dictated by curvature exclusively. A non-dispersive lens will therefore exhibit the same

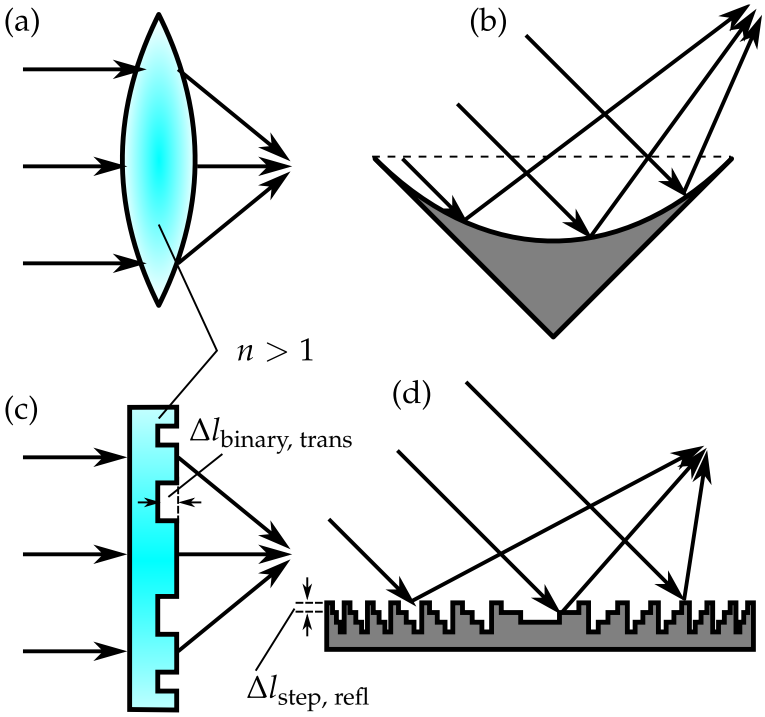

Figure 2.8. Path-length optics. Examples of lensing operations performed using path-length techniques shown in cross-sectional view, including (a) a biconvex lens, (b) an off-axis parabolic reflector, (c) a binary-phased zone plate operating as a geometric lens, and (d) a stepped-phase device operating as an off-axis parabolic reflector.

behaviour, and have the same focal length, for any choice of operating frequency. As a result, a lens of this type has extremely high bandwidth, which is advantageous for many applications. Another way of understanding this property is that the path-length oriented delay given in Equation 2.9 scales with frequency in the same way that Equation 2.7 does, and hence it achieves the required phase distribution for all frequencies, provided refractive index remains constant.

A dielectric medium is not necessarily required for control over the path length. Similar functionality can be achieved using a reflector of the appropriate curvature, as illustrated in Figure 2.8(b). The highest point on the curve is indicated by a dashed line, and the greater the deviation below this line, the greater the delay of a reflected ray. In this case, the curve follows a parabola, which is closely related to the shape of the geometric lens given in Figure 2.8(a), and hence this reflector is intended to perform a lensing operation. However, a crucial difference is that excitation is of an oblique angle of incidence. This is a common choice with reflector devices to mitigate what is known as "feed blockage," i.e. a collision between the focal point and the incident beam, which is often undesirable for practical reasons. Devices of this type are termed off-axis parabolic reflectors, and it is noted that the desired phase distribution will need to be adjusted in order to account for the oblique incidence. As before, the behaviour of this device can be understood equally well under both a ray-tracing and a phase-delay paradigm. Additionally, much like with the previous example of a biconvex lens, the definition of the focal length is invariant upon frequency, and hence the off-axis parabolic reflector has high bandwidth as well. In fact, the bandwidth of the parabolic reflector can exceed that of the lens in practical cases. This is because realistic dielectric media are always dispersive to some degree, resulting in unintended variations to focal length. On the other hand, a parabolic reflector makes use of no such dielectric medium, and hence there can be no possibility of dispersion.

The previous two examples are both constructed using precisely-defined geometric curves, and hence they are often termed geometric optics. A consequence of this is that the topological scale of such devices is significant, making them bulky by nature. Furthermore, as aperture (i.e. the lateral extent of the device) is increased, these curves will rapidly grow to impractical scales, and this places undesirable limitations on the device. Both antenna theory and optics will attest to the benefits of large aperture, either in the form of antenna gain or imaging resolution, and hence this impacts performance. In short, although curve-oriented devices of this kind have exceptional bandwidth, they also tend to be quite bulky, and this can limit their aperture and performance. Such devices are therefore most often found in optics laboratory environments, in which their bulk is of little consequence, their electrical size is significant at a modest physical scale, and their bandwidth is most welcome. Additionally, radio and microwave applications in which the antenna is fixed in place, especially for ground stations in extra-planetary communications and radio astronomy applications, will most often make use of antennas that are closely related to the devices discussed. This is because such antennas provide the highest gain, which is of great assistance over long distances, and their fixed position means their physical size can be accommodated.

If compactness is of higher priority than bandwidth, a stepped-phase arrangement may be preferable. For such a device, first an operating frequency is selected. This allows phase to be wrapped to a 360° cycle, which does away with the need for the topological size to grow indefinitely with aperture. Subsequently, a suitable level of phase quantisation is selected, and this is translated to an appropriate step size. Two examples of such devices are illustrated in Figure 2.8(c,d). The first case is a transmissive binary-phased zone plate, which alternates between two values of thickness. The distance between the two values of device thickness, Δl, corresponds to a π-phase change,

$$\Delta l_{\text{binary, trans}} = \frac{\lambda}{2(n-1)}. \tag{2.10}$$

Thereafter, the pattern of grooves can be determined in accordance with the switching radii given in Equation 2.5. A diagram of such a structure is given in Figure 2.8(c). The second example, shown in Figure 2.8(d) is a stepped-phase version of a parabolic reflector. The diagram shows four steps, but any integer $\chi > 1$ can theoretically serve for this purpose. It is noted that a higher value of χ will result in progressively increasing performance, as discussed in Section 2.3.2, and will ultimately converge on a phase distribution that is continuous between wrap-around points. The required spacing between phase levels is dependent upon the choice of angle of incidence, θ,

$$\Delta l_{\text{step, refl}} = \frac{\lambda}{2\chi\cos\theta}. \tag{2.11}$$

It follows from this expression that the achievable level of phase quantisation is intrinsically linked to the selection of operating frequency and the tolerances associated with step height Δl.

The aperture of these two previously-mentioned stepped-phase devices can be extended indefinitely, without increasing the out-of-plane size, and hence they tend to be more compact than optics based on geometric curves. However, a drawback of this approach is that the specific thickness of the required steps, Δl, depends on frequency, as shown in Equations 2.10 and 2.11. A consequence of this is that the phase levels become increasingly erroneous as frequency deviates from the operating frequency, resulting in reduced bandwidth. Additionally, lensing devices of this type experience spatial dispersion, i.e. variation in focal length with respect to frequency, due to the phase wrap-around after a full cycle. This phenomenon is best understood in terms of a binary zone plate. If wavelength is insignificant relative to focal length, as is most often the case, then Equation 2.5 can be approximated with,

$$r_m = \sqrt{m\lambda F}, \quad m = 1, 2, 3, \ldots \tag{2.12}$$

It can be seen that, if radius is kept constant, the following relationship of proportionality between frequency and focal length arises,

$$\lambda \propto \frac{1}{F}. \tag{2.13}$$

Therefore, an increase in frequency results in an increase in focal length. Although this result has been derived for a binary zone plate, a similar rationale also applies to any given device with wrapped-phase. This is because, as shown in Section 2.3.2, there is a correspondence between two consecutive switching radii of a binary-phased zone plate and a complete phase cycle of a continuous-phase device with the same focal length. As a result, the bandwidth of such a device is inferior to that of optics based on geometric curves.

2.4.2 Phased arrays

From an antenna theory perspective, the most prominent and well-known technique associated with beam steering, beam forming, or beam manipulation in general is the phased array antenna. Such a device is essentially a direct, practical realisation of the array theory paradigm introduced in Section 2.2.3; each element in an array of identical, individually-excited antennas possesses their own particular amplitude and phase, and the overall pattern of excitation dictates the behaviour of the radiated beam (Balanis 2016). If the phase is controlled with actively-tunable phase shifters, the radiation pattern can be dynamically-scanned. A schematic diagram of a linear, 1D phased

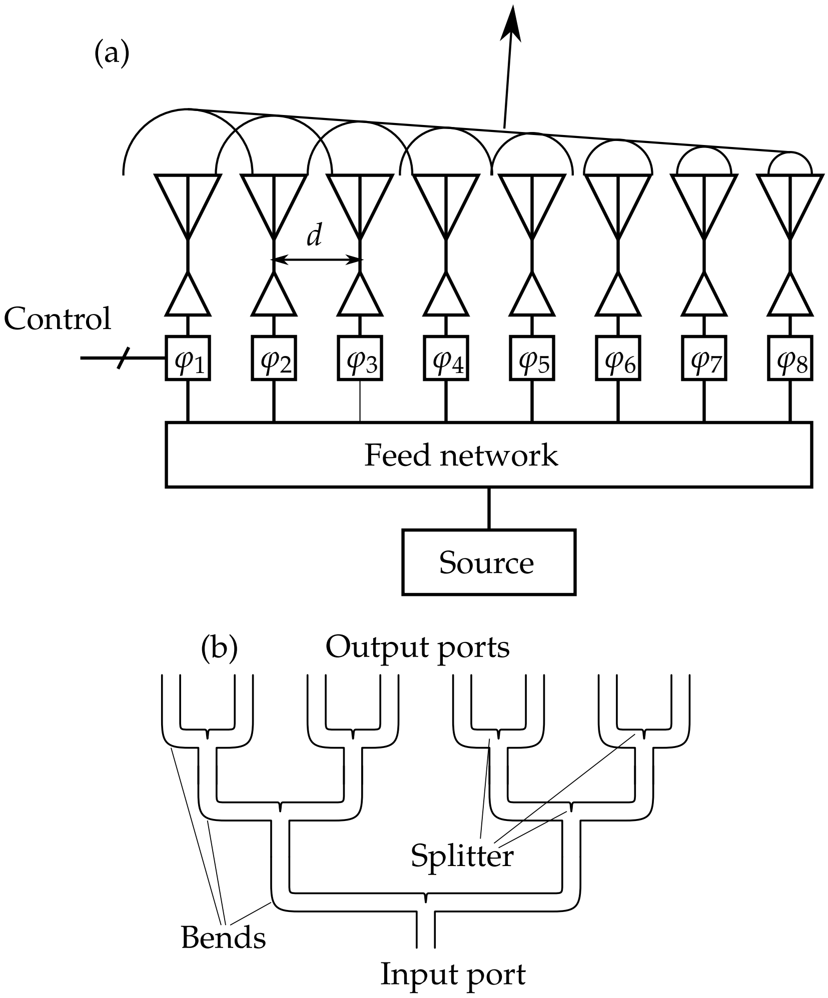

Figure 2.9. Phased array. Schematic of (a) a phased array antenna with active phase control, showing a basic beam-steering operation, and (b) an example of a feed network that splits a single input into eight outputs, of equal magnitude and phase. Note the tracks in this schematic may equally represent a transmission line or a waveguide.

array antenna of this type, with eight elements, is provided in Figure 2.9(a). In this example there is a progressive phase difference, $\Delta\varphi$, between adjacent elements,

$$\varphi_n = \varphi_{n-1} + \Delta\varphi. \tag{2.14}$$

This corresponds directly to the phase distribution for a deflector given in Equation 2.6, and as before, beam deflection off the normal direction results. The relationship between the progressive phase, $\Delta\varphi$, and the output steering angle, θ_s, is trivially derived from Equation 2.6, by substituting $\Delta\varphi$ for $\varphi(d, 0)$,

$$\Delta\varphi = k_0 d \sin(-\theta_s), \tag{2.15}$$

where it is noted that the spacing between antenna elements, d, must be lower than a free-space wavelength. Failure to observe this condition will result in the existence of grating lobes, which are so-called because they are the product of diffraction effects, and hence their directionality is dictated by the grating equation given in Equation 2.4. Beam steering of this type is certainly one of the more popular and well-known applications for phased arrays, but as mentioned in Section 2.3.2, shaped-beam techniques provide significant freedom for defining a radiation pattern.

A phased array antenna of this kind is chiefly dependent on an efficient feed network, in order to separate the power from a single source into several individual feeds. If, on the other hand, multiple independent sources were to be used, they would not be coherently-phased (i.e. their relative phase is not explicitly known or controllable), which makes phased array operation impossible. One notable exception includes separate oscillators that are electronically coupled, but there are practical limitations surrounding the number of elements that can be combined in this way. An example of a feed network is given in Figure 2.9(b), where it can be seen that numerous two-way splitters and bends are cascaded in order to distribute the energy from the input port to the output ports. The performance of a feed network is dependent on the existence of efficient guided-wave structures. Such components are certainly freely available at radio and microwave frequencies in the form of microstrip transmission lines and hollow metallic waveguides (Pozar 2009), as metals are good conductors at these frequencies. Similarly, in the optical range, advances in nanophotonics have resulted in numerous examples of dielectric waveguides (Liu *et al.* 2010). In the terahertz range, however, there is a pronounced absence of efficient guided-wave structures. For this reason, a feed network of any reasonable size is not practical in the terahertz range due to dissipation.

Of equal importance to the feed network is the electronically-controllable phase shifter. Such components are mature in the microwave range, and have been demonstrated in the millimetre range several decades ago (Jacobs and Chrepta 1974), but in the terahertz range, such components are not available. In the optical range that lies beyond, approaches such as thermo-optical tuning (Sun *et al.* 2013a) are generally preferred for active phase control. For best versatility, response time, and control, however, electronically-controlled solutions are generally preferable. Lastly, to-date there has been no demonstration of an electronically-controlled phase modulator in the terahertz range that is amenable to integration with a phased array of this type, casting the practicality of a classical phased array antenna in the terahertz range into further doubt.

2.4.3 Guided-wave techniques

As discussed in Section 2.4.1, a wave propagating through a medium will acquire phase delay that is proportional to the distance travelled, and this can be employed to construct optics. Similarly, a phase delay is acquired during the propagation of a guided wave, and this can likewise be exploited for beam-control techniques. This approach is naturally amenable to compact and integrated devices, which is highly beneficial to practical applications. In cases in which beam-control devices are intended to be portable or aerodynamic, for example, it is quite clear that an integrated solution is more attractive than, say, a lens separated from a feed by a focal length.

A leaky-wave antenna is essentially a waveguide or transmission-line structure that progressively radiates some of the energy of the travelling wave to free space. This can be performed either by defecting the guided-wave structure periodically with scatterers, or with an opening that is continuously radiating along the length of the device. Emphasis is placed upon the former case for this discussion, but a more detailed summary of travelling wave antennas of this type is provided in Walter (1970).

As a propagating wave acquires a delay that is proportional to the distance covered, scattering energy at periodic intervals along the propagation direction will yield a progressive phase difference that depends on both the spacing between the scatterers and the phase velocity of the travelling wave, as illustrated in Figure 2.10(b). A progressive phase difference in an array of uniformly-spaced radiators is a requirement for beam steering, as discussed in the previous section, Section 2.4.2. Thus, by "leaking" a small portion of the energy of the travelling wave at said periodic points, a leaky-wave antenna achieves beam steering. A straightforward example of a leaky-wave antenna is a rectangular waveguide with periodically-spaced apertures on top that behave as scatterers, as illustrated in Figure 2.10(a). In this instance, the spacing d_{Leaky} is equal to the guided wavelength of λ_{B}, and hence the radiated field is in-phase at all apertures for this frequency. The overall radiated beam at this frequency is therefore directed at surface-normal, or broadside. However, note that reflections from the apertures that are internal to the guided-wave structure will also be in-phase, resulting in constructive interference, and effectively producing a stopband at this frequency. This impairs radiation efficiency, and is not desirable in practice. Nevertheless, this particular leaky-wave antenna is selected for this discussion as it is valuable as an instructive and general example. The in-guide wavelength λ_{A} is larger than the period separating the apertures. This causes a progressive phase lead in the excitation of the apertures,

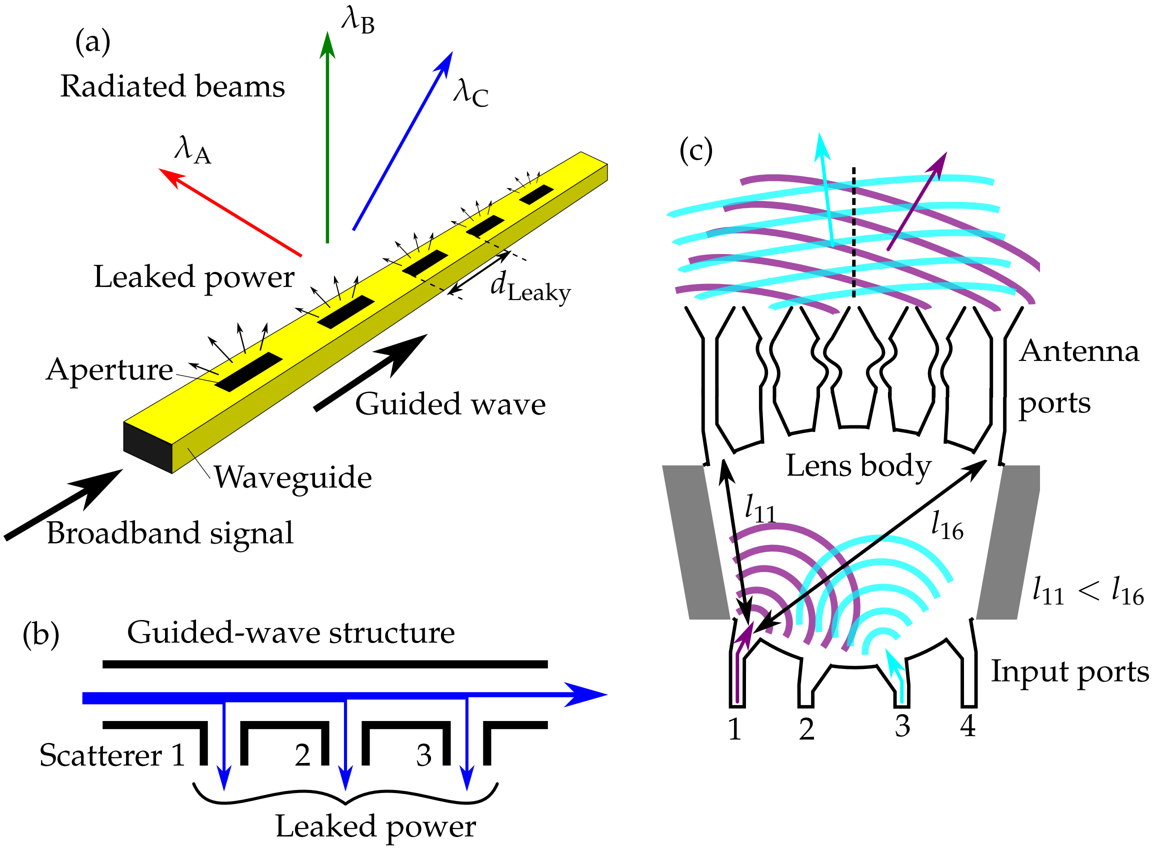

Figure 2.10. Guided-wave beam-control techniques. Beam-control techniques based on waveguides and transmission lines, showing (a) An example of a leaky-wave antenna in a waveguide, using rectangular apertures as scatterers, resulting in the steering of different frequencies to different angles in the far field (note $\lambda_A > \lambda_B > \lambda_C$), (b) a simplified, general diagram of a portion of a leaky-wave antenna, showing the path length in the guided-wave structure that separates the excitation of adjacent scatterers, resulting in progressive phase, and (c) a basic Rotman lens, with four input ports and six antenna ports. Input ports 1 and 3 are excited in order to illustrate the beam control mechanism. Grey regions show absorbing materials that prevent multipath within the lens body.

which in-turn produces steering away from the propagation direction of the guided wave. Conversely, smaller λ_C results in the progressive phase lag that produces steering towards the guided-wave propagation direction. Thus, the leaky-wave antenna produces frequency-scanning, in which the directionality of the output beam is dependent upon frequency, not unlike a diffraction grating. This is not as desirable as broadband beam-scanning, but is still valuable for many applications including imaging (Lettington *et al.* 2003) and radar (Murano *et al.* 2016).

A Rotman lens is another form of beam-control device based on guided-wave structures. This device is centred around a "lens body," which is a component that is of the same composition as the associated waveguide or transmission line, but is of a larger area. Thus, waves are free to propagate in any in-plane direction over the short distances within this lens body in the form of 2D-confined TEM waves, as opposed to being confined to specific travelling wave modes. This lens body is generally composed of a parallel-plate waveguide, and as a consequence, dispersion is significantly reduced. Ports feed into the lens body, and there are two sets of ports, namely "input ports" and "antenna ports."

A highly simplistic example of the Rotman lens concept is illustrated in Figure 2.10(c), with four input ports and six antenna ports. When operated as a transmitter, specific input ports are excited, and the energy that feeds into the lens body spreads out in its less-confined (albeit still restricted to in-plane propagation) environment, due to the principles of diffraction discussed in Section 2.2.1. In this example, sections of the lens body perimeter that are not coupled to either input or antenna ports are bordered by absorbing material, which is shown in grey. The absorbers are included to prevent multipath within the lens body. For a given input port, some energy will be accepted into every antenna port, but in each case the path length separating the input and antenna ports is unique to that particular antenna port. Furthermore, the ports are arranged such that excitation at an input port produces progressive phase at the antenna ports, and the ports follow specific curves that are engineered for this property using a ray-tracing approach. Note the waveguide or transmission line that connects the antenna port to the radiator is serpentined where appropriate, in order to compensate for differences in distance between the lens body and the output plane, and maintain the progressive phase. For the leftmost input port, it is clear to see that the distance to the leftmost antenna port (l_{11}) is shorter than the distance to the rightmost (l_{16}). Thus, the leftmost port produces a large negative progressive phase (when viewed from left-to-right), resulting in a beam projected strongly to the right, as illustrated in Figure 2.10(c). Closer to the centre, the progressive phase is less pronounced, leading to a weaker angle, and so on. Input ports on the right will steer towards the left in similar fashion. The selection of input port will therefore determine the output beam direction. Additionally, the geometric nature of this beam control mechanism lends itself to large bandwidth, in a manner similar to the physically-shaped optics discussed in Section 2.4.1. Note that, technically, beam control of this kind is not beam-scanning, but rather it is a switched-beam operation, as the output beam directionality is ultimately a choice within a finite set of options. However, the number of available angles increases with the number of input ports, and hence very fine angular resolution is achievable with a large number of ports.

Seminal work on Rotman lenses was performed many decades ago in the microwave range (Rotman and Turner 1963), and the technique has since been demonstrated in the millimetre-wave range (Hall *et al.* 2002), as well as at frequencies approaching the optical range (Sparks *et al.* 1998, Sparks 2000), which illustrates the potential for this concept to cover the electromagnetic spectrum. Additionally, the bandwidth of a Rotman-lens far exceeds that of a leaky-wave antenna. This is because the output directionality and beam-shape is better preserved by a Rotman lens with respect to frequency, whereas a leaky-wave antenna is frequency-scanned, as discussed above. They are combined in this section because the phase delay that makes beam-shaping possible is acquired in the propagation of the guided wave, and not because they exhibit equivalent functionality; the correspondence is simply one of underlying technique.

The above examples present linear, 1D arrays of radiators that jointly output a single beam in the far field, and the directionality of that beam is prescribed by progressive phase in the excitation of these radiators. Thus, the analogy to traditional phased arrays, as they are described in Section 2.4.2, is clear. This illustrates that it is possible to achieve similar functionality to a traditional phased array without the need for phase shifter devices, which may not necessarily be available.

2.4.4 Passive arrays

It is asserted in Section 2.4.3 that Rotman lenses are, conceptually, a combination of phased array antennas and geometric optics. This is because they employ path length for phase delay, as with geometric optics, but the energy is coupled to free-space via discrete radiators, as with a phased array. A similar statement can be made of the reflectarray and transmitarray antennas (henceforth “passive arrays” when considered collectively) that are to be covered in the present section, albeit in a different way. In this case, phase delay is not acquired gradually as the wave propagates through a medium, but rather it is an abruptly-introduced phase discontinuity, not unlike the phase shifters that are core to the operation of phased array antennas, as discussed in Section 2.4.2. However, in the case of passive arrays, the excitation is not provided

Table 2.1. Comparison of beam-control techniques. A summary of the conceptual differences separating distinct approaches to achieving a given phase front for beam control purposes. As in Sections 2.4.1 to 2.4.4, the categorisation is made in terms of two distinguishing features, with two options each, resulting in a total of four categories. The first is the technique with which the bespoke relative phase is achieved. This can be acquired gradually, as a wave propagates in a given medium, or instantaneously, as with a resonator or phase shifter. The second is the specific nature of the field source, which is either a discrete radiator or antenna, or an incident wave that impinges from free-space.

Field source	Origin of phase delay	
	Path-length propagation	Phase discontinuity or shifter
Discrete radiator	2.4.3—Guided-wave techniques	2.4.2—Phased arrays
Free-space excitation	2.4.1—Path-length techniques	2.4.4—Passive arrays

by a feed network or guided-wave structure. Rather, an array of phase-discontinuity-producing elements is collectively fed by a free-space beam, much like the geometric optics presented in Section 2.4.1. Table 2.1 is provided to clarify this comparison.

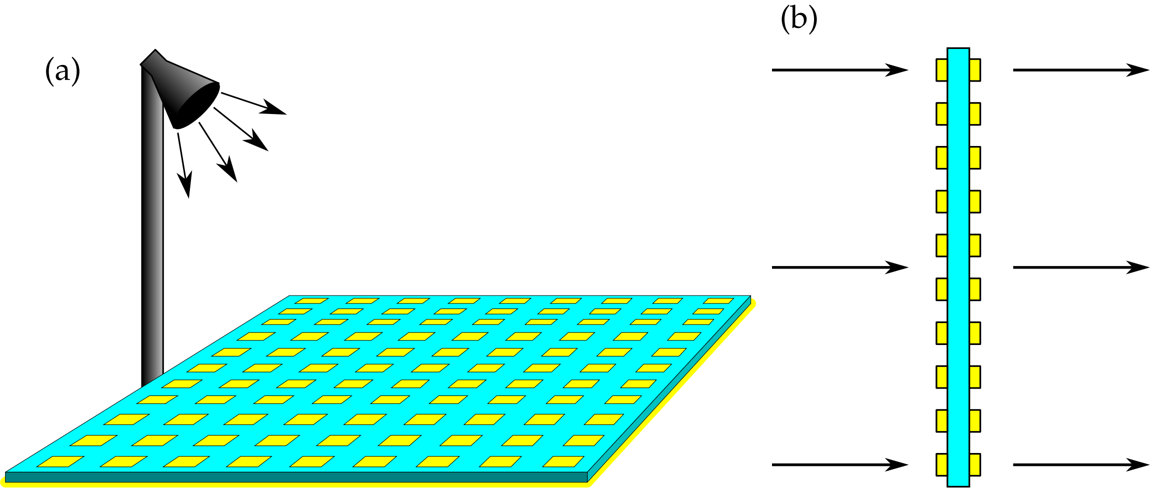

Figure 2.11. Reflectarrays and transmitarrays. Operation of passive array, with individual array elements given in yellow, showing (a) excitation of a reflectarray by a feed antenna, and (b) transmission through a transmitarray. Note that specific beam-manipulation operations are not shown, so as to preserve the conceptual generality of these devices.

For a passive array, the individual elements locally alter the phase of the incident wave, by an as-yet unstated mechanism to be discussed in Section 2.5, and then re-radiate directly back out to free space. The aggregation of local alterations in phase is engineered to produce some desired overall phase distribution. This approach has the advantage over traditional phased array antennas of not requiring a feed network, as well as supporting far greater overall antenna apertures. Furthermore, passive arrays are planar, and hence they have the advantage of being far more compact than geometric optics, and even more so than stepped optics. Lastly, passive arrays generally offer high efficiency, and the potential for birefringence (i.e. independent control of different polarisations), which are both highly beneficial properties.

A passive array of this type is essentially a planar array of regularly-spaced elements that are fed from free space, as aforementioned. Each imparts some particular phase shift to the incident terahertz waves, and the aggregation of these phases produces a phase front with some overall desirable beam-shaping behaviour. This offers a high degree of control over the resultant wavefront, and facilitates a broad selection of beam-control operations that includes those discussed in Section 2.3. Impinging radiation can either be reflected from this planar structure, resulting in a reflectarray, or transmitted through it, as in a transmitarray. Both classes are illustrated in Figure 2.11, where it is noted that the reflectarray is excited by a feed antenna, in much the same way as a dish antenna. There are advantages and trade-offs in each case; a transmitarray is generally more susceptible to loss, and may require either polarisation converters or multi-layer configurations, as illustrated in Figure 2.11(b), in order to achieve the required phase tunability range. On the other hand, a reflectarray has added complications due to feed blockage. Thus, the choice of reflectarray or transmitarray is dependent on the particular requirements of the specific application at hand. Given the power-related constraints discussed in Section 1.1.1, the reflectarray is preferable in the terahertz range due to higher efficiency, and will be a greater focus for the purposes of this thesis.

A brief summary of the historical development of the reflectarray antenna is as follows. The reflectarray concept was originally conceived of in the microwave range in the early 1960's, in the form of a bulky array of shorted waveguides of various lengths (Berry *et al.* 1963). Each waveguide is, in this case, essentially a reflective phase shifter. This design was proposed as a versatile alternative to physically-shaped reflectors, providing far greater control over radiation characteristics. In subsequent decades, progress in the field of reflectarrays was accelerated by the advent of printable microstrip antenna technology, as it enabled the development of planar and compact resonator elements (Malagisi 1978, Pozar *et al.* 1997). For the first few decades following their inception, the development of reflectarray antennas remained limited to the the microwave range exclusively. However, more recently the concept has seen adoption in other frequency ranges such as the optical (Ahmadi *et al.* 2010, Zou *et al.* 2013, Zou *et al.* 2014a, Yang *et al.* 2014b), and terahertz ranges (Hasani *et al.* 2016), which illustrates their true scope across the electromagnetic spectrum. This technique will therefore be a major focus of this doctoral thesis.

2.5 Passive resonators

The phase discontinuity-producing elements of a reflectarray of the type discussed in Section 2.4.4 are generally implemented using passive resonators. As devices of this kind are a focus of this doctoral thesis, a brief discussion of the principles of operation that govern passive resonators is given in the present section. This section focuses on reflective resonators, for reflectarray antenna devices, but similar principles of operation apply to transmissive devices.

An infinite array of identical, single-mode reflective resonators that interacts with incident free-space fields can be modelled as a one-port network with complex reflection coefficient Γ. This implies that all of the energy reflected from the array is scattered in the specular direction, which is only valid if the lattice constant is subwavelength. If, on the other hand, the inter-element spacing is greater than or equal to a wavelength, then energy will be diffracted into grating lobes (Balanis 2016). This is because the array effectively behaves as a diffraction grating, and hence it scatters radiation into multiple directions, as dictated by its periodicity. In some cases, the use of inter-element spacings of less than a sixth of a wavelength is advocated, in order to achieve a smoother phase gradient in an inhomogeneous array (Lomakin *et al.* 2006, Monticone *et al.* 2013). In practice, however, a half-wavelength spacing is sufficient for most applications. Such larger inter-element spacings will in-general provide a larger phase tunability range, and hence an inter-element spacing close to this value is adopted for all of the devices demonstrated in the present work.

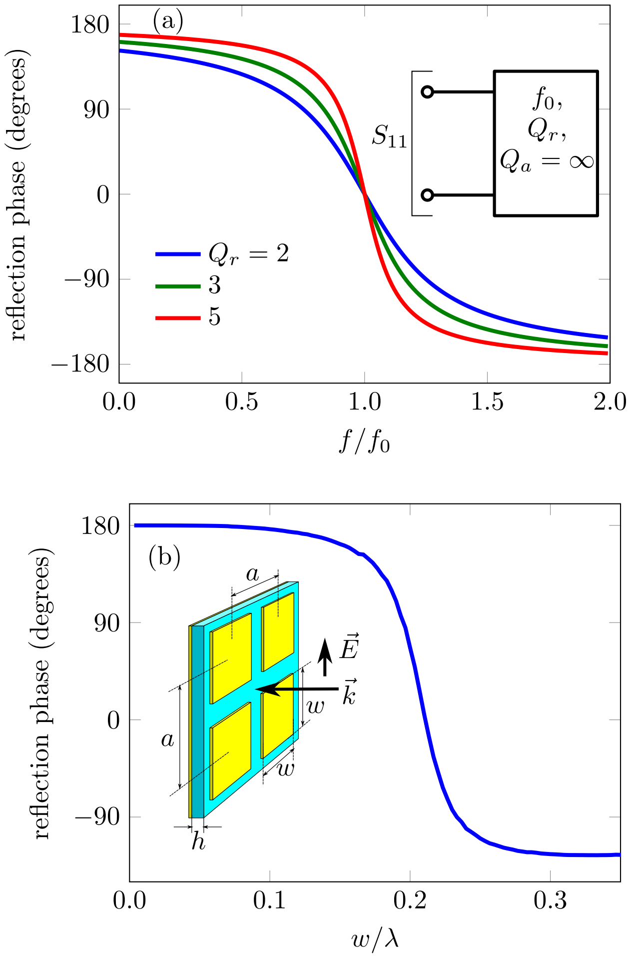

Figure 2.12. Patch resonator theory. Phase control using passive reflective resonators, presented (a) abstractly, as reflection coefficient of a lossless one-port network, and (b) with the reflection coefficient of an idealised metal patch array, in which $a = \lambda/2$ and $h = \lambda/15$. The relative permittivity of the dielectric spacer is equal to 4. After Headland *et al.* (2017).

The following expression for the reflection coefficient of a resonator is employed to explore the connection between passive resonators and phase control (Qu *et al.* 2015),

$$\Gamma = \frac{2\pi f_0 Q_\mathrm{a}}{\frac{Q_\mathrm{a}}{2} + \frac{Q_\mathrm{r}}{2} - jQ_\mathrm{r}Q_\mathrm{a}\left(\frac{f}{f_0} - 1\right)} - 1. \tag{2.16}$$

This models a resonator with a single mode of resonance, which is described by the resonance frequency f_0, the radiation quality factor Q_r, and the absorption quality factor Q_a. The latter two quantities relate to energy exchanged with free space, and energy lost to dissipation, respectively. For devices relevant to the present work, the condition $Q_\mathrm{a} \gg Q_\mathrm{r}$ is assumed, which describes efficient resonators with a large phase tunability range. An ideal case of this, in which no energy is dissipated, is presented in Figure 2.12(a). This shows very clearly that, on-resonance, the response is purely real, and reflection phase is 0°. Thus, the reflection response at the resonance frequency is identical to that of a perfect magnetic conductor (PMC), and hence a resonator of this kind can be considered to exhibit a magnetic response. By contrast, a perfect electrical conductor (PEC) also exhibits purely-real reflection response, but the reflection phase is ±180°. Whilst a resonator of this type exhibits a magnetic response on-resonance, it approaches an electrical response away from resonance, heading towards $+180°$ as $f \rightarrow 0$, and $-180°$ as $f \rightarrow \infty$. Thus, if the frequency of operation, f, is gradually detuned from the resonance frequency, f_0, the resonator can cover a range of reflection phase close to 360°. The operation of a given reflectarray antenna is therefore dependent on the capacity to tune the resonance frequency, f_0, of a passive resonator away from the operating frequency of f. In the present work, this is achieved by varying the geometry of a given resonator, but it is also possible to tune a reflective resonator electronically, at least in the microwave range (Sievenpiper *et al.* 2003). When such technology is combined with a reflectarray antenna of the sort described in Section 2.4.4, this can be employed to realise beam-scanning functionality comparable to a traditional phased array—without the need for a feed network.

In order to illustrate the technique of tuning resonance frequency by means of geometric parameters, an idealised example is contrived, and is shown in the inset of Figure 2.12(b). In this example, an infinite, homogeneous array of square metallic patches is separated from a ground plane by a dielectric spacer ($\epsilon_r = 4$), and is excited with normally-incident radiation. Both the dielectric and the metal are lossless, and hence $Q_a = \infty$. This structure is investigated with parametric analysis, which is the process of varying a geometric parameter of a given device in order to observe the alteration in its response. The analysis is performed with full-wave simulations (using CST Microwave Studio), and the parameter of interest is patch side-length. Results in Figure 2.12(b) show decreasing phase response with respect to increasing patch width w. This is because an increase in patch dimensions will result in an increase in the wavelength of the corresponding resonance frequency. Thus, the phase characteristic shown in Figure 2.12(b) corresponds closely to that which is shown in Figure 2.12(a); a larger patch results in a lower value of f_0, and hence a higher value of f/f_0. It is also worth noting that this square patch resonator is just one example of a prospective array element (Pozar *et al.* 1997), and that there is significant choice and freedom in the selection of the individual resonator, with benefits and trade-offs in each case.

It can be seen from Figure 2.12(a) that the gradient of the phase descent depends on the radiation quality factor Q_r. A larger value will result in a steeper descent, and in practical cases, can produce a larger phase tunability range. However, a steep phase gradient is inherently more sensitive to tolerances, as a minor change to resonance frequency produces a large change in phase response. There is evidently a trade-off associated with the quality factor. Good practice is to select the minimal value of quality factor that provides the required phase tunability range.

2.5.1 Passive resonators in reflectarray design

In order to realise a reflectarray antenna, the two concerns of resonator design and phase distribution are integrated, and the result is a nonuniform array of reflective resonators. In this context, the individual resonator is most often referred to as a unit cell, as the resonator is modelled as a single element in an infinite, periodic array of uniform elements. The phase response of each unit cell in the array is determined by the desired phase distribution, eg. with Equations (2.6) or (2.7), whilst accounting for the phase of the incident wave. The resonator dimensions needed to achieve this phase response are determined by parametric analysis. Each resonator thus imparts a local phase response on the reflected field, and the overall phase distribution is the aggregation of all such responses. The design flow of a reflectarray antenna is illustrated in Figure 2.13. In such an approach to reflectarray design, parametric analysis is employed in order to determine the mapping from device dimensions to phase response. This mapping is subsequently reversed, and desired phase response at a given point is used as a look-up key to extract the corresponding unit cell dimensions that produce this phase response.

There are some well-known limitations and approximations to this approach to reflectarray design that pertain to inter-element coupling. Firstly, the design of an individual resonator typically operates under the assumption of an infinite array of identical elements with uniform plane-wave excitation. In practice, however, excitation is provided by nonuniform sources such as Gaussian beams. Thus, the amount of energy incident upon a given element may differ from that of its neighbours, which can influence inter-element coupling effects. Secondly, the reflectarray must necessarily be nonuniform in order to achieve any useful beam-shaping operation, and this is not consistent with the unit cell assumption of total uniformity. Thus, the fact that neighbouring elements are

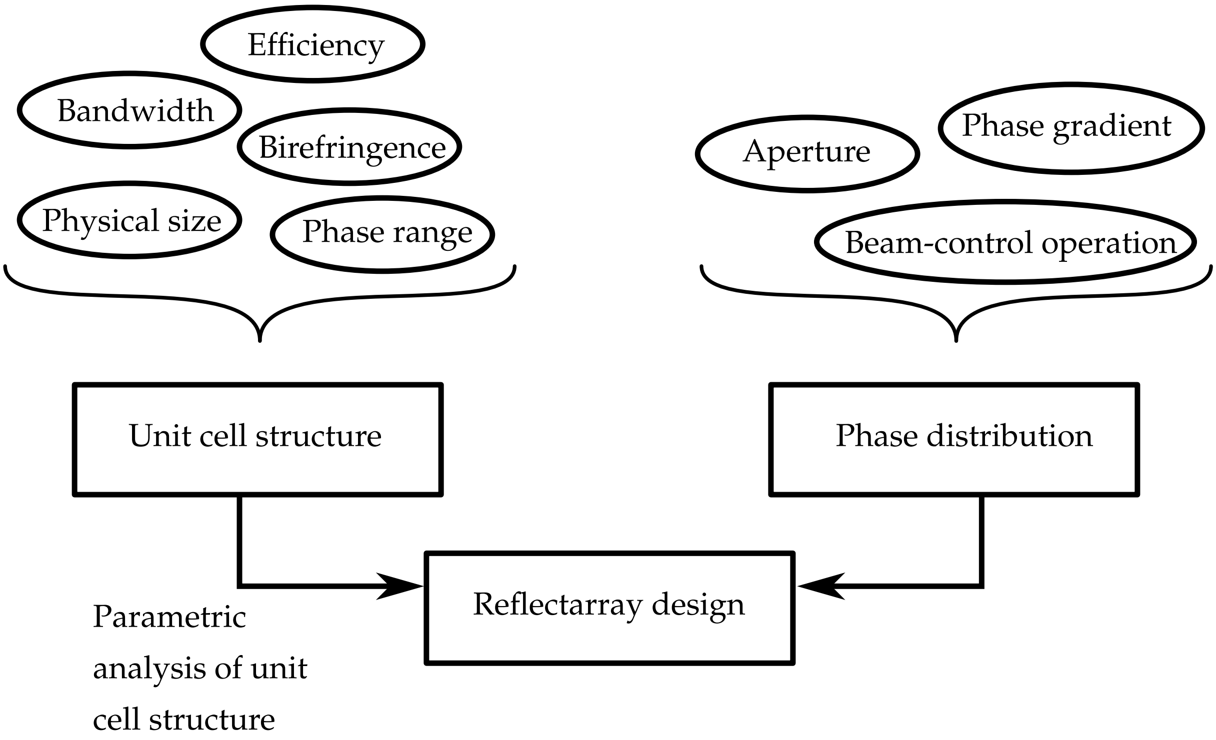

Figure 2.13. Reflectarray design. Combination of unit-cell design considerations with the desired phase distribution in order to realise the total array design.

not identical breaks resonator symmetry, which can excite asymmetrical modes of resonance, and significantly impact the resultant phase response (Singh *et al.* 2011). The first issue can be discounted by the fact that the field distribution changes gradually, and hence a given element effectively experiences locally-uniform excitation. The second issue, however, is more challenging to address. Most often, it is asserted that the change in resonator dimensions is sufficiently gradual that differences between immediate neighbours is negligible, or very close to negligible. This is often referred to as the assumption of “local periodicity.” However, this ceases to be accurate when steep phase gradients are required, for example, when designing flat lenses of high numerical aperture. In some such cases, parametric unit cell analysis is treated as a guideline, and individual elements are optimised in their array configuration, but this becomes extremely labour-intensive for any reasonably-complicated design.

2.6 Conclusion

Basic principles for understanding the propagation of electromagnetic waves are presented in this chapter. Scalar diffraction theory and array theory are provided as means to quantify this phenomenon, and are subsequently employed to investigate wavefront engineering employing both magnitude and phase-based techniques, for a variety of beam-control operations. It is found that phase is unambiguously the superior choice for beam control, in terms of both performance and versatility. Some practical techniques to achieve a bespoke phase front are briefly introduced, in the form of geometric optics, phased array antennas, guided-wave techniques, and passive arrays. The focus of this chapter is subsequently refined to reflectarray antennas, a subset of passive arrays, and the operation and design of such a device is described in more detail, as this beam-control device is most relevant to the present doctoral thesis.

The following chapter will give examples of demonstrations of terahertz beam control that make use of the principles and techniques that have been introduced in this chapter.

Chapter 3

Background

PREVIOUS demonstrations of beam control in the terahertz range are presented. As opposed to the preceding chapter, in which principles and techniques are given in a general and abstract way, this chapter discusses the performance, features, advantages, and drawbacks of specific designs that have been reported in the literature. This is intended to provide some much-needed context to the later chapters of this thesis, and show how the contributions therein address the limitations of existing work by investigating as-yet unexplored opportunities.

3.1 Introduction

A review of beam-control devices reported in the literature is given in this chapter. The scope of this review is limited to the terahertz range exclusively, and hence even closely related beam-control devices in the optical or microwave ranges are not covered. Additional to that, articles that lack a practical demonstration component have been omitted. This is because the potential value of a given design is always contingent on the possibility of a physical realisation, no matter how sophisticated or innovative it is. Furthermore, modelling without associated experimentation is of limited utility to evaluate the performance of a device. This is because all forms of modelling must be approximations to a degree, and the validity of these approximations cannot be confirmed without a physical demonstration. Another important point regarding the scope of work reviewed in this chapter is that demonstrations of static beam control, as well as devices with dynamic scanning capabilities, are both included. Although the contributions to be reported in this thesis fall in the former category exclusively, the development of the two is intrinsically linked.

The organisation of this chapter is intended to reflect the conceptual flow of the preceding chapter. Section 3.2 briefly covers demonstrations of magnitude-based beam control in the terahertz range, utilising the principles discussed in Section 2.3.1. Subsequent sections present a deeper summary of various implementations of the more popular and useful phase-based paradigm. Sections 3.3 through 3.7 correspond to the organisation of Section 2.4; covering path-length optics, phased array antennas, guided-wave techniques, and passive arrays, respectively. It is noted that passive arrays are broken into two sections, covering terahertz transmitarrays and reflectarrays separately, as such devices are a major focus of this thesis. Lastly, Section 3.8 highlights some promising directions for research into terahertz beam control, given the perspective provided by this review.

3.2 Amplitude-blocking for diffractive optics

It is asserted in the previous chapter, Chapter 2, that phase-based beam control techniques are generally preferred over magnitude-based techniques in the terahertz range, owing to superior efficiency, versatility, and control. Whilst this is true, there are a few demonstrations of magnitude-based beam control in the literature that make use of a radiation-blocking mask to achieve beam control, utilising the principles that are described in Section 2.3.1. For instance, an off-axis transmissive diffractive lens operating at 500 GHz has been demonstrated in Siemion *et al.* (2011), using a straightforward metal grating with curved slits. Although it reflected roughly half of incident power, and had a modest 10% diffraction efficiency, the straightforwardness of such a device may be desirable in some applications.

Dynamically-reconfigurable amplitude-based beam control in the terahertz range has also been demonstrated. One technique is based on the photoexcitation of semiconductors, as it is well-known that incident photons will produce free carriers in such a material. This locally increases the material's electrical conductivity, resulting in a decrease in terahertz transmission (Kannegulla *et al.* 2015). The existence of these free carriers is temporary, and depends on the carrier lifetime of the material, which is in the range from 0.1 to 1 ms for terahertz-transparent semiconductors such as silicon and germanium. By exposing a slab of intrinsic semiconductor to a particular light pattern of the appropriate intensity and wavelength, a terahertz radiation-blocking mask is temporarily patterned across the surface. This technique has been used to generate diffraction grating patterns for terahertz beam-scanning in a frequency range from 50 to 250 GHz (Busch *et al.* 2012), as illustrated in Figure 3.1. In another work employing the same methodology, beam scanning through a 12° angle and zone plate patterns for lensing were demonstrated at an operating frequency of 750 GHz (Shams *et al.* 2015). In both cases, a partially-reflective indium tin oxide window was employed to superimpose the masking light pattern over the incident terahertz radiation. The bespoke light pattern was achieved with a digital light processing projector. Note, neither work explicitly reported the diffraction efficiency that results from this methodology.

Electronic control is generally preferable to optical control, as an optical spatial light modulator of the sort discussed above requires highly specialised equipment. By contrast, an electronic device is typically more amenable to integration into compact devices. Electronic amplitude modulation based on metasurfaces has previously been demonstrated in the terahertz range (Chen *et al.* 2006), exhibiting $\sim$5 dB modulation

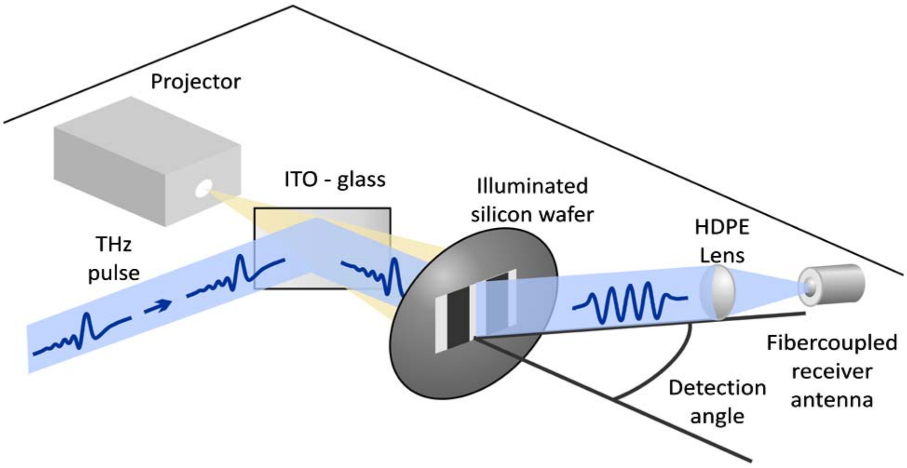

Figure 3.1. Optically-controlled magnitude-blocking mask. Illustration of the use of a photoexcited semiconductor to achieve terahertz beam scanning, by temporarily imprinting a magnitude-blocking diffraction grating, after Busch *et al.* (2012).

depth at an operating frequency of 900 GHz. For this device, the metallic resonators that comprised the metasurface were fabricated on a doped semiconductor, where the metal-semiconductor junction forms a Schottky barrier, which is essentially a form of diode junction. A reverse-bias to this junction creates a depletion region in the vicinity of the metal, reducing the conductivity of the material that surrounds the resonator and altering the characteristics of its resonance. This principle has been employed for amplitude modulation (Chen *et al.* 2006), and by grouping cells into columns of width greater than a wavelength, a switchable diffraction grating may be realised. Note that the grating period is effectively inbuilt into the structure of a device of this type, and hence it is less versatile and reconfigurable than the aforementioned optically-controlled spatial light modulators. An amplitude-blocking terahertz spatial light modulator using electronic switching of an active metasurface in this way has been experimentally demonstrated (Karl *et al.* 2014). This device had a fixed diffraction angle of 36.1°, 9.4 dB insertion loss, and a modest diffraction efficiency of 0.53%. Whilst performance may improve with refinement, it seems to indicate that the efficiency with which devices of this type steer radiation is insufficient for practical applications.

3.3 Path-length optics

As discussed in Section 2.4.1, a straightforward technique to achieve a given required phase distribution is to employ a piece of transparent dielectric of varying thickness.

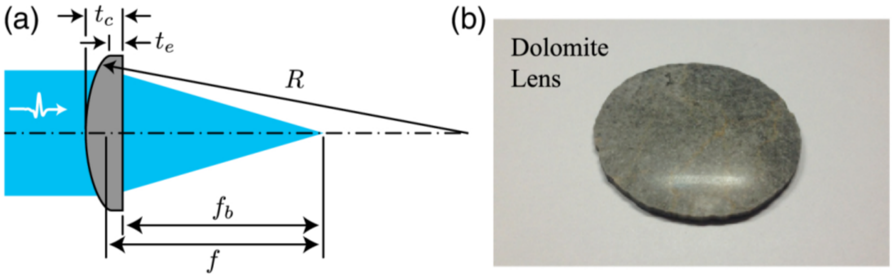

Figure 3.2. Stone terahertz lens. Terahertz lens made of natural stone, showing (a) plano-convex structure and principle of operation, and (b) photograph of fabricated dolomite lens, after Han *et al.* (2013).

A brief discussion of noteworthy demonstrations of this approach in the terahertz range is as follows. Traditional lenses operating in the terahertz range have been commercially available for several years (Kropotov and Tsygankova 2010), composed of materials such as polymers, which offer efficiency in the order of 65 to 80%, as well as crystalline substances and quartz, with efficiency of ∼25%. The origins of loss in devices of this kind are linked to reflection at the dielectric-air boundary, as well as dissipation loss as the beam propagates through the material, as its thickness is non-negligible. Polymer terahertz lenses are also detailed in the literature, having been fabricated with techniques including compression moulding and machining (Scherger *et al.* 2011b, Wichmann *et al.* 2013, Chernomyrdin *et al.* 2017). These devices operate over a broad bandwidth due to the non-dispersive nature of the polymers employed. Focal lengths from 7 to 60 mm were demonstrated, and the thickness of these devices was up to 15 mm, which is quite large compared to a terahertz wavelength. Additional to the dielectrics previously mentioned, there are a few examples of slightly more exotic materials being used for this purpose, including natural stone (Han *et al.* 2013), as shown in Figure 3.2, which was 4.1 mm thick, and focused to a distance of ∼95 mm over a frequency range from 0.2 to 0.7 THz. Another example is mould-set caramel (Sterczewski *et al.* 2016). However, this device had a limited bandwidth of 0.15 to 0.4 THz due to the absorptivity of caramel at higher frequencies. This planoconvex lens had a focal length of approximately 18 mm, and was 5 mm thick.

A drawback of all of the traditional lens devices presented above is the physical thickness, which is a hindrance in applications demanding compactness. Transmissive, stepped-phase diffractive optics have also been demonstrated in the terahertz range. These address the issue of thickness, albeit at the cost of reduced bandwidth. Silicon is highly suitable for this purpose, as intrinsic silicon can have very low dissipation, and mature etching techniques are well-suited to produce a quasi-planar device with a finite number of levels (Wang *et al.* 2002, Saha *et al.* 2013, Minkevičius *et al.* 2017). These devices were significantly thinner than traditional lenses; the latter cited work had a device thickness of less than 500 µm. In another work, the negative shape of a stepped-lens structure was etched into silicon, and this was used in a stamp-like manner to imprint a stepped-phase lensing structure into a commonly-used terahertz transparent polymer known as polypropylene (Walsby *et al.* 2007). This material has lower refractive index than silicon, and hence exhibits better matching to free-space at the cost of increased physical step size for the same phase difference. This resulted in a device that was 3 mm thick. A slightly more unusual choice of dielectric material is ordinary cartridge paper, which was stacked to the requisite thickness for a binary phase difference with respect to free-space, which is $\sim$1.3 mm, and then the zones of lower-delay were defined by laser-cutting. This resulted in a binary-phase zone plate, as reported in Siemion *et al.* (2012), and the use of cartridge paper in particular represents a highly inventive, low-cost demonstration of a terahertz beam-shaping device.

In recent years, one particular method of fabrication, namely 3D printing, has been gathering significant attention as a means to produce path-length based optics in the terahertz range, and hence it merits a specific mention. The family of fabrication techniques known as 3D printing is loosely defined as the automated fabrication, in layered fashion, of a near-arbitrary structure that is defined by a model generated in computer-aided design (CAD) software. This technique has been employed to fabricate terahertz polymer zone plates (Furlan *et al.* 2016), Fresnel lenses (Sypek *et al.* 2012), traditional lenses (Busch *et al.* 2014, Squires *et al.* 2015, Busch *et al.* 2015), cylindrical (i.e. line-focusing) lenses (Suszek *et al.* 2015), and integrated lenses (Yi *et al.* 2016). The proliferation of such diverse terahertz devices is testament to the versatility of 3D printing, and the basis for this fast-growing field of study.

Aside from bulk dielectrics and metals, it is also possible to contrive artificial, effective media using periodic, subwavelength structures. From the perspective of an electromagnetic wave, such a structure is experienced as a homogeneous material with properties that are dependent on the structure, and potentially different from the those of the constituent materials (Choy 2015). For instance, an array of subwavelength air-holes in a given dielectric material will produce an effective medium that an electromagnetic wave experiences as an artificial dielectric, with an effective refractive index that lies between that of the bulk dielectric and air. This index depends on hole radius and hole density, and hence it can be controlled by varying the size of the holes with respect to position. A device analogous to a traditional lens has been constructed from intrinsic silicon based on this principle, where effective index (as opposed to device thickness) varied with position in order to achieve the required output phase-front (Park *et al.* 2014). This device had the advantage of a large bandwidth that is comparable to that of traditional lenses, namely 0.4 to 1.6 THz, combined with the extremely thin profile of 100 µm. Additionally, its reduced refractive index resulted in better matching to free-space compared bulk-silicon devices, and hence in greater efficiency. This is an example of a gradient-index (GRIN) lens, and a related device has also been fabricated using 3D printing (Hernandez-Serrano *et al.* 2016). Both of these artificial dielectrics are constructed entirely from bulk dielectric materials, but other options are available; perhaps counter-intuitively, all-metal designs can also be employed to realise artificial dielectrics. Such effective media have been utilised for terahertz lenses (Navarro-Cía *et al.* 2011, Mendis *et al.* 2016). Interestingly, these all-metal artificial dielectrics exhibit properties not found in natural media, namely the effective refractive index of the medium is lower than unity, which is impossible for bulk dielectrics. This means that the phase front is accelerated with respect to free space, rather than delayed, as in a conventional medium. Thus, the curvature of lenses of this type is concave, where a traditional lens of the same functionality is convex, as shown in Figure 3.3.

Scannable and switchable path-length optics Terahertz beam-control devices based on path-length mechanisms can also be made dynamically-reconfigurable, and a few

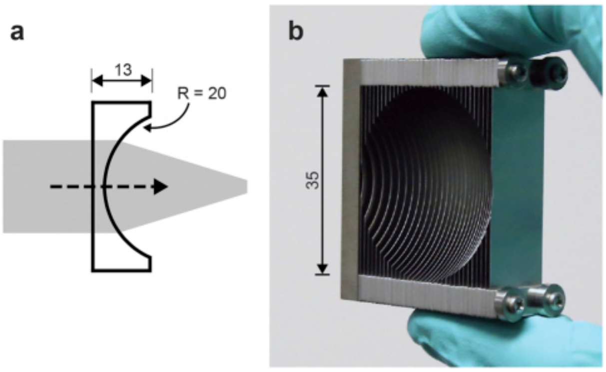

Figure 3.3. All-metal artificial dielectric lens. Metal-based artificial dielectric lens, showing (a) operation schematic diagram, and (b) photograph of fabricated sample, after Mendis *et al.* (2016).

examples of such techniques are discussed in this section. Perhaps the most straightforward example is a mechanically-actuated flat mirror, which can be employed as a trivial beam-scanning mechanism. There are numerous examples in the literature of terahertz scanning systems of this type (Cooper *et al.* 2008, Cooper *et al.* 2011, Kos and Gerecht 2013). However, the need for motorised control, as well as the physical scale of devices of this type, pose a serious disadvantage. A more compact, flat-profile approach to mechanically-actuated terahertz beam scanning has been demonstrated, which made use of a one-dimensional array of electronically-switched reflective cantilevers (Monnai *et al.* 2013). Each cantilever could switch between two positions that were separated by a vertical distance of 80 µm, which is an appropriate scale for binary phase difference upon reflection in the terahertz range. This device can therefore achieve dynamic, binary-phase beam scanning, as well as variable focusing in a single dimension in a manner similar to a cylindrical lens. A scanning range of 42° was demonstrated at an operating frequency of 0.33 THz. Although the binary phase is a drawback for reasons discussed in Section 2.3.2, the electronic control and compactness of the device are certainly great advantages.

Previously-given examples of switchable path-length optics were reflective devices exclusively, but dynamic control of path-length is also possible for transmissive devices. For instance, one demonstration of a variable-focus lens has made use of a liquid

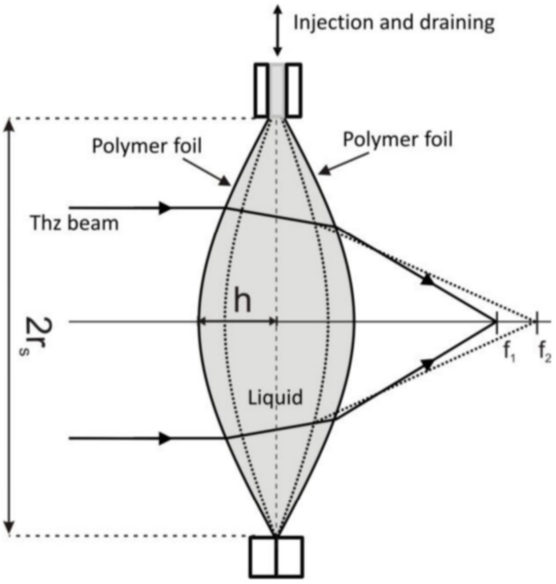

Figure 3.4. Variable-focus liquid lens. Lens composed of terahertz-transparent liquid enclosed by a polymer bag, where the radius of curvature, and hence the focal length, can be varied by altering the quantity of liquid, after Scherger *et al.* (2011a).

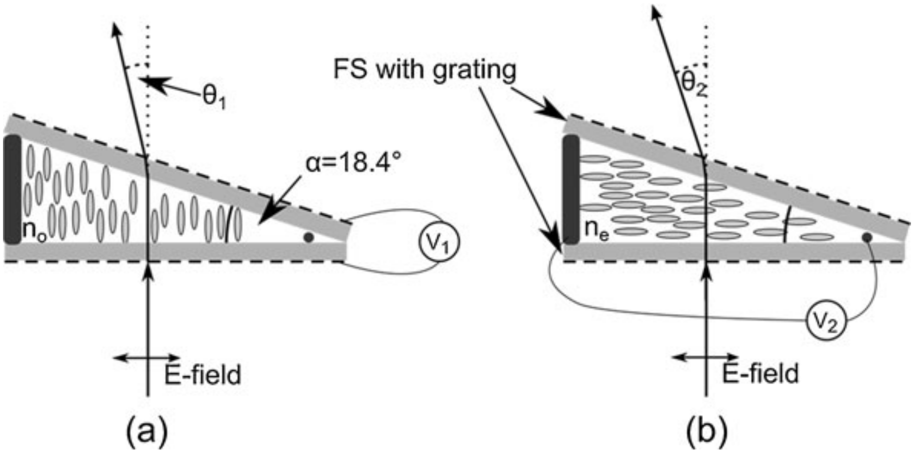

Figure 3.5. Electronically-controlled switched-beam device. Terahertz switched-beam device based on voltage-controlled refractive index of liquid crystals, after Scherger *et al.* (2012).

terahertz-transparent dielectric material rather than a solid (Scherger *et al.* 2011a). In order to maintain a lens-like shape, this liquid was piped into a volume enclosed by a polymer foil, and the curvature was dependent on the amount of fluid enclosed. Thus, the focal length of a device of this type can be varied by injection and draining of fluid, as illustrated in Figure 3.4. In another example from the same author, solid-state control was employed for a wedge-shaped beam-scanning device (Scherger *et al.* 2012), as shown in Figure 3.5. The refractive index of this device was varied by applying a bias voltage to liquid crystal. For a liquid crystal, the DC electric field aligns the molecules of the birefringent material, and this altering its refractive index. In this way, the output directionality was switchable between two beams separated by a modest ∼6°.

3.4 Phased arrays

There are no examples of traditional phased array antennas operating at terahertz frequencies in the literature, for reasons detailed in Section 2.4.2. However, there are demonstrations of phased array devices that operate using slightly different principles, and a few are detailed here.

Phased-array-like antennas based on photonics principles have previously been demonstrated in the terahertz range. For instance, one example replaced the need for an impractical terahertz-range feed network with an equivalent network composed of optical fibres, which carried infrared light (Bauerschmidt *et al.* 2013). These fibres terminated in nonlinear devices, in which optical power was converted to terahertz power by difference frequency generation. This is a well-established method of generating terahertz radiation based on the photomixing of two infrared laser beams of differing frequencies, where the difference between the two colours lies in the terahertz range. Terahertz radiation will therefore be among the mixing products, and can be selected for with filtering techniques (Matsuura *et al.* 1997, Tani *et al.* 2000). Controlling the delay in the optical fibres results in a corresponding relative delay of terahertz pulses, which is sufficient for dynamic beam control. This principle was employed to generate a terahertz-range focal spot at a dynamically-adjustable position, but the demonstrated scanning range was quite low. A related approach to manipulate the phase of terahertz radiation produced by difference frequency generation is to modulate the phase of one of the input infrared lasers, as this will produce an identical modulation of the output phase of the terahertz radiation (Sinyukov *et al.* 2008). This can be exploited for beam control. By introducing a linear phase gradient to one of the input infrared beams, a corresponding phase gradient is observed in the terahertz beam that is output from the photomixing device. As shown in Figure 3.6, this is achieved quite straightforwardly by tilting one of the incident infrared beams, which has been demonstrated in Maki

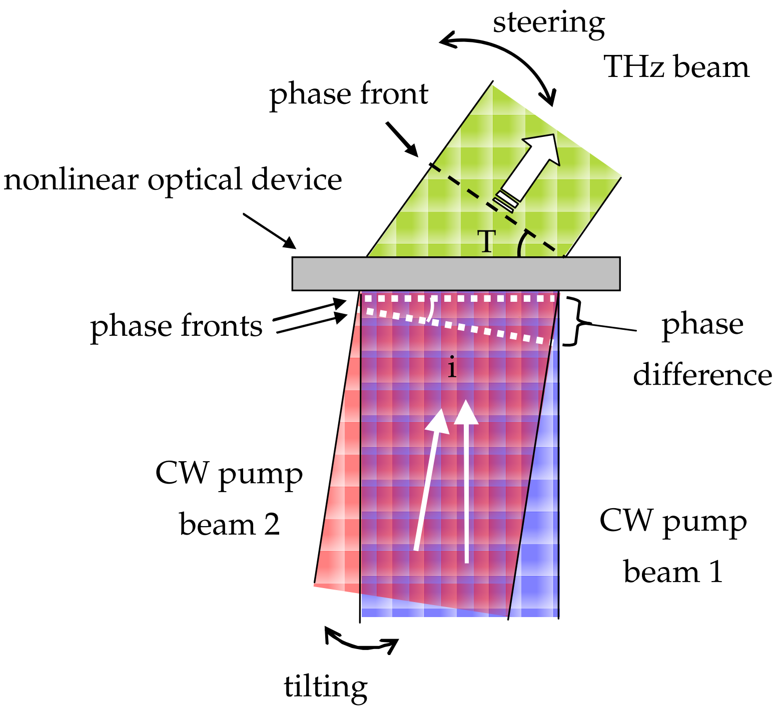

Figure 3.6. Pump beam-tilt terahertz beam scanning. An illustration of terahertz beam control based on difference frequency generation, in which one of the input pump beams was tilted, which translated to a linear phase ramp characteristic in the output beam, after Maki and Otani (2008).

and Otani (2008) and Maki *et al.* (2009). In these examples, the terahertz photomixer was fed from free-space, rather than optical fibres. Equation 2.6 shows that the steering angle is relative to wavelength, and hence a given phase gradient will result in a far larger steering angle in the terahertz range than in the infrared range. Thus, there is an amplification of the incident steering angle. By tilting the pump beam through a modest 0.155°, the terahertz beam was steered through 29°. The particular demonstration yielding these values was performed at 0.6 THz, but the cited work gives experimental results spanning from 0.3 to 1.7 THz, which illustrates the capacity for this technique to span a broad portion of the terahertz range. This is certainly an encouraging demonstration, but the fact that it requires a sophisticated dual-laser apparatus places stringent limitations on feasible practical applications.

Aside from photomixing-oriented techniques, a more practical approach to realise a phased array antenna in the terahertz range is to employ electronic terahertz sources, based on complementary metal-oxide-semiconductor (CMOS) technology, which are coupled directly to their associated radiators. As the terahertz power generation occurs at the radiator itself, this once again avoids the need for a lossy terahertz feed

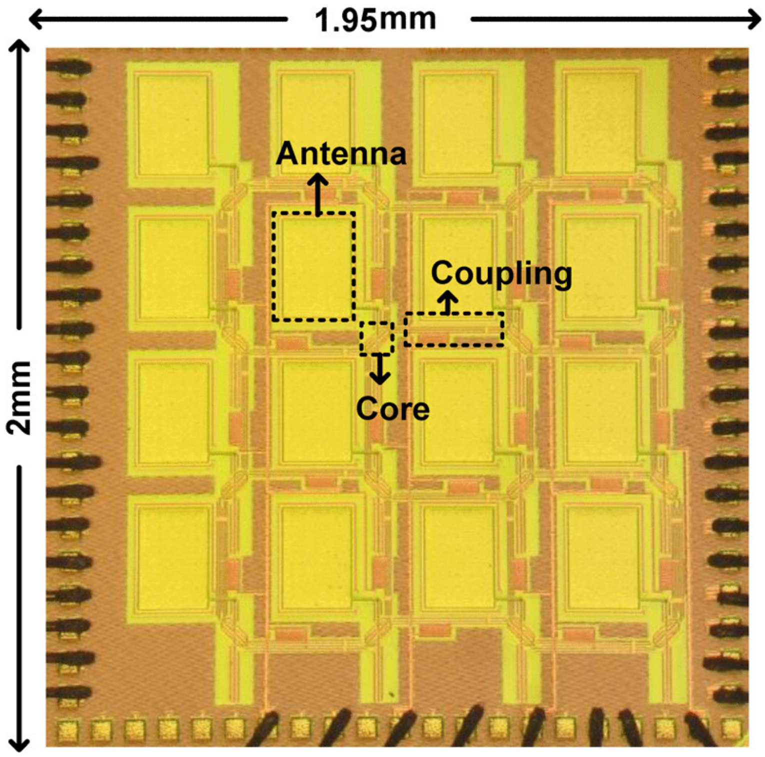

Figure 3.7. **Terahertz CMOS phased array.** A micrograph of a terahertz phased array antenna with 4×4 elements, after Tousi and Afshari (2015).

network. However, the key challenge to address for phased array operation is the synchronisation of the different sources such that they are of well-defined relative phase, as is necessary for beam control. In one such example, terahertz power was generated by a frequency-multiplier chain. A millimetre-wave frequency reference oscillator was distributed via a feed network to multiple terahertz sources that individually radiated (Sengupta and Hajimiri 2012). In the process of feeding, the reference signal frequency was halved, and split into quadrature signals, which could be added with particular weights at the terahertz source in order to achieve specific values of output phase. This is a clear demonstration of a dynamic-scanning phased array architecture operating in the terahertz range. In this work, a 4×4-element array was fabricated, demonstrating +9.4 dBm EIRP at 280 GHz, with an impressive 2D scanning range of over 80°. However, there are limits to the scalability of a millimetre-wave feed network, albeit less stringent than in the terahertz range. A more scalable approach to a frequency multiplier-oriented terahertz phased array is to de-centralise the millimetre-wave feed network by coupling individual nodes to their neighbours, rather than to a single millimetre-wave source (Tousi and Afshari 2015). Varactor (electronically-tunable capacitor)-based phase shifters were employed in order to produce a relative phase shift between adjacent nodes, and this phase shift in the millimetre-wave signal translated to a corresponding phase shift in the radiated terahertz signal. Although the demonstrated device was of the same number of elements as in the previously-discussed work (i.e. 4×4), it is more promising for the development of larger arrays. Furthermore, the array exhibited higher output power, namely +17.1 dBm EIRP at 338 GHz, with a scanning range of 45° in one dimension and 50° in the other. An image of the fabricated CMOS chip is given in Figure 3.7. Another approach to synchronisation is to mutually couple neighbouring terahertz sources via near-field effects, which has been demonstrated at 200 GHz (Sengupta and Hajimiri 2015). However, the limitations to array scalability in this case are more restrictive, and hence a 2×2 array was demonstrated. The output power was −1.9 dBm EIRP at 191 GHz, and the 2D scanning range was 70°.

3.5 Guided-wave and plasmonic techniques

Guided wave-based beam-control techniques have previously been demonstrated in the terahertz range, most notably in the form of leaky-wave antennas implemented with metallic parallel-plate waveguides (Karl *et al.* 2015), as shown in Figure 3.8. In this design, the radiation mechanism consists of a slot that spans the length of the waveguide's top plate. It was argued in this work that the frequency-scanning properties of the leaky-wave antenna's radiation pattern can be employed to realise a frequency-domain multiplexing scheme for practical communications systems. In a related work, the separation between the plates of the waveguide was tapered in order to vary the phase velocity along the device's propagation length (McKinney *et al.* 2015). In this way, a paraboloid phase distribution was engineered along the length of the radiating aperture in order to focus radiation, as opposed to a linear ramp distribution for beam steering. In a separate example, a leaky-wave antenna was integrated into a quantum cascade laser (QCL) (Tavallaee *et al.* 2011), but it is noted that such devices require cryogenic cooling, which is unsuitable for practical applications.

Aside from leaky-wave antennas, it is noted that a conceptually-related terahertz device based on rectangular waveguides that has been reported in the literature. For this device, a 1×8 array of dielectric rod antennas was fed by means of a waveguide-based feed network (Camblor-Diaz *et al.* 2012). The waveguides employed for this work were commercially-available WR-3 air-filled rectangular waveguides. A progressive difference in length between the waveguide feed for adjacent antennas resulted in a progressive phase in the excitation of the dielectric rod antennas. This produced a steered beam, and the dispersive nature of the waveguides results in frequency-scanning. Thus, this was a guided-wave device that used in-guide path length to produce the required relative phase, and output a frequency-scanned radiation pattern;

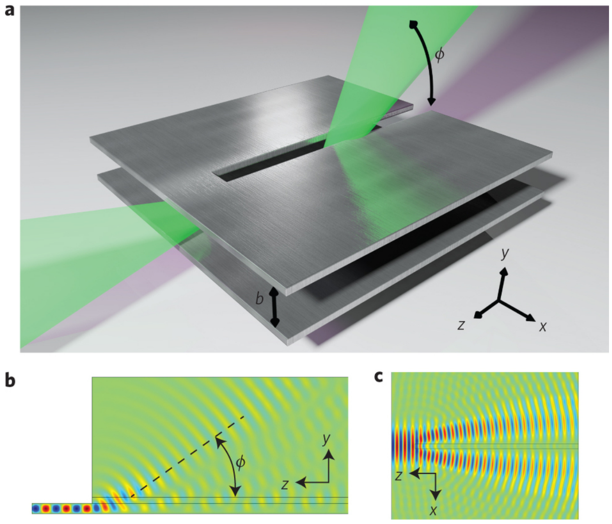

Figure 3.8. Parallel-plate leaky-wave antenna. Leaky-wave antenna composed of a parallel-plate waveguide with a slotted aperture along its length, after Karl *et al.* (2015).

the analogy to leaky-wave antennas is clear. However, the use of the feed network limits performance at higher frequencies, and hence this device was centred around ∼300 GHz. Leaky-wave antennas are therefore preferable for higher-frequency applications requiring this manner of functionality.

Previous examples have focused on the use of classical waveguide structures that confine radiation by means of metallic barriers that are insurmountable to electromagnetic radiation. Plasmonic effects offer another means to achieve confinement of a travelling wave. This makes use of subwavelength, periodic corrugations in conductors in order to couple radiation into a propagating surface wave of a high degree of confinement (Mills and Maradudin 1989, Williams *et al.* 2008), without the need for such barriers. If the groove depth is modulated at periodic intervals, some energy in the surface wave is coupled to free-space fields at these points, and hence a plasmonic guided-wave structure can be employed to realise a leaky-wave antenna. This principle has been demonstrated as an output coupler for a QCL-based terahertz source operating at ∼3 THz,

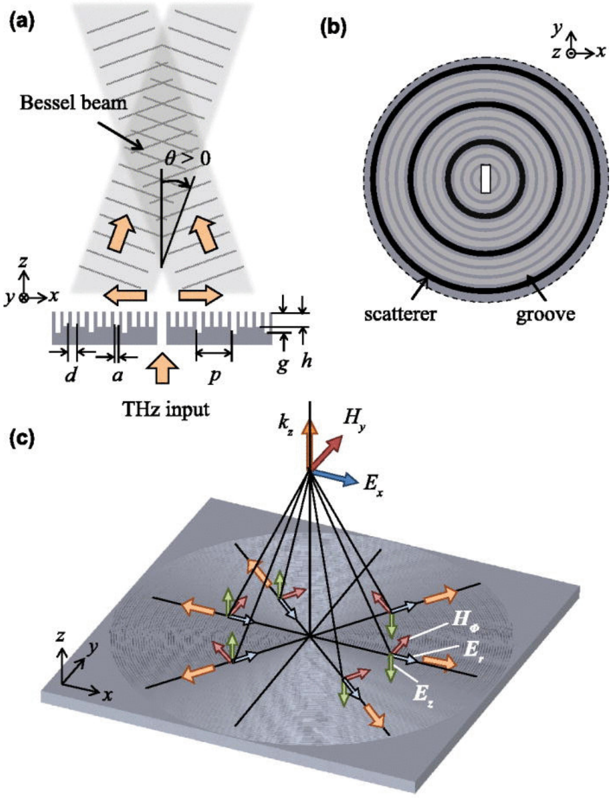

Figure 3.9. Plasmonic Bessel beamformer. Radial plasmonic guided-wave structure fed by slot in the centre, with depth modulation at periodic intervals of radius in order to launch a Bessel beam, after Monnai *et al.* (2015).

where the grooved structure was integrated directly into the substrate of the laser, resulting in an integrated device that directly radiated a collimated beam (Yu *et al.* 2010). Although such a device requires cryogenic cooling, as before, it is mainly mentioned in this review as an illustration of the principles of terahertz plasmonic leaky-wave antennas. In another example, a similar corrugated structure was etched into stainless steel, but with the important difference that the modulation of groove depth was chirped, rather than periodic (Monnai *et al.* 2012). Thus, the radiated energy was not coupled into a collimated beam, as in the previous example, but rather into a beam that converged to a focal point that is 30 mm above the waveguide at the operating frequency of 300 GHz. This particular design made use of a linear guided-wave structure, but in a subsequent publication, the authors extended the concept into two dimensions (Monnai *et al.* 2015). In the latter example, the surface wave travelled radially outward from a slot, and the guided-wave structure was implemented using a concentric array of annular grooves. The modulation of groove depth was at periodic intervals of radius that were slightly shorter than a wavelength, which resulted in free-space beams directed towards the optical axis. This produced a Bessel beam that may have applications in deep focal imaging. This concept is illustrated in Figure 3.9, and as with the previous example, the operating frequency of this device is around 300 GHz.

3.6 Transmitarrays

The most prolific type of passive beam-shaping array in the terahertz range is a form of transmitarray in which the polarisation of the shaped beam is orthogonal to that of the incident beam. For such a device, the energy that is commuted into the same polarisation as the incident beam (co-polarisation) is minimised, and the orthogonal (cross-polarisation) is maximised. In general, this technique provides a higher degree of phase tunability than is achievable when utilising transmitted co-polarisation. Typically the unit cell of such a transmitarray is an anisotropic, metallic resonator. The mode of resonance consists of current vectors with components in the direction of both the co- and cross-polarised electric field directions. Currents that are excited by the co-polarised incident field will therefore radiate in the cross-polarisation. For this reason, “C” (Zhang *et al.* 2013b, Wang *et al.* 2015) and complementary “V”-shaped metallic resonators (Hu *et al.* 2013, Jiang *et al.* 2013, He *et al.* 2013, Hu *et al.* 2014) are a popular choice, as the shape is naturally amenable to this form of commutation of current vector. A micrograph of an array of “V”-shaped resonators is given in Figure 3.10.

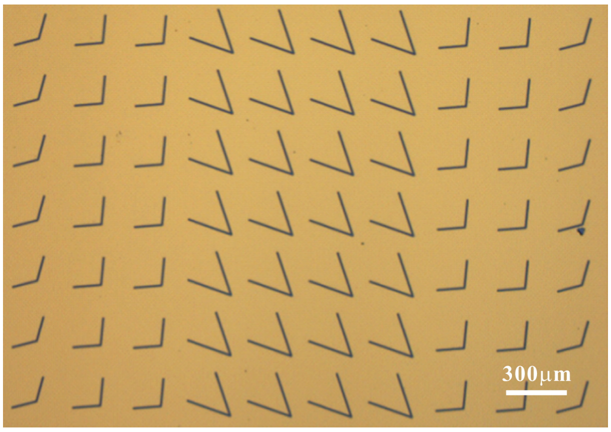

Figure 3.10. Complementary "V"-shaped resonators. Micrograph of a nonuniform array of complementary "V"-shaped resonators, which is a portion of a transmitarray device, after Hu *et al.* (2014).

Devices of this sort offer conversion to cross-polarisation with modest efficiency up to ∼25%, and have been demonstrated for terahertz flat lenses, frequency-scanning beam steerers, and vortex beams. The operating bandwidth of the "V"-shaped resonators is typically in the order of 200 GHz, and the "C"-shaped resonators can achieve 2–3 times that, but it is worth noting that this does not translate directly to practical device bandwidth due to the spatial dispersion characteristics of flat optics.

A related device made use of a multi-layer structure, for which the first and third layers were essentially wire-grid polarisers, and the middle layer was the resonator. The polariser layers block co-polarised transmission through the device, as well as cross-polarised reflection from the resonator layer, and this improved the conversion to cross-polarised transmission. This device not only achieves a peak efficiency of 60–80%, but also results in a broad usable bandwidth from 0.5 to 1.8 THz (Grady *et al.* 2013).

For transmitarrays that shape the co-polarisation rather than the cross-polarisation, multiple layers of resonators are needed to achieve the required phase tunability range (Monticone *et al.* 2013, Yang *et al.* 2017). For instance, a three-layer device consisting of "I"-shaped resonator unit cells has been employed for a frequency-scanning beam-steerer operating around 0.9 THz, with peak efficiency of 44% (Liu *et al.* 2015a). Another example of a three-layer device performs lensing, in which the individual resonator element is a complementary metallic annulus, and the phase response is tuned by its radius (Neu *et al.* 2010). One drawback of employing structures of this type is that the transmittance is only acceptable close to the resonance frequency, and hence by detuning the resonance frequency away from the operating frequency in order to manipulate phase response, the efficiency is severely impacted. For instance, at the operating frequency of 1.3 THz, the peak efficiency of the resonator was ∼68%, but when the centre-frequency of the resonator's passband is closer to 1.6 THz, the efficiency at 1.3 THz dropped to 1.7%. Subsequent work by the same author employed a single resonator layer, resulting in efficiency above 35% at the operating frequency of 1.3 THz, and this was deployed for a beam-steering device (Neu *et al.* 2013). However, the use of a single layer has the pronounced disadvantage of a reduced phase tunability range, and this is evidenced in the modest deflection angle of 6° at 1.3 THz.

3.7 Reflectarrays

Reflectarrays are less prolific than transmitarrays in the terahertz range, but a few noteworthy devices have been reported in the literature. One such demonstration involved the use of metallic resonators separated from a ground plane by a polypropylene slab, operating at 350 GHz (Kuznetsov *et al.* 2015). This device exhibited 80% overall efficiency, which outperforms comparable resonator-based transmitarrays, and is a testament to the efficiency advantage of reflectarrays. Focusing, as well as a simple example of a Gerchberg-Saxton hologram, were both experimentally demonstrated with this approach. In another work, a reflectarray antenna operating at 650 GHz was demonstrated (Tamminen *et al.* 2013). This device also employed metallic resonators separated from a ground plane by a polymer spacer, with the difference that polyimide

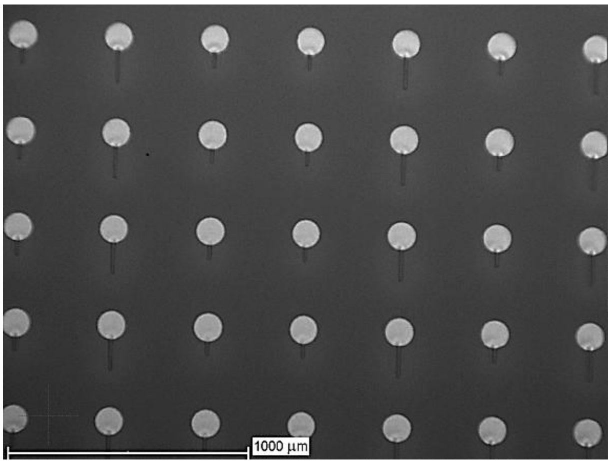

Figure 3.11. Reflectarray at 650 GHz. Micrograph of a binary-phase reflectarray device operating at 650 GHz, after Tamminen *et al.* (2013).

was used for the spacer. The reflection phase was controlled by varying the length of a resonator-coupled transmission line stub, and two values of transmission line length were employed, resulting in binary phase levels with a minimal efficiency of ∼50%.

Lastly, terahertz reflectarrays operating at 1 THz have previously been reported in the literature (Niu *et al.* 2013, Niu *et al.* 2014b, Niu *et al.* 2015). Prior to the initial demonstration by Niu *et al.* (2013), there had been no reports of reflectarray antennas in the terahertz range, and hence this represents the advent of research activities centred around the development of terahertz reflectarray antennas. Additional to that, these studies were undertaken in our research group at The University of Adelaide. Thus, they provide the context for my own contributions, to be reported in subsequent chapters in this thesis, far more directly than any other article of the relevant literature. For this reason, it is prudent to present these studies in a greater degree of detail, and to this end, the remainder of this section provides a detailed summary of each reflectarray device.

3.7.1 Beam-shaping operation of 1 THz reflectarrays

All devices presented below were deflectors of the type illustrated in Figure 2.6(a,b,e). Their intended beam-shaping operation was therefore to steer incident radiation away from the specular reflection path. Section 2.3.2 explains that a deflector requires a sawtooth phase distribution, with each period covering a 360° cycle. Owing to the periodicity of this phase distribution, the deflection angle θ_s can be determined in accordance with Equation 2.4, which is also known as the grating equation. For a deflector, the steering operation generally corresponds to first-order diffraction (i.e. $s = \pm 1$). When implemented with an array of discrete resonators, this translates to a progressive phase shift of $\Delta\varphi$ between adjacent elements, which is related to the deflection angle by the following expression, for all diffraction orders,

$$\sin\theta_s = \frac{s\Delta\varphi}{ak_0} - \sin\theta_i. \tag{3.1}$$

Note that, although a deflector of this kind is periodic, it avoids a symmetrical diffraction pattern of the sort observed in Figure 2.5(a,b,e). Whilst it is true that the periodicity dictates the directionality of each and every diffraction order, the precise order that is most strongly excited is determined by the direction and slope of the associated phase ramp within each period, and depending on the quality of this phase distribution, a high degree of selectivity is possible. In all deflector designs presented below, a full phase cycle fits into a discrete number of elements, M, and hence the grating period can be expressed as $D = Ma$, and the progressive phase shift is simply,

$$\Delta\varphi = \frac{360^\circ}{M}. \tag{3.2}$$

Thus, the design of the total array is adequately described by a single period of the array, which is henceforth referred to as the "sub-array," or the less well-known "supercell." The required phase response of each resonator can be straightforwardly expressed in discrete fashion,

$$\varphi_m = 360^\circ \frac{m}{M} + \varphi_0, \quad m = 0, 1, 2, ..., M - 1, \tag{3.3}$$

where φ_0 is some arbitrary baseline phase. Note that the total phase range to be covered by the resonators is not 360° exactly, but rather $\frac{M-1}{M}360^\circ$, as a value of 360° is equivalent to 0°. A smaller overall phase range is therefore required for a coarser phase quantisation, which is useful in instances in which the total 360° range is not practically achievable.

Based on Equations 2.4 and 3.1, for deflecting reflectarrays of this type, if the lattice constant is fixed then the deflection angle is determined by the choice of sub-array size, M. For this reason, this approach does not provide a high degree of freedom for the selection of the output deflection angles. For instance, if a lattice constant of $a = \lambda/2$ is employed under normal incidence, the possible values of θ_s are 41.8°, 30.0°, 23.6°, 19.5°, and so on, which may be too coarse for some applications. However, other angles are available if the sub-array contains multiple 360° phase cycles, where a single cycle does not fit into an integer number of elements. In this way, there is more freedom in the selection of phase gradient. However, the single-cycle sub-array approach is selected in this instance for simplicity, as it is sufficient for a proof-of-concept.

As explained in Section 2.5.1, the coupling between non-uniform elements can lead to inconsistencies between the reflectarray operation and unit cell design. To mitigate this, resonator dimensions are fine-tuned in order to optimise the reflectarray for maximal power deflected into the desired direction. The sub-array design approach makes this possible, as there is a manageable number of elements requiring adjustment.

3.7.2 Fabrication of metallic resonators for 1 THz reflectarrays

The reflectarrays presented here make use of metallic resonators, and the fabrication methodology to realise such resonators is discussed in this section. All devices that

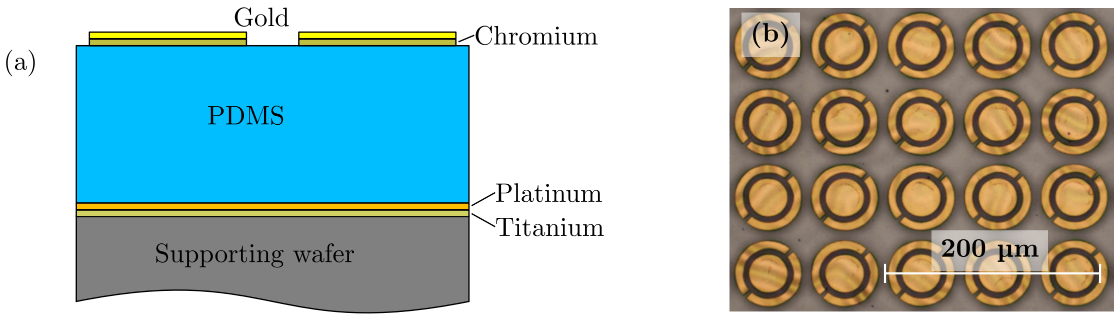

Figure 3.12. Realisation of terahertz metallic resonators. Structure of resonators of the sort presented in this section, showing (a) gold metallic resonators separated from a platinum ground plane by a polymer dielectric, and (b) micrographs of terahertz resonators of terahertz metallic resonators, after Cheng *et al.* (2014).

are presented below operate at 1 THz, where a free-space wavelength is equal to 300 µm. Several key microfabrication techniques can therefore access the relevant physical scales. For instance, spin-coating of elastomeric polymers can be employed in order to realise a dielectric spacer in the order of a few tens of microns (Walia *et al.* 2015). Vacuum-based evaporation techniques such as electron beam deposition can produce metal films of thickness greater than a skin-depth in the terahertz range, which is necessary for operation as a good conductor (Laman and Grischkowsky 2008). Additionally, techniques such as wet chemical etching (Wang *et al.* 2010, Ebrahimi *et al.* 2015) and deep reactive ion etching (DRIE) (Jukam and Sherwin 2003, Zhuang *et al.* 2015, Cheng *et al.* 2015) can define structures of sizes amenable to strong interaction with terahertz radiation.

The construction of the metallic resonator is given in Figure 3.12(a). In order to realise this structure, first a polished silicon wafer, to be employed as structural support, is cleaned with solvents. A platinum film is then deposited onto the wafer by electron beam evaporation, using titanium as an adhesion layer. This film is thicker than a skin depth in the terahertz range, and hence the metal operates as a ground plane, which shields the supporting wafer from radiation. A polydimethylsiloxane (PDMS, for which $\epsilon_r \sim 2.25$ and $\tan\delta \sim 0.06$ (Khodasevych *et al.* 2012) at 1 THz) liquid prepolymer is spin-coated onto the platinum ground plane, and is subsequently cured. A gold layer is then deposited onto the PDMS layer via electron beam evaporation, using chromium as an adhesion layer. Lastly, photolithography and wet chemical etching were employed to define the resonator structures. The use of platinum in the ground plane, as opposed to higher-conductivity metals such as gold, is to ensure selectivity during the wet chemical etching process. A micrograph of an example of a terahertz metallic resonator array of this type is given in Figure 3.12(b), showing highly-regular planar resonators.

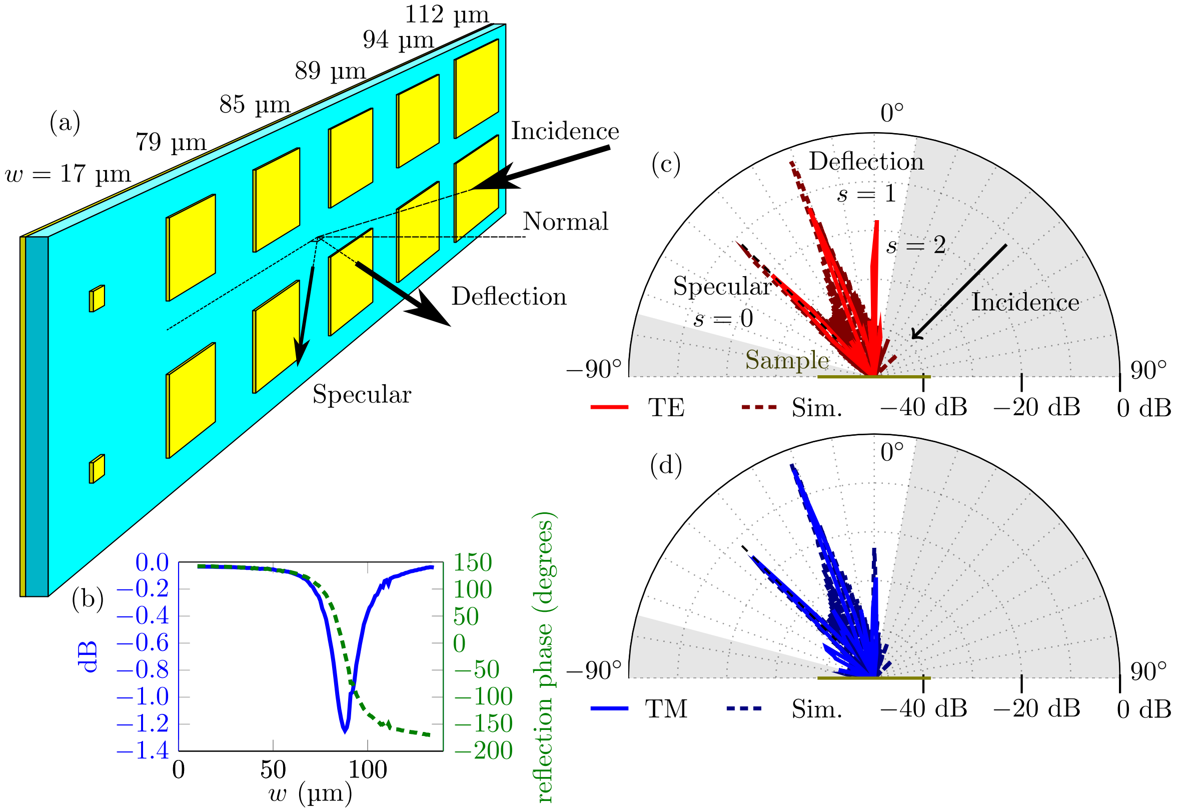

Figure 3.13. Isotropic deflection reflectarray. Isotropic metallic resonator reflectarray, showing (a) two sub-array periods with intended operation, where lattice constant $a = 140$ µm and dielectric thickness is $h = 15$ µm, (b) parametric analysis of side-length of square patch at 1 THz, and (c) and (d) radiation patterns of fabricated reflectarray at 1 THz, for TE and TM polarisations respectively, with diffraction order indicated for each major peak, and angles not covered by the scan are shaded in grey. Simulated radiation patterns are also given for comparison, where it is noted that the sidelobe level is higher than in measured results due to uniform, non-Gaussian excitation. After Headland *et al.* (2017).

3.7.3 Isotropic deflection reflectarray

The first reflectarray to be discussed from this body of work is the isotropic deflector reflectarray. This device employed a square patch as the resonator unit cell (Niu *et al.* 2013). As discussed in Section 2.5, a larger patch will result in a lower resonance frequency, and hence a greater negative phase shift. Thus, the patch size is designed to monotonically increase across the sub-array. A diagram of the sub-array, illustrating the intended beam-shaping operation, is shown in Figure 3.13(a). Terahertz radiation is incident at an oblique angle, and is deflected away from the specular reflection path, towards the surface-normal. There were six elements in the sub-array for this design, and hence the required progressive phase between neighbouring elements was 60°. The lattice constant was 140 μm, the operating frequency was 1 THz ($\lambda = 300$ μm), and the incidence angle is 45°, and hence Equation 3.1 gives an output angle of $-20.5°$.

Full-wave simulations were employed to investigate the reflection response of the unit cell. As in Section 2.5, this was modelled as a uniform array of infinite extent that is excited by a normally-incident plane wave. The fourfold symmetry of the patch resulted in isotropic response, and hence no particular polarisation vector need be specified. Parametric analysis based on these full-wave simulations was employed in order to determine the required patch dimensions to produce progressive phase between adjacent elements, and to this end, the patch side-length was swept in increments of 1 μm. Results are shown in Figure 3.13(b). It can also be seen from these results that the maximum loss was in the order of 1.2 dB, where it is noted that the majority of the absorption is contributed by the polymer spacer.

This design was fabricated in accordance with the procedure described in Section 3.7.2, and its radiation pattern was experimentally characterised using a goniometric terahertz time-domain spectroscopy (THz-TDS) setup. In this experiment, the sample was excited with obliquely-incident radiation at a 45° angle by an emitter that was held in a fixed position. A detector was scanned in a sample-centred arc, from $-75°$ to 10°, taking THz-TDS measurements at 2° intervals, and a gold mirror was used as a reference. This procedure was performed for both TE and TM polarisations, and the resulting radiation patterns are shown in Figure 3.13(c). It can be seen for both polarisations that the radiation maximum is at $\sim -21°$, rather than the specular direction of $-45°$, as intended. A good overall judge of the performance of such a device is the sidelobe level, as this is telling of the fidelity with which the intended phase distribution has been produced by the reflectarray. For this device, the sidelobe level of the TM polarisation is ∼10 dB lower than the main lobe, whereas for TE it is ∼5 dB, and hence the TM-performance is superior. This disparity is partly due to the oblique incidence, as the different polarisations see distinct effective projected patch sizes. It is deduced that the TM-polarised wave is less strongly affected by the oblique incidence than TE. Note that the use of THz-TDS in the measurement makes it possible to evaluate that the -3 dB spectral bandwidth of the measured peak is ∼5%. This limited bandwidth is evidence of the previously-noted dispersion exhibited by flat beam-control devices of this type.

3.7.4 Polarising beam splitter

If the metallic resonators are rectangular, rather than square, then the resonator will exhibit birefringent response. This is because the wavelength that produces a standing wave along the long-edge dimension will be lower in frequency than for the short-edge dimension. Thus, it is possible to engineer rectangular patches that interact very strongly with one polarisation, causing significant phase shift, but leave the orthogonal polarisation unaltered, for a given operating frequency. For this design, this birefringent rectangular patch concept was employed in order to realise a deflector reflectarray that manipulates the TE and TM polarisations of normally-incident radiation separately (Niu *et al.* 2014b). Controllable birefringence of this type is a highly desirable property for reflectarray antennas in communications applications. This is because orthogonal polarisations can be manipulated independently, which can be used to provide two orthogonal channels in the same link.

It is possible to use a single rectangular or cross-shaped patch to interact with both polarisations, but this can result in the excitation of an undesirable cross-polarisation component due to symmetry-breaking in the inhomogeneous array. An alternative arrangement is therefore adopted, as shown in Fig 3.14(a). The unit cell effectively contains two different rectangular patches; a horizontally-aligned patch to interact with TM polarisation, and a vertically-aligned patch to interact with TE. In order to allow for clearances and mitigate strong coupling, whilst maintaining the sub-wavelength periodicity, these differently-oriented patches are staggered. As with the previous design, a progressive phase difference is achieved by varying patch dimensions. By monotonically increasing the length of the TE-patches in one direction, whilst decreasing the length of the TM-patches in the other, the TM polarisation is deflected to a positive angle, whilst the TE polarisation is deflected to a negative angle. As the sub-array size is common to both polarisations, the deflection angle is symmetrical for this design. In this instance, the grating period was $D = 600$ µm, resulting in a deflection angle of ±30° for the normal incidence employed. Asymmetrical deflection angles are also possible, but this requires a different array period for each polarisation. In order to incorporate both, the width of the sub-array must be the least common multiple of the two individual periods (Niu *et al.* 2014a).

In order to minimise loss over the relevant phase tunability range, and provide a gradual phase characteristic, patch width was varied with patch length in accordance with

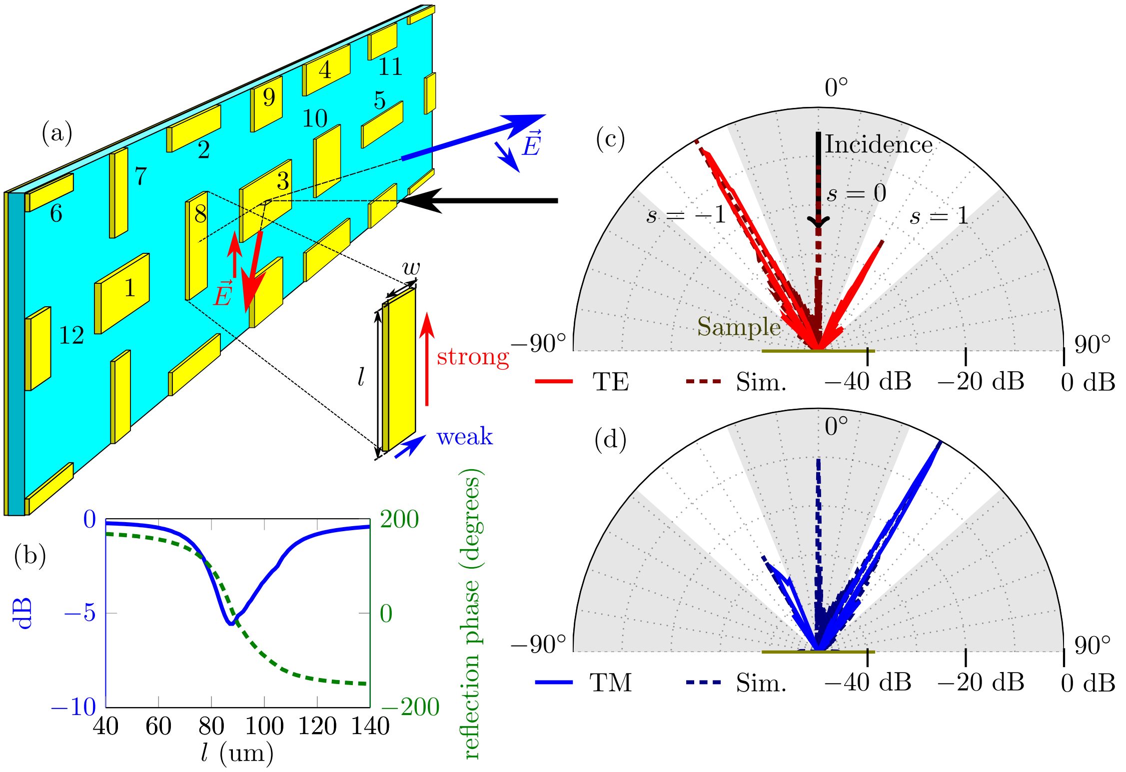

Figure 3.14. Polarising beam splitter reflectarray. Polarising metallic reflectarray, showing (a) sub-array design, with illustration of intended operation, where all patches are numbered to show correspondence with the dimensions given in Table 3.1, lattice constant $a = 100$ µm, and dielectric spacer thickness $h = 20$ µm, (b) parametric analysis of rectangular patch length at 1 THz, for polarisation parallel to long-edge, and (c) and (d) radiation patterns of fabricated reflectarray at 1 THz, for TE and TM polarisations respectively, with simulated results for comparison. Angles not covered by the scan in the measurement are shaded in grey. After Headland *et al.* (2017).

the following piecewise-linear expression, for which all units are micrometers,

$$w = \begin{cases} 32 + 0.2l, & \text{if } l \in [40, 90], \\ 230 - 2l, & \text{if } l \in [90, 105], \\ 20, & \text{if } l \in [105, 140]. \end{cases} \tag{3.4}$$

By making patch width dependent on patch length in this way, the number of independent variables was reduced to one. Additionally, for a given patch, the impact of the nearest orthogonally-polarised neighbours was small, and was therefore safely neglected. Lastly, due to the normal incidence, orthogonal polarisations can be considered equivalent for patches rotated through 90°, and hence a single parametric sweep can describe both polarisations adequately. These factors simplified parametric analysis significantly by reducing the search-space. Parametric analysis of patch length was performed using full-wave simulations, and the results are shown in Figure 3.14(b). For this analysis, the polarisation of incident radiation was parallel to the long edge of the rectangular patch. As before, a unit cell approach was employed, and side length was swept in increments of 1 µm. The results show a large phase tunability range, but it is noted that the loss is greater than in the previous design. This increased loss is intrinsically linked to the narrow patch geometry, and hence there is an evident trade-off between engineered birefringence and efficiency. In the final design, mutual coupling effects that are not accounted for in the unit cell analysis were mitigated by fine-tuning the dimensions of the individual patches. The final configuration of the sub-array is given in Table 3.1, with element number corresponding to the diagram in Figure 3.14(a).

As before, this device was fabricated, and characterised with THz-TDS, using a goniometric setup to measure the radiation pattern. In this instance, excitation was in the surface-normal direction, and wire-grid polarisers were employed in order to isolate and test the TE and TM polarisations individually. Due to practical constraints of laboratory clearances, the scanning range was limited to the ranges $-48°$ to $-22°$, and 22° to 48°. The results of this procedure are shown in Figure 3.14(c), and it can be seen from the radiation patterns that the TE polarisation is indeed deflected to $-30°$, and the TM polarisation is deflected to $+30°$. Due to feed blockage, it is not possible to characterise the amount of energy lost to specular reflection directly, but full-wave simulations given in the same plot indicate that the difference between deflected and specular reflection is greater than 10 dB.

Table 3.1. Optimised birefringent patch dimensions. Optimised dimensions of patches in sub-array for birefringent terahertz reflectarray.

Element	long-edge dimension, l (μm)	short-edge dimension, w (μm)
1	55	38
2	75	48
3	85	49
4	91	50
5	100	30
6	122	24
7	120	20
8	97	34
9	88	45
10	82	52
11	76	48
12	55	43

3.7.5 Polariser-based reflectarray

A wire-grid polariser is a device consisting of regularly-spaced, parallel striplines. The separation and width of the striplines are both deeply sub-wavelength, but the striplines themselves are far longer than a wavelength. As a consequence of this, the interaction of incident electromagnetic radiation with the wire-grid polariser will depend on the polarisation. The polarisation that is parallel to the orientation of the striplines is able to induce a current in the striplines, and as the striplines are extremely long, no standing wave pattern is established. A consequence of this is that the incident wave effectively sees a short circuit, and is therefore reflected. However, for the orthogonal polarisation, the conducting portions are interrupted by gaps, and as the spacing is deeply subwavelength, the currents induced in this dimension are negligible. This polarisation does not interact strongly affected by the striplines, and it is transmitted. Therefore, a wire-grid polariser is ideally a device that simply reflects one polarisation, and passes the orthogonal polarisation.

For the third and final metallic resonator-based device presented in Section 3.7, the concept of a wire-grid polariser was incorporated into a reflectarray design (Niu *et al.*

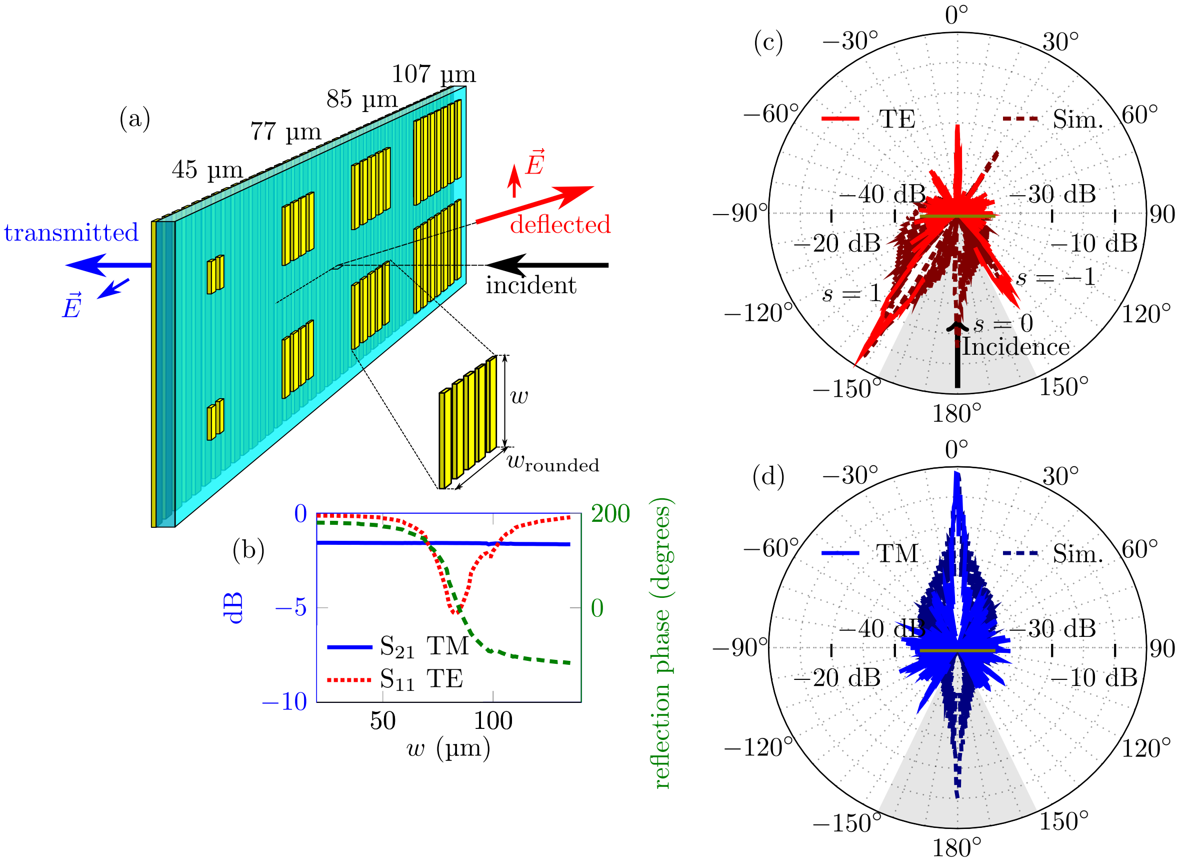

Figure 3.15. Stripline polariser-based reflectarray. Stripline polariser-based reflectarray, showing (a) two sub-array periods, illustrating intended operation, where lattice constant $a = 140$ µm and dielectric thickness $h = 20$ µm, (b) parametric analysis of resonator unit cell at 1 THz, and (c) and (d) radiation patterns of fabricated reflectarray at 1 THz, for TE and TM polarisations respectively, with simulated results for comparison. Angles not covered by the scan are shaded in grey. After Headland *et al.* (2017)

2015). This was achieved by using deeply-subwavelength metallic striplines to make up both the ground plane and the resonant patches in the reflectarray. The result is a reflectarray that deflects one polarisation, and passes another, as shown in Figure 3.15(a). For the resonator element, stripline segments were arranged so as to collectively approximate a square patch that interacts with the TE polarisation exclusively. The stripline width was 5 µm, and the separation between striplines is 5 µm. Thus, although the resonator was intended to approximate a square patch, the horizontal width of this patch is necessarily rounded-down. For this design, the grating period is $D = 560$ µm, resulting in a deflection angle of ∼32° under normal incidence.

As before, parametric analysis was employed in order to determine the required patch sizes for the array, and the results are presented in Figure 3.15(b). For TM polarisation, the majority of the power is simply passed, and the size of the resonator exhibits negligible impact upon the transmitted power, as intended. It can also be seen that the TE polarisation exhibits a reasonably large phase tunability range on reflection, albeit with loss comparable to the previously-presented design.

In order to observe the TM-polarised transmission, the use of a supporting silicon wafer must be abandoned for this design. The procedure described in Section 3.7.2 must therefore be modified to accommodate this limitation. A 100 µm-thick layer of PDMS was spin-coated directly onto the supporting wafer, and the stripline ground plane was patterned onto this layer. Thereafter, the procedure continued as previously described, and the PDMS structure was lifted-off from the supporting wafer after the resonators were etched. The 100 µm-thick PDMS layer acted as a support for the structure after lift-off. The radiation pattern of the fabricated structure was experimentally characterised with a goniometric setup, which scans with a angular resolution of 0.5° over a range from $-155°$ to $+155°$. Both polarisations were tested in this way, and the results are presented in Figure 3.15(c). It can be seen that the TM polarisation is passed, and the TE polarisation is deflected to a 32° angle, as expected. Additional to that, full-wave simulations given in the same plot indicate that specular reflection is $\sim$12 dB lower than the deflected peak.

3.8 Challenges and opportunities

From the above analysis of published works in this field of study, a few things become immediately apparent. Firstly, the physical bulk of traditional lenses such as those presented in Section 3.3 poses a drawback. Stepped-phase devices sacrifice bandwidth for a quasi-flat profile, but such devices typically remain several wavelengths thick. Additionally, most reported stepped-phase devices are transmissive, meaning there is a trade-off between insertion loss and device thickness that is mediated by selection of refractive index. With regards to phased arrays, although the photonic beam control mechanisms discussed in Section 3.4 are impressive demonstrations, they require highly specialised laser equipment that is unlikely to be amenable to practical, consumer-oriented applications. The electronic beam-control devices presented in the same section are encouraging, but there are limitations in achievable physical scale and operating frequency, and hence these cannot be considered viable as a complete solution to the problem of terahertz beam control. Although the guided-wave techniques presented in Section 3.5 are amenable to compact and integrated devices, their functionality is quite limited, and there is generally non-negligible loss in the guided-wave structure itself. The passive arrays presented in Sections 3.6 and 3.7 are capable of achieving a thin, planar profile, large aperture, and a high degree of versatility in terms of the beam-shaping operation that they perform. Thus, they address many of the limitations posed by these beam-shaping techniques. However, the majority of the passive arrays presented exhibited quite low efficiency.

In view of the above summary, the aim of this thesis is to investigate prospective techniques for efficient, compact devices for terahertz beam control. To this end, reflectarrays and reflective stepped-phase devices are considered, given their natural efficiency-advantage over transmissive devices. It is of interest to improve upon the efficiency of the 1 THz reflectarrays given in Section 3.7, and to explore other prospective approaches to achieving terahertz reflectarrays. Additional to that, specific transmissive devices have been shown to exhibit quite high efficiency, including the previously-discussed gradient-index flat lens based on through-holes in a silicon slab (Park *et al.* 2014), as well as the multi-layer transmitarray, which is enhanced by wire-grid polarisers (Grady *et al.* 2013), and hence these techniques are also investigated in more detail.

This concludes Part I of the thesis, which aimed to provide the necessary context for the investigation at hand. The following chapter will explore the issue of improving the efficiency of a metallic resonator, by modifying the intrinsic loss of constituent materials.

PART II

Metallic resonators

Chapter 4

Doped polymer for efficient metallic resonators

THE dielectric properties of an elastomeric polymer are modified with the inclusion of dopants in order to reduce dielectric loss in the terahertz range. In light of the results reported in Section 3.7, the ultimate aim of this study is to produce efficient metallic resonators for use in terahertz reflectarrays. The host polymer is PDMS, and micro/nanoparticle powders of either alumina or polytetrafluoroethylene (PTFE) are employed as dopants. Composite samples are prepared, and are characterised with THz-TDS. The samples exhibit reduced dielectric loss, with a maximum reduction of 15.3% in loss tangent reported for a sample that is 40% PTFE by mass. However, whilst a reduction in loss tangent is confirmed, simulations reveal that terahertz metallic resonators implemented with these new materials do not exhibit a significant increase in efficiency.

4.1 Introduction

As expounded in Section 3.7, elastomeric polymers such as PDMS are useful for the realisation of terahertz resonators, as they can be spin-coated to form a dielectric spacer of a required thickness. However, such polymers exhibit moderate loss in the terahertz range (Walia *et al.* 2015, Khodasevych *et al.* 2012, Jin *et al.* 2006), and when integrated with a metallic resonator, this loss is exacerbated by field confinement due to resonance. Although lower-loss dielectric materials such as ceramics and intrinsic semiconductors are available, they are rigid, and are not compatible with microfabrication techniques such as spin-coating. It is possible to modify the material properties of a polymer by introducing powder materials, and this technique has been used in the terahertz range to improve the performance of Dällenbach absorbers (Giles *et al.* 1993), to increase the refractive index of a dielectric material at the expense of increased loss (Ung *et al.* 2011, Scheller *et al.* 2009, Jansen *et al.* 2010), and to show that THz-TDS can be used to determine the composition of a sample (Wietzke *et al.* 2007). However, so far no attempts have been made to produce low-loss effective media for terahertz waves.

This chapter presents a technique for reducing the dielectric loss of PDMS with low-loss dopants in order to form an effective medium, with dielectric properties determined by the intrinsic properties and fractions of the constituent media. Alumina (Al_2O_3) and polytetrafluoroethylene (PTFE) are selected as dopants, as they exhibit low loss in the terahertz range (Cunningham *et al.* 2011, Berdel *et al.* 2005). As bulk materials, however, these are not suitable for microfabrication techniques. This procedure therefore aims to combine the desirable electromagnetic properties of low-loss dielectric materials with the desirable mechanical properties of PDMS.

4.2 Fabrication

In order to prepare the samples, a known amount of liquid PDMS, comprising a 1:10 mixture of pre-polymer and a curing agent, is mixed with a known amount of powder dopant in order to yield a desired mass percentage. Liquid composite mixtures are then degassed in a vacuum chamber for a period of two hours in order to extract trapped air bubbles, and then poured onto a planar silicon wafer. The liquid-phase elastomer is then cured at room temperature and atmospheric pressure over a period of 48 hours in order to realise pliable elastomeric materials. Alumina and PTFE particles, of $\sim$50 nm and <12 µm, respectively, are utilised as dopants. Samples of 10%, 20%, and 40% of

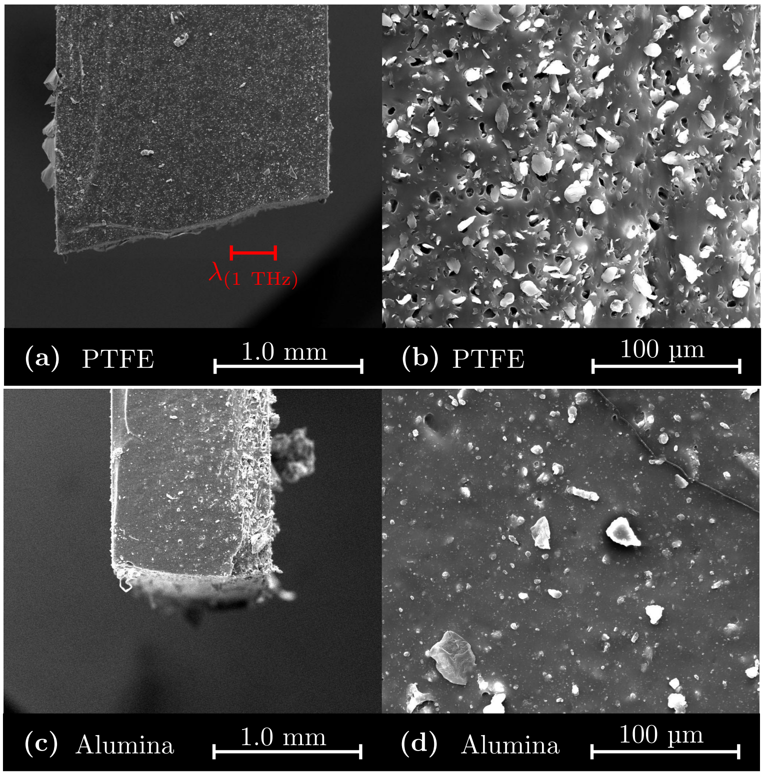

Figure 4.1. Doped PDMS samples. SEM images of 40%wt PTFE-doped sample at (a) 100× and (b) 1000× magnification, and the alumina-doped sample at (c) 100× and (d) 1000× magnification. The scale of a free-space wavelength at 1 THz is shown in red in (a). After Headland *et al.* (2015c).

each dopant by weight are prepared, as well as a pure PDMS sample for comparison. All samples are sectioned into 3×3 cm^2 squares, with thicknesses ranging from 1.0 mm to 4.5 mm.

Scanning electron microscope (SEM) images of the samples that are 40% dopant by weight are given in Figure 4.1. Given that the wavelength at 1 THz is 300 µm, the wavelength is greater than the largest particle size by a factor of 25. The effective medium theory approximation of homogeneity is therefore applicable. Note that the PTFE samples contain voids in the host medium, due to particles being dislodged from the surface at the edge of the sample as a result of sectioning the sample. This effect does not penetrate the sample volume, and is therefore negligible.

In terms of microfabrication compatibility, although the doping increases the viscosity of the liquid polymer, the materials remain compatible with microfabrication processes such as spin-coating. Mechanically, the doped samples remain elastic like PDMS, but their Young's modulus is significantly modified. Doping also renders the PDMS optically opaque, which can compromise manual alignment in multi-layer structures.

4.3 Experiment

Samples are characterised using a photoconductive antenna (PCA)-based THz-TDS system, which utilises off-axis parabolic mirrors to focus the beam onto the sample (Ung *et al.* 2013). The waist of the focused beam has a diameter of 2 to 3 mm. Given that the samples are flexible and elastic, they are not expected to be of uniform thickness, and this is accounted for by taking five measurements at random locations on each sample. This also accounts for any fluctuation in dopant concentration within the sample volume.

As the thickness of all samples is required in order to extract their material properties, this is characterised experimentally in two ways. Firstly, SEM-based thickness measurements are performed on offcuts at multiple locations. Secondly, a micrometer is employed to gage the sample thickness directly. Given the pliable nature of the samples, due care is taken in order to avoid exerting excessive force with the micrometer, which can deform the sample and produce spurious measurements. This results in readouts from both SEM and micrometer measurements that are in close agreement, with values summarised in Table 4.1.

Table 4.1. Thickness of doped PDMS samples. Thicknesses of all PDMS samples, as measured with both SEM and micrometer readout, including standard deviations.

Dopant	%wt	SEM readout (mm)	Micrometer readout (mm)
None	–	4.45 ± 0.10	4.38 ± 0.01
PTFE	10%	1.04 ± 0.03	1.05 ± 0.03
	20%	2.00 ± 0.02	1.92 ± 0.01
	40%	1.94 ± 0.04	2.08 ± 0.01
Alumina	10%	2.08 ± 0.02	1.98 ± 0.01
	20%	1.90 ± 0.05	1.85 ± 0.05
	40%	1.02 ± 0.02	1.01 ± 0.01

4.4 Results

The dielectric properties of all samples are extracted using a standard parameter estimation process (Withayachumnankul and Naftaly 2014). The ensuing relative permittivities and loss tangents are presented in Figure 4.2. For clarity, material properties at 0.7 THz, where the dynamic range is at maximum, are also presented in Table 4.2. As expected, the doped samples exhibit a reduction in loss, and samples with higher dopant concentrations exhibit less loss. In addition to reduced loss tangent, samples doped with alumina also exhibit an increase in the relative permittivity. The greatest reduction of loss tangent is achieved with the sample that is doped with 40% PTFE by weight. This sample exhibits an average reduction of 15.3% in loss tangent over

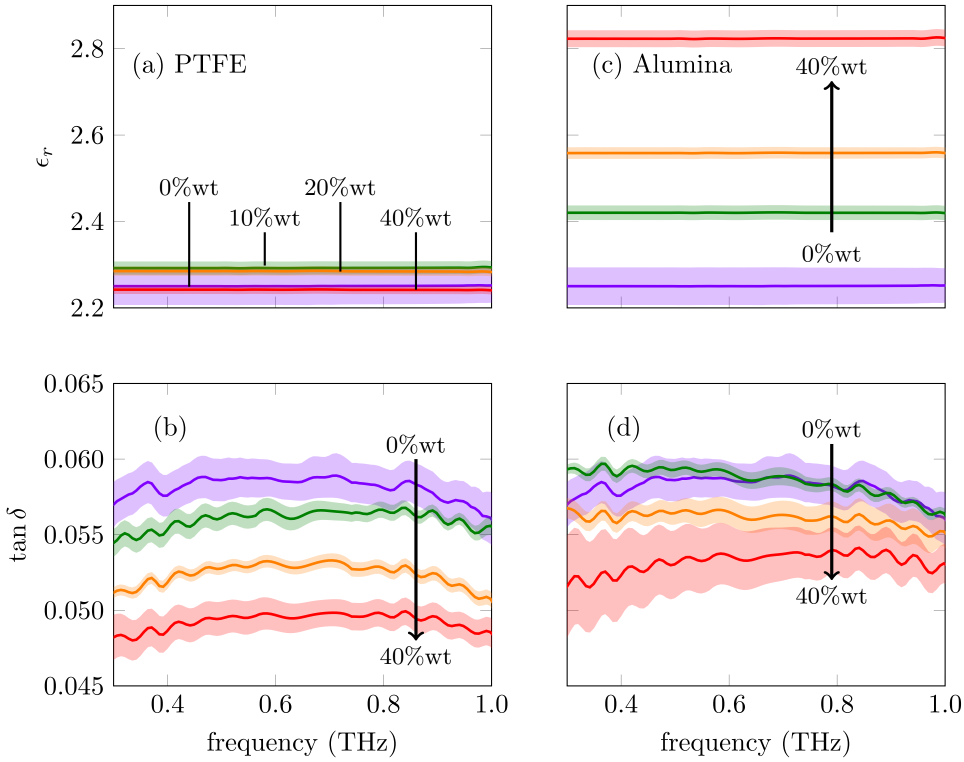

Figure 4.2. Properties of doped PDMS. Material properties of doped PDMS samples, showing; (a) relative permittivity of PTFE-doped samples, (b) loss tangent of PTFE-doped samples, (c) relative permittivity of alumina-doped samples, and (d) loss tangent of alumina-doped samples. The dopant percentage by mass varies from 0%, 10%, 20%, to 40%. Error ranges due to variation in sample thickness and dopant aggregation are indicated with coloured regions. After Headland *et al.* (2015c).

Table 4.2. Properties of doped PDMS. Measured material properties of doped PDMS samples, extracted at the frequency of 0.7 THz for dynamic range reasons.

Dopant	%wt	ϵ_r	$\tan\delta$ ($\times 10^{-2}$)	n	α (cm^{-1})
None	–	2.25 ± 0.04	5.88 ± 0.13	1.501 ± 0.014	12.9 ± 0.2
PTFE	10%	2.29 ± 0.01	5.66 ± 0.06	1.515 ± 0.005	12.5 ± 0.2
	20%	2.29 ± 0.01	5.33 ± 0.04	1.512 ± 0.003	11.8 ± 0.1
	40%	2.24 ± 0.01	4.98 ± 0.09	1.498 ± 0.003	10.9 ± 0.2
Alumina	10%	2.42 ± 0.02	5.89 ± 0.06	1.557 ± 0.005	13.4 ± 0.2
	20%	2.56 ± 0.01	5.63 ± 0.09	1.600 ± 0.004	13.2 ± 0.2
	40%	2.82 ± 0.02	5.37 ± 0.17	1.681 ± 0.005	13.2 ± 0.4

a range from 0.3 to 1.0 THz, as compared to pure PDMS. With regards to dispersion characteristics, the real relative permittivities of all samples presented in Figure 4.2 exhibit negligible variation over the relevant frequency range. It is therefore concluded that doping has not increased dispersion. Note the slight non-monotonic trend in the relative permittivity of PTFE-doped PDMS can be ascribed to jitter, as the pulse in the employed THz-TDS system has a tendency to drift slightly with respect to time.

4.4.1 Effective medium theory

In order to better understand and quantify the reduction in material loss, effective medium theory is deployed as a means to model the doped PDMS samples. There are multiple approaches to effective medium theory modelling, such as the Maxwell-Garnett formula (Sihvola 2001, Garnett 1904) and the Landau-Lifshitz-Looyenga model (Looyenga 1965, Hernandez-Serrano *et al.* 2014). However, these techniques are derived for spherical inclusions, and the dopant particles in this case do not conform to any regular geometry, as shown in Figure 4.1. For this reason, the Lichtenecker logarithmic mixture formula (Simpkin 2010) is selected to model the properties of the effective medium, as it is valid for homogenised dielectric mixtures in which the shapes and orientations of the components are randomly distributed. This formula is given in

Equation 4.1, for a combination of N constituent materials,

$$\epsilon_{\text{eff}} = \prod_{m=1}^{M} \epsilon_m^{v_m}, \tag{4.1}$$

where ϵ_m and v_m are the complex permittivity and volumetric fraction of the mth such material, respectively, and ϵ_{eff} is the complex permittivity of the overall mixture. In order to apply the Lichtenecker logarithmic mixture formula to the samples under investigation, mass fractions are converted to volumetric fractions using Equation 4.2,

$$v_{\text{volume}} = \frac{v_{\text{mass}}\rho_H}{v_{\text{mass}}\rho_H + (1 - v_{\text{mass}})\rho_D}, \tag{4.2}$$

where v_{volume} is the volumetric fraction of the dopant, v_{mass} is the mass fraction of the dopant, ρ_H is the density of the host medium, and ρ_D is the density of the dopant material. Here, the density of PDMS, alumina, and PTFE are $\sim$1.0 g/cm^3, $\sim$4.0 g/cm^3, and $\sim$2.2 g/cm^3 respectively (Peelen and Metselaar 1974, Chenoweth *et al.* 2005, Nelson *et al.* 2007). The Lichtenecker logarithmic mixture formula is inverted, and applied to the measured data in order to extract the complex permittivities of the bulk dopants, which are found to be 2.71 + j0.03 and 21.5 + j0.9, for PTFE and alumina respectively. The Lichtenecker logarithmic mixture formula is then utilised, with the extracted bulk

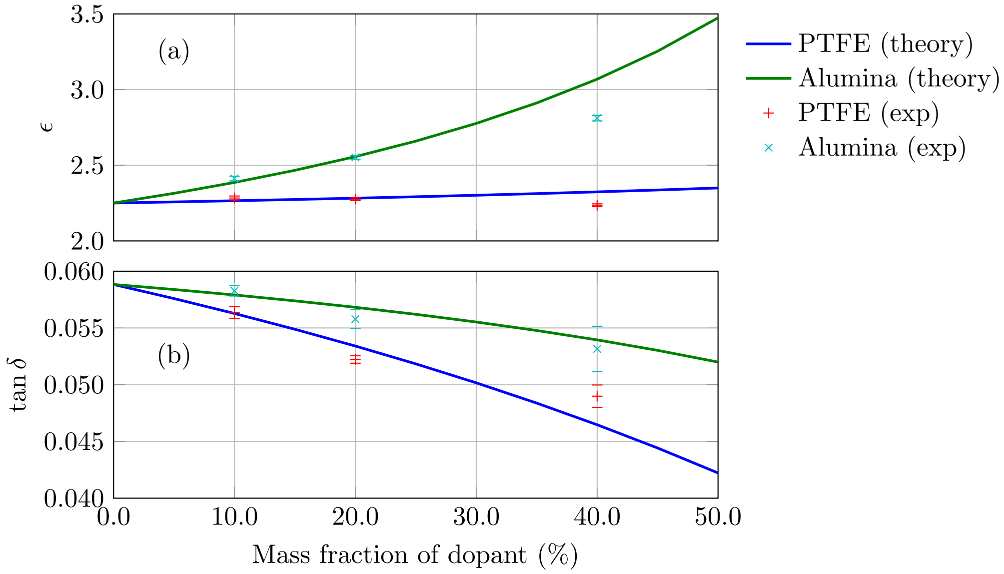

Figure 4.3. Effective medium theory. Comparison of measured results with effective medium theory at 0.7 THz. Error bars on measured results show the measurement uncertainty due to variation in sample thickness and experimental uncertainty. After Headland *et al.* (2015c).

material properties, to determine the effective permittivity and loss tangent in the continuous range of mass fractions from 0% to 50%, and results are given in Figure 4.3. This effective medium theory modelling is carried out at 0.7 THz. The results show reasonable agreement with the measured values, with discrepancy being potentially due to agglomeration of dopant particles that compromises the homogenisation of the dielectric, especially at higher dopant concentrations.

4.5 Resonator efficiency

The ultimate aim of this study is to investigate whether doping PDMS with lower-loss dielectrics has the potential to produce efficient resonators for use in terahertz reflectarray antennas. Full-wave simulations are therefore performed in order to determine the impact that the inclusion of powder dopants will have on a hypothetical array of metallic resonators. The structure of a unit cell of this resonator is given in Figure 4.4(a); it

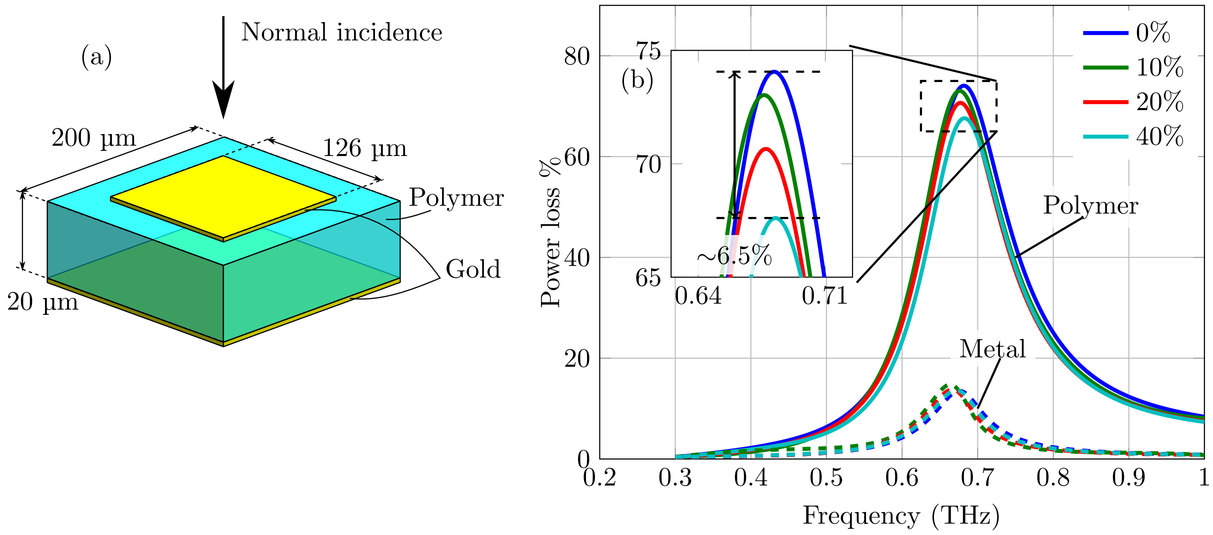

Figure 4.4. Doped PDMS-based resonator. Simulations to determine the impact of this new doped PDMS material on a hypothetical metallic resonator, showing (a) the structure of a unit cell of the resonator, showing incident excitation, where it is noted that the polymer in question is doped PDMS, and (b) a breakdown of the origins of loss in the metallic resonator, for the four different concentrations of PTFE tested, where dielectric loss is given with solid lines and Ohmic dissipation is represented with dashed lines.

is a square metallic patch separated from a ground plane by a polymer spacer. The dielectric properties of this spacer are extracted directly from the measured results given in Figure 4.2 in broadband. Excitation is provided by normally-incident terahertz radiation, and no polarisation vector need be specified for this diagram, as the patch in question is isotropic. This analysis is limited to the dopant PTFE, and hence does not consider alumina, for two reasons. Firstly, the results in Figure 4.2 show that PTFE provides a more pronounced reduction in loss than alumina, and hence is a better indicator of the true potential of this technique. Secondly, the relative permittivity of alumina is significantly higher than that of PDMS. A consequence of this is that the alumina-doped PDMS exhibits higher refractive index, which results in a dramatic alteration in the resonance frequency of the patch resonator in question, thereby making a direct comparison of efficiency unclear. By contrast, the relative permittivity of PTFE is near-identical to that of PDMS, and hence there is no such issue.

The results of these simulations are given in Figure 4.4(b). Power loss due to absorption in the metallic and polymer components of the resonator are of key interest, and hence nothing else need be displayed. It is immediately apparent from these results that the polymer spacer contributes $\sim 5\times$ the dissipation of the metallic spacer, and hence this validates the overall premise of this study that, in order to be effective, efforts to improve the efficiency of resonators of this sort must target the polymer spacer. However, it can also be seen from these results that, whilst there is a definite reduction in power loss with respect to increased concentration of PTFE, it is a modest reduction at best; the maximum reduction of peak power loss is a difference of $\sim$6.5%.[2] The reason that the reduction in loss tangent is not proportional to the reduction in overall loss is that the relationship between power absorption in the polymer and loss tangent is non-linear for such a resonator. These results show that the difference in power absorption due to the doping of PDMS is not significant when compared to the total peak loss. It must therefore be ceded that the particular materials developed in this study will not lead directly to the realisation of high-efficiency reflectarrays.

4.6 Conclusion

This chapter presents a technique for reducing dielectric loss of elastomeric polymers in the terahertz range by doping with micro/nano-particles of a lower-loss material.

---

[2] Here the value of 6.5% refers to the absolute reduction in percentage points, not the relative reduction from initial to final value

This process makes it possible to modify the dielectric loss tangent, and this is demonstrated by changing it from 0.058 to 0.049 (15.3%) in a sample doped with 40% PTFE by weight. The doped PDMS maintains its compatibility with microfabrication processes.

Simulations are employed in order to evaluate whether or not this technique will lead to efficient terahertz reflectarray antennas. It is found that, whilst the use of these materials provides a perceptible increase in the efficiency of a hypothetical metallic resonator, it is not a significant increase, and is unlikely to lead to a dramatic improvement in overall reflectarray performance. That said, the principle demonstrated in this work is quite general, and hence can validly be applied to other combinations of polymer and dopant. A similar methodology can potentially be employed to improve the efficiency of a lower-loss polymer, resulting in high-efficiency resonators.

This chapter investigated the possibility of improving the efficiency of a terahertz metallic resonator by modifying the properties of constituent materials. The following chapter will explore a different approach to achieve the same aim; the structure and functionality of the resonator is revised in order to yield a more-sophisticated device that exhibits higher efficiency.

Chapter 5

Polarisation-converting transmitarray for flat lens

A polarisation-converting transmitarray is presented in this chapter. This device is based on a tri-layer structure that supports multiple interactions of terahertz radiation with an anisotropic resonator prior to re-radiation to free space. This approach is innately suited toward desirable performance, and unit cell simulations show a high degree of phase tunability, transmission bandwidth, and efficiency. The transmitarray device is designed to function as a flat lens, with a focal length of 50 mm at an operating frequency of 400 GHz. The design is realised using microfabrication techniques, and subsequent experimental characterisation confirms that the fabricated device is capable of focusing radiation, as intended. The overall efficiency at the nominal operating frequency is found to be $\sim$68%.

5.1 Introduction

The device to be presented in this chapter is a terahertz transmitarray. A series of resonators designed for transmitarrays in the terahertz range has previously been reported in Grady *et al.* (2013), as detailed in Section 3.6. That work made use of an innovative structure in order to minimise power lost to reflection and dissipation. The unit cells exhibited 60–80% transmission efficiency over a broad bandwidth that is centred around $\sim$1.2 THz, which outperformed comparable transmitarrays reported in the literature by a significant margin. These resonators were deployed in a periodic arrangement for a beam-deflection device.

In this chapter, the aforementioned approach is adapted to create a flat lens operating at 400 GHz. This makes use of an aperiodic layout, and hence it bears additional complexities. For this design, the number of phase quantisation levels is doubled in comparison to that which is employed in Grady *et al.* (2013), by increasing the number and diversity of resonator designs. As explained in Section 2.3.2 this increase in the number of phase quantisation levels leads to improved performance and control. The demonstrated flat lens can potentially be employed to enhance antenna gain for high-volume communications (Yu *et al.* 2016), and focus radiation for imaging applications (Ojefors *et al.* 2009)—with no modification to its structure or functionality. Additionally, the selection of a lower operating frequency is informed by lower attenuation due to atmospheric gases (ITU-R 2013), as well as a greater degree of compatibility with compact electronic terahertz sources and detectors (Pfeiffer *et al.* 2014, Grzyb *et al.* 2016).

5.2 Design

Figure 5.1(a) illustrates a unit cell of the array, consisting of three layers of subwavelength metallic structures—an array of anisotropic resonators sandwiched between two orthogonal wire-grid polarisers. When the resonator is excited by x-polarised radiation under normal incidence, the resultant mode of resonance has a component that is orthogonal to the incident polarisation, i.e., in the y-direction. Consequently, it radiates waves in the cross-polarisation. The use of two non-resonant wire-grids forms a cavity; the front wire grid allows the incident waves to transmit through and interact with the resonator, and at the same time blocks the back-propagating waves with cross-polarisation generated from the resonator. The back wire grid reflects the

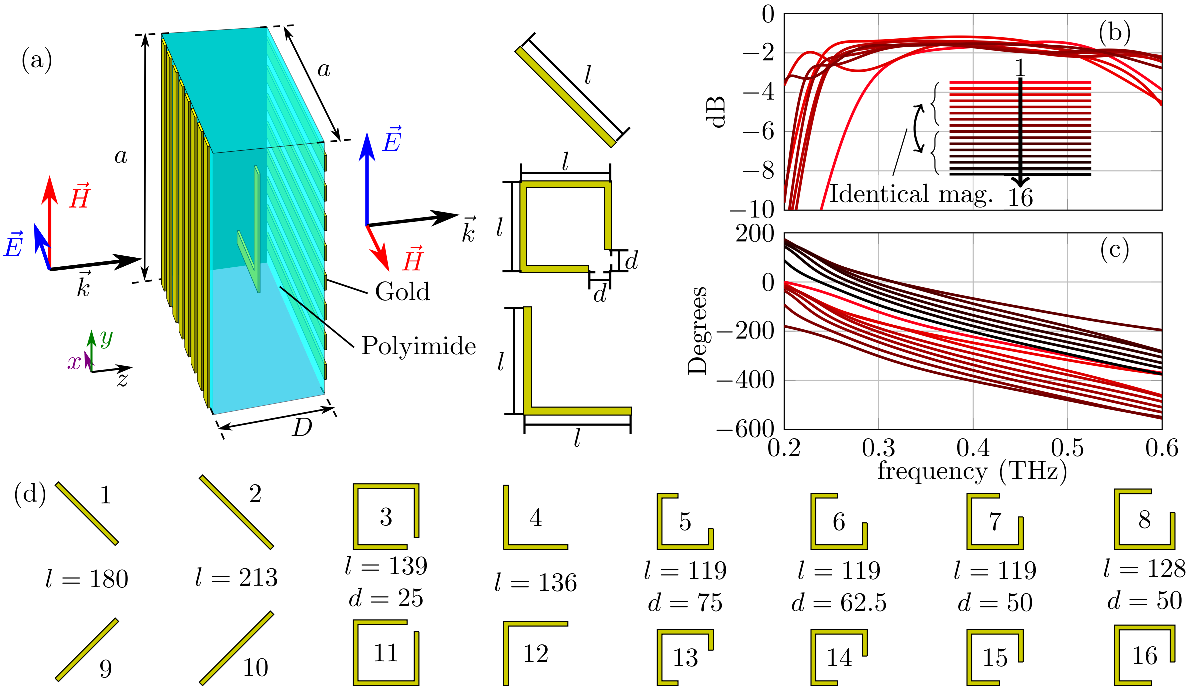

Figure 5.1. Unit cell of transmitarray. The unit cell of the tri-layer transmitarray, showing (a) structure and polarisation-conversion operation, where $a = 160$ µm and $D = 120$ µm. The adjacent diagrams show three different classes of resonator shape used in this work. There are 2µm-thick polyimide cap layers at the input and output surfaces, which are omitted for clarity. (b) Magnitude and (c) phase response of the cross-polarised transmission for the 16 resonator structures shown in (d). Note that resonators 9–16 are formed by flipping resonators 1–8 in the x-axis. Consequently, their magnitude responses correspond identically, and are omitted from (b). Track width of all metal microstructures is 10 µm, and the unit for the specified dimensions in (d) is µm. After Chang *et al.* (2017).

co-polarised waves back to the resonator for additional interactions, but allows the transmission of the cross-polarisation. Thus, multiple interactions with the resonator are experienced by radiation that enters the tri-layer structure. This enhances the efficiency of the conversion to cross-polarisation in the forward direction, and ultimately there is only cross-polarised transmission (desirable) and co-polarised reflection (undesirable).

An alternative way of understanding the operation of this resonator is that it is simply birefringent, and oriented diagonally. Thus, it converts the incident linear-polarised wave into an elliptical polarisation, and creates the cross-polarised component in the process. In principle, any anisotropic resonator can be applied in such tri-layer configurations to achieve the linear polarisation conversion, and crucially, two different resonator structures will exhibit distinct overall complex transmission response. Thus, varying the resonator geometry will result in different values of transmission phase, and this can be exploited for beam control (Grady *et al.* 2013). In this chapter, three different basic resonator forms are used, as shown in Figure 5.1(a). For each, the associated modes of resonance have vector components in both x and y-dimensions, as is required for the polarisation-conversion operation of the device.

The unit-cell response of a given resonator is investigated using full-wave simulations that model the individual element as a member of an infinite, uniform array that is excited with normally-incident radiation. The obtained cross-polarised transmission magnitude and phase are plotted in Figure 5.1(b) and (c), respectively, for a total of sixteen different resonator designs shown in Figure 5.1(d). It can be seen from the results in Figure 5.1(b) that the transmission efficiency at the nominal operating frequency of 400 GHz ranges from 68% to 76%, and it has at least 50% efficiency over a 250 GHz range that spans 300 GHz to 550 GHz, equivalent to 62.5% fractional bandwidth. More importantly, the phase response results in Figure 5.1(c) show a smooth, near-linear phase gradient for all resonators, with an approximate phase step of $\pi/8$ separating adjacent phase responses across the entire usable frequency range. A full 2π phase tunability range is therefore covered by this design. Note that resonators 9–16 are obtained by simply flipping resonators 1–8 in the x-axis, which alters their phase response by 180° by reversing the polarity of the cross-polarised current vector, but maintains identical transmission magnitudes between corresponding resonators, as evidenced in Figure 5.1(b,c).

In order to exhibit the bespoke lensing functionality, the transmitarray must impart the phase distribution given in Equation 2.7 onto the transmitted radiation, as discussed in Section 2.3.2. This phase distribution can be mapped to the appropriate layout of resonators via their discrete phase responses. As previously stated, there are sixteen distinct resonators, and their phase responses are spaced evenly around a full 2π cycle at the 400 GHz operating frequency. It is therefore quite straightforward to translate a given required phase distribution into a resonator layout; one need only quantise it into sixteen discrete steps, and map each step to the appropriate resonator. For this design, a focal length of 50 mm at the nominal operating frequency of 400 GHz is

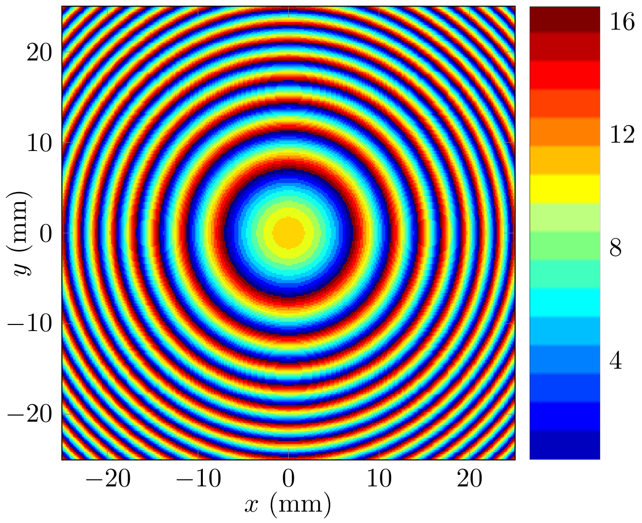

Figure 5.2. Array-level design of transmitarray. The spatial distribution of required elements for the terahertz transmitarray sample, where the colour coding represents the use of the 16 different resonators listed in Figure 5.1(d), spanning a full 2π phase range. Note the resolution of this element distribution corresponds to the lattice constant of the array itself, and hence there is a one-to-one mapping between pixels and resonators. After Chang *et al.* (2017).

selected, and the mapping to resonator layout that results from this procedure is given in Figure 5.2(a).

5.3 Fabrication

The structure that is the subject of this chapter consists of alternate layers of polymer and metal, as shown in Figure 5.3(a). The fabrication procedure is essentially a cycle of successive passes of spin-coating and curing a polymer spacer of a given thickness, depositing a metal film onto the spacer, and patterning the metal into the required planar microstructures. First, a 2 µm-thick polyimide layer is spin-coated onto a 4″ Si substrate and cured. A 200 nm-thick gold (Au) back grating (track width = 10 µm; duty cycle = 50%) is then fabricated using conventional contact lithography, electron-beam evaporation, and metal lift-off. A 60 µm-thick polyimide layer is subsequently spin-coated and thermally cured on hotplates at 300°C for 150 minutes, with a temperature ramp of 2.5°C/min. The resonator array containing sixteen different classes of Au resonator is fabricated atop this polyimide layer, following the same steps used to realise the Au back grating. A second 60 µm-thick polyimide layer is then spin-coated and thermally cured on top of the resonator layer, followed by the fabrication of the Au

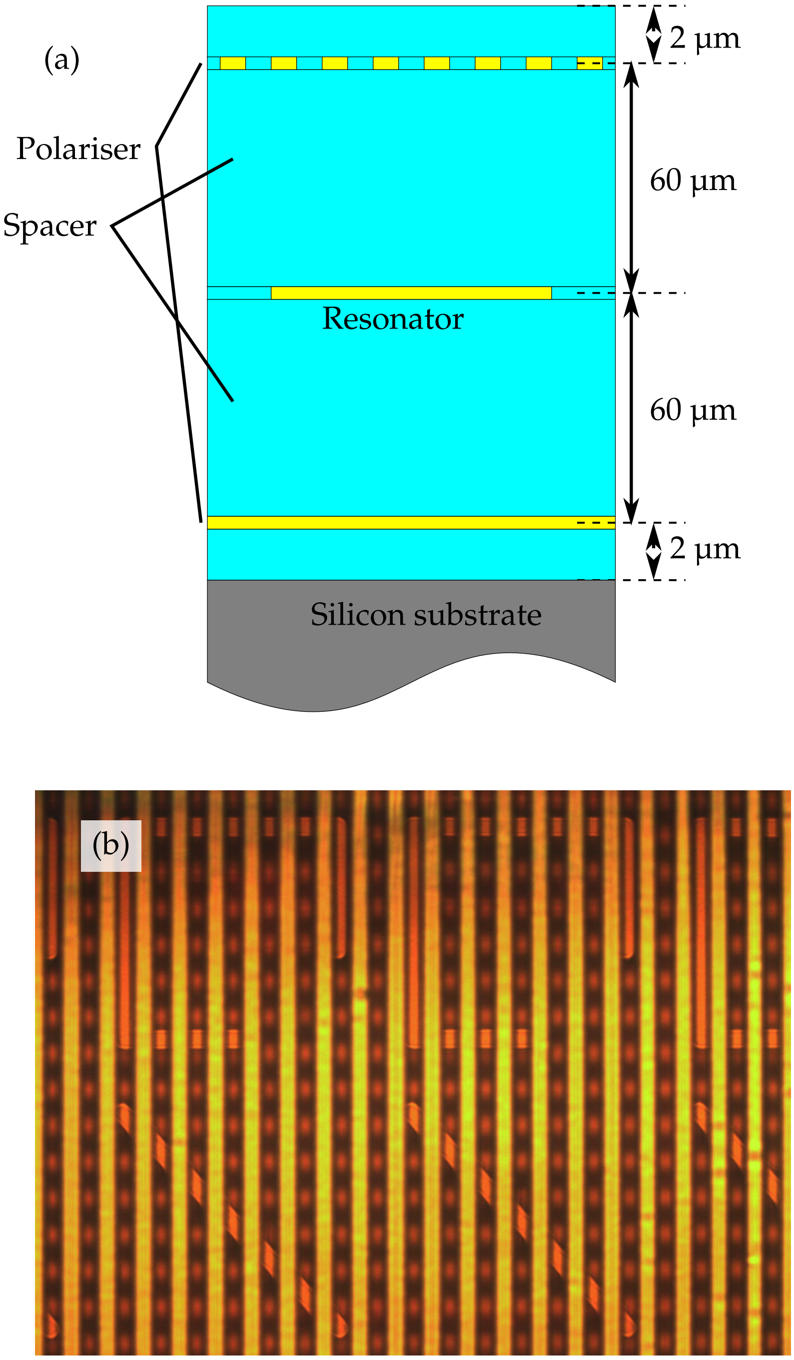

Figure 5.3. Fabricated transmitarray. The fabrication of the tri-layer transmitarray, showing (a) the cross-section of the structure prior to peel-off, and (b) a micrograph of a portion of the fabricated terahertz transmitarray sample, with two different classes of resonator visible; namely 16 and 1. Part (b) is after Chang *et al.* (2017).

front grating, which is oriented orthogonally to the Au back grating. Another 2 µm-thick polyimide cap layer is subsequently deposited and thermally cured in order to encapsulate the entire structure. Finally, the fabricated structure is mechanically peeled off from the Si substrate in order to establish a pliable, free-standing sample. A micrograph of a portion of the resulting sample is given in Fig 5.3(b), showing well-defined resonators and wire grids. The patterned area of the sample occupies $\sim 50 \times 50$ mm^2, and hence there is a total of ~98,000 individual resonator elements.

5.4 Characterisation of focal spot

The sample is excited with a collimated beam of the appropriate polarisation. At the operating frequency, the central portion of the incident beam is approximated by a Gaussian beam with a radius of 12 mm, but it also exhibits some intrinsic, frequency-dependent irregularities, as shown in Figure 5.4.

The cross-section (xy) and profile (xz) of the focused beam are raster-scanned, with scanning resolution of 0.1×0.1 mm^2 and 0.1×0.2 mm^2 respectively, and results are presented in Figure 5.5. See Appendix C.2 for details on the scanning procedure. Scans are presented at three frequencies of interest, namely 350 GHz, the designed operating frequency of 400 GHz, and 450 GHz. It is apparent from the xy-scan that a focal spot is produced at the operating frequency, as shown in Figure 5.5(c), and hence this validates the functionality of the device. The central portion of this focal spot is closely approximated by a narrow Gaussian beam, albeit with some undesired fields surrounding the focus. These fields are associated with irregularities in the incident beam, which causes the output phase distribution to deviate from that which is specified by Equation (2.7). The beam diameter of the central portion is determined by curve fitting to be 2.3 mm, but it is worth noting that this is spread by the detector. The particular detector in question exhibits a full-width half-maximum of ~12.5° in its radiation pattern (Menlo Systems 2016). When this divergence is approximated as diffraction from a Gaussian aperture, this corresponds to a 1.32 mm diameter (Svelto and Hanna 1998). Aperture spreading of this form is mathematically equivalent to convolving the field distribution by the aperture distribution, and hence that which is presented in Figure 5.5(a,c,e) has essentially been convolved by a 2D Gaussian function. It is well-known from probability theory that the convolution of two Gaussian distributions is also a Gaussian distribution, with variance equal to the sum of the variances of the input distributions (Ciuryło *et al.* 2001). This result generalises to two-dimensional field distributions. The true beam diameter is therefore determined to be ~1.88 mm. According to Equation 2.8, the diffraction-limited value is expected to be ~1.98 mm based on the input beam radius of 12 mm and focal length of 50 mm. As such, the focus conforms to expectation.

From the xz-scan at the operating frequency presented in Figure 5.5(d), the progression of the beam is revealed, and it can be seen that the beam passes through its focus,

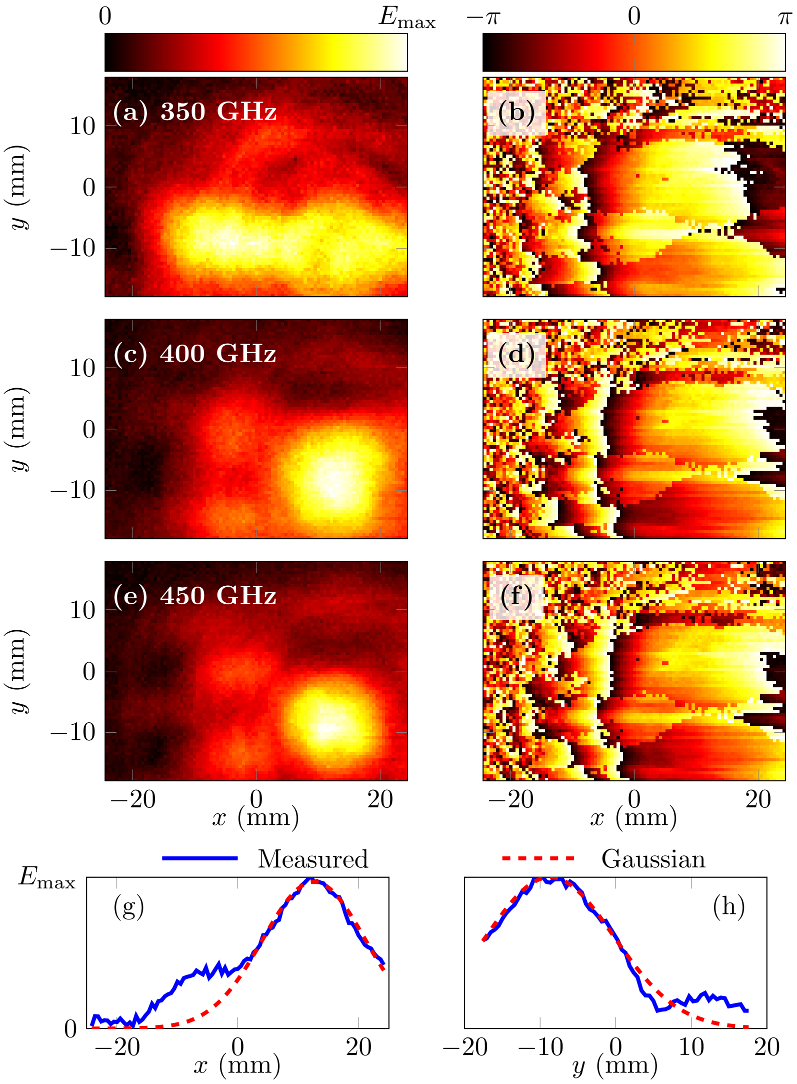

Figure 5.4. Incident beam. The incident, collimated beam that is employed to characterise the terahertz transmitarray sample, where it is noted that the view is not centred on the beam due to scanning-range limitations. (a,c,e) Magnitude profiles at 350, 400, and 450 GHz, and (b,d,f) phase profiles at corresponding frequencies. Axial field distributions at 400 GHz are given in (g) and (h), for the x and y-dimensions respectively, as well as the Gaussian function that is best-fit to the beam, which is of radius 12 mm.

as expected. However, the aforementioned irregularities of the incident beam are also evident here, as the beam does not exhibit a strictly-Gaussian intensity profile. For instance, there are sub-maxima at either side of the optical axis after it passes through its

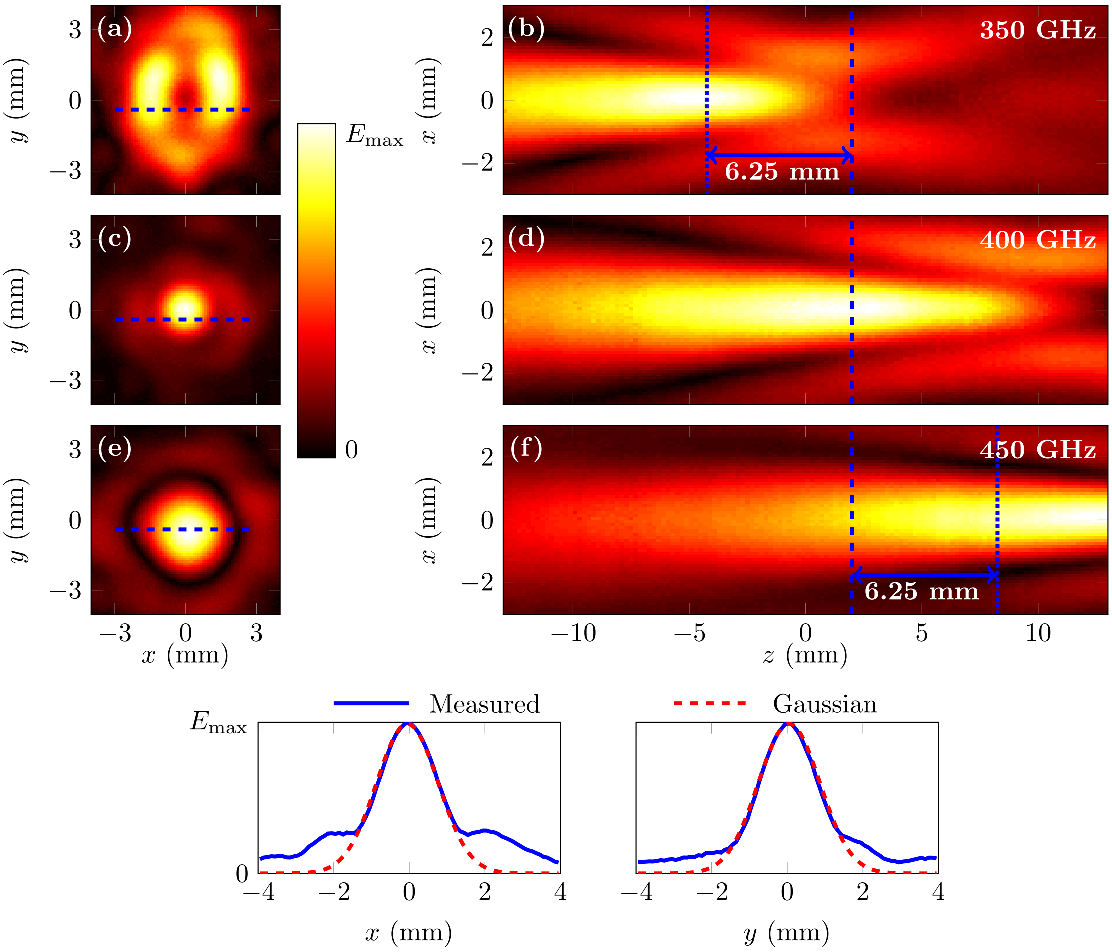

Figure 5.5. Focal spot of transmitarray. Measured raster-scanned field distributions spanning a 100 GHz range around the nominal 400 GHz operating frequency. (a,c,e) xy-plane cross sections of the focused beam at 350, 400, and 450 GHz respectively, and (b,d,f) xz-plane beam profiles for corresponding frequencies. Blue dashed lines give the intersection between the xy and xz planes in each of the plots, and blue dotted lines give the expected location of the focal spots based on a simplified dispersion model. One-dimensional, axial field distributions of the beam cross-section at 400 GHz are shown in (g) and (h), for x and y-dimensions respectively, as well as the Gaussian function that is best-fit to the beam, which is of radius 1.15 mm. All field plots are normalised to their respective maxima, in linear scale. After Chang *et al.* (2017).

focus, which appear to correspond to the aforementioned undesired fields surrounding the focus in the xy-scans in Figure 5.5(c). It is also noted that the z-coordinate position of the metasurface is not known in detail, due to obfuscating factors including the non-ideal collimated input beam and the structure of the detector PCA.

Given the approximately-proportional relationship between focal length and frequency for the frequency-invariant relative phase distribution described in Equation 2.7, a flat lens of this type is expected to be dispersive. This is especially true given the near-constant difference in phase between resonator elements across the usable frequency range shown in Figure 5.1(c). For this particular flat lens, this dispersion relation predicts a difference of ∼6.25 mm in focal length for a 50 GHz difference in frequency. As such, the xy-scans shown in Figures 5.5(a) and (e) are not at the device's focal plane, resulting in a broader spread in the electric field distribution. It is also noted that the scan in Figure 5.5(a) shows an annular-like field distribution, as opposed to a central maximum, which is ascribed to irregularities in the incident beam. The calculated focal plane positions for 350 and 400 GHz are consistent with the xz-scans given in Figures 5.5(b) and (d). However, the distance is greater for the scan shown in Figure 5.5(f). This is attributed to the frequency-dependent divergence of the incident beam, which exaggerates the spatial dispersion of the transmitarray.

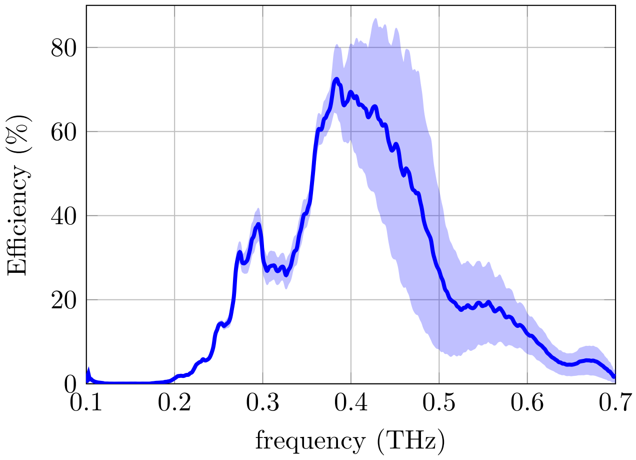

Figure 5.6. Efficiency of tri-layer transmitarray. Overall efficiency of tri-layer transmitarray device, investigated by single-pixel measurements, with error bars at one standard deviation given as a coloured region. After Chang *et al.* (2017).

5.5 Efficiency

Of key interest to the performance of this device is the overall efficiency, and hence this is evaluated experimentally. The approach that is employed is to compare the peak power delivered to the focal spot at 400 GHz with the power delivered by a standard polymethylpentene (TPX) lens of the same focal length that serves as a reference. With the TPX lens installed, the detector position is varied in order to determine whether or not the focus has moved from its original position, and find the new position of the focal spot. This mitigates errors in the measured magnitude response. Discrepancies in output polarisation and device aperture are compensated by setting the detector at a 45° angle, and passing the incident beam through an iris of $\sim$25 mm diameter, ensuring identical coverage of the incident terahertz beam. The dissipation and reflection losses of the reference lens are compensated analytically, by multiplying the response by the following factor,

$$\frac{4n}{(1+n)^2}\exp\left(-\alpha d\right), \tag{5.1}$$

where d is the mean thickness of the lens, and n and α are material properties from the literature (Podzorov and Gallot 2008). This is equivalent to dividing the reference measurement by the above less-than-unity factor, and hence it removes the insertion loss of the lens from this reference measurement. This measurement procedure is repeated five times in order to evaluate the associated degree of uncertainty. The results are presented in Figure 5.6, revealing a mean peak efficiency of $\sim$68% at the nominal operating frequency of 400 GHz, which is consistent with the unit cell simulations. Additionally, a -3 dB spectral bandwidth of 150 GHz is extracted from these results, spanning from 340 to 490 GHz. Note that the standard error increases markedly above the operating frequency, which is likely due to diminishing dynamic range with increase in frequency.

5.6 Conclusion

In summary, this chapter presents the design, fabrication, and characterisation of a terahertz flat-lens transmitarray operating in the vicinity of 400 GHz. The demonstrated diffraction-limited focusing capability and operating frequency are amenable to practical applications including terahertz imaging and high-volume communications. The bandwidth of this focusing capability is mainly limited by spatial dispersion, and is found to be approximately 37%, which corresponds to 150 GHz of absolute spectral bandwidth. The transmission efficiency of the device is experimentally evaluated to be $\sim$68% at the operating frequency.

This successful demonstration concludes Part II of the doctoral thesis, which was concerned with improving the efficiency of terahertz metallic resonator-based beam control devices. The following chapter will explore dielectric resonators as an alternative to metallic resonators, in order to determine if they will yield higher efficiency.

PART III

Silicon-on-gold microstructures

Chapter 6

Fabrication and characterisation of dielectric resonator antennas

---

DIELECTRIC resonator antennas (DRAs) composed of silicon microstructures on a gold ground plane are investigated as an efficient alternative to reflective metallic resonators such as those given in Section 3.7, in order to improve the performance of terahertz reflectarray antennas. The realisation of such resonators requires relatively-thick single-crystal intrinsic silicon to be incorporated onto a metal-covered substrate. To this end, an unconventional microfabrication procedure is developed that makes use of a combination of SU-8 assisted bonding, photolithography, and deep reactive ion etching. In order to verify the functionality of the DRA unit cells, a homogeneous array is designed and fabricated. The DRAs exhibit a magnetic dipole mode of resonance, and hence the overall array behaves as a magnetic mirror, with a 30% useful bandwidth. The efficiency of the DRA array is determined by numerical simulation to be 97% on resonance at 0.8 THz—a marked improvement upon the resonators covered in previous chapters.

6.1 Introduction

One of the most pressing issues that arises from the use of terahertz metallic resonators in the previous three chapters is efficiency. This is most apparent in Section 3.7, where peak absorption loss is up to ∼5 dB, which corresponds to ∼70% of incident power being dissipated. The dissipation loss in these metallic resonators is mainly due to the choice of PDMS ($\tan\delta = 0.06$ at 1 THz) as the dielectric spacer. This material is moderately lossy, and this loss is exacerbated dramatically by field confinement due to resonance of conduction current. Furthermore, as found in Section 4.5, the material loss intrinsic to PDMS cannot be significantly reduced by doping with less-lossy materials. Polyimide is a lower-loss polymer, with loss tangent $\tan\delta = 0.035$ at 1 THz (Ree *et al.* 1992), and this is partly responsible for the higher efficiency of the transmitarray that is presented in Chapter 5, although it is noted that the innovative multilayer structure of that device also contributed significant improvement to efficiency. The overall loss reported is 32% for this transmitarray. Whilst polyimide is certainly lower-loss than PDMS, the ensuing efficiency is hardly ideal, and hence the use of such higher-efficiency polymers in passive arrays is not a complete solution to the issue of resonator loss. Furthermore, polymers are not the sole contributors to the loss of a terahertz metallic resonator, as the metal component also dissipates some power. Whilst metals are good conductors in the microwave range, their conductivity decreases with respect to increase in frequency to the point where their behaviour is closer to that of lossy dielectrics in the optical range (Drude 1900). In the terahertz range that lies in between, metals such as gold are reasonable, albeit not ideal, conductors. Thus, the fact that metallic resonators make use of conduction current in their mode of resonance makes them susceptible to Ohmic dissipation. The efficiency of metallic resonators in the terahertz range is therefore intrinsically limited, and this fact provides strong motivation to investigate alternative means of devising a reflective resonator for operation in the terahertz range.

An alternative to the metallic resonator is the dielectric resonator. At its most straightforward, a dielectric resonator is essentially a small volume of dielectric, which most commonly takes either a cylindrical or hexahedral form, as illustrated in Figure 6.1, but in principle there are no stringent restrictions upon resonator shape. A brief summary of the resonance mechanism of a dielectric resonator is as follows. A strong discontinuity in refractive index at a dielectric boundary will result in significant reflection of

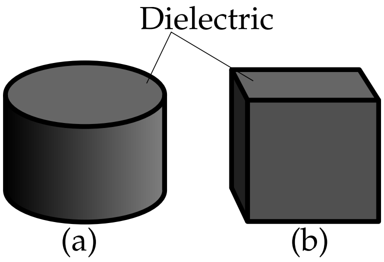

Figure 6.1. Illustration of dielectric resonator antennas. A diagram of common dielectric resonator forms, showing (a) a cylindrical and (b) a hexahedral resonator. The particular dielectric material is ideally low-loss, non-dispersive, and of refractive index $n > 3$.

electromagnetic energy. For example, a wave originating in a dielectric of moderate-to-high refractive index (i.e. $n > 3$), upon encountering a boundary to free space, will be partially reflected back into the dielectric. Thus, a small volume of this dielectric will behave as a resonant cavity, as a wave will reflect internally off one boundary, only to reflect off another, forming a standing wave at certain particular resonance frequencies. A given dielectric resonator may have numerous such non-harmonic modes of resonance that conjoin to deliver an overall phase range much larger than 360°. The characteristics (i.e. f_0, Q_r, and Q_a) of each mode of resonance will be dependent on the resonator's structure and dielectric properties. Note that the resonance of a dielectric resonator relies on displacement current, which is related to the rate of change of electric field magnitude, as opposed to conduction current, which pertains to the flow of charges in a conductor. A consequence of this is that the Ohmic dissipation of a dielectric resonator is considerably lower than for metallic resonators.

If a dielectric resonator is intended to couple to free-space fields, it can be considered a dielectric resonator antenna (DRA). Typically this is achieved by leaving the resonator unshielded, and constructing it out of sufficiently moderate-index dielectric material. According to Long *et al.* (1983), antennas of this form were initially conceived of as an efficient alternative to metallic resonators at millimetre-wave frequencies and beyond, due to increased ohmic dissipation at such frequencies. The aforementioned work presents a directly-driven DRA, in which the mode of resonance is excited by a point-feed structure, as indicated in Figure 6.2.

This chapter presents the realisation of an array of uniform terahertz DRAs. Each DRA is a cylinder of high-resistivity float-zone intrinsic silicon (HR Si) on a gold ground plane. Unlike the directly-fed dielectric resonator antenna shown in Figure 6.2, excitation is provided by incident free-space fields, and it is expected that the phase response

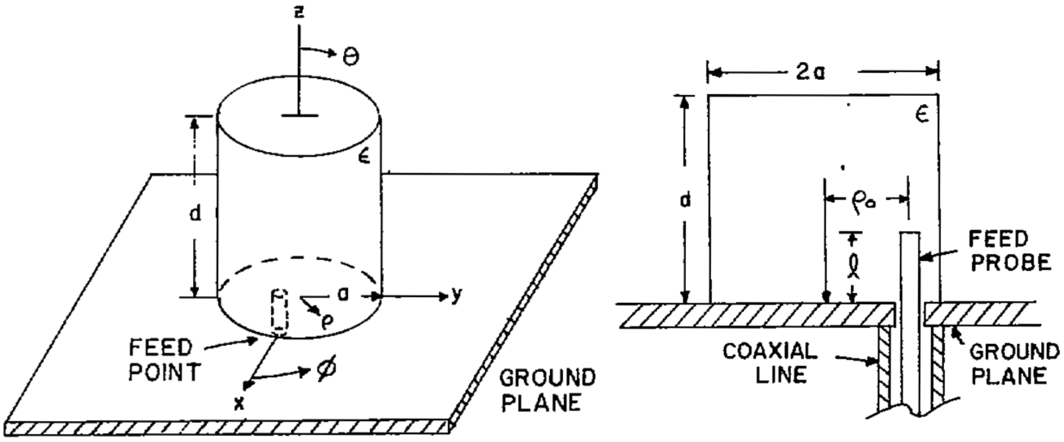

Figure 6.2. Long's resonant cylindrical dielectric cavity antenna. Illustration of the antenna geometry and feed configuration associated with one of the first demonstrations of dielectric resonator antennas in the microwave range, after Long *et al.* (1983).

of the reflected field is modified by resonance, without incurring significant dissipation. As prior work on DRAs at terahertz frequencies is limited in comparison to metallic resonators, and as the microfabrication procedure employed is unconventional, it is desirable to know the unit cell behaviour of the DRA in more detail than the resonators presented in previous chapters. Experimental means are therefore employed to characterise the unit cell, and in doing so, validate the associated fabrication procedure. The fabrication and characterisation of a uniform array of terahertz DRAs is therefore the main focus of this chapter. The realised structure exhibits a magnetic response at the operating frequency of 0.8 THz, with near-negligible loss, and hence the overall structure closely-approximates the behaviour of a perfect magnetic conductor, so called an artificial magnetic conductor (AMC). Such structures have applications in a broad range of applications from compact antennas (Feresidis *et al.* 2005, Guclu *et al.* 2011, Vallecchi *et al.* 2012, Miri *et al.* 2013) to sensing platforms (Yagitani *et al.* 2013).

6.2 Terahertz dielectric resonator antenna design

Key to the operation of the DRA are the quality factors: Q_a is associated with energy lost to dissipation and Q_r is associated with energy radiated to free space, as discussed in Section 2.5. These are determined by the geometry and constituent materials of the resonator. In general, a lower value of loss tangent leads to higher Q_a, and a higher value of relative permittivity leads to higher Q_r. In the majority of cases it is beneficial for a DRA to have high Q_a, as this ensures efficient operation. Low-loss dielectrics are therefore sought to construct DRAs. However, the choice of Q_r depends on the desired application. High Q_r is generally beneficial for sensing applications in order to maximise resonator sensitivity. Such high-Q_r DRAs, composed of a dielectric of high relative permittivity, have previously been demonstrated in the terahertz range (Takano *et al.* 2013). However, a drawback of high Q_r is narrowband operation, and stronger peak loss at the operating frequency. Reducing Q_r of the DRAs by selecting a

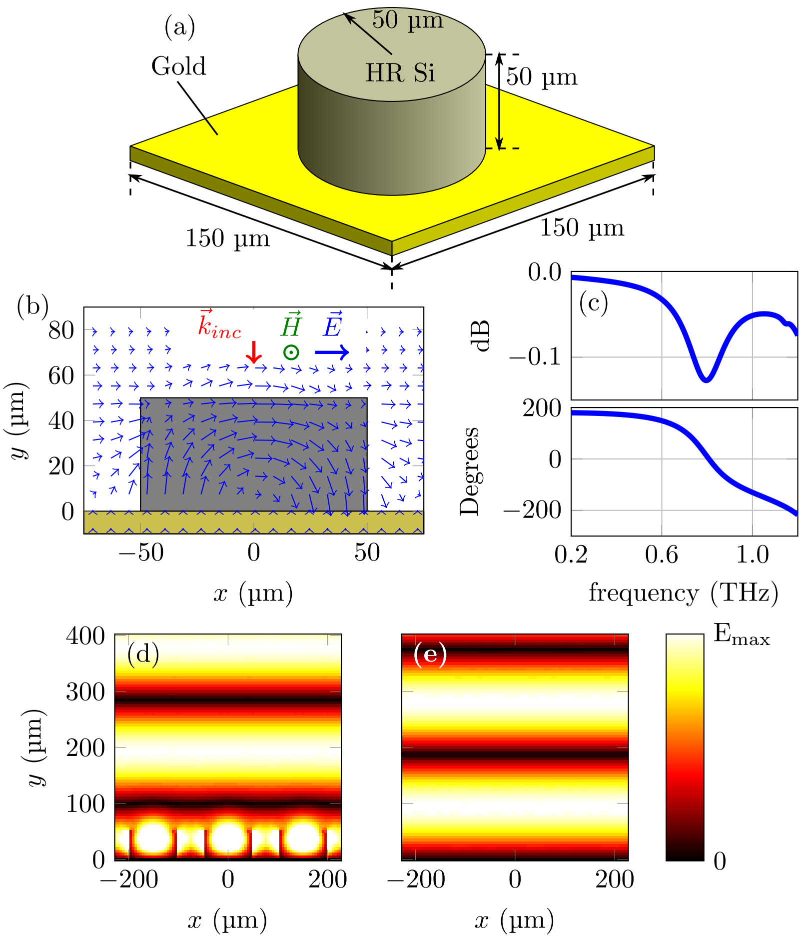

Figure 6.3. DRA unit cell. Single cylindrical DRA element, showing (a) schematic diagram (b) cross-sectional instantaneous field plot of single element in uniform array, when illuminated by normally incident plane wave, showing $\mathrm{HEM}_{11\delta}$ mode excited in dielectric resonator, (c) reflection coefficient for normally-incident radiation, (d) E-field standing wave pattern of DRA array, and (e) E-field standing wave pattern of un-patterned gold ground plane. After Headland *et al.* (2015b).

moderate-permittivity dielectric material will enhance bandwidth, improving suitability for communications and beam-control applications. High-resistivity single-crystal float-zone intrinsic silicon (HR Si) is chosen due to its moderate relative permittivity (ϵ_r= 11.68) and exceptionally-low dielectric loss (tan$\delta < 4\times10^{-5}$) in the terahertz range (Dai *et al.* 2004). These properties make HR Si suitable for terahertz DRAs with high Q_a and moderate Q_r.

The resonators employed in this chapter are micro-scale silicon cylinders, and this particular shape is chosen due to isotropic response and practical fabrication concerns. Such a design has previously been employed for a terahertz absorber (Liu *et al.* 2017), for which the objective is to maximise dissipation, rather than minimise it. The reason that such different functionalities are accessible to this form of resonator is because of the particular type of silicon employed in each case. For the absorber, doped silicon was employed, for which the presence of free carriers produces sufficient conductivity for dissipation. In contrast to this, the resonators presented in this chapter are composed of HR Si, which is a low-loss dielectric, as stated above. As shown in Figure 6.3(a), the cylindrical resonator is adhered directly to a gold ground plane, and hence there is no need for a polymer dielectric spacer in such a design, which is an advantage over metallic resonators. The dimensions of the passive DRA are optimised for lowest-frequency resonance at 0.8 THz. The thickness of the gold layer is 200 nm, which is well above the skin depth in the relevant frequency range ($\sim$90 nm at 0.8 THz). Given that the lattice constant at the resonance frequency is equal to 0.4λ, there are no array diffraction effects associated with this device, as grating lobes require a lattice constant that is $\geq \lambda$.

Full-wave simulations are utilised in order to investigate the field-matter interaction and resonance of the structure in detail. For these simulations, the resonator is modelled as a single unit cell in an infinite, homogeneous array of identical elements that is excited by an incident plane wave. A Drude model is employed in order to account for realistic material losses to a high degree of fidelity (Drude 1900). Based on the minimum resistivity of 2 kΩ·cm provided by the manufacturer, the carrier concentration is estimated to be around 2×10^{12} cm^{-3}, and the mobility to be around 1360 cm^{2}V^{-1}s^{-1}. Thus, the plasma frequency and relaxation time are equal to f_p = 0.025 THz and τ_c = 0.202 ps respectively. For the gold ground plane, given the low penetration depth of field into the metal, a surface impedance model is considered adequate (Zou *et al.* 2014b). A Drude model is also employed in order to calculate the frequency-dependent surface impedance of gold across the relevant frequency range (Lucyszyn 2007), with DC conductivity of $\sigma_{\mathrm{DC}} = 4.1 \times 10^7$ S·m^{-1}, and scattering relaxation time $\tau = 0.15$ ps (Ordal *et al.* 1983). The results of these simulations are given in Figure 6.3(b-d).

The field plot in Figure 6.3(b) shows the hybrid mode of resonance in a single DRA element, commonly denoted as $\mathrm{HEM}_{11\delta}$, or magnetic dipole mode (Petosa 1997),[3] which is excited by a normally-incident plane wave. According to the response given in Figure 6.3c, the simulated peak loss of the DRA is 0.13 dB, and this is equivalent to reflecting incident energy with 97% efficiency. Furthermore, after phase de-embedding, phase zero-crossing is observed at $\sim$0.8 THz, which is indicative of a magnetic response. Thus, these simulation results indicate AMC operation at this operating frequency. By contrast, an electrical conductor will exhibit a $\pm180^\circ$ value of reflection phase, and in the standing wave produced by the interference of the incident and reflected waves, this results in a node at the conductor's surface. For the AMC, however, the absence of this negation of reflection phase results in an anti-node, and hence the field is strongest near to the ground. This difference is confirmed via E-field standing wave results given in Figure 6.3(d) and (e). It is clear that the maxima in the field magnitude for the DRA indicate the phase contrast with the minima for the un-patterned ground plane, as expected.

6.3 Comparison with metallic resonators

In order to clearly illustrate the advantages of DRAs over metallic resonators in the terahertz range, an example of an equivalent metallic resonator is contrived and studied with full-wave simulations. This resonator, which is henceforth known as the metallic resonator antenna (MRA), consists of a circular metallic patch separated from a ground plane by a polymer spacer, as illustrated in Figure 6.4(a). This particular resonator design is selected because the isotropic nature of its response and the field orientation of its mode of resonance are similar to those of the DRA. The loss tangent of the polymer spacer is varied in order to evaluate the main contributors to absorption in the resonator. The unit cell dimensions of the MRA are identical to those of the DRA, and the

---

[3] This magnetic dipole is the lowest-frequency mode of resonance, but it is noted that, for a cylindrical DRA of this sort, the lowest-frequency mode can be either an electric or a magnetic dipole, depending on the aspect ratio of the cylinder.

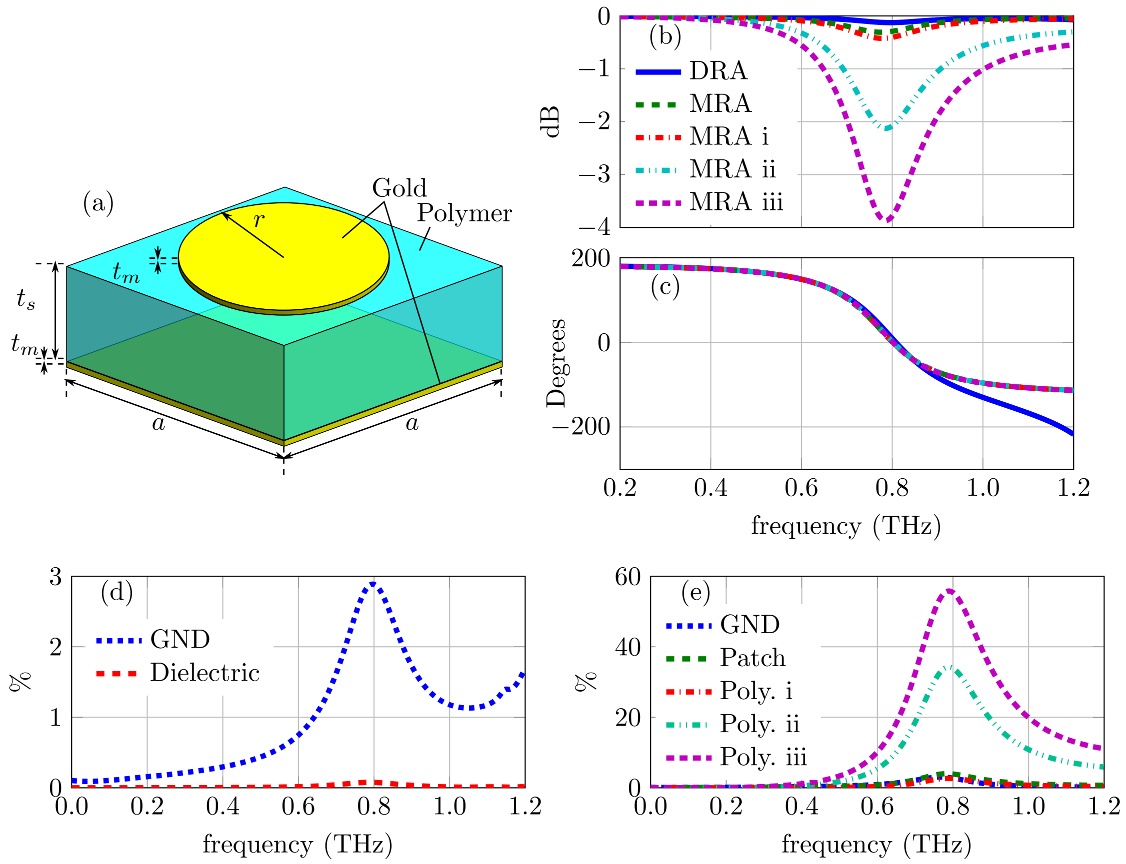

Figure 6.4. DRA comparison with metallic resonator. Comparison of the cylindrical DRA with a circular patch-based metallic resonator antenna (MRA) that is engineered to have comparable phase response. (a) Simulated metallic resonator structure, with $a = 150$ μm, $r = 59$ μm, $t_s = 21$ μm, and $t_m = 0.2$ μm, and (b,c) magnitude and phase responses of the DRA with the MRA, where the dielectric properties of the polymer spacer are $\epsilon_r = 2.25$. Loss tangent values simulated are $\tan\delta = 0.0$, (i) $\tan\delta = 0.002$, corresponding to PP (Hejase *et al.* 2011), (ii) $\tan\delta = 0.031$, corresponding to polyimide (Ree *et al.* 1992), and (iii) $\tan\delta = 0.06$, corresponding to PDMS (Khodasevych *et al.* 2012), where all values are given for 0.8 THz. (d) Analysis of individual origins of loss in the DRA, and (e) analysis of individual origins of loss in the MRA. After Headland *et al.* (2015b).

spacer thickness and patch diameter are optimised so as to exhibit the same resonance frequency, and similar phase response.

A comparative numerical study of the response of the DRA and the MRA is given in Figure 6.4(b). Note that, due to differences in the nature of higher-order resonances in both resonators, the phase response of the MRA is not well-matched to the DRA above the fundamental resonance of 0.8 THz. Several values for the dielectric loss tangent of the polymer spacer are simulated. These include a lossless case, as well as selected values of loss tangent that correspond to polypropylene (PP) (Hejase *et al.* 2011), polyimide (Ree *et al.* 1992), and polydimethylsiloxane (PDMS) (Khodasevych *et al.* 2012), as these are all commonly-used polymer dielectrics in the terahertz range (Aznabet *et al.* 2008, Tao *et al.* 2008b, Tao *et al.* 2008a, Tao *et al.* 2010, Kim *et al.* 2012b, Kim *et al.* 2012a, Lee *et al.* 2012, Wang *et al.* 2013, Grady *et al.* 2013, Niu *et al.* 2014b, Cheng *et al.* 2014, Ortuño *et al.* 2014, Kuznetsov *et al.* 2015, Liu *et al.* 2015b).

It is found that, in the idealised case in which the dielectric spacer of the MRA is lossless, the DRA outperforms the MRA by a small margin of 0.17 dB. It can be inferred from this that, because the ground plane is common to both designs, and the MRA's dielectric spacer is lossless in this case, the added loss originates in Ohmic dissipation in the resonant patch itself. In the case corresponding to PP, the low dielectric loss leads to the DRA outperforming the MRA by a similarly-small margin of 0.3 dB. The advantage of the DRA becomes more apparent when lossier dielectrics are utilised. When the loss tangent corresponds to polyimide, the DRA outperforms the MRA by 2 dB. In the highest-loss case considered, corresponding to PDMS, the DRA outperforms the MRA by 3.7 dB. In order to gain further insight into the loss in the DRA and MRA, analysis of the individual origins of loss is given in Figures 6.4(c) and (d). It is found that the majority of the loss in the DRA on resonance is in the ground plane, and hence Ohmic loss is exacerbated by field confinement on resonance. In the case of the MRA, the dielectric spacer corresponding to PP exhibits low loss, which is comparable to the Ohmic loss in the patch and ground plane. In both other cases, however, the majority of the loss on resonance is contributed by dielectric loss in the polymer spacer, which is once again exacerbated by resonance.

6.4 Fabrication

Whilst single-crystal silicon is abundantly available in the form of wafers, it cannot be grown on metal-coated substrates. This restriction has historically limited the exploration of single-crystal silicon microstructure applications. As they cannot be grown, single-crystal silicon wafers must be diced and bonded to a substrate prior to patterning into microstructures. This issue of bonding is therefore of high concern.

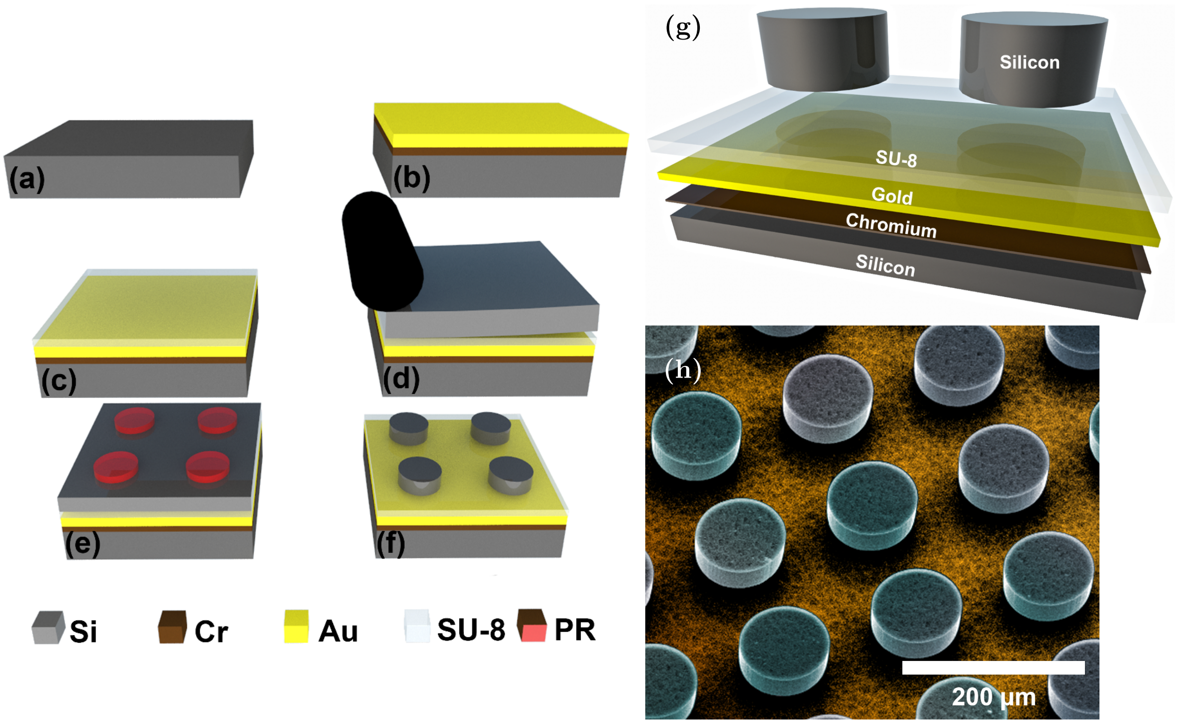

Figure 6.5. Fabrication of terahertz DRAs. The physical realisation of the HR Si on metal microstructures, showing (a-f) fabrication process, (g) layered view of complete structure, and (h) false colour SEM micrograph. After Headland *et al.* (2015b).

The fabrication process developed to realise the design presented in Section 6.2 is as follows, and a schematic of this process is depicted in Figure 6.5(a) to (f). A ∼75-mm silicon wafer is cleaned with solvents and dried with compressed nitrogen. A 200 nm film of gold is then deposited on to the wafer, along with a 20 nm chromium adhesion layer, by electron beam evaporation at a rate of 0.1 nm/s, after pumping down to a base pressure of 1×10^{-7} Torr. To achieve the adhesion of the single-crystal silicon wafer to this metal-coated substrate, the following procedure is employed. The gold-coated silicon wafer is spin-coated with a layer of SU-8 2000.5 at 3,000 rpm to achieve a film thickness of ∼500 nm, which functions as an adhesion layer for subsequent steps. The SU-8 film is cross-linked using ultra-violet exposure for 10 s with 65 mJ/cm^2 energy. A HR Si wafer of thickness 125 µm is diced into 35×35 mm^2 sections. This HR Si section is then bonded to the SU-8 and gold-coated substrate by passing it through a table-top laminator at 100°C and slow speed, which cures the SU-8, and forms a strong bond to the HR Si. The bonded 125 µm-thick HR Si is thinned down to the required

50 µm, corresponding to resonator height, by plasma-enhanced deep reactive ion etching (DRIE). This etching is performed in a single step with a gaseous mixture of C4F8 (10 sccm) and SF6 (200 sccm) and inductively coupled plasma (ICP) power of 1500 W for 6 min. Subsequently, photolithography is performed using a thick AZ4562 photoresist (PR) spun at 2,500 rpm, which results in a 7.5 µm thick layer for defining patterns corresponding to the diameter of the terahertz dielectric resonators. Photolithography is followed by DRIE as above, but with cyclic processing known as Bosch silicon etching. Each cycle of the etching recipe is composed of three steps: deposition, break, and etching. In the deposition step, a gaseous mixture of C4F8 (200 sccm) and SF6 (10 sccm) with ICP power of 1000 W for 3 s is utilised. The break step utilises C4F8 (10 sccm), SF6 (100 sccm), and ICP power of 1000 W for 2 s. The etching step comprises a gaseous mixture of C4F8 (10 sccm) and SF6 (200 sccm) with ICP power of 1500 W for 3 s. With this recipe an approximate etch rate of 0.8 µm/cycle is obtained for the HR Si. The required 50 µm-deep etch is achieved in 65 cycles. Lastly, the photoresist is stripped off and the height of pillars verified with a scanning electron microscope (Nova NanoSEMm FEI Systems). A diagram of the layered construction of the completed structure is given in Figure 6.5(g), and a false-colour SEM micrograph, showing cylinders of high quality, is given in Figure 6.5(h).

6.5 Experiment

The reflection response of the DRA array is characterised using a THz-TDS setup, as illustrated in Figure 6.6. Both normally-incident and obliquely-incident radiation at a 45° angle are considered. If a focused beam were employed to excite the resonators, it would introduce a range of angles of incidence, resulting in a poor approximation of the plane-wave excitation used in the simulations given in Section 6.2. It is therefore deemed necessary to probe the response of the DRA array with a collimated terahertz beam. As the size of the patterned area of the sample is less than the ∼24 mm beam waist of the collimated terahertz beam, a ∼5 mm-diameter iris is required to isolate the reflection from the patterned portion of the sample, at the cost of reduced dynamic range. Another consequence of clipping the beam to a ∼5 mm diameter is the introduction of diffractive effects, which result in increased beam divergence. This beam divergence is common to both measurements, and hence normalisation is valid to remove the influence of the iris. In the case of the normally-incident measurements, a polished silicon wafer is utilised as a beam splitter, and this is expected to impose further reductions on dynamic range. For the normal-incidence measurements, the setup in Figure 6.6(a) is utilised, and a peak dynamic range of 35 dB with a bandwidth of 1.4 THz is observed. For the oblique-incidence measurement setup illustrated in Figure 6.6(b), peak dynamic range and bandwidth are 39 dB and 1.6 THz, and 36 dB and 1.8 THz, for the TE and TM measurements, respectively. All measurements are performed in a dry-air atmosphere, using a gold mirror as a reference. The sample holder is fixed in place, to prevent inconsistencies in rotational misalignment between the sample and reference measurements from leading to spurious results. The total path length in all experiments is ∼30 cm.

6.6 Results

The response to normally-incident radiation is given in Figure 6.7(a) and (b), and close agreement with the simulated phase response is attained. The results show the zero phase crossing characteristic of a magnetic conductor occurring at ∼0.81 THz, as predicted from simulations. The useful bandwidth of the AMC, typically defined as the frequency range between +90° and −90° (Feresidis *et al.* 2005), is about 30%, spanning 0.71 to 0.95 THz. The magnitude response appears to exceed unity around resonance,

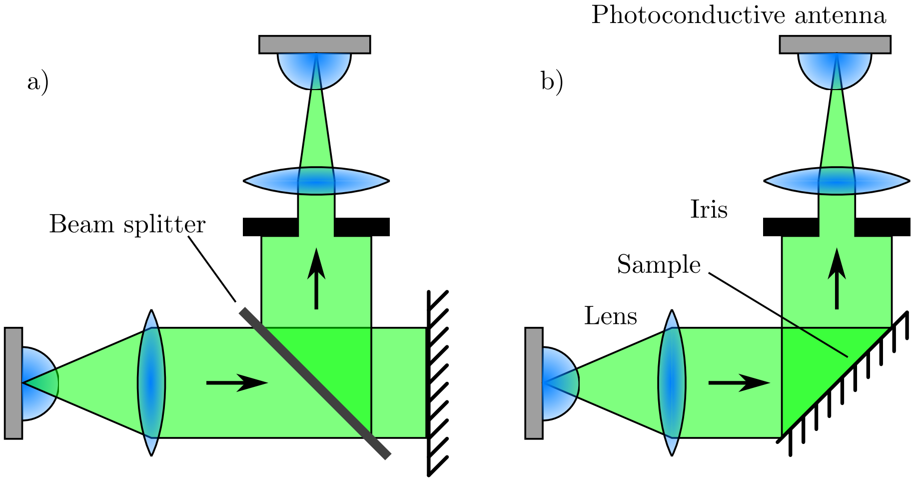

Figure 6.6. Characterisation of DRA-based AMC. Measurement setup for (a) measurement of normally-incident radiation, and (b) oblique measurement at 45° angle of incidence. After Headland *et al.* (2015b).

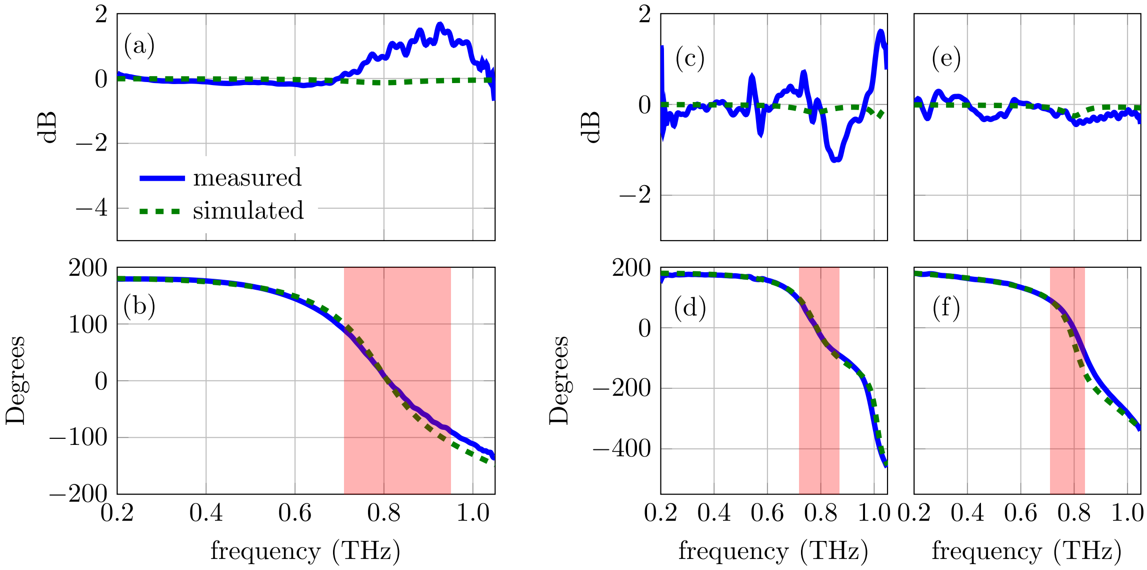

Figure 6.7. Measured response of AMC sample. Reflection characteristics of the THz DRA array, showing (a,b) response to normal incidence, (c,d) response to oblique incidence at 45° with TE polarisation, and (e,f) response to oblique incidence with TM polarisation. Useful bandwidth for AMC functionality is lightly shaded in red. After Headland *et al.* (2015b).

which is contrary to the slight loss in the simulated response. This is attributed to an enhancement in the effective aperture of the overall array due to mutual coupling between DRA elements (Ranjbar Nikkhah *et al.* 2014), and the mechanism by which this occurs is as follows. Due to the nonuniform-magnitude excitation provided by the incident beam, certain elements are excited more strongly than one or more of their immediate neighbours. However, due to mutual coupling between adjacent resonators, a strongly-excited resonator will contribute energy to a less-excited neighbour, resulting in an increased spread of the re-radiated field distribution. This enhances overall aperture, which reduces the beam divergence, and therefore results in greater magnitude than the un-patterned reference mirror. Note this effect was not accounted for in the simulated response. Additionally it is noted that, given the large number of elements in the array, factors such as Mie scattering and the radar cross section of individual elements are insignificant compared to array factor and coupling effects.

The response to obliquely-incident radiation at an incidence angle of 45° is given in Figure 6.7(c)-(f). There is substantial variation in the magnitude response, possibly due to reductions in dynamic range imposed by the use of the iris, as described in Section 6.5. Other possible explanations include minor alignment issues and array coupling effects. This magnitude fluctuation issue, however, does not wholly diminish confidence in the veracity of the phase response, as the phase component is less vulnerable than magnitude to noise in THz-TDS (Withayachumnankul *et al.* 2008, Withayachumnankul *et al.* 2014). As with the results for normal incidence, there is strong agreement with simulation in the phase response, and resonance at ∼0.8 THz is observed for oblique incidence in both polarisations. In the case of the TE polarisation, the phase response shows the zero phase crossing at 0.78 THz, and useful bandwidth from 0.72 to 0.87 THz. For TM, the simulated response shows a zero-crossing at 0.78 THz, but the measured response shows the crossing at 0.8 THz. This discrepancy is potentially due to some small misalignment in the THz-TDS system. The measured useful bandwidth in the TM polarisation is 0.71 to 0.84 THz. The reason for the disparity in the phase response for the normal and oblique incidences is that different higher-order modes of resonance may be lightly excited in each case, and these resonances jointly contribute to the overall phase response. The intersection of the useful ranges for all cases tested is 0.72 to 0.84 THz, and hence the common bandwidth for normal and oblique incidence is 15%. Lastly, although a precise value for efficiency cannot be quoted based on these experimental results, the fact that effects other than material loss appear to dominate indicates that overall efficiency is near-ideal.

6.7 Conclusion

An array of passive terahertz DRAs operating at 0.8 THz has been reported in this chapter. An unconventional fabrication process is utilised to realise the single-crystal silicon on metal microstructures. The demonstrated device behaves as an AMC with 30% bandwidth for normal incidence, and exhibits a tolerance to oblique excitation up to at least 45°, albeit with reduced useful bandwidth.

The AMC device itself may find applications in compact terahertz antennas and sensing devices, but that is not the main significance of this demonstration in the context of this thesis. Rather, the terahertz DRA in question can be considered a high-efficiency alternative to metallic resonators in beam-shaping reflectarray applications. Having successfully devised and demonstrated efficient terahertz resonators based on silicon microstructures, it is of interest to deploy these resonators in a beam-control device, and this will be the subject of the following chapter.

Chapter 7

Dielectric-resonator-based reflectarray

TERAHERTZ DRAs of the sort discussed in the Chapter 6 are deployed in order to realise an efficient reflectarray antenna with an operating frequency of 1 THz. The same procedure is employed to fabricate this array of DRAs, albeit with the added complexity of a nonuniform mask layout. This reflectarray is engineered to exhibit functionality equivalent to an off-axis parabolic reflector, and hence it is capable of lensing. The intended functionality and efficiency of this device are experimentally verified, and the -3 dB bandwidth is found to be $\sim$18%. Thus, the demonstrated reflectarray is a compact and highly efficient terahertz beam control device, and this satisfies the main motivation for this investigation, which was discussed in Chapter 1. Furthermore, Section 2.3.2 asserts that the principles of wavefront engineering are general, and hence the layout of the terahertz reflectarray that is the main focus of this chapter can potentially be adapted to serve a great variety of different application requirements.

7.1 Introduction

Chapter 6 presents a technique to fabricate single-crystal silicon microstructures that operate as highly efficient terahertz resonators, and these resonators are deployed in an artificial magnetic conductor device. However, the process of design and modelling reveals that the resonators exhibit numerous attributes that are beneficial for a terahertz beam control application; the loss of the resonators is negligible, and there are several resonances of moderate quality factor that jointly produce a large phase tunability range. In this chapter, these traits are exploited in order to realise a terahertz reflectarray. Although the general resonator structure and fabrication process are not altered in any way, the functionality of the resulting device is quite different, from an electromagnetics perspective.

In accordance with the procedure outlined in Section 2.5.1, the dielectric resonator design is integrated with a desired beam-shaping behaviour, which is a lensing operation in this case, and the result is a total reflectarray design. This design is fabricated and experimentally characterised in order to verify its functionality. Its antenna gain is determined to be close to 50 dB, which constitutes very high antenna gain, and hence the demonstrated device has the potential to support terahertz links for high-volume communications, as outlined in Sections 1.2 and 1.3.

7.2 Unit-cell design

As in the previous chapter, Chapter 6, the unit cell is a cylinder of HR Si on a gold ground plane, and it is excited by free-space terahertz waves. In the case of normal incidence this results in total resonator symmetry, which suppresses any modes requiring asymmetry. However, TE-polarised oblique incidence at 45° is employed for the off-axis focusing mirror, as shown in Figure 7.1(a). This breaks resonator symmetry for a homogeneous array, and hence asymmetric modes are excited. As in Chapter 6, the response and modes of resonance of the DRA are investigated with full-wave simulations. As the details of these simulations were presented in-depth in the previous chapters, they will not be repeated here.

When set to have a radius of $r = 35$ µm, and height of $h = 50$ µm, the DRA exhibits lowest-frequency resonance at 1 THz. This takes the form of a horizontal magnetic dipole on a ground plane, or $\mathrm{HEM}_{11\delta}$ mode, as shown in Figure 7.1(b). When radius

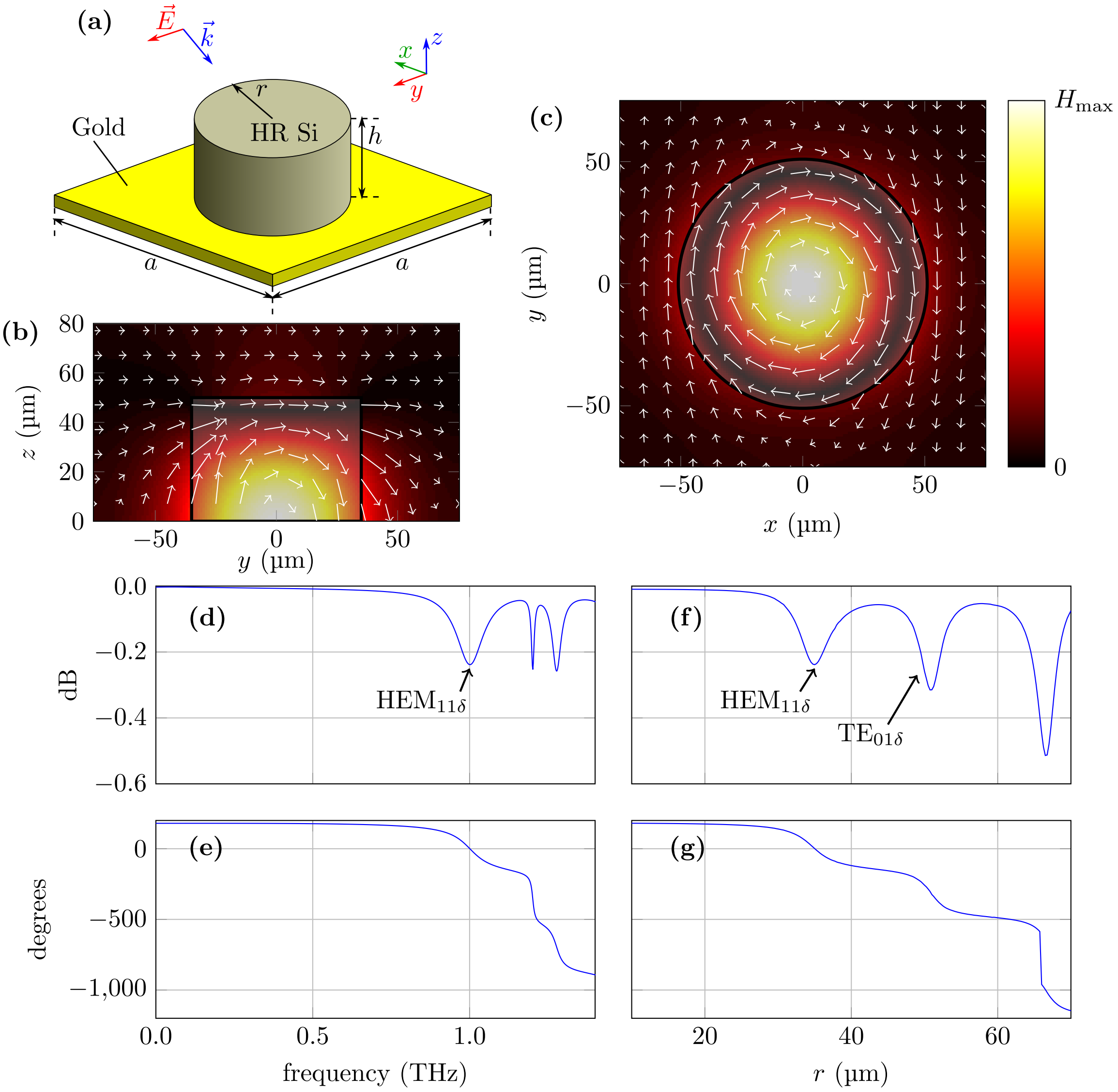

Figure 7.1. Parametric analysis of DRA. Design and simulated elecromagnetic response of the dielectric resonator antenna unit cell. (a) Resonator structure, where $h = 50$ µm and $a = 150$ µm, and incident TE excitation is at a 45° angle of incidence, (b) $\mathrm{HEM}_{11\delta}$ mode of resonance at 1 THz, when $r = 35$ µm, with magnetic field strength shown as a heat map and electric field shown as a quiver plot, viewed from the side, (c) $\mathrm{TE}_{01\delta}$ mode of resonance at 1 THz, when $r = 51$ µm, viewed from above, at a distance of 34 µm away from the ground plane, (d,e) broadband amplitude and phase responses when $r = 35$ µm, showing lowest-frequency resonance at 1 THz, and (f,g) amplitude and phase responses for parametric sweep of cylinder radius, at an operating frequency of 1 THz. After Headland *et al.* (2016a).

is set to $r = 51$ µm, the DRA exhibits a higher-order resonance at 1 THz, and the field distribution inside the DRA is a vertically-oriented magnetic dipole, or $\mathrm{TE}_{01\delta}$ mode (Zou *et al.* 2012), as shown in Figure 7.1(c). The magnetic dipole orientation results in electric fields that are parallel to the ground plane. Given that tangential electric field vanishes at the surface of a good conductor, the fields are strongest a distance away from the metal. For this reason, the field plot shown in Figure 7.1(c) is at a distance of 34 µm from the ground plane. Note, modes such as this $\mathrm{TE}_{01\delta}$ mode of resonance can only be excited with asymmetry, which in this case is the result of the obliquely-incident excitation.

The $r = 35$ µm configuration, which exhibits lowest-frequency resonance at 1 THz, is investigated in more detail, and broadband response is given in Figure 7.1(d,e). This shows the expected 0° reflection phase on resonance, as well as higher-order resonances beyond 1.2 THz. The multiple resonances jointly form a large phase transition, with dissipation loss that does not exceed 0.25 dB.

The resonance frequency is tunable by varying the radius of the micro-scale cylinder. Thus, parametric analysis at 1 THz is performed in order to determine the phase tunability of the DRA structure with respect to the cylinder radius r. The parametric sweep results given in Figure 7.1(f,g) show resonances at radius values of $r = 35$, 51, and 67 µm. Given that the first two resonances form a smooth phase tunability range of more than 360°, it is not necessary to employ the slightly lossier resonance of the $r = 67$ µm configuration in the final design. Therefore, the DRA has a large phase tunability range, over which it exhibits loss no greater than 0.32 dB, which is highly beneficial to a reflectarray application (Yang *et al.* 2012).

7.3 Array-level design

As a proof-of-concept, the DRA-based reflectarray is designed to function as an off-axis focusing mirror at 1 THz, as shown in Figure 7.2. The polar coordinate system in this diagram is illustrated with an arbitrary point $P = (d, \theta, \phi)$. A collimated beam impinges on the surface of the reflectarray obliquely, with an incidence angle of 45°, and is focused to the point F, which is defined by the polar coordinates $d_F = 150$ mm, $\theta_F = 45°$, and $\phi_F = 180°$. The transformation from a collimated beam to a focused beam is achieved with the phase distribution shown in the inset of Figure 7.2.

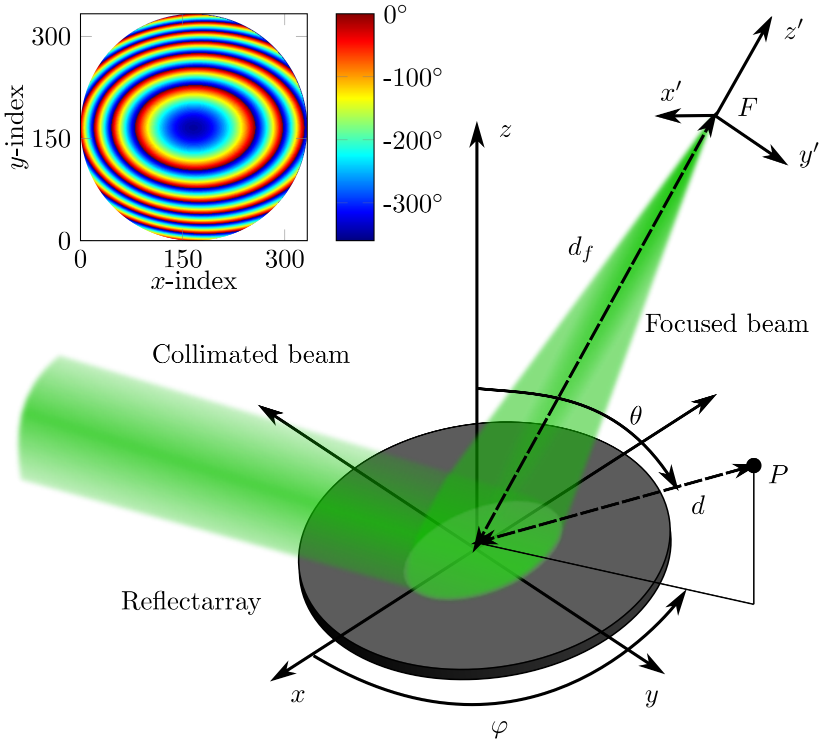

Figure 7.2. Beam-shaping operation of DRA-based reflectarray. Expanded view of the focused terahertz reflectarray general architecture. Note the point F is the origin of a secondary coordinate system, (x', y', z'), which coincides with the focal plane of the reflectarray, and is defined in order to simplify the presentation of results. Inset shows the required phase distribution on the reflectarray surface, which is roughly 50 mm in diameter. After Headland *et al.* (2016a).

The focusing reflectarray design is performed using a simplified inverse process, which is valid due to reciprocity. The propagation direction is effectively reversed, and hence the focal point is replaced by a point-source virtual feed at point F that illuminates the surface, as in conventional reflectarrays. The reflectarray transforms the spherical wave radiated by the virtual feed into a collimated beam towards the direction defined by $\theta = 45°$, $\phi = 0°$ by means of phase discontinuities introduced by the DRA elements. In general, the phase-shift, φ_i, which is introduced by each element of the reflectarray in order to convert a spherical wave from a point-source feed into a collimated beam towards a given spatial direction (θ, ϕ) in the far-field is computed using the following equation (Huang and Encinar 2008):

$$\varphi(x_i, y_i) = k_0(d_i - (x_i \cos\phi + y_i \sin\phi)\sin\theta), \tag{7.1}$$

where k_0 is the wavenumber in free-space, $(x_i, y_i, 0)$ are the Cartesian coordinates of the element i, and d_i is the distance from the phase centre of the feed to the centre of each element of the reflectarray,

$$d_i = \sqrt{(x_F - x_i)^2 + (y_F - y_i)^2 + (z_F - z_i)^2}. \tag{7.2}$$

Note that, in the designed reflectarray, $d_i = d_F = 150$ mm only at the centre of the reflectarray. In the present design, the point F is defined by the $(x_F, y_F, z_F) = (-106.066, 0, 106.066)$ mm. The resulting phase distribution is given in the inset of Figure 7.2. By convention, the phase-shift has been defined as a negative value.

During the array design procedure, a divergent beam impinges on the surface of the reflectarray, and hence the incident rays are not parallel. Although the variation of the angle of incidence from the feed point, F, to the centre of each reflectarray element is small, it was taken into consideration for an accurate design. Figures 7.3(a) and (b) show respectively the angles of incidence θ_{inc}, ϕ_{inc} at each element of the array. Both angles have been discretised to the closer value $\theta_{\text{inc}} = 39.75°$, $45.00°$ or $50.25°$; and $\phi_{\text{inc}} = -9°$, $0°$ or $9°$, before being used in the design of the reflectarray. For all nine angles of incidence considered, a separate parametric sweep is performed, and the results are utilised to inform the selection of cylinder radius.

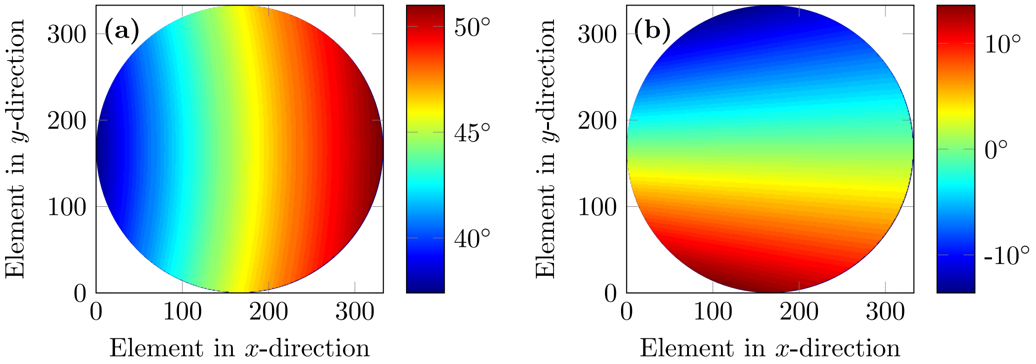

Figure 7.3. Accounting for divergent incident beam. Angles of incidence from the feed point onto each element of the reflectarrays (a) θ_{inc} and (b) ϕ_{inc}. After Headland *et al.* (2016a).

In order to realise the required phase distribution, the phase response is controlled locally by careful selection of cylinder radius, as dictated by parametric analysis of the relationship between radius and phase response. This parametric analysis is used to map required phase distribution to required radius, with results shown in Figure 7.4. For practical reasons, a relatively-large circular area of ∼50 mm diameter is employed for the array, which equates to a row of 333 elements across the diameter. The resulting structure has more than 87,000 elements in an aperiodic arrangement, producing a nonuniform array.

The distribution of cylinder radii is necessarily inhomogeneous, which results in neighbouring elements of different sizes. There are two concerns that arise from this fact. Firstly, this is inconsistent with the modelling of the individual elements, in that it employs unit cell analysis that assumes periodicity, and hence homogeneity. However, the variation in cylinder radius is sufficiently gradual that local periodicity can be assumed, and hence any alteration in response that results from the inhomogeneity can be neglected. Secondly, the non-uniform arrangement breaks resonator symmetry. In the case of normal incidence, this results in the excitation of asymmetric modes, which alters the response (Singh *et al.* 2011). However, it is asserted in Section 7.2 that the observed $\mathrm{TE}_{01\delta}$ mode of resonance is observed due to the asymmetry provided by the

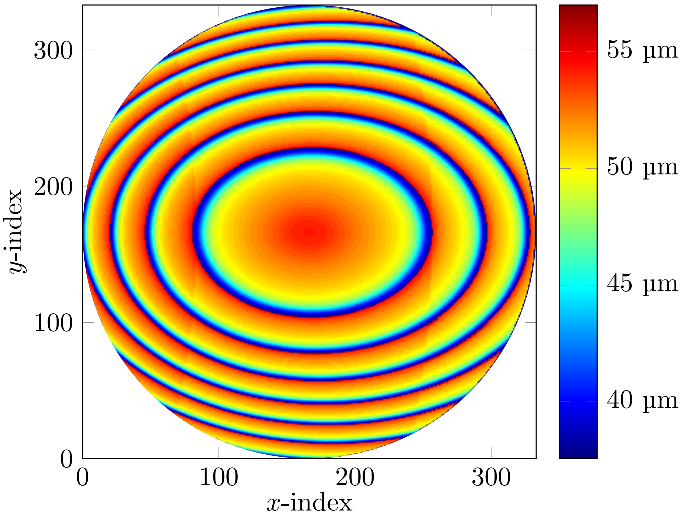

Figure 7.4. Reflectarray layout. Layout of required cylinder radii in order to achieve the bespoke beam-shaping operation. The specific value of cylinder is given in the colour bar. After Headland *et al.* (2016a).

obliquely-incident excitation. This oblique excitation is therefore of great assistance, as these asymmetric modes are present in the unit cell analysis, and are therefore accounted for.

7.4 Fabrication of terahertz reflectarray

A mask is required in order to commute the design that is presented in Figure 7.4 into physical microstructures. In order to realise the photolithography mask required for this relatively complicated layout, an automated procedure is required. This automation is realised via a python script, which interfaces the data output from the simulation results with the IPKISS mask creation software (Bogaerts *et al.* 2012) to output a GDSII design file that is compatible with commercial mask foundries.

This device is fabricated using a process involving SU-8 assisted bonding, photolithography, a conventional desktop laminator, and plasma-enhanced deep reactive ion etching, as detailed in Chapter 6. This fabrication procedure is very precise, and has tolerances in the order of ±1 µm for resonator diameter, which is well below the values for diameter employed in the reflectarray, as they range from 75 to 114 µm. Micrographs of the fabricated device, showing silicon cylinders on a gold thin film, are given in

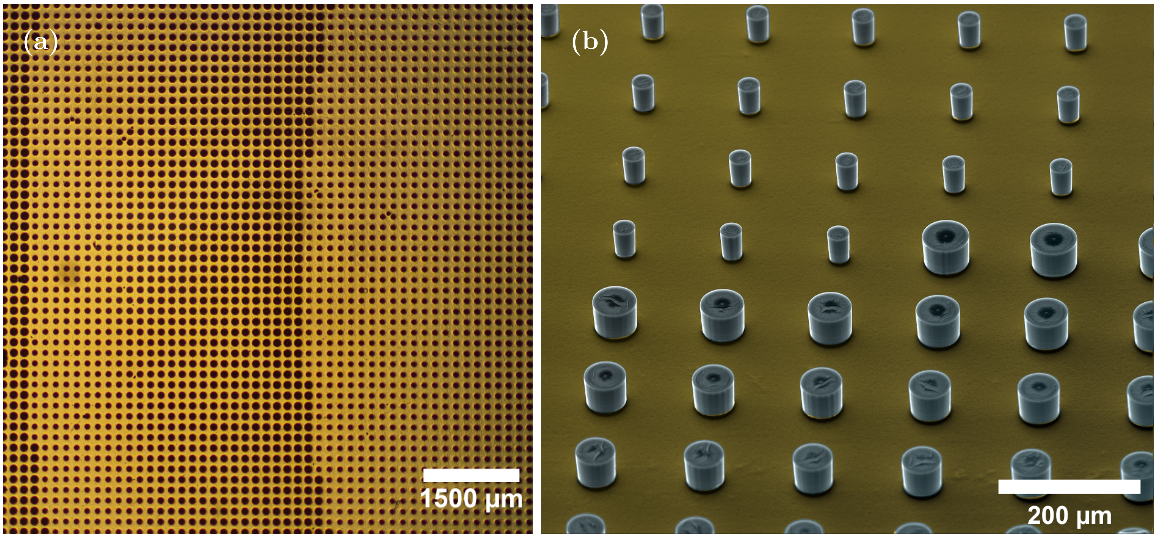

Figure 7.5. Fabricated terahertz reflectarray design. Realised reflectarray structure, showing (a) optical microscope image, and (b) and false-colour scanning electron micrograph. After Headland *et al.* (2016a).

Figure 7.5, and the nonuniformity required to perform beam manipulation is clearly visible. These images show clearly defined, high-quality silicon cylinders, with sharp edges. This attests to the efficacy of the fabrication procedure utilised to realise these microstructures.

7.5 Characterisation of focal spot

The reflectarray is employed to focus a collimated beam, and the focal spot is characterised using THz-TDS in order to validate its performance. Characterisation of the focal spot is performed using the experimental setup shown in Figure 7.6. A fibre-coupled THz-TDS system is employed, which allows the receiver to move freely, and facilitates raster-scanning. The sample is set at a 45° angle with respect to the transmitter and receiver, and is excited by a collimated beam with TE polarisation. The collimated beam is best approximated by a Gaussian beam, but in practice the beam cannot be of infinite extent, and hence it is truncated to a certain radius. In this case, both the beam waist radius and the truncation radius are 17 mm. The receiver is raster-scanned in the $x'y'$-plane at point F in order to determine the field profile of the focal spot. The scanning resolution is 60 µm, which is equal to $\lambda/5$ at the operating frequency. An area of 3.06×3.06 mm^2 is scanned, with a total measurement time of ~20 hours, and the results are shown in Figure 7.7(a,d). The measured magnitude cross-section in Figure 7.7(a) clearly shows a well-defined focal spot. Additionally, the measured phase

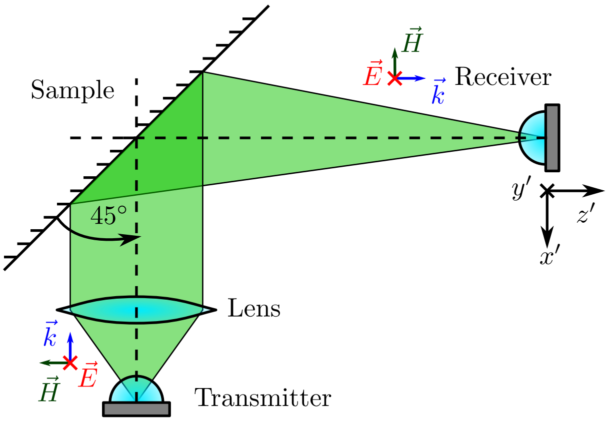

Figure 7.6. Characterisation of terahertz reflectarray. Measurement setup, using TE-polarised fibre-coupled photoconductive antennas. The reflective sample is set at a 45° angle, and the detector is raster-scanned in the focal plane. After Headland *et al.* (2016a).

cross-section is shown in Figure 7.7(d), and it can be seen that phase is approximately constant over the area of the focal spot, as expected for a focused beam.

In order to confirm that the measured spot is in agreement with expectation, a numerical simulation is employed that involves the Huygens-Fresnel principle that is presented in Section 2.2. For this procedure, the reflected field distribution at the surface of the reflectarray is determined element-wise by means of the parametric analysis given in Figure 7.1(f,g). A 2D Gaussian function, truncated to a 17 mm radius, is employed to simulate the collimated beam excitation. Thus, the overall field at a given location on the array is the product of the reflection coefficient of the element and the field magnitude of the Gaussian function at that position. To account for oblique excitation, the lattice constant in the x-dimension is scaled by a factor of $\cos(\pi/4)$. Finally, the Huygens-Fresnel principle is employed to forward-propagate the field distribution by the focal length of 150 mm. The results of this procedure are shown in Figure 7.7(b,e), and it can be seen that the simulated field profile is consistent with measured results, as there is a focal spot of comparable size in the magnitude plot, and the phase response is approximately constant.

Additional to modelling the focal spot numerically, an analytical approach is taken. The finite-size focusing mirror reflectarray can be treated abstractly as the focusing of a Gaussian beam that is truncated to a certain radius, for which an analytical solution exists (Horváth and Bor 2003). This analytical model is employed as a secondary means to predict the field distribution of the focal spot, as shown in Figure 7.7(c,f). In order to compare the measured, simulated, and analytically-predicted focal spot in detail, cross-sectional field amplitude distributions are given in Figure 7.7(g,h). It can be seen that they are all in strong agreement.

A smaller focal spot size may be desirable for various applications, such as high-resolution imaging. It is therefore worth noting that the size of the focal spot is approximately proportional to focal length (Saleh and Teich 2007), and hence it is possible to reduce focal spot size by reducing the focal length of the reflectarray. This is achieved by adjusting the phase distribution accordingly, as expounded in Section 7.3. There are, however, practical limitations to this approach, as a shorter focal length will introduce larger deviations from the nominal incidence angle of 45°, which invokes undesirable modes and blind spots. Additionally, due to the diffraction limit, the minimum diameter of a focused beam is approximately equal to a wavelength.

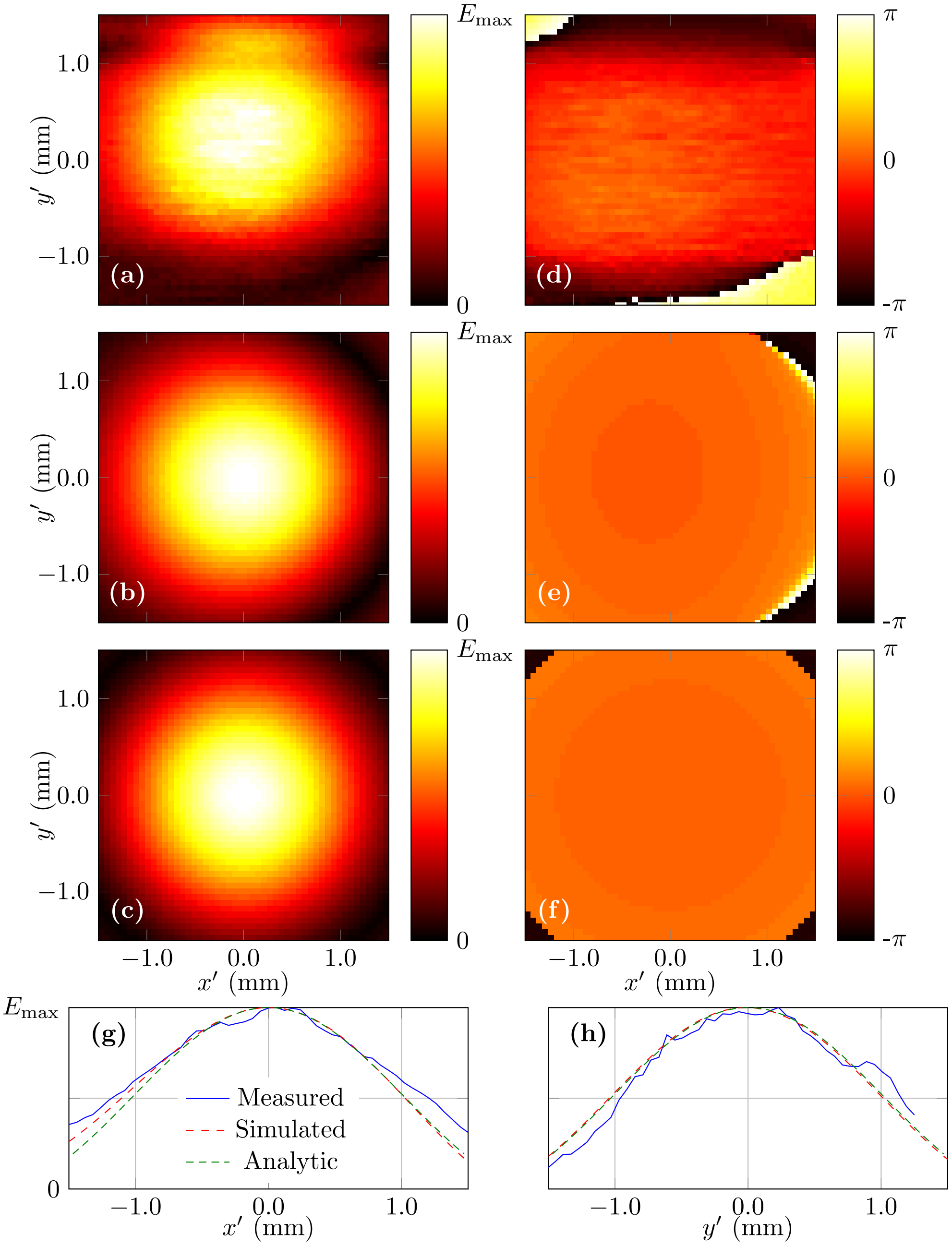

Figure 7.7. Measured focal spot of DRA-based reflectarray. Beam profile of focal spot at 1 THz. (a) Measured field magnitude distribution, (b) simulated field distribution, (c) analytically predicted field distribution (Horváth and Bor 2003), (d,e,f) corresponding phase profiles for (a,b,c) respectively, and (g,h) cross-sectional linear field distribution amplitudes. Note the measured profile in (h) is offset to coincide with the other plots. All plots are in linear scale. After Headland *et al.* (2016a).

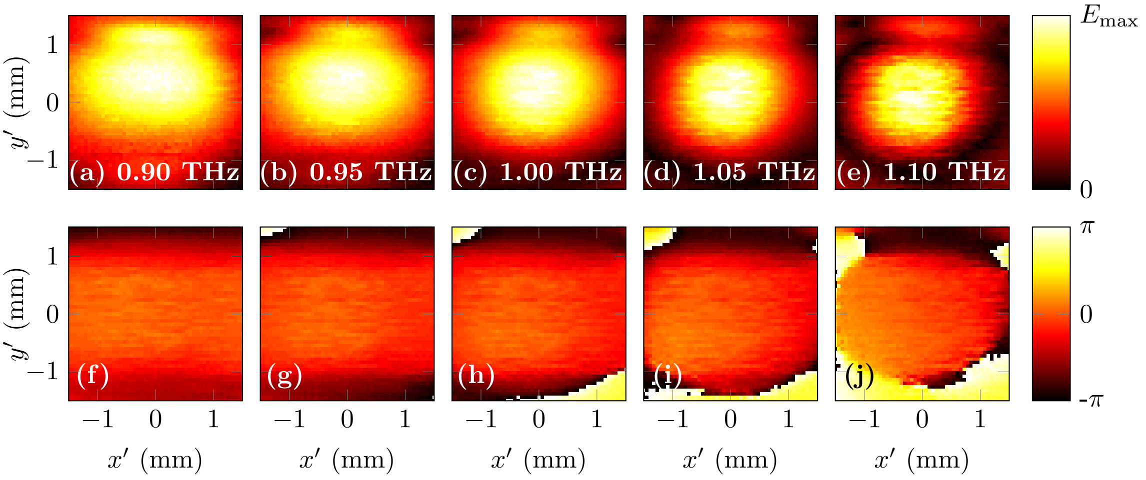

Figure 7.8. Measured focal spots at other frequencies. Broadband performance of DRA reflectarray. (a-d) Linear magnitude distribution of focal spot from 0.90 to 1.10 THz, and (e-h) phase distribution of focal spot from 0.90 to 1.10 THz. After Headland *et al.* (2016a).

7.5.1 Broadband performance

Given that THz-TDS is employed to characterise the DRA reflectarray, it is possible to evaluate the field profile at frequencies other than the operating frequency of 1 THz. The focal spots at frequencies within a 20% bandwidth are therefore given in Figure 7.8. Both linear magnitude and phase are given for each frequency. The results show that a focal spot is maintained over a frequency range of at least 200 GHz, from 0.9 THz to 1.10 THz. From the corresponding phase profiles in this frequency range given in Figures 7.8(e-h), it is clear that, as with the results at 1 THz, the phase profile is approximately constant in the vicinity of the focal spot.

From comparison between Figures 7.8(c) and (e), the focal spot at 1.1 THz is slightly smaller than at 1.0 THz. This is likely due to the fact that the beam waist of a focused Gaussian beam is roughly proportional to wavelength (Saleh and Teich 2007). Additionally, it is possible that the distance between the reflectarray centre and the plane of measurement is slightly too great, leading to a system that is better-aligned for a slightly higher frequency. This is due to the fact that the focal length of flat lenses typically increases with frequency, as the phase gradient of a flat lens scales linearly with wavelength.

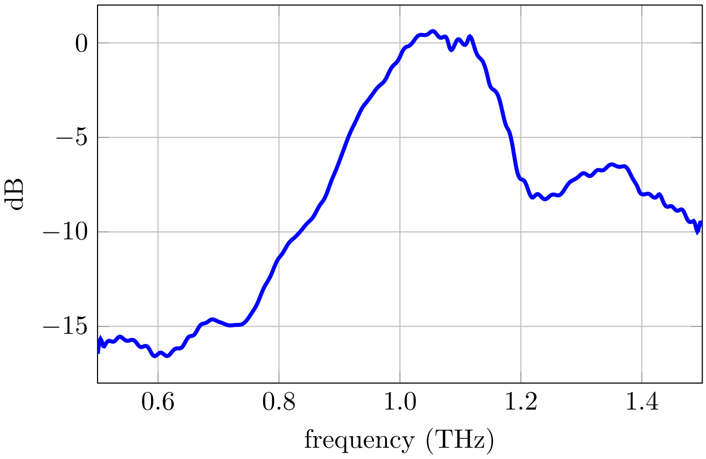

Figure 7.9. Efficiency of DRA-based reflectarray. The experimentally-evaluated efficiency of the DRA-based terahertz reflectarray. After Headland *et al.* (2016a).

7.6 Efficiency

Further measurements are taken in order to determine the overall efficiency of the reflectarray, as this is of key interest. In order to evaluate the efficiency of the reflectarray, a single-pixel measurement is taken at the maximum of the field profile in the focal plane. Subsequently, the focusing mirror sample is replaced with a flat gold mirror, and a TPX lens with a 50 mm focal length is placed in the path of the reflected beam. As a reference, a measurement is taken at the maximum of the focal plane of the lens. The measurement of the focusing mirror is normalised against the reference, accounting for the absorption and reflection losses due to TPX (Podzorov and Gallot 2008). Note that, in both cases, the acceptance angle of the receiver is such that the majority of the energy is collected.

The results are presented in Figure 7.9, and it can be seen that, within experimental tolerances, the device has negligible loss. This is evidence of the high efficiency of the intrinsic silicon DRAs. Furthermore, from this measurement a −3 dB bandwidth of 18% is extracted. Note that the operating frequency has slightly shifted from the design frequency of 1.0 THz to 1.05 THz. This is consistent with previous observations that suggested that the system may be better aligned for a maximum at a slightly higher frequency than the nominal operating frequency of 1.0 THz.

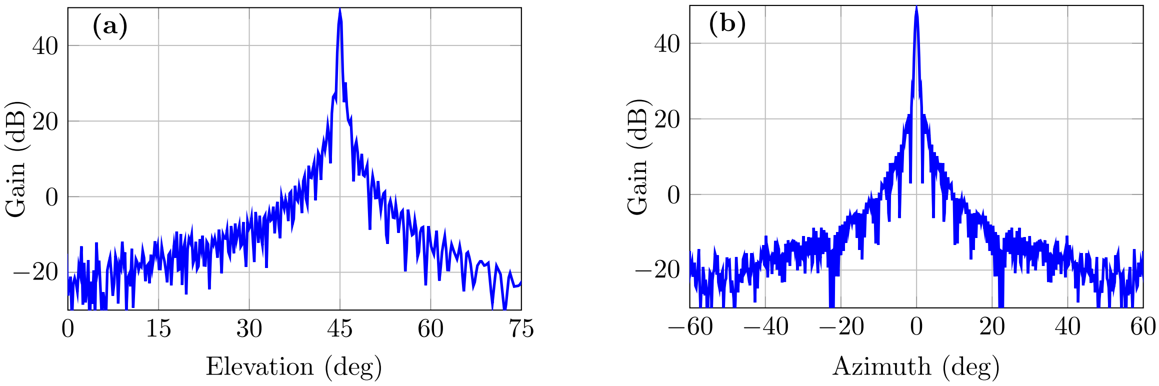

Figure 7.10. Antenna gain of DRA-based reflectarray. Far-field radiation patterns in gain for the designed reflectarray antenna working as collimator. (a) Elevation plane. (b) Azimuth plane, with an elevation angle of 45°. After Headland *et al.* (2016a).

7.7 Antenna gain

Given that the reflectarray is capable of focusing a collimated beam to a fine point, by the principle of beam reciprocity, the same device is also capable of collimating a divergent beam. Both modes of operation can be utilised in order to provide high antenna gain; when collimating it operates as a transmitter, and when focusing it operates as a receiver. With the aim of evaluating antenna gain, the far-field radiation patterns in gain are evaluated. The gain of the reflectarray is computed using the method described in Huang and Encinar (2008), and demonstrated extensively in the literature (Encinar and Zornoza 2003, Encinar and Zornoza 2004, Huang and Encinar 2008, Carrasco *et al.* 2012, Carrasco *et al.* 2013), which assumes quasi-uniform illumination on the surface of the reflectarray. Firstly, the field incident at each element is calculated by modelling the radiation pattern of the feed as a $\cos^q\theta$ function. From the incident field, and the scattering parameters of each element, the reflected field is calculated in Cartesian coordinates for the corresponding polarisation. Then, from the tangential component of the reflected electric field on the surface of the reflectarray, the radiation patterns are computed. Finally, the reflectarray gain is computed as

$$G(\theta,\phi) = \frac{|E(\theta,\phi)|^2 4\pi r^2}{2Z_0 P}, \tag{7.3}$$

where $Z_0 = 376.7\ \Omega$ is the intrinsic wave impedance of free space, and P is the total power radiated by the feed. With the aim of having a uniform illumination on the surface of the array that is impacted solely by the path length, $q = 1$ has been chosen to describe the feed. This results in less than 2 dB difference between the maximum and minimum illumination, while neglecting spillover losses. The evaluated radiation patterns are presented in Figure 7.10. The maximum gain computed for these idealised illumination conditions is 48.5 dB, which demonstrates the capability of the reflectarray to provide high antenna gain, and hence its suitability to terahertz communications applications. Note that these modelling-oriented methods have been chosen to determine antenna gain, as opposed to direct measurement, due to practical constraints concerning experimental evaluation of radiation pattern.

7.8 Conclusion

A highly efficient, DRA-based terahertz reflectarray is presented in this chapter. As proof of concept, this particular device is designed to operate as an off-axis focusing mirror. Measurements reveal a focal spot that conforms to expectation, with negligible loss and a -3 dB bandwidth of 18%. Thus, this study has achieved the main objective of this doctoral thesis; the realisation of a highly efficient, flat-profile terahertz beam-control device. This demonstration of a lensing device in particular is simply one example of a family of potential devices of the same sort, as per the various techniques described in Section 2.3.2. Such efficient and versatile devices are expected to make a significant impact across broad fields of terahertz technology. Terahertz communications in particular will benefit from the ability to increase antenna gain, and customise radiation patterns, without notable loss to power.

This demonstration of a DRA-based terahertz reflectarray concludes Part III of this doctoral thesis. The following chapter will investigate a possible alternative to resonator-based terahertz beam control in general, in the form of a 3D-printed zone plate.

PART IV

Non-resonant techniques

Chapter 8

Characterisation of 3D-printed metal for terahertz optics

THIS chapter presents an alternative to the resonator-based beam-control mechanisms given in previous chapters. A stepped-phase, path-length approach is sought, in part due to simplicity, but also as a means to avoid adverse effects associated with resonance. The additive manufacture technique known as 3D printing is utilised to prototype terahertz stepped optics due to low cost, rapid turnaround time, and versatility. A titanium alloy is employed as a build material, as metals are naturally suited to reflective devices. Factors impacting performance such as printing resolution, surface roughness, oxidation, and material loss are investigated via analytical, numerical, and experimental approaches. The high degree of control offered by a 3D-printed topology is exploited to realise a binary-phase zone plate operating at 530 GHz. The reflection efficiency of the printed metal at this frequency is found to be over 90%. This chapter constitutes a pilot study into the general feasibility of utilising 3D-printed metal to realise custom terahertz optics.

8.1 Introduction

Up to this point, the contributions of this thesis have been focused on passive arrays of the sort introduced in Section 2.4.4; resonator-array-based beam-control devices. However, the use of resonators to achieve phase control is not without drawbacks. Firstly, the phase transition of a resonator is invariably associated with a local maximum in absorption due to field confinement in lossy media. Granted, this loss is very close to negligible for the DRAs presented in Chapters 6 and 7, but there remain complications associated with inter-resonator coupling. It is therefore also of interest to investigate beam-control techniques that do not make use of a resonator of any sort. To this end, this chapter is concerned with stepped-phase, path-length optics, of the sort discussed in Section 2.4.1.

In recent years, the form of additive manufacture known as 3D printing has gained significant attention, in part due to its generality, versatility, and compatibility with computer-aided design tools (CAD). This technique is a computer-controlled process in which a three-dimensional digital model, eg. from CAD software, is translated into a physical object by the progressive addition of build materials. It is well-suited to rapid prototyping, small- to medium-scale manufacture, and the fabrication of replacement parts and custom equipment on demand (Berman 2012, Anzalone *et al.* 2013, Zhang *et al.* 2013a). Additionally, 3D printing technology has been employed in cutting-edge applications to construct compact microbatteries (Sun *et al.* 2013b), miniaturised chemical reactors (Kitson *et al.* 2012, Symes *et al.* 2012), scaffolding for visceral (Kim *et al.* 1998) and bone tissue growth (Seitz *et al.* 2005), and custom surgical implants and models (Seitz *et al.* 2005, Habibovic *et al.* 2008)—all a striking testament to its versatility.

The ability of 3D printing to realise complex and high-precision structures opens a path for printing devices that manipulate electromagnetic radiation. For example, 3D-printed lenses that operate in the optical range are presently a commercially available product (Blomaard and Biskop 2015). This capacity also extends to the terahertz range. The resolution of 3D printers is typically in the order of a few tens to a few hundreds of micrometres, and such a scale is highly suitable for the manipulation of terahertz waves, as it is comparable to a wavelength. Furthermore, the maximal achievable dimensions of 3D-printed structures are typically in the order of several hundreds of terahertz wavelengths, making it possible to realise devices of large aperture. The 3D printing of dielectric materials has therefore been utilised extensively in order to realise numerous transmissive devices for shaping terahertz radiation, as detailed in Section 3.3. On the other hand, metals are naturally suited to reflective devices and guiding structures, which are of critical importance in the terahertz range, and techniques such as selective laser melting (SLM) (Thijs *et al.* 2010, Bremen *et al.* 2012) make it possible to 3D-print directly in solid metals (Ladd *et al.* 2013, Frazier 2014). Despite this, there have been no previous demonstrations of direct metal printing in the context of terahertz technologies. The most closely-related demonstrations have presented terahertz guided-wave structures that were made from 3D-printed polymers, with a metal layer deposited on the surface (Pandey *et al.* 2013, Liu *et al.* 2013).

This chapter presents a pilot study into the previously-unexplored approach of using direct 3D printing of metals to realise terahertz devices. Grade-5 titanium is selected for the build material, as it is a common titanium alloy of wide-spread use in areas including aerospace, automotive, marine, and medical applications (Welsch *et al.* 1993). The efficiency of this alloy as a reflector is investigated using experimental and analytical means. As a demonstration, a 3D-printed metal zone plate operating at 530 GHz is realised, and its capacity to focus terahertz radiation is demonstrated. The operating frequency of 530 GHz is selected as suitable to achieve a binary phase difference, accommodating a conservative estimate of the vertical resolution limitations imposed by the 3D-printing procedure. As opposed to transmissive zone plates made of terahertz-transparent polymers (Furlan *et al.* 2016), the demonstrated device is a reflective zone plate. The trade-off between these different approaches is that transmissive devices undergo reflection losses, whilst reflective devices experience feed blockage. Given the power-related constraints discussed in Section 1.1.1, the reflective approach is preferred due to efficiency.

Even quite low-conductivity metals make for efficient reflection in the terahertz range. That is to say, although a very high-conductivity metal is required in order to devise a resonator, as in Section 3.7 and Chapter 5, the constraints upon conductivity are markedly less stringent in the case of reflection from a bulk metal. This is because there is no concentrated matter-field interaction, as is typically associated with resonance. This relaxation of the constraints on the build materials expands capabilities for prospective approaches to fabrication considerably.

8.2 Characteristics of 3D-printed metal

There are numerous metal build materials available, and a substantial amount of choice surrounding the particular 3D-printing machine and process to be used. In order to constrain this study to a manageable scope, inquiries are limited to one particular 3D-printed alloy; a titanium alloy that is commonly known as "Grade-5 titanium," "Ti6Al4V," "Ti6-Al4-V," or "Ti 6-4," fabricated with a ProX 200 SLM printer.

8.2.1 Fabrication of 3D-printed metal

In the 3D-printing technique known as SLM, a structure is built-up in a layered fashion, by alternate passes of deposition of the powder build material, and selective exposure to a high-intensity raster-scanning laser. The laser melts a certain portion of the powder material, which fuses, and subsequently cools down, to form the solid portions of the relevant layer (Bremen *et al.* 2012). The ProX 200 SLM printer employs a 1070-nm laser at 300 W. The focal spot size of the laser is approximately 70 µm, and the scanning speed is 1,800 mm/sec. The printing procedure takes place in an argon gas chamber, with oxygen averaging at 1000 ppm. The grade-5 titanium alloy employed is composed of ∼90% titanium, ∼6% aluminium, and ∼4% vanadium, and the particle size of the metal powder used in 3D printing is at most 40 µm. Post 3D-printing fabrication, the structure is annealed in an open-air furnace at 650° for a period of two hours in order to relieve stresses that are created within the material during the build process. This annealing step results in the development of an oxidation layer as an unintended side-effect. Finally, the sample is sandblasted at 600 kPa with a particle mixture that is 70% garnet and 30% glass, and particle sizes in the range from 90 to 400 µm, in order to smooth the surface and minimise random scattering of terahertz radiation.

For characterisation purposes, a flat, featureless metal disk that is ∼75 mm in diameter and ∼1 mm-thick is fabricated using the above procedure. This sample is shown in Figure 8.1(a). Its surface roughness is determined using an optical interferometric profiler, and acquired images are presented in Figures 8.1(b) and 8.1(c). There appears to be some quasi-periodic regularity to the roughness in the form of grains of several hundred micrometres. These features are a consequence of the dynamics of the liquid-phase metal during the fabrication procedure, combined with the sequential hatching of the laser (Thijs *et al.* 2010). Analysis of these optical profiler measurements of the

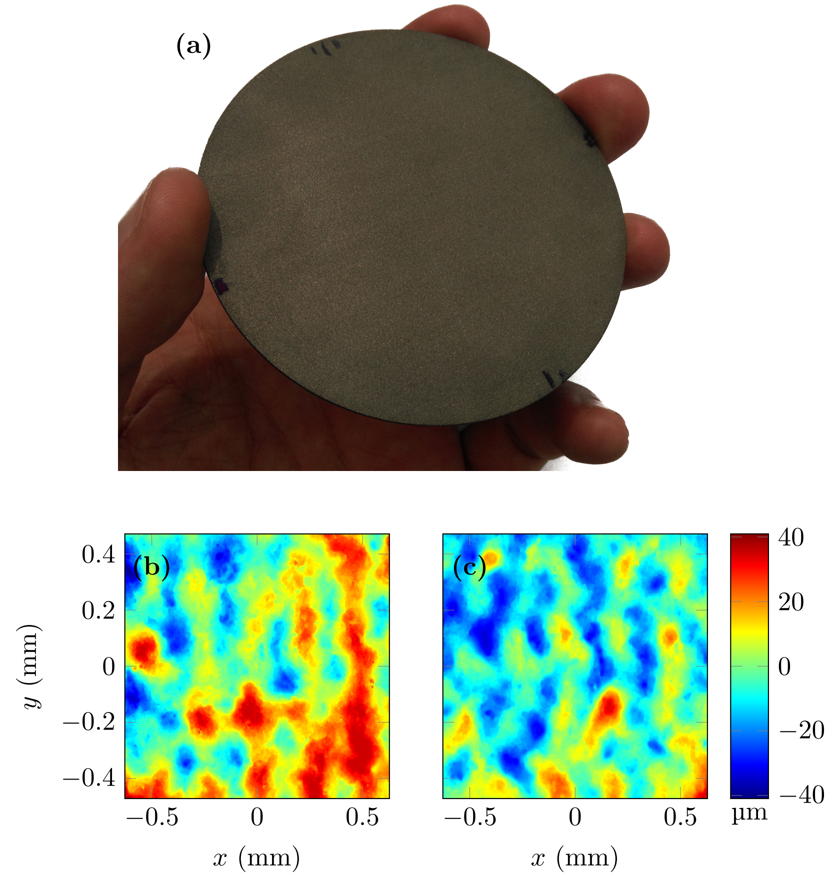

Figure 8.1. 3D-printed featureless disk. Fabricated flat metal disk, showing (a) photograph of ∼75 mm-diameter sample, and (b,c) optical profiler data at two different locations on the sample surface, with standard deviations σ_h of 10.78 and 10.28 µm respectively. After Headland *et al.* (2016b).

3D-printed metal reveals the standard deviation of the surface height to be $\sigma_h = 10$–11 µm, which is in the order of the particle size employed in 3D printing. Note the value σ_h can alternatively be called the root mean squared of the surface perturbation, commonly denoted S_q, as the mathematical definitions are identical.

In order to determine the presence of oxygen, and any possible contaminations in the surface layer after annealing and sandblasting, energy-dispersive X-ray spectroscopy (EDX) is performed, and the results are given in Figure 8.2. The relevant system is a Quanta 450 SEM, which makes use of a focused beam of electrons to bombard the sample, and information is acquired from secondary electrons, backscattered electrons, and X-rays. For secondary electrons, contrast is dependent upon surface morphology, whereas the contrast in the backscattered-electron image is dictated by the atomic number of elements in the sample, and X-rays provide the emission spectrum to determine elemental composition (Egerton 2005). Secondary and backscattered-electron images are shown in Figures 8.2(a) and (b), respectively. Four distinct compounds are identified from these images, and the emission spectra given in Figure 8.2(c) provide some insight into likely candidate materials for each. The most common material in the sample surface is titania, followed by alumina, which is shown in a blue circle in Figure 8.2(b). This is to be expected, as titanium and aluminium readily oxidise in air at the annealing temperature of 650°. There are also pieces of garnet embedded in the surface, as a result of the sandblasting steps, and one such example is indicated with

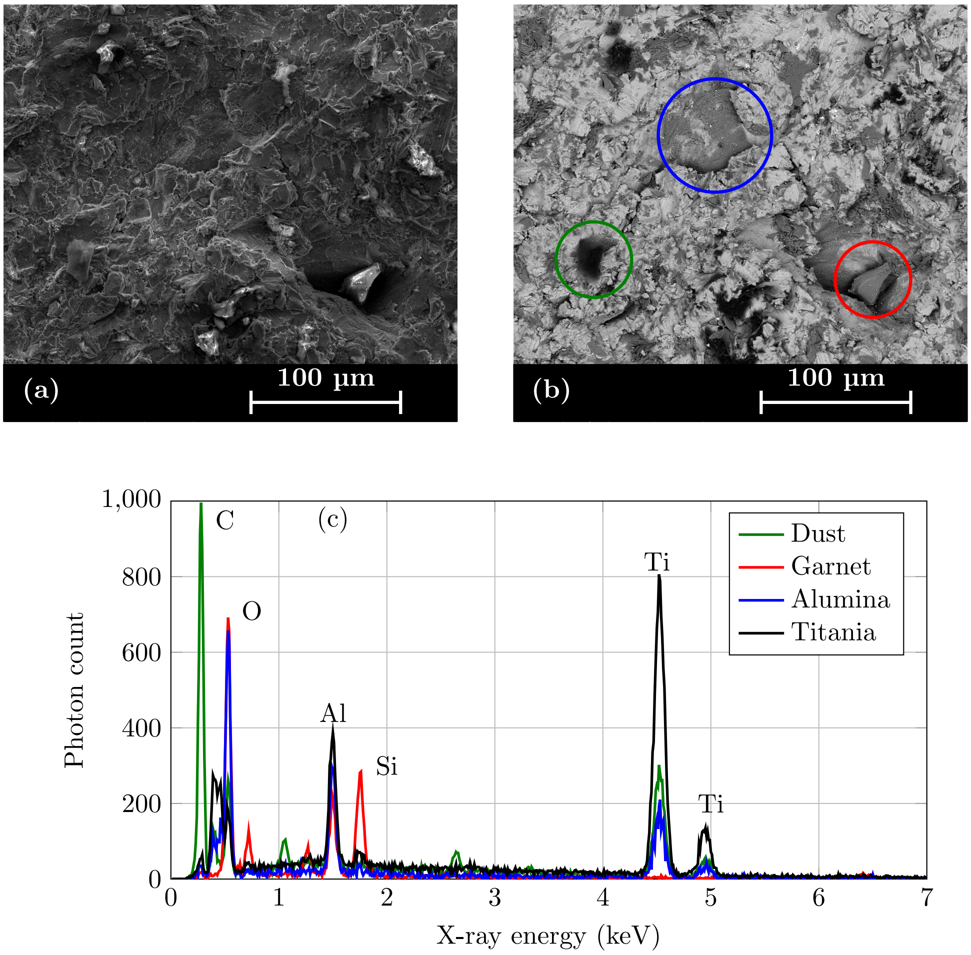

Figure 8.2. EDX characterisation of titanium alloy surface. Results of EDX characterisation of the surface layer of the 3D-printed titanium alloy, showing (a) secondary-electron image, for which contrast is an indication of topological structure, (b) backscattered-electron image, for which higher luminance corresponds to greater atomic number, and (c) X-ray emission spectra of the four distinct compounds identified.

the red circle in Figure 8.2(b). Finally, there are particles of carbon-rich material, most likely dust, on the surface, as illustrated with a green circle in Figure 8.2(b). Note, the presence of vanadium was not detected in EDX characterisation, due to low concentration in the alloy used.

8.2.2 Terahertz properties of 3D-printed metal

In order to determine the efficiency of reflector devices created with 3D-printed grade-5 titanium, it is necessary to characterise the material for its reflection coefficient in the terahertz range. The terahertz response of the flat sample given in Figure 8.1(a) is characterised with THz-TDS, using the normally-incident reflection setup given in

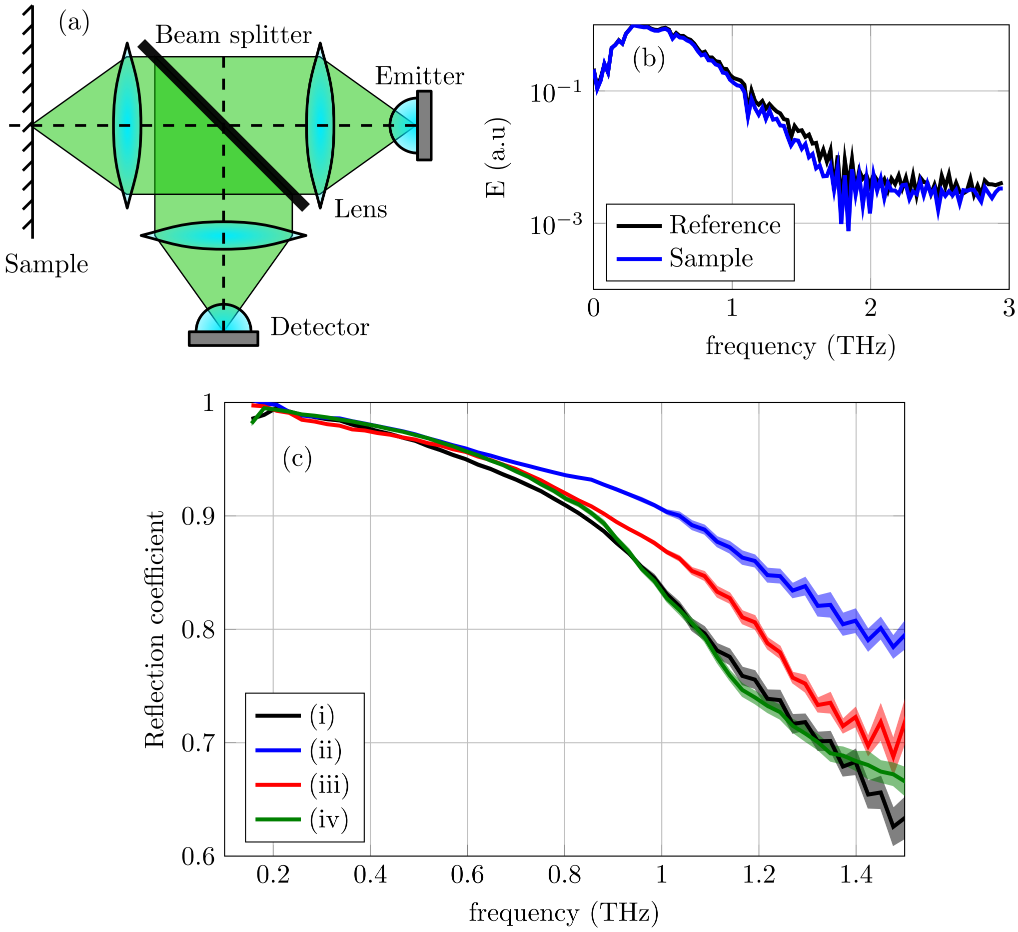

Figure 8.3. Reflective efficiency of 3D-printed metal. Characterisation of 3D-printed titanium alloy, showing (a) measurement setup, (b) examples of measured spectra, and (c) measured reflection coefficient at normal incidence, where error bars are shown as coloured regions, and (i-iv) represent different locations on the sample surface. After Headland *et al.* (2016b).

Figure 8.3(a), where a polished silicon wafer is employed as a beam splitter. A focused beam is used to probe the properties of the metal, in order to effectively isolate the surface properties at a given point, and determine the degree to which these properties vary across the surface. The beam waist of the focused beam is ∼1 mm, which results in a Rayleigh range of ∼5 mm. As the terahertz radiation is incident on the sample at the approximate location of the beam waist, normal incidence of all rays can be assumed.

Measurements are taken at four arbitrary points on the sample surface, and five measurements are taken for each point. The reference spectrum is measured by replacing the sample with a gold-coated silicon wafer. Example spectra from this measurement set are given in Figure 8.3(b), showing bandwidth up to ∼1.75 THz. The normalised and averaged results are given in Figure 8.3(c), with standard deviations shown as coloured regions. There are significant discrepancies between the different sets of measurements at frequencies above ∼700 GHz, which suggests a variation in reflectance across the sample surface. Reflection efficiency is defined as the square of the reflection coefficient magnitude. Around the nominal operating frequency of 530 GHz, the reflection coefficient magnitude is over 95%, which is equivalent to efficiency of over 90%. In all cases, for frequencies below 900 GHz, overall efficiency is greater than 80%.

8.2.3 Modelling of reflection characteristics

A model is developed in order to explain the reflection response of the 3D-printed metal. This model takes into account losses due to both material dissipation and surface irregularities. The reflection coefficient considering only scattering loss due to surface roughness, Γ_{r}, can be determined using Equation 8.1 (Dikmelik *et al.* 2006), where σ_h represents the standard deviation of the surface height,

$$\Gamma_{\mathrm{r}} = \exp\left[-2\left(\frac{2\pi f \sigma_h}{c}\right)^2\right]. \tag{8.1}$$

This expression is based on the summation of delayed responses introduced by perturbations in the z-position of the surface, and is independent of polarisation. The result is effectively a form of low-pass filter, with Gaussian roll-off. This is because an increase in frequency is associated with a proportional decrease in wavelength, and hence a surface perturbation of a given size has a more severe impact on the resulting phase.

Another source of loss that must be considered is dissipation, both in the bulk metal, and in a thin oxidation layer on the surface. A transmission-line model, illustrated

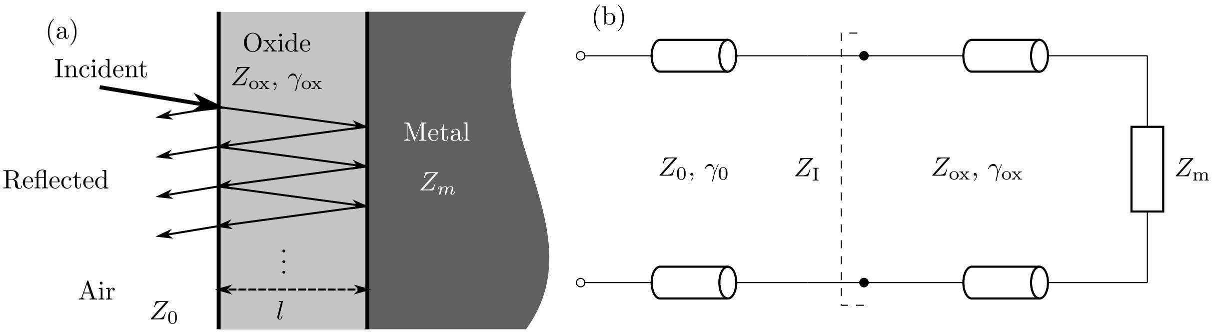

Figure 8.4. Transmission-line model of oxide layer. Reflection of radiation from sample surface, neglecting surface roughness, showing (a) oxide-on-metal structure, with internal reflection in the dielectric layer, and (b) Equivalent transmission-line model, where Z_{I} is the input impedance of the surface. After Headland *et al.* (2016b).

in Figure 8.4, is employed for this system. Both the bulk metal and the oxide layer are assumed to be non-magnetic. Thus, the wave impedance, Z, and propagation constant, γ, of a given material are calculated using Equations 8.2, 8.3 (Pozar 2009), where μ_0 and ϵ_0 are the vacuum magnetic permeability and electric permittivity respectively, and $\epsilon_r - j\epsilon_i$ is the complex relative permittivity of the relevant medium,

$$Z = \sqrt{\frac{\mu_0}{\epsilon_0(\epsilon_r - j\epsilon_i)}}, \tag{8.2}$$

$$\gamma = j2\pi f \sqrt{\mu_0\epsilon_0(\epsilon_r - j\epsilon_i)}. \tag{8.3}$$

The wave impedances for metal and oxide are given by Z_{m} and Z_{ox} respectively, and the complex propagation constant in the oxide is given by γ_{ox}. The material properties of pure grade-5 titanium are determined in accordance with a Drude model (Wieting and Schriempf 1976), which gives plasma and collision frequencies of 1.99×10^{16} rad/s, and 5.12×10^{15} rad/s, respectively. Additionally, the DC electrical conductivity of grade-5 titanium at room temperature is ~0.68 MS/m (Welsch *et al.* 1993). These values are employed to model the material properties of the metal portion of the metal-oxide structure. For the oxide layer, the material is approximated as pure titania, and the properties of this material are known in the literature. The relative permittivity of titania is $\epsilon_r = 109.96$ (Scheller *et al.* 2009). The absorption coefficient, in cm^{-1}, is empirically modelled with a quadratic expression, $\alpha = 25.5f^2 - 5.5f + 4.2$, where f is the terahertz frequency (Ung *et al.* 2011). The approximation of modelling the oxide layer as titania is valid for two reasons. Firstly, grade-5 titanium is 90% titanium, and hence titania is expected to make up the majority of the oxide layer, as has been confirmed by EDX characterisation. Furthermore, although there are impurities in the form of alumina, garnet, and dust, the relative permittivity of titania is extremely high, and hence titania dominates the response of the material. Lower-index impurities such as alumina will simply result in a local reduction in the effective thickness of the oxide layer.

As the thickness of the oxide layer is not precisely known, it is treated as a normally-distributed random variable L, with mean and standard deviation μ_l and σ_l respectively. The input impedance of the transmission line system, Z_I, and hence the reflection coefficient, Γ_TLM, are therefore random variables as well, as follows,

$$Z_\mathrm{I}(L) = Z_\mathrm{ox}\frac{Z_\mathrm{m} + Z_\mathrm{ox}\tanh(\gamma_\mathrm{ox}L)}{Z_\mathrm{ox} + Z_\mathrm{m}\tanh(\gamma_\mathrm{ox}L)}, \tag{8.4}$$

$$\Gamma_\mathrm{TLM}(L) = \frac{Z_\mathrm{I}(L) - Z_0}{Z_\mathrm{I}(L) + Z_0}. \tag{8.5}$$

Given that an incident beam will cover an area of the surface, the overall reflected beam will effectively average the distribution of oxide thicknesses. Thus, the reflection coefficient of the system according to the transmission-line model, Γ_l, is the expected value of the reflection coefficient of the transmission line system Γ_TLM,

$$\Gamma_l = \langle \Gamma_\mathrm{TLM}(L) \rangle = \frac{\langle Z_\mathrm{I}(L) \rangle - Z_0}{\langle Z_\mathrm{I}(L) \rangle + Z_0}. \tag{8.6}$$

The expected value of the input impedance can be computed with the following integral, which discounts non-physical negative values of the thickness,

$$\langle Z_\mathrm{I}(L) \rangle = \frac{1}{\sigma_l\sqrt{2\pi}} \int_0^\infty Z_\mathrm{I}(l)\exp\left(-\frac{(l-\mu_l)^2}{2\sigma_l^2}\right)\mathrm{d}l. \tag{8.7}$$

This integral is computed numerically, as a Riemann sum. Note that, in order for the probability density function of the truncated Gaussian distribution to be valid, the result in Equation 8.7 must be normalised by the factor $1 - I_\mathrm{lower}$,

$$I_\mathrm{lower} = \frac{1}{\sigma_l\sqrt{2\pi}} \int_{-\infty}^0 \exp\left(-\frac{(l-\mu_l)^2}{2\sigma_l^2}\right)\mathrm{d}l. \tag{8.8}$$

This is to ensure that the total integral of the probability density function sums to 1. Although this means the value μ_l is no longer the true mean of the distribution, this variable does not correspond to any directly-measured value, and hence this is of no consequence. The overall reflection coefficient is computed by taking the product of the reflectivities due to the surface roughness and the loss, or

$$\Gamma_\mathrm{total} = \Gamma_\mathrm{r}\Gamma_l. \tag{8.9}$$

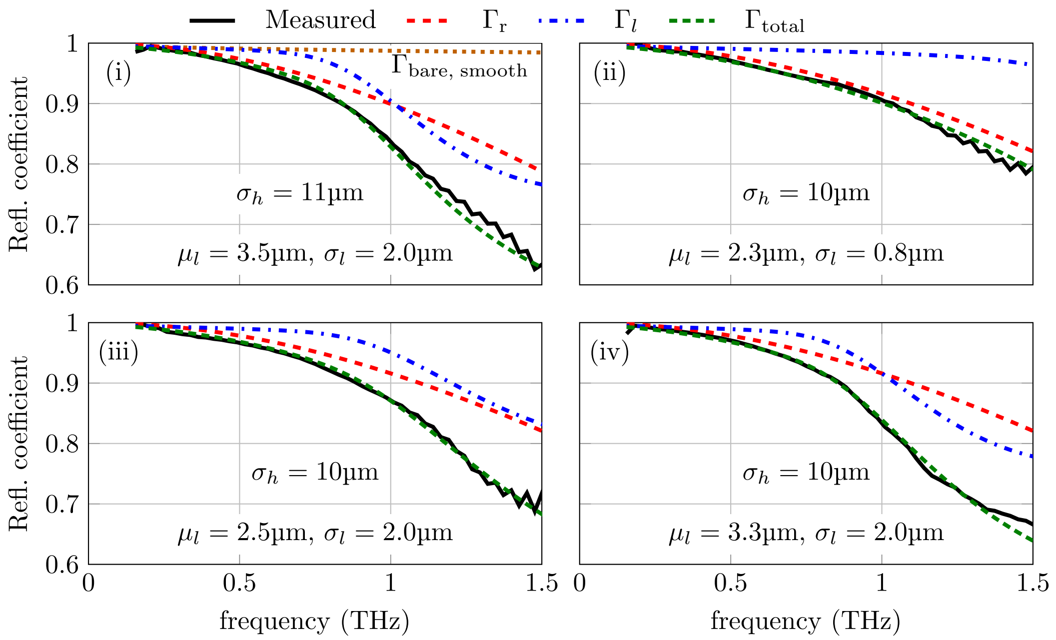

Figure 8.5. Results of modelling procedure. Modelling of printed metal, fit to measured results, where (a-d) correspond to measurements (i-iv) in Figure 8.3(c), respectively. Scattering reflection coefficient, transmission-line model reflection coefficient, and overall modelled reflection coefficient are given by Γ_r, Γ_l, and Γ_{total}, respectively. The fitting parameters σ_h, μ_l, and σ_l are the standard deviation of surface roughness, and the mean and standard deviation of oxide layer thickness, respectively. The reflection coefficient of perfectly smooth grade-5 titanium metal is also given in (i), as $\Gamma_{bare, smooth}$. After Headland *et al.* (2016b).

The statistical properties of the roughness and the oxidation layer thickness are treated as free parameters, in order to match them to each set of measured results. Results of this procedure are presented alongside measured results in Figure 8.5. For further insight, the theoretical reflection coefficient of perfectly smooth, bare grade-5 titanium is determined, and is presented in Figure 8.5(i). This is determined by substituting Z_m for Z_I in Equation 8.5, and 0 for σ_h in Equation 8.1.

Strong agreement is achieved between the measured results and the model. Additionally, the standard deviation of surface level that best fits the measured curve is in agreement with the optical profiler measurements presented in Figure 8.1. It can be seen that the statistical properties of the surface topology and oxide layer thickness play a significant role in the frequency-dependent response. Furthermore, given that the measured response is different for measurements taken at different points on the sample surface, these statistical properties must vary across the surface of the sample. Lastly, reflection coefficients Γ_l and Γ_r are significantly lower than the reflection coefficient of idealised bare grade-5 titanium, and hence it is deduced that surface roughness and the oxide layer are the most significant contributors to reflection loss, especially at higher frequencies.

8.3 3D-printed zone plate

This section presents a 3D-printed metal terahertz beam-control device as a proof-of-concept demonstration. A lensing operation is considered for this purpose, as it is both useful in practical applications, and also because it engenders a relatively-simple design. Note that, whilst the prototype presented below can potentially have been fabricated by conventional machining rather than 3D printing, this work serves as foundational for future studies involving more complicated topologies such as binary-phase holograms (Yang *et al.* 2014a), which are more difficult to directly machine.

8.3.1 Required phase distribution

The terahertz beam-control device to be presented in this chapter is a reflective, stepped-phase lensing device of the sort that is presented in Section 2.4.1, or more specifically, in Figure 2.8(d). The minimal viable step size is limited by the resolution of the 3D printer in question, and a conservative estimate of this limit is 200 µm. According to Equation 2.11, the fact that Δl is equal to this value fixes the relationship between operating frequency, angle of incidence, and the number of phase levels employed. It is evident that there is an inverse relationship between the operating frequency and the number of phase levels used, and hence binary phase is employed in order to ensure that the operating frequency is well into the terahertz range. Equation 2.11 therefore reduces to,

$$\Delta l_{\text{step, refl}} = \frac{\lambda}{4\cos\theta}, \tag{8.10}$$

and hence the specific value of operating frequency is wholly dependent upon the choice of angle of incidence, θ. The lowest possible value is $\theta = 0°$, which corresponds to an operating frequency of 375 GHz. However, this will incur feed blockage due to the reflective nature of the device in question, and hence an oblique angle must be sought. In the interest of simplicity, a 45° angle is employed, and the ensuing frequency of operation is 530 GHz.

This device is a binary-phase zone plate. As discussed in Sections 2.3.1 and 2.3.2, such a device is described by a series of alternating zones of 0° and 180° phase, with radii given by Equation 2.5. In this case, however, the oblique incidence adds a minor complication to the design. As opposed to circular zones, elliptical rings are employed such that they present as circular when viewed at a 45° angle, as shown in Figure 8.6(a). The following equation describes the elliptical curve tracing the edge of zone m,

$$\left(x\cos\frac{\pi}{4}\right)^2 + y^2 = r_m^2. \tag{8.11}$$

A focal length of 50 mm is employed for this design, and the fabricated zone plate is shown in Figure 8.6(b). The device has eleven zones in total, and the x-domain width of the smallest zone is over six times the ridge height. Therefore, topological shadowing effects can be neglected. Lastly, the device is composed of solid metal, and hence it

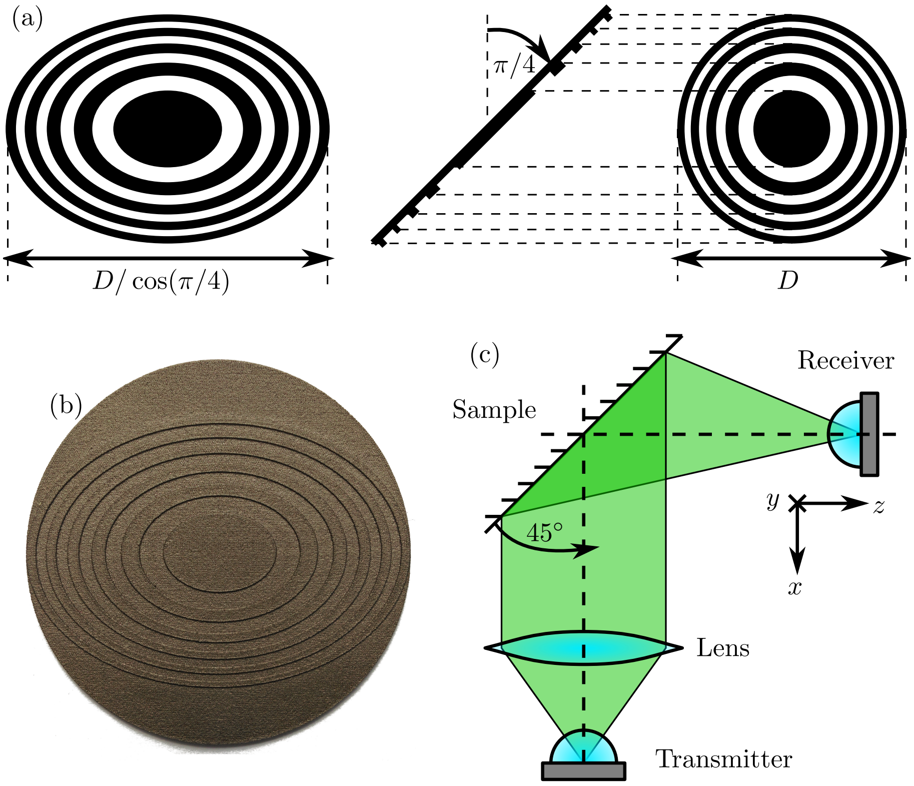

Figure 8.6. 3D-printed zone plate. Zone plate design, showing (a) skewing of concentric circles into ellipses, (b) photograph of fabricated ∼50 mm-diameter sample, with chosen zone radii r_m = 5.33 mm, 7.54 mm, 9.25 mm, 10.70 mm, 11.98 mm, ..., and ridge height of $\Delta h = 200$ µm, and (c) measurement setup for oblique characterisation of focal spot. After Headland *et al.* (2016b).

is highly physically robust in comparison to the microfabricated devices presented in previous chapters.

8.3.2 Characterisation and modelling of zone plate

A fibre-coupled THz-TDS system is employed to characterise the fabricated sample, with experimental setup shown in Figure 8.6(c). The sample is set at a 45° angle with respect to the transmitter, and is excited by a collimated beam. This beam is best approximated by a Gaussian beam, of ∼17 mm radial beamwidth, which is truncated to a 17 mm radius to reflect the finite extent of the collimating lens illustrated in Figure 8.6(c). Note that TE-polarised light is employed, but this is not expected to impact

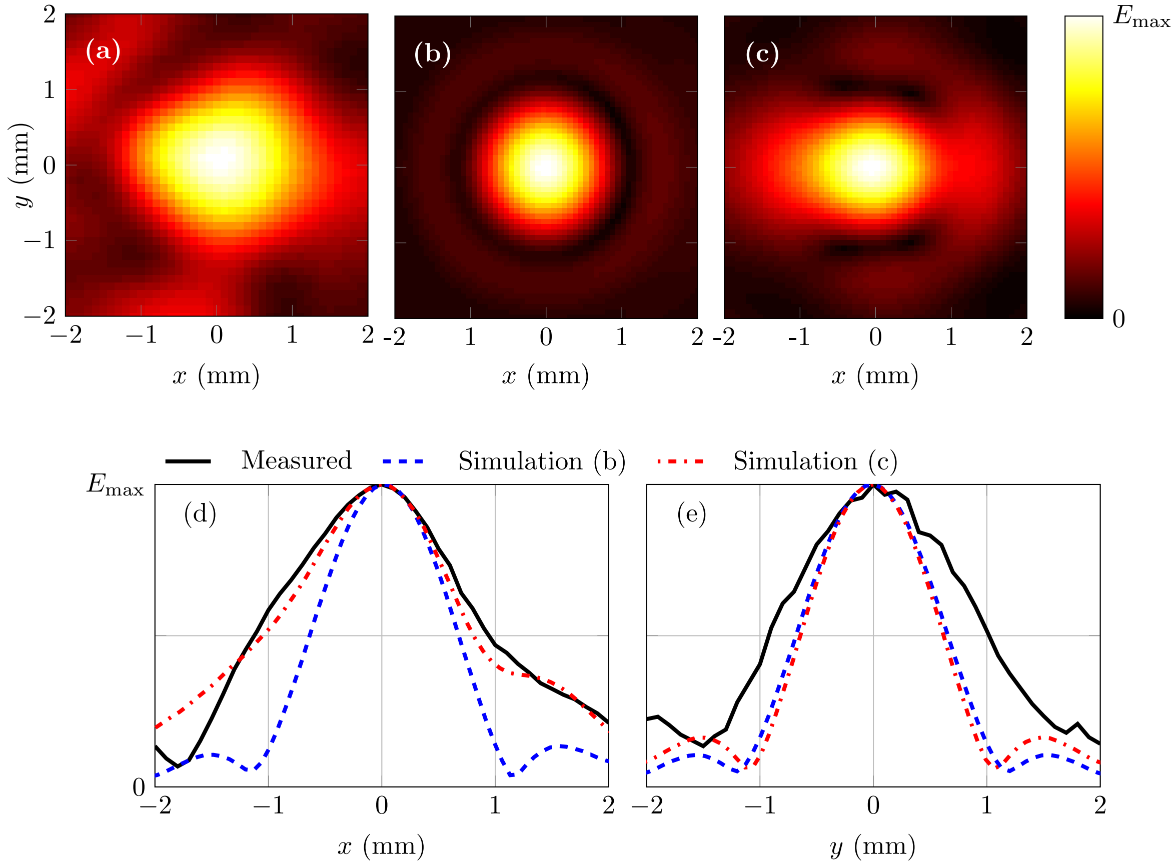

Figure 8.7. Focal spot at operating frequency. Field distribution in the focal plane at 530 GHz, showing (a) measured linear amplitude distribution, (b) simulated results, and (c) simulated result, incorporating 3° angular misalignment. For closer comparison, cross-sectional field distributions along x and y-axes are given in (d) and (e) respectively. After Headland *et al.* (2016b).

the relative path length of the alternating zones, and hence it has no effect on diffractive behaviour. The receiver raster-scans in the focal plane in order to image the focal spot. The measured amplitude profile at 530 GHz is shown in Figure 8.7(a), and a focal spot can be seen, albeit with some aberration and ringing effects. Additionally, the beam is slightly wider in the x-dimension than in the y-dimension.

In order to evaluate the veracity of the measured results, the zone plate structure is modelled using a procedure involving both full-wave simulations and the Huygens-Fresnel principle introduced in Section 2.2. The entire zone plate structure is considered in a full-wave simulation, although it is noted that the volume of space that separates the device and the focal spot is not included, as this requires infeasible computational resources. Oblique plane-wave incidence is employed, in order to approximate a TE-polarised collimated beam impinging upon the surface of the structure with a 45° angle of incidence. The structure is electrically large, and hence it is necessary to approximate the metal with PEC in order to reduce the simulation complexity. This is valid, as the properties of the metal and the surface at subwavelength scales are not expected to impact larger-scale diffractive behaviour, but rather will only result in some losses. The resulting field distribution is extracted into a text file for further processing. In order to isolate the scattered field from the total field, a second simulation is performed considering only the bounding box, and the resulting field distribution is subtracted from the field distribution of the zone plate simulation. The scattered field from the zone plate structure is imported into Matlab for further processing. It is necessary to account for oblique excitation in order to effectively view the structure at a 45° angle. To this end, a linear phase profile of $x2\pi\sin(\pi/4)/\lambda$ is imposed on the field distribution, and the x-axis is shortened by a factor of $\cos(\pi/4)$. This transformation is the mathematical equivalent of the procedure described in Figure 8.6. The full-wave simulation package employed is most amenable to plane-wave excitation, i.e. incident field magnitude is uniform. However, the collimated beam that is employed in the measurement is finite in extent, and the width of the beam impacts the resulting focal spot. In order to better-approximate the collimated beam of the fibre-coupled THz-TDS system employed, a Gaussian beam profile, of radial beamwidth 17 mm, and truncated to a 17 mm radius, is imposed on the scattered field distribution. Finally, the Hugens-Fresnel principle (Goodman 2005) is employed to forwards-propagate the resulting field profile to the focal plane, over a distance of 50 mm.

The result of this simulation is shown in Figure 8.7(b), and a focal spot is clearly visible. Furthermore, the beam widths in the x- and y-dimensions appear to be equal, and there is far less aberration than in the measured results. The most likely explanation for the disparity in x and y beam waist in the measured results is a slight rotational misalignment of the sample. This shortens the effective aperture of the zone plate in the x-dimension, which results in a broader focal spot.

In order to determine the effect of rotational misalignment experienced during experimental characterisation of the zone plate, further alterations are made to the scattered field profile prior to employing the Huygens-Fresnel principle. Rotational misalignment is approximated by employing an angle other than $\pi/4$ in the transformation described above, which compensates for the oblique excitation. This effectively results in 'viewing' the sample at the wrong angle. An error of 3° is incorporated into the model in this way, and the result is the focal spot shown in Figure 8.7(c). It can be seen that this rotational misalignment has resulted in a focal spot that is broader in the x-dimension than in the y-dimension, much like the measured focal spot given in Figure 8.7(a). Additionally, a possible explanation for general aberration in the focal spot is the variation in surface height over a more gradual scale than the characterised surface roughness. This imparts some randomness to the phase of the reflected beam, which slightly degrades overall focal spot quality.

In order to facilitate closer comparison, cross-sectional field distributions of measured and simulated focal spots along the x- and y-axes are given in Figures 8.7(d) and 8.7(e). It can be seen from these results that the simulation incorporating rotational misalignment is a better match to the measured results in the x-dimension than the simulation

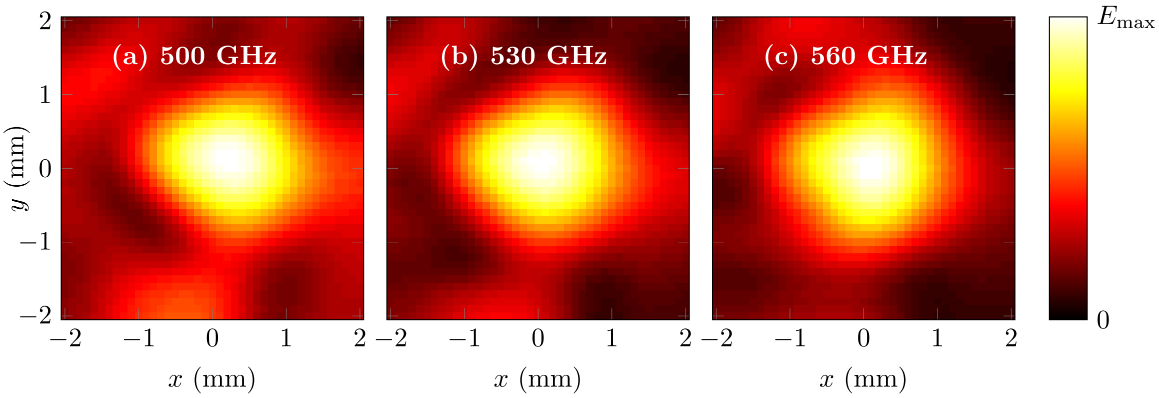

Figure 8.8. Measured focal spots at other frequencies. Measured focal spot (a) below operating frequency, (b) at operating frequency, and (c) above operating frequency. After Headland *et al.* (2016b).

without rotational alignment. Additionally, whilst there is approximate agreement, both simulated field distributions are narrower than the measured profile in the y-dimension. This is likely due to degradations in beam quality imposed by surface randomness, and vertical tilt of the sample may also be a contributing factor. Another possible explanation for this discrepancy is that the width of the collimated beam employed for the measurement is lower than that which is employed for the simulation, resulting in a proportional increase in the focal spot size.

It is of interest to observe the zone plate's focusing performance at frequencies other than the operating frequency. To this end, measured focal spot results are provided, over a 60 GHz range about the operating frequency, in Figure 8.8. It can be seen that a focal spot of similar quality is maintained over this frequency range, in spite of the spatial dispersion that is typical to devices of this sort. This illustrates the capacity of this device to operate over a reasonable bandwidth.

8.4 Conclusion

This chapter evaluates the applicability of 3D-printed metal to terahertz technology. A 3D-printed titanium alloy is identified as being potentially suitable for reflective optics in the terahertz range. This alloy is characterised with THz-TDS, and it is shown to have efficiency of reflection above 80% for frequencies below 900 GHz, and above 90% for frequencies at and below the nominal operating frequency of 530 GHz. A model incorporating surface roughness and variation in oxide layer thickness is employed to explain the reflection characteristics of the 3D-printed titanium alloy. Based on this model, it is concluded that the most significant contributors to loss are surface roughness, which results in scattering losses, and the presence of oxide at the surface, which causes dissipation. Despite its present use to describe the reflectivity of a specific titanium alloy, the developed analytical model is general, and can be applied to other metals.

As a proof-of-concept, a terahertz zone plate with an operating frequency of 530 GHz is printed, and the focal spot is characterised with THz-TDS. The device is significantly more robust and durable than comparable devices realised with microfabrication techniques. Other such zone plates can be produced on-demand to arbitrary specification, as the additive manufacture process is rapid and readily customisable. Furthermore, other reflective devices, including the Gerchberg-Saxton holograms discussed in Section 2.3.2, may be produced in the same way to serve arbitrary beam-shaping requirements. Additionally, guiding structures such as hollow-tube waveguides and mode converters may also be printed directly in metal, at scales that are challenging for conventional machining and assembly. Therefore, this work opens opportunities for rapid prototyping of numerous diverse devices for the manipulation of terahertz radiation.

More advanced 3D-printers can provide finer resolution, potentially supporting beam-shaping applications towards 1 THz. Additionally, the conductivity of the alloy employed in this work is fairly low for a metal (Welsch *et al.* 1993). Alternative metals are available for 3D printing, including other alloys of titanium, steel, and aluminium (Frazier 2014), which may have higher conductivity, and importantly, may oxidise less readily. For instance, 3D printing in $AlSi_{10}Mg$ has previously been demonstrated in other applications (Brandl *et al.* 2012), and the electrical conductivity of this material is two orders of magnitude higher than that of grade-5 titanium (Uliasz *et al.* 2012). Therefore, such alloys may exhibit higher reflectivity than the material presented in this work.

Having investigated a reflective resonator-less beam-control device in this chapter, the following chapter will explore a flat-profile transmissive option, which makes use of an all-silicon effective medium to achieve high transmission.

Chapter 9

Hole lattice zone plate

It is of interest to develop a transmissive beam-control device with efficiency that is comparable to the reflectarray presented in Chapter 7. To this end, an all-silicon terahertz beam-control device is presented in this chapter. An effective medium is devised by means of a sub-wavelength through-hole array in a uniform-thickness HR Si slab, for which the effective refractive index, and hence the optical path length experienced by transmitted radiation, is dependent on hole radius. It is found that reflection can be cancelled out in certain cases, and as HR Si is a low-loss material, the ensuing transmission is close to unity. However, the achievable phase levels that satisfy this high-transmission condition are separated by 180°, and hence devices based on this principle are limited to binary phase. A transmissive, binary-phase zone plate based on a silicon through-hole array is designed, but fabrication is not completely successful. Experimental characterisation is attempted, but the associated results do not conform to the modelling employed in the design procedure.

9.1 Introduction

The reflectarray antenna that is presented in Chapter 7 is of exceptionally-high efficiency, with near-negligible loss. By comparison, the transmitarray that is presented in Chapter 5 is of lower efficiency, with roughly 30% of incident power being lost to reflection and dissipation. It is therefore of interest to investigate whether transmissive beam-control devices can achieve efficiency on a par with the aforementioned reflectarray, and this is the main subject of this chapter. For this purpose, a high-resistivity single-crystal silicon dielectric-based solution is sought. The silicon through-hole array that is presented in Park *et al.* (2014) is revisited as a basis for this study, as it holds underutilised potential. In order to improve the efficiency with which power is transmitted through this structure, the structure is optimised in order to achieve cancellation of reflection loss. However, a drawback of this approach is that it is limited to binary phase, and hence the enhancement of transmission efficiency is tempered by a decrease in diffractive efficiency.

9.2 Unit cell

Although the device that is detailed in this chapter is not a passive array of the sort detailed in Chapters 4 to 7, it makes use of a periodic, subwavelength structure, and hence the paradigm of a unit cell applies. The individual element, shown in Figure 9.1(a), is a block of high-resistivity float-zone intrinsic silicon (HR Si) with an air through-hole that passes through the centre. Terahertz radiation is transmitted through the structure, and the direction of propagation is in the through-hole direction. Provided that the both size and lattice constant of the holes are subwavelength, and that there are no resonant effects within the unit cell, or coupling effects between adjacent cells, effective medium theory holds. The above stipulations are met in this case, the hole array is therefore experienced by terahertz radiation as a bulk medium, with effective refractive index depending on the radius and density of the holes. This effective index can therefore be controlled by varying hole radius, and the transmission magnitude and phase through a finite-thickness slab will vary accordingly.

The transmission response of the unit cell shown in Figure 9.1(a) is investigated parametrically using full-wave simulations, and results at 1 THz are presented in Figure 9.1 (b,c). It can be seen from this parametric analysis that the phase tunability range exceeds a full 360° cycle. A more interesting feature, however, lies in the magnitude

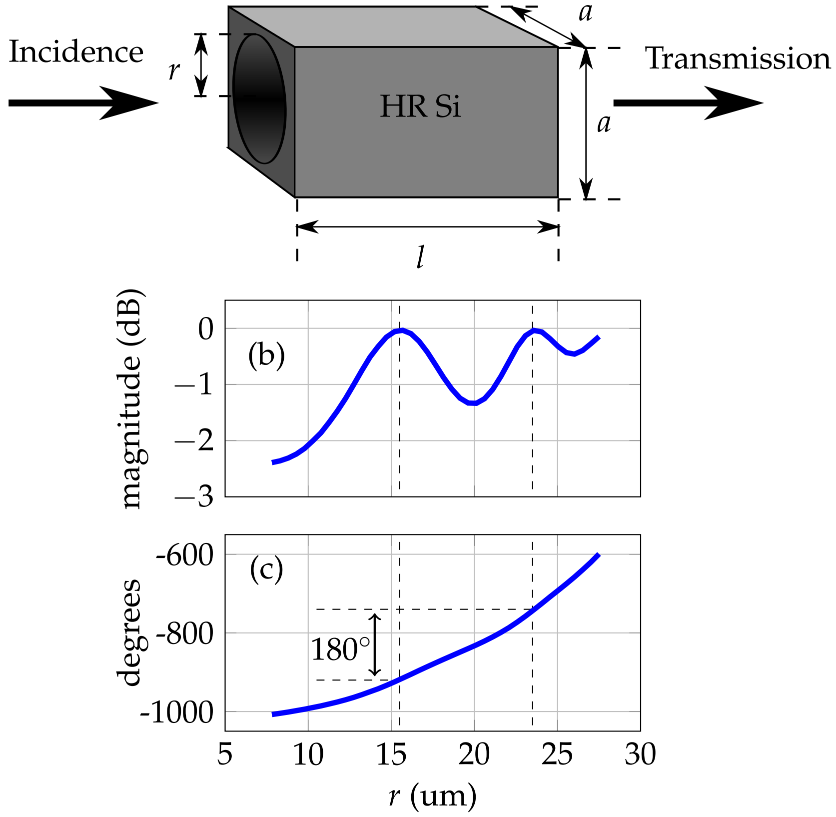

Figure 9.1. Hole lattice unit cell. Unit cell of hole lattice array device, showing, (a) structure of individual element, where $a = 60\ \mu$m, and $l = 250\ \mu$m, and (b) Simulated response at 1 THz as a function of hole radius *r*.

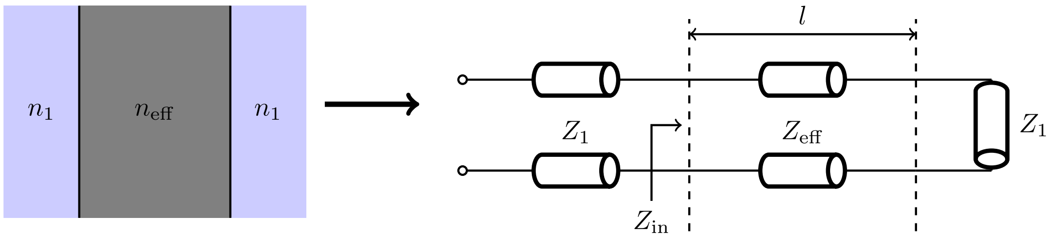

Figure 9.2. Transmission-line modelling of hole lattice. Illustration of the equivalent transmission-line circuit that is employed to model transmission through the hole lattice effective medium. In this case, medium 1 (i.e. n_1 and Z_1) represents air, and medium "eff" represents the effective medium.

response; it appears that transmission magnitude is near-unity when hole radius is set to either 15.5 or 23.5 µm. In order to investigate this feature in further detail, a simplified transmission-line model is employed, which treats the hole lattice medium that is the main subject of this chapter as a length of lossless transmission line, as shown in

Figure 9.2. Lossless transmission lines in particular are chosen as this simplifies analysis, and it is valid because HR Si is a low-loss material. For this analysis, λ_{eff} and k_{eff} are the wavelength and wavenumber in the effective medium, respectively. The latter is defined as $k_{\text{eff}} = \frac{2\pi}{\lambda_{\text{eff}}}$. The wave impedance observed at the input to the effective medium is defined as,

$$Z_{\text{in}} = Z_{\text{eff}} \frac{Z_1 + jZ_{\text{eff}} \tan(k_{\text{eff}} l)}{Z_1 + jZ_{\text{eff}} \tan(k_{\text{eff}} l)}, \tag{9.1}$$

where it is noted that this takes a different form to Equation 8.4, because in this case, the medium is lossless. The ensuing observed reflection coefficient is as follows,

$$\Gamma = \frac{Z_{\text{in}} - Z_1}{Z_{\text{in}} + Z_1} = \frac{j\tan(k_{\text{eff}} l)(Z_{\text{eff}}^2 - Z_1^2)}{2Z_1 Z_{\text{eff}} + j\tan(k_{\text{eff}} l)(Z_{\text{eff}}^2 + Z_1^2)}. \tag{9.2}$$

The aforementioned condition of interest, under which transmission is close to unity, must therefore occur when the numerator of Equation 9.2 is equal to zero. There exists a trivial solution, namely when the wave impedances of the two media are equal; $Z_1 = Z_{\text{eff}}$, and hence there can be no reflection. However, this condition is of little interest, as the index of the effective medium must be equal to that of free space in order to satisfy this condition. Thus, the effective medium exhibits material properties identical to those of air, and is not capable of imparting a nonuniform phase distribution on transmitted radiation. No form of beam control is possible under this condition. On the other hand, the trigonometric portion of the numerator, namely $\tan(k_{\text{eff}} l)$, exhibits periodic zeroes when its argument is equal to an integer multiple of π, and this can be exploited as follows,

$$\Gamma = 0 \quad \forall \quad k_{\text{eff}} l = \frac{2\pi l}{\lambda_{\text{eff}}} = m\pi; \quad l = m\frac{\lambda_{\text{eff}}}{2}, \quad m = 0, 1, 2, ..., \tag{9.3}$$

and hence the reflection coefficient is equal to zero when the thickness of the effective medium slab, l, is equal to an integer multiple of half the in-medium wavelength, λ_{eff}. As slab thickness is fixed, this is achieved by tuning the in-medium wavelength by means of the hole radius. Note that the two maxima given in Figure 9.1(b) are observed in Figure 9.1(c) to be separated in phase by 180°. This is not a coincidence, but rather it is because both maxima correspond to different multiples of half-wave thickness, and hence the optical path length, and the output phase, differs by a half-wave between the two.

The above analysis can also be described phenomenologically. Essentially, there is reflection at both the input and output surfaces of the effective medium. This has the capacity to support multiple internal reflections, in a manner not unlike in a Fabry-Pérot etalon (Saleh and Teich 2007).[4] However, in the case of the maxima indicated in Figure 9.1(b), cancellation occurs; the reflection from the air-medium interface where the wave enters the medium is effectively annulled by that which is reflected from the medium-air interface where the wave is transmitted to free space. It is noted that the second path is out of phase with the first, although it has traversed two half-wave lengths; one prior to reflection, and one following. This is because one of the waves is of negative phase, as is the case when a wave is reflected from a lower-impedance medium.

9.3 Array-level design

It is found in Section 9.2 that transmission magnitude through a hole lattice effective medium of this kind can be made close to unity by careful selection of hole radius, and it is of interest to exploit this phenomenon for efficient terahertz beam-control devices. However, there is a trade-off associated with this technique, namely that only binary phase levels are achievable. As presented in Section 2.3.2, binary phase is sufficient for beam control, albeit at the cost of reduced efficiency, as energy is projected into undesired directions. That said, binary phase is sufficient for numerous applications, and hence there remains sufficient incentive for an investigation into beam-control suitability.

In order to demonstrate efficient beam control that makes use of this principle of reflection cancellation, a binary-phase zone plate is designed. This consists of alternating, concentric circular zones of 0° and 180°-phase transmission, with switching radii described in Equation 2.5. In this case, the holes that populate these alternating zones are of radius 15.5 and 23.5 μm. The chosen operating frequency is 1 THz, which is consistent with the parametric analysis presented in Figure 9.1, and the selected focal length is 5 mm. The resulting phase distribution is shown in Figure 9.3(a), and a portion of the corresponding zone plate design is illustrated in Figure 9.3(b). It is noted that 5 mm is significantly shorter than the focal lengths of the other lensing devices reported in this

---

[4] It is noted that a Fabry-Pérot etalon effect is a form of resonance, and hence this may appear to be in contradiction to the previous assertion that there are no resonance effects internal to the unit cell, which is a requirement for effective medium theory to be valid. However, the Fabry-Pérot effect is a resonance of the effective medium that is produced by the large array of unit cells, and not of the unit cell itself. As such, there is no contradiction.

thesis. However, a short focal length is beneficial for communications applications requiring compact devices with high antenna gain, as well as imaging applications that benefit from a fine focal spot, as focal length is proportional to spot size. The reason that such a short focal length was not previously employed is that, in the case of the passive arrays in Chapters 5 to 7, the strong obliquity that this introduces produces spurious modes, which impairs the veracity of the parametric analysis upon which such designs rely. Additionally, a short focal length is not be possible for the reflective device presented in Chapter 8 due to practical issues associated with clearances and

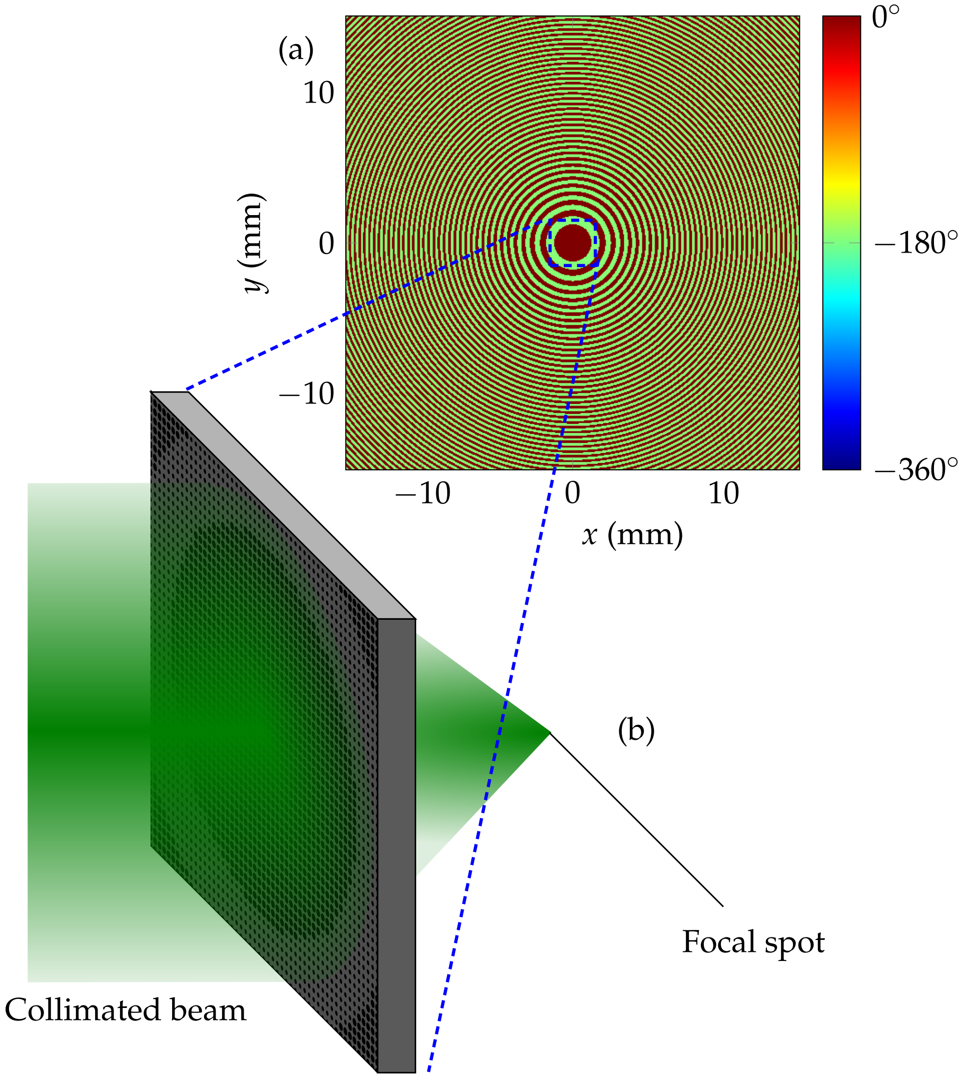

Figure 9.3. Hole lattice zone plate. Array-level design of the hole lattice zone plate, showing (a) the required binary phase distribution for the desired lensing operation, and (b) a diagram of the operation and zone structure of a portion of the hole lattice zone plate, showing concentric zones populated with holes of the appropriate radii.

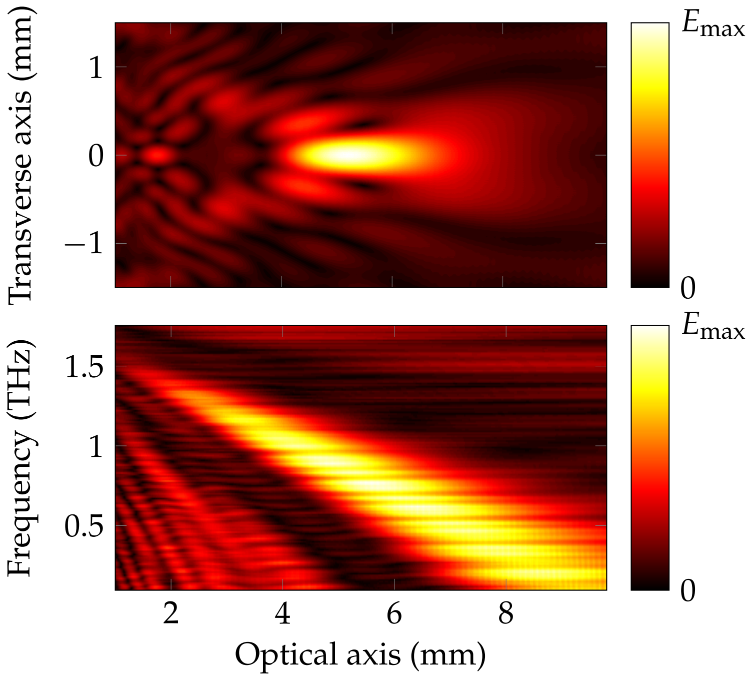

Figure 9.4. Hole lattice zone plate simulation. Simulated focusing behaviour of hole lattice zone plate, showing (a) field amplitude profile at 1 THz, and (b) frequency-dependent field amplitude distribution along the optical axis.

feed blockage. For the transmissive device presented in this chapter, however, there is no resonance as such. Furthermore, this device is transmissive, so there is no potential for feed blockage. This is therefore the only device to be reported in this thesis that is capable of such a short focal length.

Full-wave simulations are employed to accurately model the focusing behaviour of the zone plate. As computational resources are limited, the full area of the structure is not considered, but rather a 5×5 mm^2 portion of the sample is sufficient to provide confirmation of the intended functionality. The results of this simulation, in the form of a beam profile at the operating frequency of 1 THz, are presented in Figure 9.4(a). It can be seen that the device does indeed produce a focal spot at a 5 mm distance. In order to evaluate spatial dispersion, the frequency-dependent field distribution along the optical axis is presented in Figure 9.4(b). It can be seen that the focal length has an approximately-linear relationship with frequency, as expected. Additional to that, it is noted that there is some fluctuation in maximal field magnitude with respect to change in frequency. This is due to migration of the Fabry-Pérot fringes, as well as the detuning of the relative phase away from 180°, in accordance with Equation 2.9. As phase wraps in a 2π cycle, this produces alternation in minima and maxima.

9.4 Fabrication

In order to fabricate this device, a HR Si wafer of the appropriate thickness is diced, and photolithography and deep reactive ion etching (DRIE) are employed to define the through-holes. The hole geometry that is considered in Sections 9.2 and 9.3 is that of a cylinder, which corresponds to an ideal, 90° etch, as illustrated in Figure 9.5(a). However, it is challenging to define holes of high aspect ratio using this technique due to factors including inefficient removal of etch products from the bottom of the well during etching, as well as diffusion phenomena. These detrimental effects become progressively more significant with respect to a deeper etch, and hence it is possible for holes to taper, as shown in Figure 9.5(b), or even to fail to etch all the way through the silicon slab, as in Figure 9.5(c). For holes of uniform radius, this issue can be compensated by progressively altering the DRIE-system settings as the hole is etched. However, the specific required etch profile will vary with respect to hole radius, and hence both hole sizes cannot simultaneously be etched correctly.

Micrographs of the fabricated device are given in Figure 9.6, as viewed from the backside, i.e. opposite to the side from which it is etched. It can be seen that, for alternate zones, there is no apparent hole. It is therefore concluded that these zones correspond to the case illustrated in Figure 9.5(c), as the etch is incomplete. These zones must contain holes of the lesser, 15.5 µm radius, as the opposing zones exhibit a complete, if potentially tapered, etch.

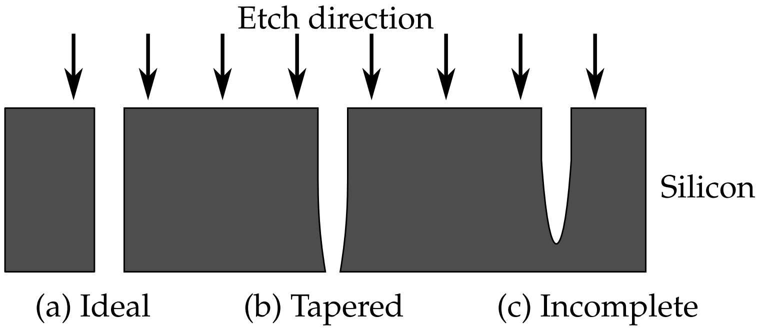

Figure 9.5. Non-ideal geometry with DRIE process. Illustration of potential non-ideal effects associated with etching high aspect-ratio holes using a DRIE process, showing (a) an ideal etch, with 90° walls, (b) a tapering etch, in which the width of the etched void progressively narrows, and (c) an incomplete etch, in which the hole does not penetrate through the entire sample thickness.

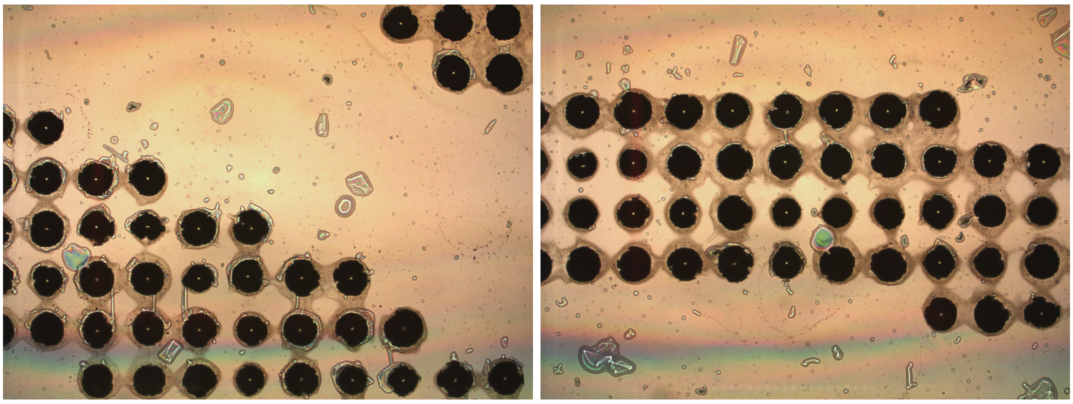

Figure 9.6. Hole lattice zone plate sample. Optical micrographs of back-side of fabricated hole lattice sample, showing incomplete etch, as evidenced by the apparent lack of holes in alternating zones.

9.5 Experimentation

The undesired fabrication effects presented in the Section 9.4 will unavoidably alter the response of transmitted radiation, and in doing so, introduce spurious effects. The tapering of the hole radius produces a progressive increase in effective refractive index, and the incomplete etching presents a portion of bulk silicon that a transmitted wave must pass through, which will likely incur significant reflection losses. Additional to that, the reflection-cancellation effects discussed in Section 9.2, which are the main novelty of this device, depend upon a very precisely-defined structure. This deviation from the intended geometry will prevent the cancellation of reflection, resulting in lower transmission efficiency.

In spite of the above difficulties, attempts are made to characterise the focal spot of the zone plate using THz-TDS. The sample is excited by a collimated beam, and the field distribution in the focal plane is imaged by raster-scanning the detector. The results of this procedure are presented in Figure 9.7, for two frequencies of interest. The results at 1 THz, shown in Figure 9.7(a), appear to exhibit a vague focal spot, with a concentric ring surrounding it, as expected of a binary-phase zone plate of this type. However, there is significant noise in these results, which indicates that the field amplitude at the focal spot is quite low. By inspection of the field distribution at various frequencies, a higher-quality field pattern is found at 625 GHz, and is shown in Figure 9.7(b). Thus, although the device does not function exactly as intended, it remains capable of achieving the broad definition of its desired purpose; the focusing of terahertz radiation. This is because, whilst the transmission response exhibits undesired alterations

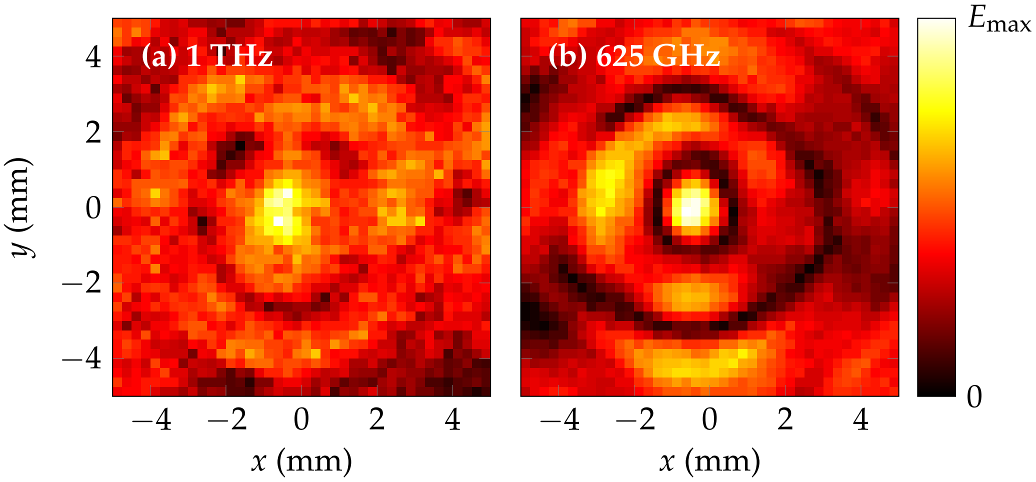

Figure 9.7. Focal spot of hole lattice zone plate. The experimentally-characterised focal spot of the hole lattice zone plate at (a) 1 THz, and at (b) 625 GHz.

due to the aforementioned fabrication difficulties, the pattern of concentric zones remains the same. So long as there is some difference in transmission between the two zones, either magnitude or phase, there will be diffractive focusing to an extent. That said, the efficiency of this device is likely quite low due to the aforementioned fabrication issues, although it is not possible to verify this for practical reasons; focusing efficiency can only be verified with a conventional lens of identical focal length, and no such lens is available.

9.6 Conclusion

This chapter presents an innovative concept for highly efficient binary-phase transmissive optics that exploit Fabry-Pérot effects in order to achieve cancellation of reflection. A terahertz zone plate is designed as a proof of concept. Whilst the theoretical foundation for this idea is sound, there were difficulties in the fabrication of the zone plate associated with incomplete etching of high aspect ratio through-holes in silicon. Despite this, a focal spot was experimentally characterised, albeit at a frequency other than the nominal operating frequency of 1 THz.

This concludes Part IV of this thesis, which also completes the dissertation of technical contributions that are provided. The following chapter will present a summary of key points and important results reported in Chapters 1 to 9.

PART V

Conclusion

Chapter 10

Thesis summary

THIS chapter concludes the doctoral thesis, and provides an overview of the information and main contributions in each chapter. Part I of the thesis contains Chapters 1 to 3, which give the context for this project. This includes motivation, underlying theory, and previously-reported demonstrations of related work in the literature. Subsequently, Chapters 4 to 9 contain the original contributions made during this doctoral program, and are divided into three major parts that contain two chapters each. Part II describes efforts to enhance the efficiency of metallic resonator-based beam-control devices, Part III details the development of efficient dielectric-resonator-based beam-control devices, and Part IV gives examples of resonator-less approaches to realise terahertz beam-control devices.

10.1 Part I—Context

This part provided justification for the relevance of the project undertaken in this doctoral program. Additionally, explanations were given for the rationale regarding particular approaches taken.

10.1.1 Chapter 1—Introduction

This chapter presented an introduction to terahertz technology, as well as the motivations for the study undertaken in this doctoral thesis. Basic definitions of the terahertz range were provided, and the unique properties and limitations associated with terahertz waves were discussed.

Due to the high frequency of terahertz waves relative to other ranges of electromagnetic radiation that are employed for free-space communications, this form of radiation was identified as being capable of supporting wireless communications at exceptionally high data rates. Additional to that, properties including micro-scale wavelength, the non-ionising nature of terahertz radiation, and the capacity to penetrate through solid objects make terahertz radiation a promising candidate for applications including safe sub-dermal medical imaging and security screening. Lastly, spectroscopy applications were also identified, as numerous interesting substances including drugs and explosives exhibit spectral features in the terahertz range.

The main obstacle to the realisation of practical terahertz technologies was identified as pertaining to power—the so-called "terahertz gap." This is impacted both by relatively-low available power, and also by high atmospheric attenuation, in the terahertz range. Terahertz devices must therefore minimise all forms of power loss. This necessitates the development of beam-control techniques in the terahertz range, to minimise power projected into directions in which it will not be received. These beam-control techniques must be highly efficient, so as to preserve the original motivation for the study. Additional to that, compact and flat-profile devices are generally preferable.

10.1.2 Chapter 2—Theory

In order to control the propagation, and directionality of terahertz waves, one must first understand the behaviour of electromagnetic radiation in free space. This chapter presented a brief overview of the relevant underlying principles. Analytical tools were deployed in order to associate transverse-plane field distributions with ensuing propagating beam behaviour. Subsequently, these tools elucidated the means by which a required beam shape may be prescribed—by manipulation of aperture distributions of field magnitude and phase. Phase-based control was identified as superior to magnitude-based alternatives in terms of efficiency and versatility, and hence this doctoral thesis is overwhelmingly concerned with phase-based techniques.

Some relevant techniques to achieve a given bespoke phase distribution for beam control were presented abstractly. The benefits and drawbacks of each such approach were given, and the scope was subsequently narrowed to techniques pertaining most directly to this doctoral thesis, namely those that make use of arrays of passive resonators; reflectarrays and transmitarrays. An overview of the general approach to reflectarray design was subsequently presented.

10.1.3 Chapter 3—Background

Previous work on terahertz beam control was reviewed in this chapter. The scope of the review was limited to work that has presented a practical demonstration, as this is evidence of the potential for use in real-world applications. It is of interest to evaluate the trade-offs between various approaches in order to determine the technique that is best suited to serve the aims of this project. This review was therefore instrumental in identifying key under-explored areas that exhibit potential to advance the main aims of the investigation.

10.2 Part II—Metallic resonators

Efforts were made to improve the efficiency of metallic resonators, and to construct practical terahertz beam-control devices that make use of such resonators.

10.2.1 Chapter 4—Doped polymer for efficient metallic resonators

Aim Loss is a major issue with metallic resonator-based devices in the terahertz range. Typically such resonators make use of a polymer dielectric, and it is commonplace for this dielectric to account for the majority of dissipation. the aim of this study was to modify the dielectric properties of these polymers so as to reduce dissipation, whilst maintaining compatibility with microfabrication processes.

Method The elastomeric polymer PDMS was doped with lower-loss ceramic materials, namely alumina and PTFE. Care was taken to ensure deeply-subwavelength particle size, so as to avoid unwanted scattering effects. The material properties of the composite samples were then probed with THz-TDS. Thereafter, these extracted material properties were utilised in simulations in order to determine their impact upon the efficiency of metallic resonators.

Result The loss tangent of PDMS was successfully reduced by $\sim$15%. However, the subsequent simulations show that, whilst resonator efficiency is enhanced to a degree, the improvement is not significant.

Original contribution Whilst doping of polymers in this way has previously been employed in order to increase either loss or refractive index of a terahertz-range dielectric, this is the first demonstration of this technique as a means to reduce loss.

10.2.2 Chapter 5—Polarisation-converting transmitarray for flat lens

Aim The objective of this chapter was to develop an efficient metallic resonator-based beam-control device. The intended beam-control operation is lensing, as this is of practical value in potential applications of terahertz technology.

Method An innovative tri-layer structure, adapted from Grady *et al.* (2013), was designed to focus terahertz radiation at 400 GHz. The ensuing device was realised using microfabrication techniques, and subsequently characterised using THz-TDS.

Result Focusing at the operating frequency was successfully demonstrated, with overall efficiency of 68%. Although this is not ideal, it is a significant improvement upon comparable previously-reported terahertz flat-lens transmitarrays, for which the reported focusing efficiency was below 25%.

Original contributions This study presents the highest-efficiency terahertz flat lens transmitarray structure to-date, by a margin of over 40%.

10.3 Part III—Silicon-on-gold microstructures

In the interests of improving the performance of passive array devices for terahertz beam control, alternatives were sought to metallic resonators in the form of dielectric microstructures.

10.3.1 Chapter 6—Fabrication and characterisation of dielectric resonator antennas

Aim In order to improve efficiency, an alternative to metallic resonators was investigated. Intrinsic silicon-based dielectric resonators were nominated, as the mode of resonance makes use of displacement current rather than conduction current. Overall, this makes the resonator far less susceptible to Ohmic loss.

Method A means to realise silicon-on-gold microstructures was developed, and subsequently employed to realise a homogeneous array of dielectric resonator antennas. The reflection response of this array was characterised using THz-TDS.

Results The fabrication of the silicon-on-gold microstructures, undertaken at RMIT University, was successful. Experimental characterisation yielded excellent agreement between simulated and measured phase response. The device was shown to operate as an artificial magnetic conductor at a frequency of 800 GHz. Additionally, experiments reveal negligible loss to within experimental error.

Original contributions The contribution of this chapter is the development and demonstration of a new class of highly efficient terahertz resonator.

10.3.2 Chapter 7—Dielectric-resonator-based reflectarray

Aim The objective of this study was to employ the resonators that were developed in Chapter 6 for a reflectarray antenna, with the ultimate aim of highly efficient beam control in the terahertz range.

Methodology Parametric analysis was deployed in order to determine mapping between resonator size and reflection phase, and this analysis was utilised in order to translate the phase distribution required for lensing at 1 THz into a layout of nonuniform resonators. This design was fabricated as per the procedure employed in the previous chapter, Chapter 6, and THz-TDS was utilised in order to verify its functionality.

Results The focusing capability of the reflectarray was experimentally verified. Furthermore, experiments revealed near-negligible loss, and 18% bandwidth.

Original contributions The main contribution of this study is that the efficiency of the dielectric-resonator-based reflectarray, which out-performs any other terahertz passive array structure to-date. Furthermore, in demonstrating a device capable of highly efficient terahertz beam control, this study has achieved the main aim of this doctoral thesis.

10.4 Part IV—Non-resonant techniques

Having so-far employed resonator-based solutions exclusively, it is also of interest to investigate the potential of designs that do not make use of any sort of resonator.

10.4.1 Chapter 8—Characterisation of 3D-printed metal for terahertz optics

Aim The aim of this chapter was to leverage the natural reflectivity of metals, including relatively low-conductivity metals, to achieve terahertz beam control in a straightforward manner. Additionally, it was desirable to evaluate the feasibility of 3D printing of metals as a means to rapid-prototype terahertz optics.

Method A flat, featureless titanium disk was 3D-printed in order to investigate the reflection characteristics of the relevant metal in isolation, and a model was developed in order to determine the primary origins of reflection loss. A binary-phase zone plate, designed for operation at 530 GHz, was subsequently 3D-printed in the same way, in order to determine whether or not such a structure can be employed for beam control in the terahertz range. Both samples were characterised using THz-TDS.

Result Reflective efficiency was found to be over 90% at the nominal operating frequency, and over 80% for all frequencies below 900 GHz. The primary origins of loss were found to be scattering due to topological variation, as is common with 3D printing, as well as oxidation at the surface due to annealing in an oxygen-rich environment, which produced a layer of lossy dielectric. Focusing of radiation at 530 GHz was successfully demonstrated.

Original contributions This constitutes the first demonstration of a 3D-printed reflective device in the terahertz range. Furthermore, there have been no other reports to-date of terahertz-range devices fabricated using direct 3D printing of metals.

10.4.2 Chapter 9—Hole lattice zone plate

Aim The objective of this study was to develop a transmissive device with efficiency on-par with the aforementioned dielectric-resonator-based terahertz reflectarray presented in Chapter 7.

Method An all-dielectric, non-resonant array of subwavelength through-holes in an intrinsic silicon slab was designed as a means to achieve an effective medium. Hole radius was manipulated in order to achieve cancellation of reflection loss. The reflection-cancellation bears the trade-off that it is limited to binary phase, and hence a binary-phased zone plate was designed for an operating frequency of 1 THz. This device was fabricated using a DRIE process, and subsequently characterised using THz-TDS.

Result There were complications in the fabrication process, associated with difficulties in etching the high-aspect ratio holes. As a result, the realised device did not conform to specification. Despite this, characterisation was attempted. The results are of low quality at the operating frequency of 1 THz, but a focal spot was successfully identified, albeit at 650 GHz. There was no practical way to evaluate efficiency.

Original contribution The main novelty of this study is the cancellation of reflection loss, although there was not a successful experimental demonstration of this functionality due to tapered and incomplete etching. Note that refinements to the mask layout and fabrication procedures will likely yield a vertical-walled etch, and will therefore produce a successful realisation of the bespoke hole lattice structure.

10.5 Executive summary of original contributions

1. The reduction of the intrinsic loss of a dielectric polymer material by inclusion of powder dopants (Headland *et al.* 2015c).
2. The demonstration of a terahertz flat lens transmitarray that exhibits 68% focusing efficiency (Chang *et al.* 2017).
3. The development of intrinsic silicon microstructures as efficient terahertz resonators (Headland *et al.* 2015a).
4. The demonstration of a terahertz reflectarray composed of silicon resonators, with near-negilible loss (Headland *et al.* 2016a).
5. The use of 3D-printed solid metals for terahertz devices in general, and specifically, the use of 3D-printing to realise a reflective terahertz beam-control device (Headland *et al.* 2016b).
6. The design of an all-silicon transmissive terahertz beam-control device that exhibits near-ideal transmission efficiency due to reflection-cancellation and low intrinsic loss (Headland *et al.* 2014).

10.6 Outlook

The advances presented in this doctoral thesis are worthy of note. But they are not, of themselves, sufficient for widespread adoption of such technologies by the general public. In order to expedite progress towards practical applications, the field of terahertz beam control will benefit significantly if research efforts are concentrated in certain areas. These include the development of solid-state electronic beam-scanning capability, devising means for high-efficiency birefringence, and enhancing bandwidth.

Electronic scanning All of the designs reported in this thesis are examples of static beam-control devices, i.e. their phase distributions cannot be actively reconfigured. However, such a capability is key to achieving dynamic scanning, which will likely be required for practical terahertz technologies in the future. Although Section 3.3 detailed some work on dynamically-reconfigurable reflector devices for terahertz beam control based on mechanical actuation, solid-state, electronically-controlled devices are preferable due to superior modulation speed, versatility, compactness, and control. Granted, Section 3.4 presented some examples of electronically-controlled beam steering using CMOS phased array technology, but such devices are unlikely to scale well in frequency and aperture size. Thus, an electronically-reconfigurable terahertz passive array remains a highly sought-after achievement. As with the static devices presented here, efficiency is key, and whilst the DRAs detailed in Part III offer high efficiency, they are unlikely to be amenable to actively-tunable control. That said, further investigation into incorporating semiconductors of variable carrier concentration (Sharma *et al.* 2012, Al-Naib *et al.* 2013) may yield new techniques to realise tunable terahertz DRAs. In general, however, metallic resonators are more suitable for dynamic tunability, but the polymer-based resonators presented in Section 3.7 and Chapter 5 will not likely be compatible with the integration of nonlinear materials for tunable devices. Therefore, we must investigate new methods for fabricating resonators that can accommodate dynamic, tunable, electronic control, whilst ideally maintaining efficiency on-par with the DRAs presented in Part III. This will potentially facilitate dynamic steerability of terahertz radiation, which will in-turn unlock significant potential for new applications.

Birefringence As discussed in Section 3.7, engineerable birefringence is a highly desirable property for terahertz reflectarrays. However, this comes at the cost of reduced efficiency for the terahertz metallic resonators presented in that section, and this concern is a general one; the added demands of independently phasing two separate polarisations will invariably impact the resonator efficiency. For a higher-efficiency birefringent resonator, one might attempt to adapt the DRAs introduced in Part III, and break their radial symmetry in order to produce a birefringent response. However, such asymmetric DRAs are highly vulnerable to detrimental effects due to coupling between heterogeneous elements. Engineered birefringence is therefore challenging to realise in a DRA-based terahertz reflectarray.

Enhancing bandwidth Birefringence is advantageous because it can provide orthogonal channels, which effectively doubles the overall data rate in practical communications applications. Another approach to improving data rate is to increase the spectral bandwidth of a single channel. Flat beam-shaping devices of the sort presented in this work are inherently dispersive, for reasons including the phase-wrapping outside the bounds of a full cycle. However, there are efforts in the microwave range to address the issue of dispersion in reflectarray antennas by the use of a technique known as true-time delay phase compensation (Carrasco *et al.* 2008). For this approach, phase is not wrapped in a 2π cycle, and the phase response is engineered so as to approximate the delay that is experienced with the use of a comparable geometric optic. If similar techniques were to be scaled to terahertz frequencies, then this will potentially provide high spectral bandwidth—even relative to the high carrier frequencies employed in the terahertz range.

10.7 Concluding remarks

This project has been successful in its main aim to develop and demonstrate techniques to achieve high-efficiency beam control in the terahertz range. In particular, the reflectarray antenna presented in Chapter 7 constitutes a successful demonstration of lensing in the terahertz range with near-negligible loss. The demonstrated devices are of great practical value to support numerous fruitful applications in the terahertz range, including medical imaging, security screening, and high-volume communications over a short distance. The successful realisation of such technologies will contribute benefits public health, security, economic development, and productivity.

Appendix A

Miscellaneous relations

USEFUL mathematical descriptions, and relationships between certain relevant quantities, are provided in this appendix. Many of these relations have been used, either directly or implicitly, in the work in this thesis. Others are fundamental to ideas and techniques employed in the thesis, and have therefore been made use of indirectly. Note that the overall style of this thesis is phenomenologically descriptive, and focused upon prosaic explanations accompanied by diagrams over mathematical derivation, as it is my personal opinion that this approach is both more general, and suited to a deeper level of understanding. Nevertheless, a sound and rigorous mathematical foundation underpins all such descriptions, and hence this warrants a brief explanation.

A.1 Cartesian and polar axes

As the work presented in this thesis pertains to both near and far-field quantities, it is useful to consider the relationships between definitions for polar and Cartesian space. The position of a point, P, can be expressed in terms of both Cartesian coordinates, (x, y, z), and polar coordinates, (d, θ, ϕ). An illustration of these spatial quantities is shown in Figure A.1. The description of polar space in terms of Cartesian coordinates is as follows,

$$d = \sqrt{x^2 + y^2 + z^2}, \tag{A.1}$$

$$\theta = \cos^{-1}\left(\frac{z}{\sqrt{x^2 + y^2 + z^2}}\right), \tag{A.2}$$

$$\phi = \tan^{-1}\left(\frac{y}{x}\right). \tag{A.3}$$

Likewise, Cartesian space may be understood in terms of polar coordinates,

$$x = d \sin\theta \cos\phi, \tag{A.4}$$

$$y = d \sin\theta \sin\phi, \tag{A.5}$$

$$z = d \cos\theta. \tag{A.6}$$

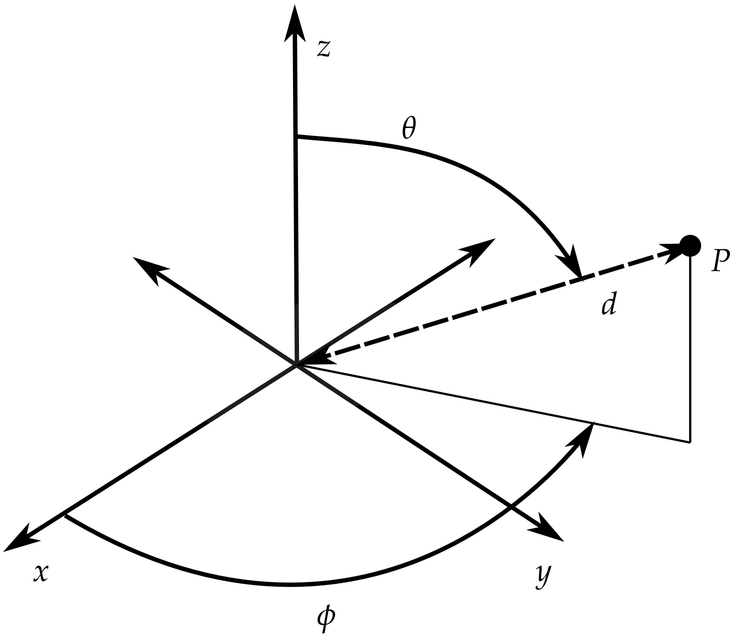

Figure A.1. Illustration of axes. Diagram describing both Cartesian and polar space.

A.2 Fundamentals of wave propagation

Maxwell's equations give a complete description of all wave phenomena in any given circumstance, provided the relevant boundary conditions are known. The standard differential form of Maxwell's equations, in a medium characterised by permittivity ϵ and permeability μ, are as follows,

$$\nabla \cdot \mathbf{E} = \frac{\rho_q}{\epsilon}, \tag{A.7}$$

$$\nabla \cdot \mathbf{H} = 0, \tag{A.8}$$

$$\nabla \times \mathbf{E} = -\mu \frac{\partial \mathbf{H}}{\partial t}, \tag{A.9}$$

$$\nabla \times \mathbf{H} = \epsilon \frac{\partial \mathbf{E}}{\partial t} + \mathbf{J}. \tag{A.10}$$

Equation A.7 makes use of charge density ρ_q, in order to describe how a certain quantity of static charge generates electric field.

The following derivation illustrates how Maxwell's equations can describe wave propagation in either free space or a dielectric medium. This derivation assumes a field source-free region, and thus ρ_q and $\mathbf{J}$ are both zero. Firstly, the curl of both sides in Equation A.9 is determined.

$$\nabla \times \nabla \times \mathbf{E} = -\mu \frac{\partial}{\partial t} \nabla \times \mathbf{H}. \tag{A.11}$$

Equation A.10 is substituted for the curl of the magnetic field, and this reduces to,

$$\nabla(\nabla \cdot \mathbf{E}) - \nabla^2 \mathbf{E} = -\mu\epsilon \frac{\partial^2 \mathbf{E}}{\partial t^2}. \tag{A.12}$$

This medium encloses no net charge, and hence Equation A.7 becomes $\nabla \cdot \mathbf{E} = 0$, and the above reduces to,

$$\nabla^2 \mathbf{E} - \mu\epsilon \frac{\partial^2 \mathbf{E}}{\partial t^2} = 0. \tag{A.13}$$

Similar rationale applies for the magnetic field component,

$$\nabla^2 \mathbf{H} - \mu\epsilon \frac{\partial^2 \mathbf{H}}{\partial t^2} = 0. \tag{A.14}$$

Differential equations of this form are well-known as wave equations. In one particular case of interest, the electric field vector is oriented in the x direction, and the magnetic field is in the y direction, exclusively. Furthermore, both fields are uniform in the x

and y-directions, varying only in the z-direction, and hence this is now a pair of one-dimensional wave equations, where it is noted that $v_p = 1/\sqrt{\epsilon\mu}$,

$$\frac{\partial^2 \mathbf{E}}{\partial z^2} = \frac{1}{v_p^2}\frac{\partial^2 \mathbf{E}}{\partial t^2}, \tag{A.15}$$

$$\frac{\partial^2 \mathbf{H}}{\partial z^2} = \frac{1}{v_p^2}\frac{\partial^2 \mathbf{H}}{\partial t^2}. \tag{A.16}$$

It can be shown that the solutions of these partial differential equations take the form of a sinusoid that varies in both spatial and temporal dimensions,

$$\mathbf{E}(z,t) = \hat{\mathbf{x}}\left(E^+\cos(\omega t - kz) + E^-\cos(\omega t + kz)\right), \tag{A.17}$$

$$\mathbf{H}(z,t) = \hat{\mathbf{y}}(H^+\cos(\omega t - kz) + H^-\cos(\omega t + kz)). \tag{A.18}$$

In this case, the superscripts indicate the direction in which the wave is travelling; a positive superscript represents motion toward the positive-z direction, whereas the negative superscript is in the contrary direction. Essentially, the notion of ‘travelling’ indicates that, as time progresses, the shape of the function does not change, but rather it is displaced along the z-axis. Thus, wave propagation can be understood as a natural consequence of the interrelation of electric and magnetic fields, as described by Maxwell’s equations.

A.3 Properties of homogeneous, isotropic media

When treated as a phasor, the amplitude and phase of a wave that is propagating in an isotropic, homogeneous medium can be described in terms of its initial value and the distance travelled,

$$\mathbf{E}(z) = \mathbf{E}(0)\exp(-\gamma z), \tag{A.19}$$

where it is assumed that propagation is in the z-direction, and γ is the complex propagation constant, which is defined in terms of absorption coefficient and wavenumber as,

$$\gamma = \alpha + jk. \tag{A.20}$$

It can be seen that α is associated with exponential decay of field amplitude, and k determines the phase of the resulting wave. These values can be related to the physical properties of the relevant medium. Firstly, the real-valued wavenumber k is defined in terms of an in-medium wavelength, which is in-turn defined by the real component of complex refractive index, n, of the medium,

$$k = \frac{2\pi}{\lambda} = \frac{2\pi n}{\lambda_0}. \tag{A.21}$$

Similarly, the attenuation coefficient is related to the imaginary component of the refractive index of the medium, κ,

$$\alpha = \frac{4\pi\kappa}{\lambda_0}. \tag{A.22}$$

Materials may also be characterised in terms of their complex relative permittivity, with real and imaginary components ϵ_{r} and ϵ_{i} respectively. Note that, unless specified, any mention of relative permittivity in this doctoral thesis refers to the real component exclusively. It is quite straightforward to convert between the complex dielectric constant and the aforementioned optical constants n and κ,

$$\epsilon_{\mathrm{r}} = n^2 - \kappa^2 \tag{A.23}$$

$$\epsilon_{\mathrm{i}} = 2n\kappa \tag{A.24}$$

The dielectric loss tangent, $\tan\delta$, is employed as a metric to quantify the degree to which a given dielectric is lossy. It is defined as the ratio of the imaginary to the real component of the relative permittivity of a dielectric,

$$\tan\delta = \frac{\epsilon_{\mathrm{i}}}{\epsilon_{\mathrm{r}}}. \tag{A.25}$$

A.4 Drude model

A Drude model (Drude 1900) can be employed to estimate the frequency-dependent complex relative permittivity of a medium ϵ_{c}, as a function of the plasma frequency, f_{p}, scattering relaxation time, τ_{s}, and high-frequency real relative permittivity, ϵ_∞, of the relevant medium,

$$\epsilon_{\mathrm{c}}(f) = \epsilon_\infty - \frac{f_{\mathrm{p}}^2}{f^2 + j\frac{f}{\tau_{\mathrm{s}}}}. \tag{A.26}$$

A brief explanation of the physical significance of these aforementioned quantities is warranted. The Drude model is fundamentally established upon a kinetic theory governing the dynamics of charge carriers. Inside a metal, valency electrons move about freely between the positively-charged ions, which are considered immobile in this model as they are so much more massive than the electrons. The electrons undergo repeated collisions with the ions, and the scattering relaxation time, τ_s, is the average time interval between such collisions, for a given electron. A shorter scattering relaxation time will therefore lead to an increase in material resistivity, as more kinetic energy is expended in electron-ion collisions. With time-varying (i.e. non-DC) electric current in a metal, the charge carriers require time to accelerate in response to a change in electrical field. Electric current therefore lags applied electric field, which results in a decrease in magnitude, and the existence of a complex component, in the electrical conductivity. This is the cause of the well-known fact that, as frequency increases, metals exhibit a decrease in conductivity to the point where they behave as lossy dielectrics in the optical range (Zou *et al.* 2014b). The plasma frequency is the frequency of oscillation at which this crossover occurs; an impinging electromagnetic wave oscillating below f_p will be evanescent, and will not propagate, whereas incident waves above this frequency will transmit some energy into a propagating wave in the medium. In the limit as frequency of oscillation tends towards infinity, the metal will behave as an ideal dielectric due to the decrease in conductivity. The relative permittivity will therefore be purely real, and the value of this permittivity is ϵ_∞.

Appendix B

Full-wave simulations

THE design procedures employed for this doctoral thesis make prolific use of full-wave simulation tools, and in particular, unit cell analysis. This is because of the generality of these techniques, as well as their innate applicability to arrayed structures such as reflectarrays and transmitarrays. A brief summary of relevant aspects of full-wave simulations is given in this appendix.

B.1 General concept

A full-wave simulation tool is a software package that is, in principle, capable of analysing the interaction of electromagnetic radiation with any finite-volume structure. This structure must be enclosed within a bounding box, as shown in Figure B.1(a), which contains some surrounding medium, which is most likely a vacuum. Computers deal with discrete quantities exclusively, meaning a computer is not capable of performing computations over a continuous domain. The three-dimensional structure must therefore be discretised, in a process known as meshing, which consists of dividing the finite-volume structure (and bounding box) into smaller polyhedra. The process of constructing a tetrahedral mesh is represented in Figures B.1(b,c). Having generated this mesh, the relevant electromagnetic field quantities—namely electric field, magnetic field, and current vector for a finite-conductivity medium—are computed in accordance with Maxwell's equations, where it is assumed that they are uniform over the domain defined by a given tetrahedron. The required density of tetrahedra depends on the degree of field confinement within the structure, and this is influenced by the particular field-matter interaction that takes place, which is not known explicitly prior to simulation. For this reason, an adaptive meshing process is often required, in which estimates of field behaviour are employed to refine the mesh, prior to the re-evaluation of the aforementioned estimates.

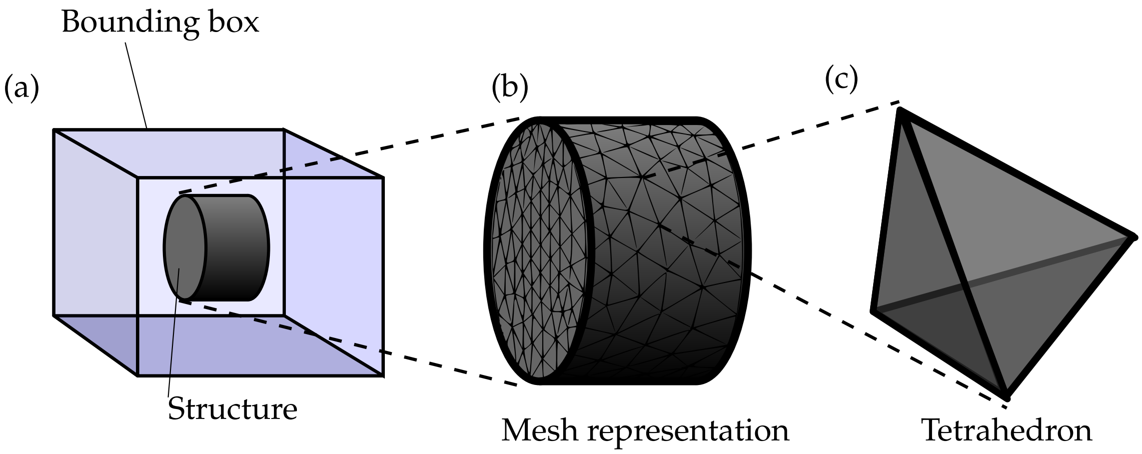

Figure B.1. Simulation and meshing. Illustration of core principles of full-wave simulations, showing (a) a defined structure, enclosed within a bounding box, (b) the mesh representation of that structure, and (c) a single tetrahedron of that mesh.

B.2 Boundary conditions

The space external to the bounding box is not explicitly defined, and hence boundary conditions are required that determine the impact of all external space upon the structure, in order to evaluate the field behaviour within the defined volume. There are numerous choices available; perfect electrical conductor, perfect magnetic conductor, open boundary condition (i.e. incident fields are absorbed), or a combination of these for the different faces. In the case of the simulations employed in Chapters 4 to 7, as well as Chapter 9, a different choice known as unit-cell boundary conditions are employed for four of the six faces of the bounding box. These boundary conditions treat the structure as a single element in an infinite array of identical structures. However, it is stated above that the structure to be simulated must be finite in volume, and hence the infinite array cannot be directly simulated. Rather, the single bounding box is simulated, and in order to achieve virtual periodicity, the distributions of electrical and magnetic fields at opposite faces are made identical. Fields that emanate from the bounding box via face B appear at face A, and vice-versa. This likewise occurs with the pair of faces C and D. In this way, it is equivalent to having an identical neighbour on all sides, and this is illustrated in Figure B.2. Such tools are essential to reliably simulate large-scale arrays of periodic or quasi-periodic structures.

For unit-cell analysis, excitation takes the form of a plane wave that impinges upon the structure. In a bounded structure, the plane wave is simulated by ports at the

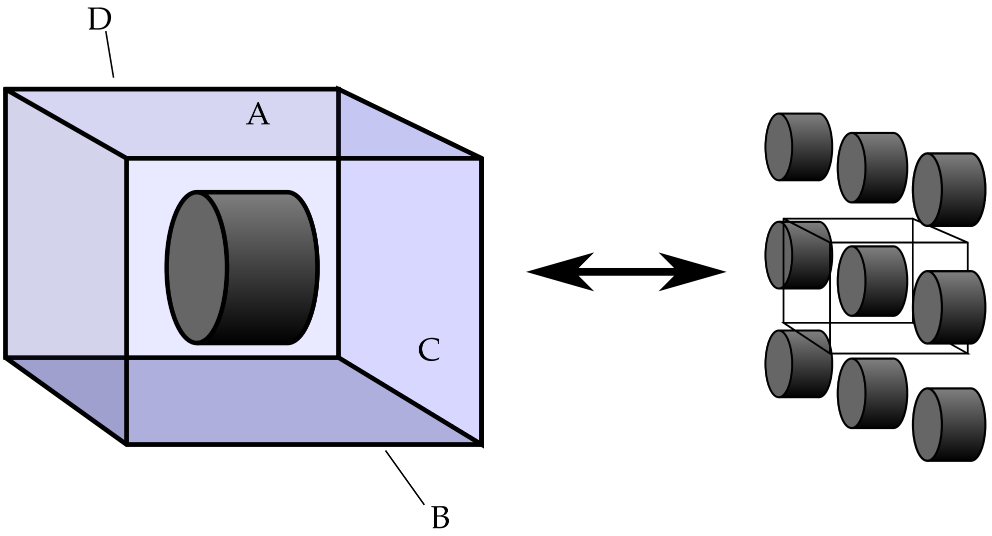

Figure B.2. Unit-cell analysis. A depiction of full-wave analysis, showing how the association of opposite faces (i.e. A to B and C to D) is equivalent to having neighbouring elements on all sides.

non-unit-cell faces, as shown in Figure B.3. As well as providing excitation, ports are capable of accepting outgoing radiation. Indeed, all energy input from the excited port is accounted for, either via absorption by another port, by the same port, or by dissipation in the structure itself. Scattering parameters, namely reflection (S_{11}) and transmission (S_{21}), are evaluated based on the amount of power absorbed by each port.

B.3 Port de-embedding

As the port absorbs incident radiation, a port placed too close to the structure may absorb fields that are in the process of interacting with the structure itself. This is because reactive fields, including modes of resonance, can exist a short distance away from the associated structure. This phenomenon has the capacity to cause erroneous alteration to the interaction of electromagnetic field with the structure, leading to spurious results. In order to mitigate this effect, good practice is to employ a bounding box that places at least a wavelength between the structure and the port. A consequence of this distance is that the calculated scattering parameters will incorporate a delay, which is evidenced in the phase response, due to the propagation between the port and the structure. This may not be desired, especially with regards to unit cell structures intended for beam control as in this present thesis, as it is of interest to evaluate the

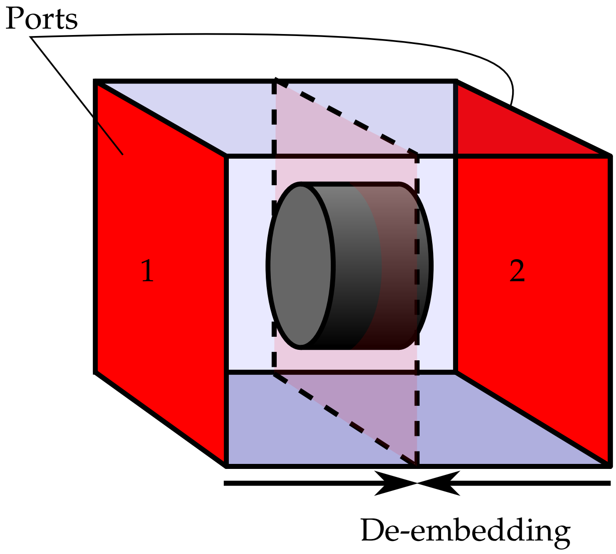

Figure B.3. Port de-embedding. Illustration of the ports that are employed to provide excitation and calculate scattering parameters, where both ports are de-embedded to the same point in order to remove the effect of optical path length.

phase response of the structure itself, without additional contributions from the propagation path. Port de-embedding can be employed to remove these contributions. This is a post-processing technique whereby the position of the port is virtually moved, by compensation of the phase response. That is to say, the details of the full-wave simulation itself are unchanged, but a certain quantity is added to (or subtracted from) the phase response so as to be equivalent to moving the port by a finite distance, in accordance with Equation 2.9. It is possible to use this technique to isolate the response of the structure itself. In the case of the two-port simulation illustrated in Figure B.3, both ports are de-embedded to the same point in the middle of the structure in question. In the absence of any structure, this is equivalent to a zero-length path. Thus, the response observed in the scattering parameters after having performed this procedure are contributed by the structure exclusively.

Appendix C

THz-TDS systems

ALL terahertz-range experiments presented in this thesis were performed using THz-TDS. Given that this work is so clearly dependent upon this technology, some explanation of THz-TDS is warranted. This appendix gives a brief summary of THz-TDS, including an overview of the principles of operation, and how it is used in in this doctoral project in particular.

C.1 Terahertz time-domain spectroscopy

Terahertz time-domain spectroscopy (THz-TDS) is a technique whereby a terahertz-range pulse can be generated and subsequently employed to characterise the broadband response of a given sample. This pulsed signal is generated photo-electrically, making use of a device known as a photoconductive antenna (PCA), which is illustrated in Figure C.1. A PCA essentially consists of a semiconductor that is biased by a strong DC field. An incident infrared laser pulse excites free carriers in the semiconductor material, which are subsequently accelerated in the direction of one of the electrodes by the aforementioned DC field. It is well-known that the acceleration of charge produces electromagnetic radiation, which in this case is within the terahertz range. Thus, a broadband, terahertz-range pulse is radiated from the PCA in response to the optical excitation.

In order to make use of this pulse for characterisation purposes, a corresponding detector PCA is employed. This second PCA is similarly excited by an optical-range pulse, but rather than impose a DC bias upon this PCA as in the case of the transmitter, the movement of the free carriers is provided by the incident terahertz field itself. The

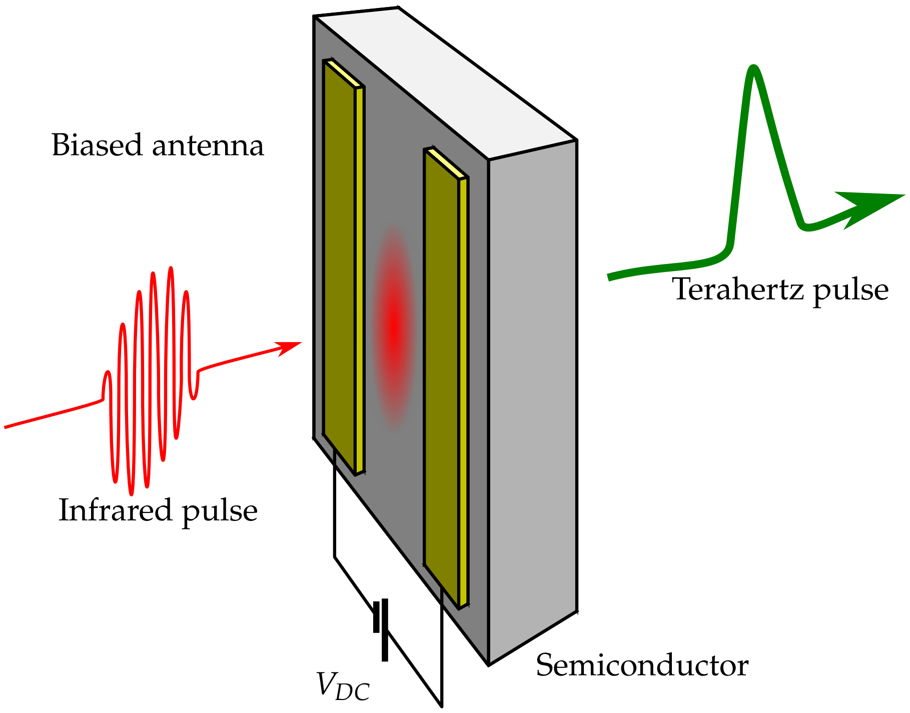

Figure C.1. Photoconductive antenna. Diagram of a photoconductive antenna operating as an emitter, illustrating the biased semiconductor junction and the conversion of optical to terahertz power.

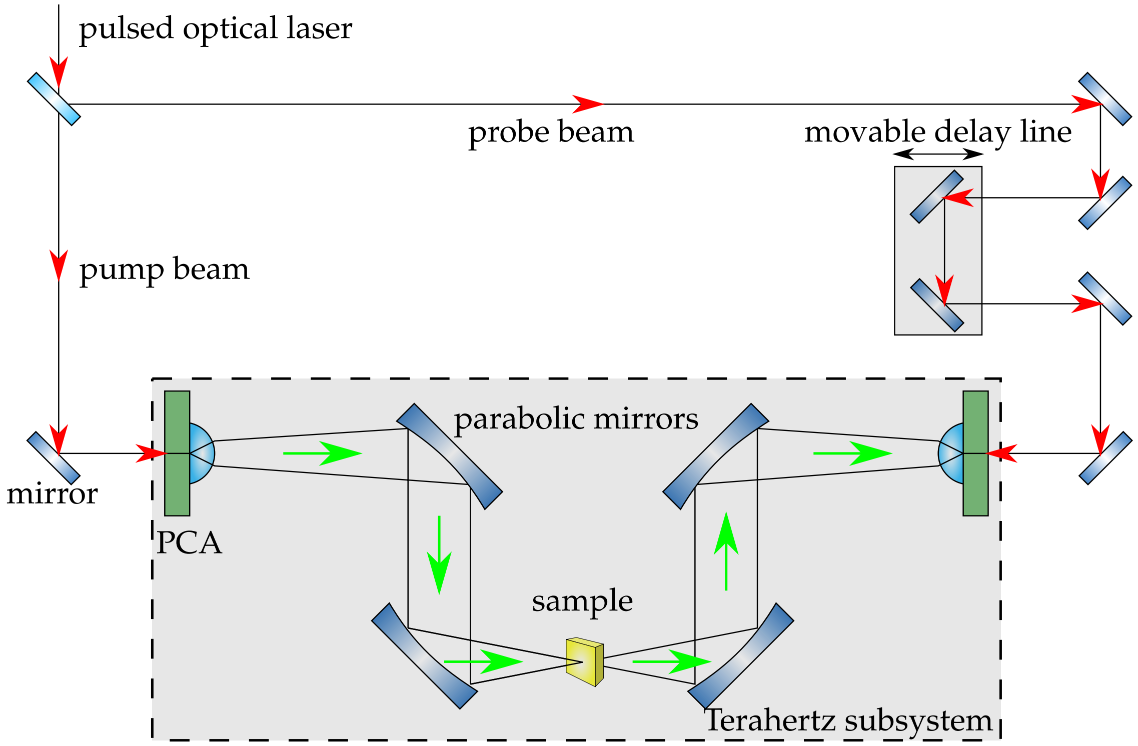

Figure C.2. THz-TDS system. Schematic illustration of a typical terahertz time-domain spectroscopy system, showing the propagation of both the infrared and terahertz beams. Note this particular setup makes use of four parabolic mirrors in order to control the terahertz radiation, but there is significant freedom when selecting a means to shape and guide the terahertz waves.

terahertz field at the precise moment of infrared-excitation causes the free carriers to migrate towards the electrodes, and this is measured at the output terminals as a voltage. Thus, two pulsed infrared beams are required; one for the excitation of the emitter (pump beam), and one for the detector (probe beam). The relative delay between the pump and probe beams dictates the specific point in the time domain of the terahertz pulse at which the incident field is to be measured, and hence the full pulse can be determined by means of a movable delay line in the path of the probe beam. Thereafter, signals-processing techniques are employed in order to extract frequency-domain quantities from the time-domain pulse. A THz-TDS system of this sort is illustrated in Figure C.2. Such systems were originally developed late in the 20th century (Van Exter *et al.* 1989a).

Early THz-TDS systems made use of free-space infrared beams to provide the excitation of the PCAs. Thus, the PCAs must remain fixed in position so as to maintain

Figure C.3. Fibre-coupled THz-TDS system. An example of a commercially-available fibre-coupled terahertz time-domain spectroscopy system, by Menlo Systems (Menlo Systems 2017).

adequate alignment with the incident infrared beam. More recently, however, optical fibre-coupled THz-TDS systems have been developed, for which each PCA is fed directly by an optical fibre. For such a system, the PCAs can move freely, without altering the nature of the infrared excitation in any way, as the path length and alignment within the fibre is unchanged. A fibre-coupled THz-TDS system will typically enclose the infrared-range components within a sealed metal box, as shown in Figure C.3. This is because the specific operation of these components is of little interest to investigations pertaining to terahertz radiation exclusively. For this reason, these systems have seen widespread adoption in terahertz research across the world, as that which previously required in-depth knowledge about laser-based optical systems is now a commercially-available, off-the-shelf device.

C.2 Automated scanning

As the PCA is free to move in a fibre-coupled THz-TDS system, it is possible to scan the position of this PCA so as to evaluate spatially-dependent terahertz field quantities. For instance, radiation pattern or radar cross-section can be evaluated by rotating a detector around a given sample, in what is known as a goniometric scan, as illustrated in Figure C.4. Alternatively, the field distribution in a given plane can be captured by scanning the detector progressively through Cartesian space, in a process known as raster-scanning, which is illustrated in Figure C.5. Both cases are examples of a cyclic

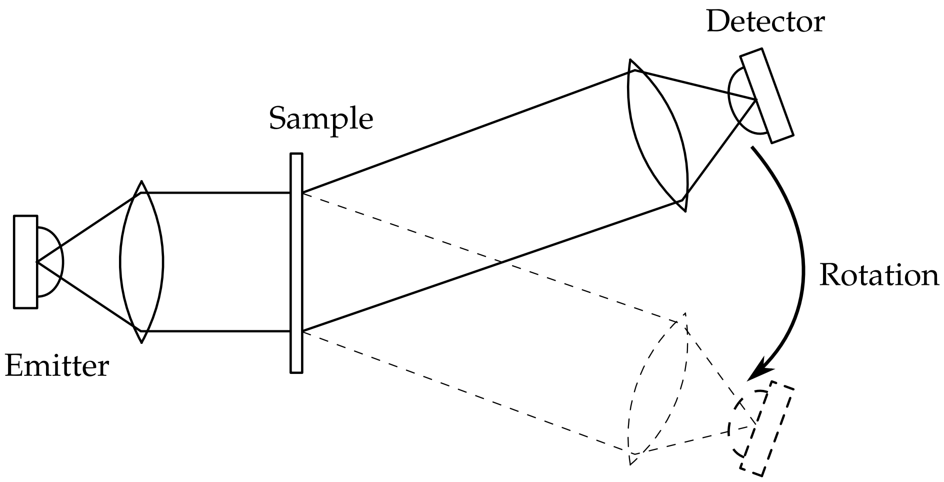

Figure C.4. Goniometer. Schematic illustration of a terahertz goniometric experimental setup, where the detector is able to rotate, at a fixed distance, around the sample in question, in order to evaluate the power projected into different in-plane directions.

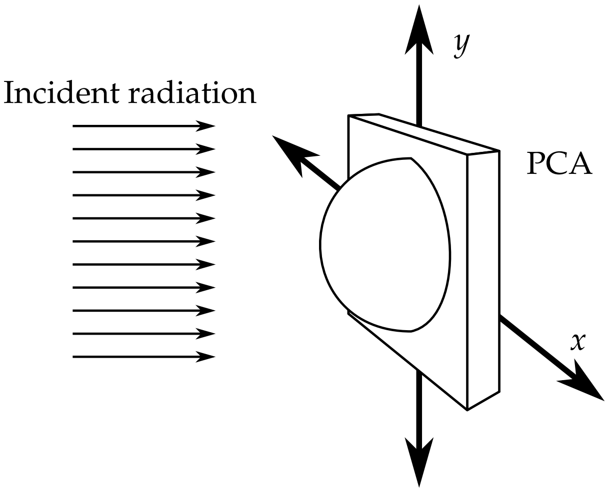

Figure C.5. Raster scanner. Illustration of a raster-scanning measurement in order to image the field distribution in a given plane. The PCA is movable in both the x- and y-dimensions.

process that alternates between moving the relevant PCA and acquiring the terahertz-range pulse. For the purposes of the investigations presented in this thesis, this process is automated using computer-controlled motorised stages. A conceptual overview of the data flow in this custom-made system design is presented in Figure C.6; the THz-TDS system takes a measurement, and subsequently passes a message to the mechanical actuation portion of the system, which steps the relevant stage, and returns control to the THz-TDS system. This process is repeated until the required range of motion is covered.

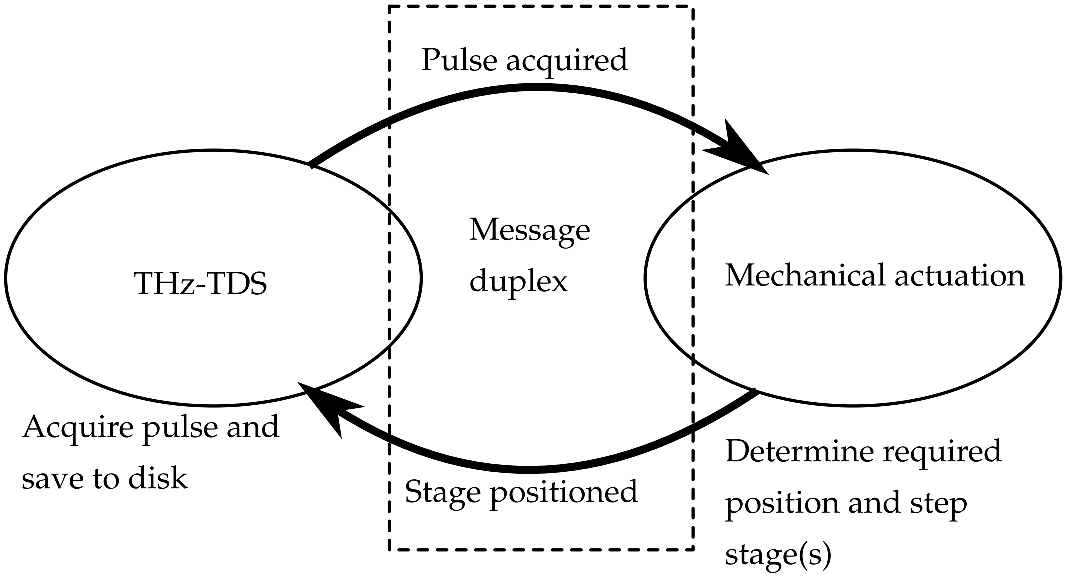

Figure C.6. Automated-scan duplex. A simplified illustration of the general algorithmic design of a given automated terahertz scanning system, consisting of a THz-TDS module and a mechanical actuation module

For the particular automated scanning system that is developed for this doctoral project, the relevant fibre-coupled THz-TDS system employed is the Terascan K15, by Menlo Systems (Menlo Systems 2017), which is shown in Figure C.3. Both a goniometric setup and a raster scanner are devised. The goniometer makes use of a Thorlabs NR360S NanoRotator stage for precise angular actuation (Thorlabs 2017), and the raster scanner makes use of a pair of Newport LTA-HS linear actuators (Newport 2017b) coupled to 443 translation stages (Newport 2017a) for two-dimensional control. A photograph of a raster-scanning setup of this sort is given in Figure C.7, which was employed for the study given in Chapter 8.

The goniometer was not deployed in any of the contributions presented in this thesis, but it was made use of for a related publication of a beam-deflecting terahertz reflectarray (Niu *et al.* 2015). On the other hand, the raster scanner was made use of for all beam control devices reported in this thesis; in Chapter 5, and Chapters 7 to 9. Prior to the development of the automated scanner, goniometric measurements had made use of manual actuation of a rotational stage (Niu *et al.* 2013, Niu *et al.* 2014b). This is because there is only one parameter to step, namely angle, and hence it is possible, if undesirable, to carry this measurement out manually. However, a raster-scanner has two axes to step, and hence the number of steps exhibits square-dependence upon the scanning resolution. Put simply, it is not practical to perform such a measurement manually.

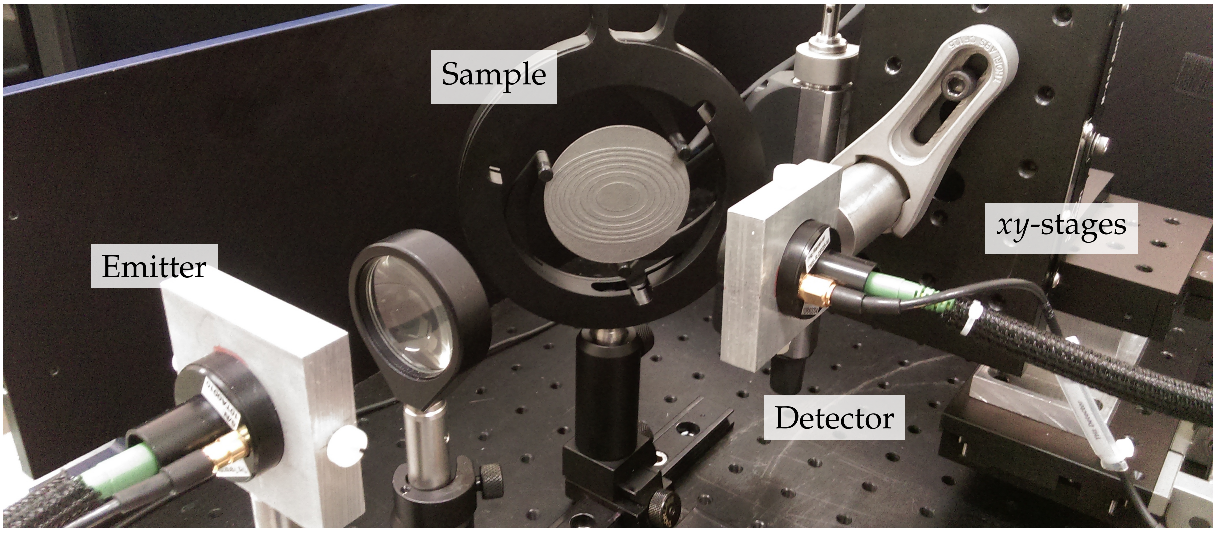

Figure C.7. Example of raster-scanning setup. Photograph of a practical raster-scanning THz-TDS setup, which in this case was employed to characterise the binary-phased terahertz zone plate presented in Chapter 8, where various components of the THz-TDS setup are annotated.

In this way, the development of automated scanning tools such as this makes measurements that were previously been inaccessible relatively straightforward. Thus, the development of the automated scanner expands the capability of the relevant laboratory in terms of the sorts of measurements that are readily available, and hence there is a greater degree of freedom in terms of the specific investigations that may be undertaken.

Bibliography

ABBOTT-D., AND ZHANG-X.-C. (2007). T-ray imaging, sensing, and retection, *Proceedings of the IEEE*, **95**(8), pp. 1509–1513.

AHMADI-A., GHADARGHADR-S., AND MOSALLAEI-H. (2010). An optical reflectarray nanoantenna: The concept and design, *Optics Express*, **18**(1), pp. 123–133.

AL-NAIB-I., SHARMA-G., DIGNAM-M. M., HAFEZ-H., IBRAHIM-A., COOKE-D. G., OZAKI-T., AND MORANDOTTI-R. (2013). Effect of local field enhancement on the nonlinear terahertz response of a silicon-based metamaterial, *Physical Review B*, **88**(19), art. no. 195203.

ANZALONE-G. C., ZHANG-C., WIJNEN-B., SANDERS-P. G., AND PEARCE-J. M. (2013). A low-cost open-source metal 3-D printer, *IEEE Access*, **1**, pp. 803–810.

ARMSTRONG-J. (2009). OFDM for optical communications, *Journal of Lightwave technology*, **27**(3), pp. 189–204.

ARNON-S. (2015). *Visible Light Communication*, Cambridge University Press.

AZHAR-A. H., TRAN-T.-A., AND O'BRIEN-D. (2013). A gigabit/s indoor wireless transmission using MIMO-OFDM visible-light communications, *IEEE Photonics Technology Letters*, **25**(2), pp. 171–174.

AZNABET-M., NAVARRO-CIA-M., KUZNETSOV-S., GELFAND-A., FEDORININA-N., GONCHAROV-Y. G., BERUETE-M., EL MRABET-O., AND SOROLLA-M. (2008). Polypropylene-substrate-based srr-and csrr-metasurfaces for submillimeter waves, *Optics Express*, **16**(22), pp. 18312–18319.

BALAKRISHNAN-J., FISCHER-B. M., AND ABBOTT-D. (2009). Sensing the hygroscopicity of polymer and copolymer materials using terahertz time-domain spectroscopy, *Applied Optics*, **48**(12), pp. 2262–2266.

BALANIS-C. A. (2016). *Antenna Theory: Analysis and Design*, John Wiley & Sons.

BANERJEE-D., VON SPIEGEL-W., THOMSON-M., SCHABEL-S., AND ROSKOS-H. (2008). Diagnosing water content in paper by terahertz radiation, *Optics Express*, **16**(12), pp. 9060–9066.

BARRY-J. R. (2012). *Wireless Infrared Communications*, Vol. 280, Springer Science & Business Media.

BAUERSCHMIDT-S., DÖHLER-G., LU-H., GOSSARD-A., MALZER-S., AND PREU-S. (2013). Arrayed free space continuous-wave terahertz photomixers, *Optics Letters*, **38**(18), pp. 3673–3676.

BERDEL-K., RIVAS-J. G., BOLÍVAR-P. H., DE MAAGT-P., AND KURZ-H. (2005). Temperature dependence of the permittivity and loss tangent of high-permittivity materials at terahertz frequencies, *IEEE Transactions on Microwave Theory and Techniques*, **53**(4), pp. 1266–1271.

BERMAN-B. (2012). 3-D printing: The new industrial revolution, *Business Horizons*, **55**(2), pp. 155–162.

BERRY-D., MALECH-R., AND KENNEDY-W. (1963). The reflectarray antenna, *IEEE Transactions on Antennas and Propagation*, **11**(6), pp. 645–651.

BLOMAARD-R., AND BISKOP-J. (2015). 3D inkjet printing of optics, *NIP & Digital Fabrication Conference*, Vol. 2015, Society for Imaging Science and Technology, Portland, USA, pp. 39–41.

BLU-RAY DISC ASSOCIATION. (2012). White paper blu-ray disc^{TM} format–general.

BOGAERTS-W., DUMON-P., LAMBERT-E., FIERS-M., PATHAK-S., AND RIBEIRO-A. (2012). IPKISS: A parametric design and simulation framework for silicon photonics, *Proceedings of the IEEE International Conference on Group IV Photonics*, San Diego, USA, pp. 30–32.

BRANDL-E., HECKENBERGER-U., HOLZINGER-V., AND BUCHBINDER-D. (2012). Additive manufactured AlSi10Mg samples using selective laser melting (SLM): Microstructure, high cycle fatigue, and fracture behavior, *Materials & Design*, **34**, pp. 159–169.

BREMEN-S., MEINERS-W., AND DIATLOV-A. (2012). Selective laser melting, *Laser Technik Journal*, **9**(2), pp. 33–38.

BUSCH-S. F., WEIDENBACH-M., BALZER-J. C., AND KOCH-M. (2015). THz optics 3D printed with TOPAS, *Journal of Infrared, Millimeter, and Terahertz Waves*, **37**, pp. 303–307.

BUSCH-S., SCHERGER-B., SCHELLER-M., AND KOCH-M. (2012). Optically controlled terahertz beam steering and imaging, *Optics Letters*, **37**(8), pp. 1391–1393.

BUSCH-S., WEIDENBACH-M., FEY-M., SCHÄFER-F., PROBST-T., AND KOCH-M. (2014). Optical properties of 3D printable plastics in the THz regime and their application for 3D printed THz optics, *Journal of Infrared, Millimeter, and Terahertz Waves*, **35**(12), pp. 993–997.

CAMBLOR-DIAZ-R., VER-HOEYE-S., VAZQUEZ-ANTUNA-C., HOTOPAN-G. R., FERNANDEZ-GARCIA-M., AND LAS HERAS ANDRES-F. (2012). Sub-millimeter wave frequency scanning 8×1 antenna array, *Progress In Electromagnetics Research*, **132**, pp. 215–232.

CARRASCO-E., BARBA-M., AND ENCINAR-J. A. (2012). X-band reflectarray antenna with switching-beam using pin diodes and gathered elements, *IEEE Transactions on Antennas and Propagation*, **60**(12), pp. 5700–5708.

CARRASCO-E., BARBA-M., ENCINAR-J. A., ARREBOLA-M., ROSSI-F., AND FRENI-A. (2013). Design, manufacture and test of a low-cost shaped-beam reflectarray using a single layer of varying-sized printed dipoles, *IEEE Transactions on Antennas and Propagation*, **61**(6), pp. 3077–3085.

CARRASCO-E., ENCINAR-J. A., AND BARBA-M. (2008). Bandwidth improvement in large reflectarrays by using true-time delay, *IEEE Transactions on Antennas and Propagation*, **56**(8), pp. 2496–2503.

CHAMBERLAIN-J. (2004). Where optics meets electronics: Recent progress in decreasing the terahertz gap, *Philosophical Transactions of the Royal Society of London A: Mathematical, Physical and Engineering Sciences*, **362**(1815), pp. 199–213.

CHANG-C.-C., HEADLAND-D., ABBOTT-D., WITHAYACHUMNANKUL-W., AND CHEN-H.-T. (2017). Demonstration of a highly efficient terahertz flat lens employing tri-layer metasurfaces, *Optics Letters*, **42**(9), pp. 1867–1890.

CHANG-M. J., ABICHAR-Z., AND HSU-C.-Y. (2010). WiMAX or LTE: Who will lead the broadband mobile internet?, *IT Professional Magazine*, **12**(3), pp. 26–32.

CHENG-Y. Z., WITHAYACHUMNANKUL-W., UPADHYAY-A., HEADLAND-D., NIE-Y., GONG-R. Z., BHASKARAN-M., SRIRAM-S., AND ABBOTT-D. (2014). Ultrabroadband reflective polarization convertor for terahertz waves, *Applied Physics Letters*, **105**(18), art. no. 181111.

CHENG-Y. Z., WITHAYACHUMNANKUL-W., UPADHYAY-A., HEADLAND-D., NIE-Y., GONG-R. Z., BHASKARAN-M., SRIRAM-S., AND ABBOTT-D. (2015). Ultrabroadband plasmonic absorber for terahertz waves, *Advanced Optical Materials*, **3**(3), pp. 376–380.

CHEN-H.-T., PADILLA-W. J., ZIDE-J. M., GOSSARD-A. C., TAYLOR-A. J., AND AVERITT-R. D. (2006). Active terahertz metamaterial devices, *Nature*, **444**(7119), pp. 597–600.

CHENOWETH-K., CHEUNG-S., VAN DUIN-A. C., GODDARD-W. A., AND KOBER-E. M. (2005). Simulations on the thermal decomposition of a poly (dimethylsiloxane) polymer using the ReaxFF reactive force field, *Journal of the American Chemical Society*, **127**(19), pp. 7192–7202.

CHERNOMYRDIN-N. V., FROLOV-M. E., LEBEDEV-S. P., RESHETOV-I. V., SPEKTOR-I. E., TOLSTOGUZOV-V. L., KARASIK-V. E., KHOROKHOROV-A. M., KOSHELEV-K. I., SCHADKO-A. O., YURCHENKO-S. O., AND ZAYTSEV-K. I. (2017). Wide-aperture aspherical lens for high-resolution terahertz imaging, *Review of Scientific Instruments*, **88**(1), art. no. 014703.

CHEUNG-K., AND AUSTON-D. (1986). A novel technique for measuring far-infrared absorption and dispersion, *Infrared physics*, **26**(1), pp. 23–27.

CHOY-T. C. (2015). *Effective Medium Theory: Principles and Applications*, Vol. 165, Oxford University Press.

CISCO. (2016). Cisco visual networking index: Global mobile data traffic forecast update, 2015–2020.

CIURYŁO-R., JAWORSKI-R., JURKOWSKI-J., PINE-A., AND SZUDY-J. (2001). Spectral line shapes modeled by a quadratic speed-dependent Galatry profile, *Physical Review A*, **63**(3), art. no. 032507.

COOPER-K. B., DENGLER-R. J., LLOMBART-N., BRYLLERT-T., CHATTOPADHYAY-G., SCHLECHT-E., GILL-J., LEE-C., SKALARE-A., MEHDI-I., AND SIEGEL-P. H. (2008). Penetrating 3-D imaging at 4-and 25-m range using a submillimeter-wave radar, *IEEE Transactions on Microwave Theory and Techniques*, **56**(12), pp. 2771–2778.

COOPER-K. B., DENGLER-R. J., LLOMBART-N., THOMAS-B., CHATTOPADHYAY-G., AND SIEGEL-P. H. (2011). THz imaging radar for standoff personnel screening, *IEEE Transactions on Terahertz Science and Technology*, **1**(1), pp. 169–182.

CUNNINGHAM-P. D., VALDES-N. N., VALLEJO-F. A., HAYDEN-L. M., POLISHAK-B., ZHOU-X.-H., LUO-J., JEN-A. K.-Y., WILLIAMS-J. C., AND TWIEG-R. J. (2011). Broadband terahertz characterization of the refractive index and absorption of some important polymeric and organic electro-optic materials, *Journal of Applied Physics*, **109**(4), art. no. 043505.

DAI-J., ZHANG-J., ZHANG-W., AND GRISCHKOWSKY-D. (2004). Terahertz time-domain spectroscopy characterization of the far-infrared absorption and index of refraction of high-resistivity, float-zone silicon, *Journal of the Optical Society of America B*, **21**(7), pp. 1379–1386.

DAVIES-A. G., BURNETT-A. D., FAN-W., LINFIELD-E. H., AND CUNNINGHAM-J. E. (2008). Terahertz spectroscopy of explosives and drugs, *Materials Today*, **11**(3), pp. 18–26.

DELBRIDGE-A. (2001). *The Macquarie Dictionary*, 3rd edn, The Macquarie Library, North Ryde, NSW, Australia.

DIKMELIK-Y., SPICER-J. B., FITCH-M. J., AND OSIANDER-R. (2006). Effects of surface roughness on reflection spectra obtained by terahertz time-domain spectroscopy, *Optics Letters*, **31**(24), pp. 3653–3655, DOI: 10.1364/OL.31.003653.

DRUDE-P. (1900). Zur Elektronentheorie der Metalle, *Annalen der Physik*, **306**(3), pp. 566–613.

DUAN-D.-W., AND RAHMAT-SAMII-Y. (1995). A generalized diffraction synthesis technique for high performance reflector antennas, *IEEE Transactions on Antennas and Propagation*, **43**(1), pp. 27–40.

EBRAHIMI-A., NIRANTAR-S., WITHAYACHUMNANKUL-W., BHASKARAN-M., SRIRAM-S., AL-SARAWI-S. F., AND ABBOTT-D. (2015). Second-order terahertz bandpass frequency selective surface with miniaturized elements, *IEEE Transactions on Terahertz Science and Technology*, **5**(5), pp. 761–769.

EGERTON-R. F. (2005). *Physical principles of electron microscopy*, Springer.

EISELE-H., AND HADDAD-G. I. (1998). Two-terminal millimeter-wave sources, *IEEE Transactions on Microwave Theory and Techniques*, **46**(6), pp. 739–746.

ENCINAR-J. A., AND ZORNOZA-J. A. (2003). Broadband design of three-layer printed reflectarrays, *IEEE Transactions on Antennas and Propagation*, **51**(7), pp. 1662–1664.

ENCINAR-J. A., AND ZORNOZA-J. A. (2004). Three-layer printed reflectarrays for contoured beam space applications, *IEEE Transactions on Antennas and Propagation*, **52**(5), pp. 1138–1148.

ENCINAR-J. A., DATASHVILI-L. S., ZORNOZA-J. A., ARREBOLA-M., SIERRA-CASTAÑER-M., BESADA-SANMARTIN-J. L., BAIER-H., AND LEGAY-H. (2006). Dual-polarization dual-coverage reflectarray for space applications, *IEEE Transactions on Antennas and Propagation*, **54**(10), pp. 2827–2837.

FEDERICI-J., AND MOELLER-L. (2010). Review of terahertz and subterahertz wireless communications, *Journal of Applied Physics*, **107**(11), art. no. 111101.

FERESIDIS-A. P., GOUSSETIS-G., WANG-S., AND VARDAXOGLOU-J. C. (2005). Artificial magnetic conductor surfaces and their application to low-profile high-gain planar antennas, *IEEE Transactions on Antennas and Propagation*, **53**(1), pp. 209–215.

FERNANDES-E. (2015a). 3rd Generation Partnership Project; Technical Specification 25.101; User Equipment radio transmission and reception (FDD) (Release 13).

FERNANDES-E. (2015b). 3rd Generation Partnership Project; Technical Specification 36.101; (E-UTRA) UE radio transmission and reception (Release 13).

FITZGERALD-A. J., WALLACE-V. P., JIMENEZ-LINAN-M., BOBROW-L., PYE-R. J., PURUSHOTHAM-A. D., AND ARNONE-D. D. (2006). Terahertz pulsed imaging of human breast tumors, *Radiology*, **239**(2), pp. 533–540.

FRAZIER-W. E. (2014). Metal additive manufacturing: A review, *J. Mater. Eng. Perform.*, **23**(6), pp. 1917–1928.

FURLAN-W. D., FERRANDO-V., MONSORIU-J. A., ZAGRAJEK-P., CZERWIŃSKA-E., AND SZUSTAKOWSKI-M. (2016). 3D printed diffractive terahertz lenses, *Optics Letters*, **41**(8), pp. 1748–1751.

GALLERANO-G. P., DORIA-A., GERMINI-M., GIOVENALE-E., MESSINA-G., AND SPASSOVSKY-I. P. (2009). Phase-sensitive reflective imaging device in the mm-wave and terahertz regions, *Journal of Infrared, Millimeter, and Terahertz Waves*, **30**(12), pp. 1351–1361.

GARNETT-J. M. (1904). Colours in metal glasses and in metallic films, *Proceedings of the Royal Society of London*, **73**, pp. 443–445.

GEORGE-D., AND MARKELZ-A. (2012). Terahertz spectroscopy of liquids and biomolecules, *Terahertz Spectroscopy and Imaging*, Springer, pp. 229–250.

GERCHBERG-R. W., AND SAXTON-W. O. (1972). A practical algorithm for the determination of phase from image and diffraction plane pictures, *Optik*, **35**, pp. 237–246.

GILES-R. H., GATESMAN-A., FITZ-GERALD-J., FISK-S., AND WALDMAN-J. (1993). Tailoring artificial dielectric materials at terahertz frequencies, *Proceedings of the Fourth International Symposium of Space THz Technology*, Los Angeles, USA, pp. 124–133.

GOODMAN-J. W. (2005). *Introduction to Fourier Optics*, Roberts and Company Publishers.

GRADY-N. K., HEYES-J. E., CHOWDHURY-D. R., ZENG-Y., REITEN-M. T., AZAD-A. K., TAYLOR-A. J., DALVIT-D. A., AND CHEN-H.-T. (2013). Terahertz metamaterials for linear polarization conversion and anomalous refraction, *Science*, **340**(6138), pp. 1304–1307.

GRISCHKOWSKY-D., KEIDING-S., VAN EXTER-M., AND FATTINGER-C. (1990). Far-infrared time-domain spectroscopy with terahertz beams of dielectrics and semiconductors, *Journal of the Optical Society of America B*, **7**(10), pp. 2006–2015.

GROBE-L., PARASKEVOPOULOS-A., HILT-J., SCHULZ-D., LASSAK-F., HARTLIEB-F., KOTTKE-C., JUNGNICKEL-V., AND LANGER-K.-D. (2013). High-speed visible light communication systems, *IEEE Communications Magazine*, **51**(12), pp. 60–66.

GRZYB-J., HEINEMANN-B., AND PFEIFFER-U. R. (2016). A 0.55 THz near-field sensor with a µm-range lateral resolution fully integrated in 130 nm SiGe BiCMOS, *IEEE Journal of Solid-State Circuits*, **51**(12), pp. 3063–3077.

GUCLU-C., SLOAN-J., PAN-S., AND CAPOLINO-F. (2011). Direct use of the high impedance surface as an antenna without dipole on top, *IEEE Antennas and Wireless Propagation Letters*, **10**, pp. 1536–1539.

HABIBOVIC-P., GBURECK-U., DOILLON-C. J., BASSETT-D. C., VAN BLITTERSWIJK-C. A., AND BARRALET-J. E. (2008). Osteoconduction and osteoinduction of low-temperature 3D printed bioceramic implants, *Biomaterials*, **29**(7), pp. 944–953.

HALL-L. T., HANSEN-H. J., AND ABBOTT-D. (2002). Rotman lens for mm-wavelengths, *Proceedings of SPIE Smart Structures, Devices, and Systems*, Vol. 4935, International Society for Optics and Photonics, Melbourne, Australia, pp. 215–221.

HAN-D., LEE-K., LIM-J., HONG-S. S., KIM-Y. K., AND AHN-J. (2013). Terahertz lens made out of natural stone, *Applied Optics*, **52**(36), pp. 8670–8675.

HASANI-H., TAMAGNONE-M., CAPDEVILA-S., MOLDOVAN-C. F., MAODDI-P., IONESCU-A. M., PEIXEIRO-C., MOSIG-J. R., SKRIVERVIK-A. K., AND PERRUISSEAU-CARRIER-J. (2016). Tri-band, polarization-independent reflectarray at terahertz frequencies: design, fabrication, and measurement, *IEEE Transactions on Terahertz Science and Technology*, **6**(2), pp. 268–277.

HEADLAND-D., CARRASCO-E., NIRANTAR-S., WITHAYACHUMNANKUL-W., GUTRUF-P., SCHWARZ-J., ABBOTT-D., BHASKARAN-M., SRIRAM-S., PERRUISSEAU-CARRIER-J., AND FUMEAUX-C. (2016a). Dielectric resonator reflectarray as high-efficiency nonuniform terahertz metasurface, *ACS Photonics*, **3**(6), pp. 1019–1026.

HEADLAND-D., NIRANTAR-S., WITHAYACHUMNANKUL-W., GUTRUF-P., ABBOTT-D., BHASKARAN-M., FUMEAUX-C., AND SRIRAM-S. (2015a). Terahertz magnetic mirror realized with dielectric resonator antennas, *Advanced Materials*, **27**(44), pp. 7137–7144.

HEADLAND-D., NIRANTAR-S., WITHAYACHUMNANKUL-W., GUTRUF-P., ABBOTT-D., BHASKARAN-M., FUMEAUX-C., AND SRIRAM-S. (2015b). Terahertz magnetic mirror realized with dielectric resonator antennas, *Advanced Materials*, **27**(44), pp. 7137–7144, DOI: 10.1002/adma.201503069.

HEADLAND-D., NIU-T., CARRASCO-E., ABBOTT-D., SRIRAM-S., BHASKARAN-M., FUMEAUX-C., AND WITHAYACHUMNANKUL-W. (2017). Terahertz reflectarrays and nonuniform metasurfaces (invited for special issue on terahertz photonics), *IEEE Journal of Selected Topics in Quantum Electronics*, **23**(4), art. no. 8500918.

HEADLAND-D., THURGOOD-P., STAVREVSKI-D., WITHAYACHUMNANKUL-W., ABBOTT-D., BHASKARAN-M., AND SRIRAM-S. (2015c). Doped polymer for low-loss dielectric material in the terahertz range, *Optical Materials Express*, **5**(6), pp. 1373–1380.

HEADLAND-D., WITHAYACHUMNANKUL-W., WEBB-M., AND ABBOTT-D. (2013). Beam deflection lens at terahertz frequencies using a hole lattice metamaterial, *38th International Conference on Infrared, Millimeter and Terahertz Waves (IRMMW-THz)*, Mainz, Germany, DOI: 10.1109/IRMMW-THz.2013.6665703.

HEADLAND-D., WITHAYACHUMNANKUL-W., WEBB-M., EBENDORFF-HEIDEPRIEM-H., LUITEN-A., AND ABBOTT-D. (2016b). Analysis of 3D-printed metal for rapid-prototyped reflective terahertz optics, *Optics Express*, **24**(15), pp. 17384–17396.

HEADLAND-D., WITHAYACHUMNANKUL-W., WEBB-M., UPADHYAY-A., BHASKARAN-M., SRIRAM-S., AND ABBOTT-D. (2014). Dielectric hole lattice for terahertz diffractive optics with high transmission, *39th International Conference on Infrared, Millimeter, and Terahertz waves (IRMMW-THz)*, Tucson, USA, DOI: 10.1109/IRMMW-THz.2014.6956000.

HEJASE-J., PALADHI-P. R., AND CHAHAL-P. P. (2011). Terahertz characterization of dielectric substrates for component design and nondestructive evaluation of packages, *IEEE Transactions on Components Packaging Manufacturing Technology*, **1**(11), pp. 1685–1694.

HE-J., WANG-X., HU-D., YE-J., FENG-S., KAN-Q., AND ZHANG-Y. (2013). Generation and evolution of the terahertz vortex beam, *Optics Express*, **21**(17), pp. 20230–20239.

HERNANDEZ-SERRANO-A., CORZO-GARCIA-S., GARCIA-SANCHEZ-E., ALFARO-M., AND CASTRO-CAMUS-E. (2014). Quality control of leather by terahertz time domain spectroscopy, *Applied Optics*, **53**, pp. 7872–7876.

HERNANDEZ-SERRANO-A., WEIDENBACH-M., BUSCH-S., KOCH-M., AND CASTRO-CAMUS-E. (2016). Fabrication of gradient-refractive-index lenses for terahertz applications by three-dimensional printing, *Journal of the Optical Society of America B*, **33**(5), pp. 928–931.

HORVÁTH-Z. L., AND BOR-Z. (2003). Focusing of truncated Gaussian beams, *Optics Communications*, **222**(1), pp. 51–68.

HUANG-J., AND ENCINAR-J. A. (2008). *Reflectarray Antennas*, John Wiley and Sons.

HUANG-P.-P., HUANG-T.-W., WANG-H., LIN-E. W., SHU-Y., DOW-G. S., LAI-R., BIEDENBENDER-M., AND ELLIOTT-J. H. (1997). A 94-GHz 0.35-W power amplifier module, *IEEE Transactions on Microwave Theory and Techniques*, **45**(12), pp. 2418–2423.

HU-D., MORENO-G., WANG-X., HE-J., CHAHADIH-A., XIE-Z., WANG-B., AKALIN-T., AND ZHANG-Y. (2014). Dispersion characteristic of ultrathin terahertz planar lenses based on metasurface, *Optics Communications*, **322**, pp. 164–168.

HU-D., WANG-X., FENG-S., YE-J., SUN-W., KAN-Q., KLAR-P. J., AND ZHANG-Y. (2013). Ultrathin terahertz planar elements, *Advanced Optical Materials*, **1**(2), pp. 186–191.

IEEE. (1983). *Standard Definitions of Terms for Antennas*, IEEE.

ISHIGAKI-K., SHIRAISHI-M., SUZUKI-S., ASADA-M., NISHIYAMA-N., AND ARAI-S. (2012). Direct intensity modulation and wireless data transmission characteristics of terahertz-oscillating resonant tunnelling diodes, *Electronics Letters*, **48**(10), pp. 582–583.

ITU-R. (2013). 676-10 Attenuation by Atmospheric Gases.

JACKSON-J. B., BOWEN-J., WALKER-G., LABAUNE-J., MOUROU-G., MENU-M., AND FUKUNAGA-K. (2011). A survey of terahertz applications in cultural heritage conservation science, *IEEE Transactions on Terahertz Science and Technology*, **1**(1), pp. 220–231.

JACOBS-H., AND CHREPTA-M. M. (1974). Electronic phase shifter for millimeter-wave semiconductor dielectric integrated circuits, *IEEE Transactions on Microwave Theory and Techniques*, **22**(4), pp. 411–417.

JANSEN-C., WIETZKE-S., ASTLEY-V., MITTLEMAN-D. M., AND KOCH-M. (2010). Mechanically flexible polymeric compound one-dimensional photonic crystals for terahertz frequencies, *Applied Physics Letters*, **96**(11), art. no. 111108.

JIANG-X.-Y., YE-J.-S., HE-J.-W., WANG-X.-K., HU-D., FENG-S.-F., KAN-Q., AND ZHANG-Y. (2013). An ultrathin terahertz lens with axial long focal depth based on metasurfaces, *Optics Express*, **21**(24), pp. 30030–30038.

JIN-Y.-S., KIM-G.-J., AND JEON-S.-G. (2006). Terahertz dielectric properties of polymers, *Journal of the Korean Physical Society*, **49**(2), pp. 513–517.

JOHNSON-R. C., AND JASIK-H. (1984). *Antenna Engineering Handbook*, McGraw-Hill Book Company.

JOVICIC-A., LI-J., AND RICHARDSON-T. (2013). Visible light communication: Opportunities, challenges and the path to market, *IEEE Communications Magazine*, **51**(12), pp. 26–32.

JUKAM-N., AND SHERWIN-M. S. (2003). Two-dimensional terahertz photonic crystals fabricated by deep reactive ion etching in Si, *Applied Physics Letters*, **83**(1), pp. 21–23.

KANNEGULLA-A., SHAMS-M. I. B., LIU-L., AND CHENG-L.-J. (2015). Photo-induced spatial modulation of THz waves: Opportunities and limitations, *Optics Express*, **23**(25), pp. 32098–32112.

KARL-N. J., MCKINNEY-R. W., MONNAI-Y., MENDIS-R., AND MITTLEMAN-D. M. (2015). Frequency-division multiplexing in the terahertz range using a leaky-wave antenna, *Nature Photonics*, **9**, pp. 717–720.

KARL-N., REICHEL-K., CHEN-H.-T., TAYLOR-A., BRENER-I., BENZ-A., RENO-J., MENDIS-R., AND MITTLEMAN-D. (2014). An electrically driven terahertz metamaterial diffractive modulator with more than 20 dB of dynamic range, *Applied Physics Letters*, **104**(9), art. no. 091115.

KHODASEVYCH-I., SHAH-C., SRIRAM-S., BHASKARAN-M., WITHAYACHUMNANKUL-W., UNG-B., LIN-H., ROWE-W., ABBOTT-D., AND MITCHELL-A. (2012). Elastomeric silicone substrates for terahertz fishnet metamaterials, *Applied Physics Letters*, **100**(6), art. no. 061101.

KIM-D.-H., KIM-D.-S., HWANG-S., AND JANG-J.-H. (2012a). Surface relief structures for a flexible broadband terahertz absorber, *Optics Express*, **20**(15), pp. 16815–16822.

KIM-D.-S., KIM-D.-H., HWANG-S., AND JANG-J.-H. (2012b). Broadband terahertz absorber realized by self-assembled multilayer glass spheres, *Optics Express*, **20**(12), pp. 13566–13572, DOI: 10.1364/OE.20.013566.

KIM-S., UTSUNOMIYA-H., KOSKI-J., WU-B., CIMA-M., SOHN-J., MUKAI-K., GRIFFITH-L., AND VACANTI-J. (1998). Survival and function of hepatocytes on a novel three-dimensional synthetic biodegradable polymer scaffold with an intrinsic network of channels, *Annals of Surgery*, **228**(1), pp. 8–13.

KIPP-L., SKIBOWSKI-M., JOHNSON-R., BERNDT-R., ADELUNG-R., HARM-S., AND SEEMANN-R. (2001). Sharper images by focusing soft X-rays with photon sieves, *Nature*, **414**(6860), pp. 184–188.

KIRZ-J., ATTWOOD-D., HENKE-B. L., KENNEDY-K. D., KIM-K.-J., KORRIGHT-J. B., PERERA-R. C., PIANETTA-P., RIORDAN-J. C., SCHOFIELD-G. S., THOMSON-A. C., UNDERWOOD-J. H., VAUGHAN-D., WILLIAMS-G. P., AND WINIC-H. (1986). *X-ray Data Booklet*, Lawrence Berkeley Laboratory, University of California.

KITAGAWA-S., SUZUKI-S., AND ASADA-M. (2016). Wide frequency-tunable resonant tunnelling diode terahertz oscillators using varactor diodes, *Electronics Letters*, **52**(6), pp. 479–481.

KITSON-P. J., ROSNES-M. H., SANS-V., DRAGONE-V., AND CRONIN-L. (2012). Configurable 3D-printed millifluidic and microfluidic lab on a chip reactionware devices, *Lab Chip*, **12**(18), pp. 3267–3271.

KLEINE-OSTMANN-T., AND NAGATSUMA-T. (2011). A review on terahertz communications research, *Journal of Infrared, Millimeter, and Terahertz Waves*, **32**(2), pp. 143–171.

KOENIG-S., LOPEZ-DIAZ-D., ANTES-J., BOES-F., HENNEBERGER-R., LEUTHER-A., TESSMANN-A., SCHMOGROW-R., HILLERKUSS-D., PALMER-R., ZWICK-T., KOOS-C., FREUDE-W., AMBACHER-O., LEUTHOLD-J., AND KALLFASS-I. (2013). Wireless sub-THz communication system with high data rate, *Nature Photonics*, **7**(12), pp. 977–981.

KOS-A. B., AND GERECHT-E. (2013). Long-wavelength beam steerer based on a micro-electromechanical mirror, *Journal of research of the National Institute of Standards and Technology*, **118**, pp. 125–139.

KREYSZIG-E. (2007). *Advanced Engineering Mathematics*, John Wiley & Sons.

KRISTENSEN-T. T. L., WITHAYACHUMNANKUL-W., JEPSEN-P. U., AND ABBOTT-D. (2010). Modeling terahertz heating effects on water, *Optics Express*, **18**(5), pp. 4727–4739.

KROPOTOV-G., AND TSYGANKOVA-E. (2010). Tydex: Optics for THz photonics, *Vestnik Novosibirsk State Univserity. Series: Physics*.

KUZNETSOV-S. A., ASTAFEV-M. A., BERUETE-M., AND NAVARRO-CÍA-M. (2015). Planar holographic metasurfaces for terahertz focusing, *Scientific Reports*, **5**, art. no. 7738.

LADD-C., SO-J.-H., MUTH-J., AND DICKEY-M. D. (2013). 3D printing of free standing liquid metal microstructures, *Advanced Materials*, **25**(36), pp. 5081–5085.

LAMAN-N., AND GRISCHKOWSKY-D. (2008). Terahertz conductivity of thin metal films, *Applied Physics Letters*, **93**(5), art. no. 051105.

LEE-S., KIM-S., KIM-T.-T., KIM-Y., CHOI-M., LEE-S. H., KIM-J.-Y., AND MIN-B. (2012). Reversibly stretchable and tunable terahertz metamaterials with wrinkled layouts, *Advanced Materials*, **24**(26), pp. 3491–3497.

LETTINGTON-A. H., DUNN-D., ATTIA-M., AND BLANKSON-I. M. (2003). Passive millimetre-wave imaging architectures, *Journal of Optics A: Pure and Applied Optics*, **5**(4), art. no. S103.

LIU-J., MENDIS-R., AND MITTLEMAN-D. M. (2013). A Maxwell's fish eye lens for the terahertz region, *Applied Physics Letters*, **103**(3), art. no. 031104.

LIU-S., CHENG-Q., XU-Q., WANG-T. Q., DU-L. L., LUAN-K., XU-Y. H., BAO-D., FU-X. J., HAN-J. G., ZHANG-W. L., AND CUI-T. J. (2015a). Free-standing metasurfaces for high-efficiency transmitarrays for controlling terahertz waves, *Advanced Optical Materials*, **4**(3), pp. 384–390.

LIU-S., CHEN-H., AND CUI-T. J. (2015b). A broadband terahertz absorber using multi-layer stacked bars, *Applied Physics Letters*, **106**(15), art. no. 151601.

LIU-X., FAN-K., SHADRIVOV-I. V., AND PADILLA-W. J. (2017). Experimental realization of a terahertz all-dielectric metasurface absorber, *Optics Express*, **25**(1), pp. 191–201.

LIU-X., OSGOOD-R. M., VLASOV-Y. A., AND GREEN-W. M. (2010). Mid-infrared optical parametric amplifier using silicon nanophotonic waveguides, *Nature Photonics*, **4**(8), pp. 557–560.

LOMAKIN-V., FAINMAN-Y., URZHUMOV-Y., AND SHVETS-G. (2006). Doubly negative metamaterials in the near infrared and visible regimes based on thin film nanocomposites, *Optics Express*, **14**(23), pp. 11164–11177.

LONG-S. A., MCALLISTER-M. W., AND SHEN-L. C. (1983). The resonant cylindrical dielectric cavity antenna, *IEEE Transactions on Antennas and Propagation*, **31**, pp. 406–412.

LOOYENGA-H. (1965). Dielectric constants of heterogeneous mixtures, *Physica*, **31**(3), pp. 401–406.

LUCYSZYN-S. (2007). Evaluating surface impedance models for terahertz frequencies at room temperature, *Piers Online*, **3**(4), pp. 554–559.

LUUKANEN-A., APPLEBY-R., KEMP-M., AND SALMON-N. (2013). Millimeter-wave and terahertz imaging in security applications, *Terahertz Spectroscopy and Imaging*, Springer, pp. 491–520.

MAKI-K.-I., AND OTANI-C. (2008). Terahertz beam steering and frequency tuning by using the spatial dispersion of ultrafast laser pulses, *Optics Express*, **16**(14), pp. 10158–10169.

MAKI-K.-I., SHIBUYA-T., OTANI-C., SUIZU-K., AND KAWASE-K. (2009). Terahertz beam steering via tilted-phase difference-frequency mixing, *Applied Physics Express*, **2**(2), art. no. 022301.

MALAGISI-C. (1978). Microstrip disc element reflect array, *Electronics and Aerospace Systems Convention*, Vol. 1, Arlington, USA, pp. 186–192.

MARATHAY-A. S., AND MCCALMONT-J. F. (2001). Vector diffraction theory for electromagnetic waves, *Journal of the Optical Society of America A*, **18**(10), pp. 2585–2593.

MATSUURA-S., TANI-M., AND SAKAI-K. (1997). Generation of coherent terahertz radiation by photomixing in dipole photoconductive antennas, *Applied Physics Letters*, **70**(5), pp. 559–561.

MAXWELL-J. C. (1881). *A Treatise on Electricity and Magnetism*, Clarendon press.

MCKINNEY-R. W., MONNAI-Y., MENDIS-R., AND MITTLEMAN-D. (2015). Focused terahertz waves generated by a phase velocity gradient in a parallel-plate waveguide, *Optics Express*, **23**(21), pp. 27947–27952.

MENDIS-R., NAGAI-M., WANG-Y., KARL-N., AND MITTLEMAN-D. M. (2016). Terahertz artificial dielectric lens, *Scientific Reports*, **6**, art. no. 23023.

MENLO SYSTEMS. (2016). *TERA15-FC: Fiber Coupled THz Antennas for 1560 nm*.

MENLO SYSTEMS. (2017). Fiber-coupled photoconductive antenna, `http://www.menlosystems.com/products/thz-antennas-and-components/tera15-fc/`. Accessed 2017/02/20.

MILLS-D., AND MARADUDIN-A. (1989). Surface corrugation and surface-polariton binding in the infrared frequency range, *Physical Review B*, **39**(3), pp. 1569–1574.

MINKEVIČIUS-L., INDRIŠIŪNAS-S., ŠNIAUKAS-R., VOISIAT-B., JANONIS-V., TAMOŠIŪNAS-V., KAŠALYNAS-I., RAČIUKAITIS-G., AND VALUŠIS-G. (2017). Terahertz multilevel phase fresnel lenses fabricated by laser patterning of silicon, *Optics Letters*, **42**(10), pp. 1875–1878.

MIRI-M., OTROOSHI-N., AND ABDI-Y. (2013). Nanoemitter in the vicinity of an impedance plane, *Journal of the Optical Society of America B*, **30**(11), pp. 3027–3034.

MOLONEY-J. V., YARBOROUGH-J. M., FALLAHI-M., SCHELLER-M., KOCH-S. W., AND KOCH-M. (2011). Compact, high-power, room-temperature, narrow-line terahertz source, *SPIE Newsroom*, DOI: 10.1117/2.1201102.003523.

MONNAI-Y., ALTMANN-K., JANSEN-C., HILLMER-H., KOCH-M., AND SHINODA-H. (2013). Terahertz beam steering and variable focusing using programmable diffraction gratings, *Optics Express*, **21**(2), pp. 2347–2354.

MONNAI-Y., ALTMANN-K., JANSEN-C., KOCH-M., HILLMER-H., AND SHINODA-H. (2012). Terahertz beam focusing based on plasmonic waveguide scattering, *Applied Physics Letters*, **101**(15), art. no. 151116.

MONNAI-Y., JAHN-D., WITHAYACHUMNANKUL-W., KOCH-M., AND SHINODA-H. (2015). Terahertz plasmonic Bessel beamformer, *Applied Physics Letters*, **106**(2), art. no. 021101.

MONTICONE-F., ESTAKHRI-N. M., AND ALÙ-A. (2013). Full control of nanoscale optical transmission with a composite metascreen, *Physical Review Letters*, **110**(20), art. no. 203903.

MURANO-K., WATANABE-I., KASAMATSU-A., SUZUKI-S., ASADA-M., WITHAYACHUMNANKUL-W., TANAKA-T., AND MONNAI-Y. (2016). Low-profile terahertz radar based on broadband leaky-wave beam steering, *IEEE Transactions on Terahertz Science and Technology*, **7**(1), pp. 60–69.

NAFTALY-M., AND MILES-R. E. (2007). Terahertz time-domain spectroscopy for material characterization, *Proceedings of the IEEE*, **95**(8), pp. 1658–1665.

NAGATSUMA-T., DUCOURNAU-G., AND RENAUD-C. C. (2016a). Advances in terahertz communications accelerated by photonics, *Nature Photonics*, **10**(6), pp. 371–479.

NAGATSUMA-T., HISATAKE-S., FUJITA-M., PHAM-H. H. N., TSURUDA-K., KUWANO-S., AND TERADA-J. (2016b). Millimeter-wave and terahertz-wave applications enabled by photonics, *IEEE Journal of Quantum Electronics*, **52**(1), art. no. 0600912.

NAGATSUMA-T., SONG-H.-J., FUJIMOTO-Y., MIYAKE-K., HIRATA-A., AJITO-K., WAKATSUKI-A., FURUTA-T., KUKUTSU-N., AND KADO-Y. (2009). Giga-bit wireless link using 300-400 GHz bands, *International Topical Meeting on Microwave Photonics (MWP)*, Valencia, Spain, paper Th.2.3.

NAN-R., LI-D., JIN-C., WANG-Q., ZHU-L., ZHU-W., ZHANG-H., YUE-Y., AND QIAN-L. (2011). The five-hundred-meter aperture spherical radio telescope (FAST) project, *International Journal of Modern Physics D*, **20**(06), pp. 989–1024.

NAVARRO-CÍA-M., BERUETE-M., CAMPILLO-I., AND SOROLLA-M. (2011). Enhanced lens by ε and μ near-zero metamaterial boosted by extraordinary optical transmission, *Physical Review B*, **83**(11), art. no. 115112.

NELSON-C., SANT-S., OVERZET-L., AND GOECKNER-M. (2007). Surface kinetics with low ion energy bombardment in fluorocarbon plasmas, *Plasma Sources Science and Technology*, **16**(4), pp. 813–821.

NEU-J., BEIGANG-R., AND RAHM-M. (2013). Metamaterial-based gradient index beam steerers for terahertz radiation, *Applied Physics Letters*, **103**(4), art. no. 041109.

NEU-J., KROLLA-B., PAUL-O., REINHARD-B., BEIGANG-R., AND RAHM-M. (2010). Metamaterial-based gradient index lens with strong focusing in the THz frequency range, *Optics Express*, **18**(26), pp. 27748–27757.

NEWPORT. (2017a). 443, https://www.newport.com/p/443. Accessed 2017/02/20.

NEWPORT. (2017b). LTA-HS, https://www.newport.com/p/LTA-HS. Accessed 2017/02/20.

NICHOLS-E., AND TEAR-J. (1925). Joining the infra-red and electric wave spectra, *The Astrophysical Journal*, **61**, pp. 17–37.

NIU-T., UPADHYAY-A., WITHAYACHUMNANKUL-W., HEADLAND-D., ABBOTT-D., BHASKARAN-M., SRIRAM-S., AND FUMEAUX-C. (2015). Polarization-dependent thin-film wire-grid reflectarray for terahertz waves, *Applied Physics Letters*, **107**(3), art. no. 031111, DOI: 10.1063/1.4927386.

NIU-T., WITHAYACHUMNANKUL-W., AND FUMEAUX-C. (2014a). Terahertz reflectarray for bidirectional beam splitting, *39th International Conference on Infrared, Millimeter, and Terahertz Waves (IRMMW-THz)*, Tucson, USA, DOI: 10.1109/IRMMW-THz.2014.6956410.

NIU-T., WITHAYACHUMNANKUL-W., UNG-B. S.-Y., MENEKSE-H., BHASKARAN-M., SRIRAM-S., AND FUMEAUX-C. (2013). Experimental demonstration of reflectarray antennas at terahertz frequencies, *Optics Express*, **21**(3), pp. 2875–2889.

NIU-T., WITHAYACHUMNANKUL-W., UPADHYAY-A., GUTRUF-P., ABBOTT-D., BHASKARAN-M., SRIRAM-S., AND FUMEAUX-C. (2014b). Terahertz reflectarray as a polarizing beam splitter, *Optics Express*, **22**(13), pp. 16148–16160.

OJEFORS-E., PFEIFFER-U. R., LISAUSKAS-A., AND ROSKOS-H. G. (2009). A 0.65 THz focal-plane array in a quarter-micron cmos process technology, *IEEE Journal of Solid-State Circuits*, **44**(7), pp. 1968–1976.

ORDAL-M. A., LONG-L. L., BELL-R. J., BELL-S. E., BELL-R. R., ALEXANDER-R. W., AND WARD-C. A. (1983). Optical properties of the metals Al, Co, Cu, Au, Fe, Pb, Ni, Pd, Pt, Ag, Ti, and W in the infrared and far infrared, *Applied Optics*, **22**(7), pp. 1099–1119.

ORTUÑO-R., GARCÍA-MECA-C., AND MARTÍNEZ-A. (2014). Terahertz metamaterials on flexible polypropylene substrate, *Plasmonics*, **9**(5), pp. 1143–1147.

PANDEY-S., GUPTA-B., AND NAHATA-A. (2013). Terahertz plasmonic waveguides created via 3D printing, *Optics Express*, **21**(21), pp. 24422–24430.

PARK-S.-G., LEE-K., HAN-D., AHN-J., AND JEONG-K.-H. (2014). Subwavelength silicon through-hole arrays as an all-dielectric broadband terahertz gradient index metamaterial, *Applied Physics Letters*, **105**(9), art. no. 091101.

PATHAK-P. H., FENG-X., HU-P., AND MOHAPATRA-P. (2015). Visible light communication, networking, and sensing: A survey, potential and challenges, *IEEE Communications Surveys & Tutorials*, **17**(4), pp. 2047–2077.

PEELEN-J., AND METSELAAR-R. (1974). Light scattering by pores in polycrystalline materials: Transmission properties of alumina, *Journal of Applied Physics*, **45**(1), pp. 216–220.

PETOSA-A. (1997). *Dielectric Resonator Antenna Handbook*, Artech House.

Pfeiffer-U. R., Zhao-Y., Grzyb-J., Al Hadi-R., Sarmah-N., Förster-W., Rücker-H., and Heinemann-B. (2014). A 0.53 THz reconfigurable source module with up to mW radiated power for diffuse illumination in terahertz imaging applications, *IEEE Journal of Solid-State Circuits*, **49**(12), pp. 2938–2950.

Podzorov-A., and Gallot-G. (2008). Low-loss polymers for terahertz applications, *Applied Optics*, **47**(18), pp. 3254–3257.

Pozar-D. M. (2009). *Microwave engineering*, John Wiley & Sons.

Pozar-D. M., Targonski-S. D., and Syrigos-H. (1997). Design of millimeter wave microstrip reflectarrays, *IEEE Transactions on Antennas and Propagation*, **45**(2), pp. 287–296.

Pozar-D., Targonski-S., and Pokuls-R. (1999). A shaped-beam microstrip patch reflectarray, *IEEE Transactions on Antennas and Propagation*, **47**(7), pp. 1167–1173.

Qu-C., Ma-S., Hao-J., Qiu-M., Li-X., Xiao-S., Miao-Z., Dai-N., He-Q., Sun-S., and Zhou-L. (2015). Tailor the functionalities of metasurfaces based on a complete phase diagram, *Physical Review Letters*, **115**(23), art. no. 235503.

Rajagopal-S., Roberts-R. D., and Lim-S.-K. (2012). IEEE 802.15.7 Visible light communication: Modulation schemes and dimming support, *IEEE Communications Magazine*, **50**(3), pp. 72–82.

Ranjbar Nikkhah-M., Loghmannia-P., Rashed-Mohassel-J., and Kishk-A. (2014). Theory of ESPAR design with their implementation in large arrays, *IEEE Transactions on Antennas and Propagation*, **62**(6), pp. 3359–3364.

Ree-M., Chen-K.-J., Kirby-D., Katzenellenbogen-N., and Grischkowsky-D. (1992). Anisotropic properties of high-temperature polyimide thin films: Dielectric and thermal-expansion behaviors, *Journal of Applied Physics*, **72**(5), pp. 2014–2021.

Reid-C. B., Pickwell-MacPherson-E., Laufer-J. G., Gibson-A. P., Hebden-J. C., and Wallace-V. P. (2010). Accuracy and resolution of THz reflection spectroscopy for medical imaging, *Physics in Medicine and Biology*, **55**(16), pp. 4825–4838.

Rotman-W., and Turner-R. (1963). Wide-angle microwave lens for line source applications, *IEEE Transactions on Antennas and Propagation*, **11**(6), pp. 623–632.

Rubens-H., and Nichols-E. (1897). Heat rays of great wavelength, *Physical Review*, **4**, pp. 314–323.

Saha-S. C., Li-C., Ma-Y., Grant-J. P., and Cumming-D. R. (2013). Fabrication of multilevel silicon diffractive lens at terahertz frequency, *IEEE Transactions on Terahertz Science and Technology*, **3**(4), pp. 479–485.

Saleh-B. E., and Teich-M. C. (2007). *Fundamentals of photonics*, 2 edn, Wiley New York.

Scheller-M., Wietzke-S., Jansen-C., and Koch-M. (2009). Modelling heterogeneous dielectric mixtures in the terahertz regime: a quasi-static effective medium theory, *Journal of Physics D: Applied Physics*, **42**(6), art. no. 065415.

Scherger-B., Jördens-C., and Koch-M. (2011a). Variable-focus terahertz lens, *Optics Express*, **19**(5), pp. 4528–4535.

SCHERGER-B., REUTER-M., SCHELLER-M., ALTMANN-K., VIEWEG-N., DABROWSKI-R., DEIBEL-J. A., AND KOCH-M. (2012). Discrete terahertz beam steering with an electrically controlled liquid crystal device, *Journal of Infrared, Millimeter, and Terahertz Waves*, **33**(11), pp. 1117–1122.

SCHERGER-B., SCHELLER-M., JANSEN-C., KOCH-M., AND WIESAUER-K. (2011b). Terahertz lenses made by compression molding of micropowders, *Applied Optics*, **50**(15), pp. 2256–2262.

SCHNEIDER-T., WIATREK-A., PREUSSLER-S., GRIGAT-M., AND BRAUN-R.-P. (2012). Link budget analysis for terahertz fixed wireless links, *IEEE Transactions on Terahertz Science and Technology*, **2**(2), pp. 250–256.

SEDRA-A. S., AND SMITH-K. C. (2004). *Microelectronic Circuits*, 5 edn, New York: Oxford University Press.

SEITZ-H., RIEDER-W., IRSEN-S., LEUKERS-B., AND TILLE-C. (2005). Three-dimensional printing of porous ceramic scaffolds for bone tissue engineering, *Journal of Biomedical Materials Research Part B*, **74**(2), pp. 782–788.

SENGUPTA-K., AND HAJIMIRI-A. (2012). A 0.28 THz power-generation and beam-steering array in CMOS based on distributed active radiators, *IEEE Journal of Solid-State Circuits*, **47**(12), pp. 3013–3031.

SENGUPTA-K., AND HAJIMIRI-A. (2015). Mutual synchronization for power generation and beam-steering in CMOS with on-chip sense antennas near 200 GHz, *IEEE Transactions on Microwave Theory and Techniques*, **63**(9), pp. 2867–2876.

SHAMS-M. I. B., JIANG-Z., QAYYUM-J., RAHMAN-S., FAY-P., AND LIU-L. (2015). A terahertz reconfigurable photo-induced Fresnel-zone-plate antenna for dynamic two-dimensional beam steering and forming, *2015 IEEE MTT-S International Microwave Symposium*, IEEE, Phoenix, USA, DOI: 10.1109/MWSYM.2015.7167052.

SHARMA-G., AL-NAIB-I., HAFEZ-H., MORANDOTTI-R., COOKE-D., AND OZAKI-T. (2012). Carrier density dependence of the nonlinear absorption of intense THz radiation in GaAs, *Optics Express*, **20**(16), pp. 18016–18024.

SHEN-Y.-C. (2011). Terahertz pulsed spectroscopy and imaging for pharmaceutical applications: A review, *International Journal of Pharmaceuticals*, **417**(1), pp. 48–60.

SIEGEL-P. H. (2002). Terahertz technology, *IEEE Transactions on Microwave Theory and Techniques*, **50**(3), pp. 910–928.

SIEMION-A., SIEMION-A., MAKOWSKI-M., SUSZEK-J., BOMBA-J., CZERWIŃSKI-A., GARET-F., COUTAZ-J.-L., AND SYPEK-M. (2012). Diffractive paper lens for terahertz optics, *Optics Letters*, **37**(20), pp. 4320–4322.

SIEMION-A., SIEMION-A., MAKOWSKI-M., SYPEK-M., HÉRAULT-E., GARET-F., AND COUTAZ-J.-L. (2011). Off-axis metallic diffractive lens for terahertz beams, *Optics Letters*, **36**(11), pp. 1960–1962.

SIEVENPIPER-D. F., SCHAFFNER-J. H., SONG-H. J., LOO-R. Y., AND TANGONAN-G. (2003). Two-dimensional beam steering using an electrically tunable impedance surface, *IEEE Transactions on Antennas and Propagation*, **51**(10), pp. 2713–2722.

SIHVOLA-A. (2001). Two main avenues leading to the Maxwell Garnett mixing rule, *Journal of Electromagnetic Waves and Applications*, **15**(6), pp. 715–725.

SIMON-M. K., OMURA-J. K., SCHOLTZ-R. A., AND LEVITT-B. K. (1994). *Spread Spectrum Communications Handbook*, Vol. 2, McGraw-Hill.

SIMPKIN-R. (2010). Derivation of Lichtenecker's logarithmic mixture formula from Maxwell's equations, *IEEE Transactions on Microwave Theory and Techniques*, **58**(3), pp. 545–550.

SINGH-R., AL-NAIB-I. A., YANG-Y., CHOWDHURY-D. R., CAO-W., ROCKSTUHL-C., OZAKI-T., MORANDOTTI-R., AND ZHANG-W. (2011). Observing metamaterial induced transparency in individual fano resonators with broken symmetry, *Applied Physics Letters*, **99**(20), art. no. 201107.

SINYUKOV-A. M., LIU-Z., HOR-Y. L., SU-K., BARAT-R. B., GARY-D. E., MICHALOPOULOU-Z.-H., ZORYCH-I., FEDERICI-J. F., AND ZIMDARS-D. (2008). Rapid-phase modulation of terahertz radiation for high-speed terahertz imaging and spectroscopy, *Optics Letters*, **33**(14), pp. 1593–1595.

SOMMERFELD-A. (1964). *Lectures on theoretical physics: Optics*, Vol. 4, Academic Press.

SONG-H.-J., AJITO-K., MURAMOTO-Y., WAKATSUKI-A., NAGATSUMA-T., AND KUKUTSU-N. (2012). 24 Gbit/s data transmission in 300 GHz band for future terahertz communications, *Electronics Letters*, **48**(15), pp. 953–954.

SONG-H.-J., AND NAGATSUMA-T. (2011). Present and future of terahertz communications, *IEEE Transactions on Terahertz Science and Technology*, **1**(1), pp. 256–263.

SONG-H.-J., KIM-J.-Y., AJITO-K., KUKUTSU-N., AND YAITA-M. (2014). 50-Gb/s direct conversion qpsk modulator and demodulator mmics for terahertz communications at 300 GHz, *IEEE Transactions on Microwave Theory and Techniques*, **62**(3), pp. 600–609.

SPARKS-R. (2000). Progress in optical Rotman beamformer technology, *Proceedings of the IEEE International Conference on Phased Array Systems and Technology*, Dana Point, USA, pp. 357–360.

SPARKS-R., SLAWSBY-N., PRINCE-J., AND MUNRO-J. (1998). Experimental demonstration of a fiber optic Rotman beamformer, *IEEE International Topical Meeting on Microwave Photonics*, Princeton, USA, pp. 127–130.

SQUIRES-A., CONSTABLE-E., AND LEWIS-R. (2015). 3D printed terahertz diffraction gratings and lenses, *Journal of Infrared, Millimeter, and Terahertz Waves*, **36**(1), pp. 72–80.

STERCZEWSKI-L. A., GRZELCZAK-M. P., NOWAK-K., AND PLINSKI-E. F. (2016). Cast terahertz lenses made of caramelized sucrose, *Optical Engineering*, **55**(9), art. no. 090505.

SUEN-J. Y., AND PADILLA-W. J. (2016). Superiority of terahertz over infrared transmission through bandages and burn wound ointments, *Applied Physics Letters*, **108**(23), art. no. 233701.

SUNDBERG-M. (2015). 3rd Generation Partnership Project; Technical Specification 45.005; Radio transmission and reception (Release 13).

SUN-J., TIMURDOGAN-E., YAACOBI-A., HOSSEINI-E. S., AND WATTS-M. R. (2013a). Large-scale nanophotonic phased array, *Nature*, **493**(7431), pp. 195–199.

SUN-K., WEI-T.-S., AHN-B. Y., SEO-J. Y., DILLON-S. J., AND LEWIS-J. A. (2013b). 3D printing of interdigitated Li-Ion microbattery architectures, *Advanced Materials*, **25**(33), pp. 4539–4543.

SUSZEK-J., SIEMION-A., BIEDA-M. S., BLOCKI-N., COQUILLAT-D., CYWINSKI-G., CZERWINSKA-E., DOCH-M., KOWALCZYK-A., PALKA-N., SOBCZYK-A., ZAGRAJEK-P., ZAREMBA-M., KOLODZIEJCZYK-A., KNAP-W., AND SYPEK-M. (2015). 3-D-printed flat optics for THz linear scanners, *IEEE Transactions on Terahertz Science and Technology*, **5**(2), pp. 314–316.

SVELTO-O., AND HANNA-D. C. (1998). *Principles of Lasers*, Springer.

SYMES-M. D., KITSON-P. J., YAN-J., RICHMOND-C. J., COOPER-G. J., BOWMAN-R. W., VILBRANDT-T., AND CRONIN-L. (2012). Integrated 3D-printed reactionware for chemical synthesis and analysis, *Nature Chemistry*, **4**(5), pp. 349–354.

SYPEK-M., MAKOWSKI-M., HÉRAULT-E., SIEMION-A., SIEMION-A., SUSZEK-J., GARET-F., AND COUTAZ-J.-L. (2012). Highly efficient broadband double-sided fresnel lens for THz range, *Optics Letters*, **37**(12), pp. 2214–2216.

TADAY-P., BRADLEY-I., ARNONE-D., AND PEPPER-M. (2003). Using terahertz pulse spectroscopy to study the crystalline structure of a drug: A case study of the polymorphs of ranitidine hydrochloride, *Journal of Pharmaceutical Sciences*, **92**(4), pp. 831–838.

TAKANO-K., YAKIYAMA-Y., SHIBUYA-K., IZUMI-K., MIYAZAKI-H., JIMBA-Y., MIYAMARU-F., KITAHARA-H., AND HANGYO-M. (2013). Fabrication and performance of TiO_2-ceramic-based metamaterials for terahertz frequency range, *IEEE Transactions on Terahertz Science and Technology*, **3**(6), pp. 812–819.

TAMMINEN-A., ALA-LAURINAHO-J., MÄKELÄ-S., GOMES-MARTINS-D., HÄKLI-J., KOIVISTO-P., RANTAKARI-P., SÄILY-J., TUOVINEN-R., LUUKANEN-A., SIPILÄ-M., AND RÄISÄNEN-A. V. (2013). Near-field measurements of submillimeter-wave reflectarrays, *Proc. SPIE*, Vol. 8715, Baltimore, USA, art. no. 871506.

TANI-M., GU-P., HYODO-M., SAKAI-K., AND HIDAKA-T. (2000). Generation of coherent terahertz radiation by photomixing of dual-mode lasers, *Optical and Quantum Electronics*, **32**(4), pp. 503–520.

TAO-H., BINGHAM-C., PILON-D., FAN-K., STRIKWERDA-A., SHREKENHAMER-D., PADILLA-W., ZHANG-X., AND AVERITT-R. (2010). A dual band terahertz metamaterial absorber, *Journal of Physics D: Applied Physics*, **43**(22), art. no. 225102.

TAO-H., BINGHAM-C., STRIKWERDA-A., PILON-D., SHREKENHAMER-D., LANDY-N., FAN-K., ZHANG-X., PADILLA-W., AND AVERITT-R. (2008a). Highly flexible wide angle of incidence terahertz metamaterial absorber: Design, fabrication, and characterization, *Physical Review B*, **78**(24), art. no. 241103.

TAO-H., STRIKWERDA-A., FAN-K., BINGHAM-C., PADILLA-W., ZHANG-X., AND AVERITT-R. (2008b). Terahertz metamaterials on free-standing highly-flexible polyimide substrates, *Journal of Physics D: Applied Physics*, **41**(23), art. no. 232004.

TAVALLAEE-A. A., WILLIAMS-B. S., HON-P. W., ITOH-T., AND CHEN-Q.-S. (2011). Terahertz quantum-cascade laser with active leaky-wave antenna, *Applied Physics Letters*, **99**(14), art. no. 141115.

THIJS-L., VERHAEGHE-F., CRAEGHS-T., VAN HUMBEECK-J., AND KRUTH-J.-P. (2010). A study of the microstructural evolution during selective laser melting of Ti-6Al-4V, *Acta Materialia*, **58**(9), pp. 3303–3312.

THORLABS. (2017). Thorlabs - NR360S/M NanoRotator Stage with Sm2-Threaded Center Hole, https://www.thorlabs.com/thorproduct.cfm?partnumber=NR360S/M. Accessed 2017/02/20.

TOUSI-Y., AND AFSHARI-E. (2015). A high-power and scalable 2-D phased array for terahertz CMOS integrated systems, *IEEE Journal of Solid-State Circuits*, **50**(2), pp. 597–609.

ULIASZ-P., KNYCH-T., PIWOWARSKA-M., AND WIECHEĆ-J. (2012). The influence of heat treatment parameters on the electrical conductivity of AlSi7Mg and AlSi10Mg aluminum cast alloys, *13th International Conference on Aluminum Alloys*, Wiley Online Library, Pittsburgh, USA, pp. 129–135.

UNG-B., DUPUIS-A., STOEFFLER-K., DUBOIS-C., AND SKOROBOGATIY-M. (2011). High-refractive-index composite materials for terahertz waveguides: Trade-off between index contrast and absorption loss, *Journal of the Optical Society of America B*, **28**(4), pp. 917–921.

UNG-B.-Y., LI-J., LIN-H., FISCHER-B. M., WITHAYACHUMNANKUL-W., AND ABBOTT-D. (2013). Dual-mode terahertz time-domain spectroscopy system, *IEEE Transactions on Terahertz Science and Technology*, **3**(2), pp. 216–220.

VALLECCHI-A., DE LUIS-J. R., CAPOLINO-F., AND DE FLAVIIS-F. (2012). Low profile fully planar folded dipole antenna on a high impedance surface, *IEEE Transactions on Antennas and Propagation*, **60**(1), pp. 51–62.

VAN EXTER-M., FATTINGER-C., AND GRISCHKOWSKY-D. (1989a). High-brightness terahertz beams characterized with an ultrafast detector, *Applied Physics Letters*, **55**(4), pp. 337–339.

VAN EXTER-M., FATTINGER-C., AND GRISCHKOWSKY-D. (1989b). Terahertz time-domain spectroscopy of water vapor, *Optics letters*, **14**(20), pp. 1128–1130.

VATANSEVER-F., AND HAMBLIN-M. R. (2012). Far infrared radiation (FIR): Its biological effects and medical applications, *Photonics and Lasers in Medicine*, **1**(4), pp. 255–266.

VILLEGAS-F. J. (2007). Parallel genetic-algorithm optimization of shaped beam coverage areas using planar 2-D phased arrays, *IEEE Transactions on Antennas and Propagation*, **55**(6), pp. 1745–1753.

WALIA-S., SHAH-C. M., GUTRUF-P., NILI-H., CHOWDHURY-D. R., WITHAYACHUMNANKUL-W., BHASKARAN-M., AND SRIRAM-S. (2015). Flexible metasurfaces and metamaterials: A review of materials and fabrication processes at micro-and nano-scales, *Applied Physics Reviews*, **2**(1), art. no. 011303.

WALKER-G. C., BOWEN-J. W., MATTHEWS-W., ROYCHOWDHURY-S., LABAUNE-J., MOUROU-G., MENU-M., HODDER-I., AND JACKSON-J. B. (2013). Sub-surface terahertz imaging through uneven surfaces: Visualizing neolithic wall paintings in Çatalhöyük, *Optics Express*, **21**(7), pp. 8126–8134.

WALSBY-E., ALTON-J., WORRALL-C., BEERE-H., RITCHIE-D., AND CUMMING-D. (2007). Imprinted diffractive optics for terahertz radiation, *Optics Letters*, **32**(9), pp. 1141–1143.

WALTER-C. H. (1970). *Traveling Wave Antennas*, Dover Publications.

WANG-J., LIU-S., GURUSWAMY-S., AND NAHATA-A. (2013). Reconfigurable liquid metal based terahertz metamaterials via selective erasure and refilling to the unit cell level, *Applied Physics Letters*, **103**(22), art. no. 221116.

WANG-J., YANG-J.-Y., FAZAL-I. M., AHMED-N., YAN-Y., HUANG-H., REN-Y., YUE-Y., DOLINAR-S., TUR-M., AND WILLNER-A. E. (2012). Terabit free-space data transmission employing orbital angular momentum multiplexing, *Nature Photonics*, **6**(7), pp. 488–496.

WANG-Q., ZHANG-X., XU-Y., TIAN-Z., GU-J., YUE-W., ZHANG-S., HAN-J., AND ZHANG-W. (2015). A broadband metasurface-based terahertz flat-lens array, *Advanced Optical Materials*, **3**(6), pp. 779–785.

WANG-S., GARET-F., BLARY-K., LHEURETTE-E., COUTAZ-J. L., AND LIPPENS-D. (2010). Experimental verification of negative refraction for a wedge-type negative index metamaterial operating at terahertz, *Applied Physics Letters*, **97**(18), art. no. 181902.

WANG-S., YUAN-T., WALSBY-E., BLAIKIE-R., DURBIN-S., CUMMING-D., XU-J., AND ZHANG-X.-C. (2002). Characterization of T-ray binary lenses, *Optics Letters*, **27**(13), pp. 1183–1185.

WELSCH-G., BOYER-R., AND COLLINGS-E. (1993). *Materials Properties Handbook: Titanium Alloys*, ASM international.

WICHMANN-M., MONDOL-A., KOCIC-N., LIPPERT-S., PROBST-T., SCHWERDTFEGER-M., SCHUMANN-S., HOCHREIN-T., HEIDEMEYER-P., BASTIAN-M., AND KOCH-M. (2013). Terahertz plastic compound lenses, *Applied Optics*, **52**(18), pp. 4186–4191.

WIETING-T., AND SCHRIEMPF-J. (1976). Infrared absorptances of partially ordered alloys at elevated temperatures, *Journal of Applied Physics*, **47**(9), pp. 4009–4011.

WIETZKE-S., JANSEN-C., RUTZ-F., MITTLEMAN-D., AND KOCH-M. (2007). Determination of additive content in polymeric compounds with terahertz time-domain spectroscopy, *Polymer Testing*, **26**(5), pp. 614–618.

WILLIAMS-B. S. (2007). Terahertz quantum-cascade lasers, *Nature Photonics*, **1**(9), pp. 517–525.

WILLIAMS-C. R., ANDREWS-S. R., MAIER-S., FERNANDEZ-DOMINGUEZ-A., MARTÍN-MORENO-L., AND GARCIA-VIDAL-F. (2008). Highly confined guiding of terahertz surface plasmon polaritons on structured metal surfaces, *Nature Photonics*, **2**(3), pp. 175–179.

WILTSE-J. C. (1984). History of millimeter and submillimeter waves, *IEEE Transactions on Microwave Theory and Techniques*, **32**(9), pp. 1118–1127.

WITHAYACHUMNANKUL-W., AND NAFTALY-M. (2014). Fundamentals of measurement in terahertz time-domain spectroscopy, *Journal of Infrared, Millimeter, and Terahertz Waves*, **35**(8), pp. 610–637.

WITHAYACHUMNANKUL-W., FISCHER-B. M., LIN-H., AND ABBOTT-D. (2008). Uncertainty in terahertz time-domain spectroscopy measurement, *Journal of the Optical Society of America B*, **25**(6), pp. 1059–1072.

WITHAYACHUMNANKUL-W., OHARA-J. F., CAO-W., AL-NAIB-I., AND ZHANG-W. (2014). Limitation in thin-film sensing with transmission-mode terahertz time-domain spectroscopy, *Optics Express*, **22**(1), pp. 972–986.

XU-J., PLAXCO-K. W., AND ALLEN-S. J. (2006). Probing the collective vibrational dynamics of a protein in liquid water by terahertz absorption spectroscopy, *Protein Science*, **15**(5), pp. 1175–1181.

YAGITANI-S., SUNAHARA-T., NAKAGAWA-T., HIRAKI-D., YOSHIMURA-Y., AND SUGIURA-H. (2013). Radio-frequency field measurement using thin artificial magnetic conductor absorber, *Proceedings of the URSI International Symposium on Electromagnetics Theory*, Hiroshima, Japan, pp. 691–694.

YANG-F., KACZOROWSKI-A., AND WILKINSON-T. D. (2014a). Fast precalculated triangular mesh algorithm for 3D binary computer-generated holograms, *Applied Optics*, **53**(35), pp. 8261–8267.

YANG-F., NAYERI-P., ELSHERBENI-A. Z., GINN-J. C., SHELTON-D. J., BOREMAN-G. D., AND RAHMAT-SAMII-Y. (2012). Reflectarray design at infrared frequencies: Effects and models of material loss, *IEEE Transactions on Antennas and Propagation*, **60**(9), pp. 4202–4209.

YANG-Q., GU-J., XU-Y., ZHANG-X., LI-Y., OUYANG-C., TIAN-Z., HAN-J., AND ZHANG-W. (2017). Broadband and robust metalens with nonlinear phase profiles for efficient terahertz wave control, *Advanced Optical Materials*, DOI: 10.1002/adom.201601084.

YANG-Y., WANG-W., MOITRA-P., KRAVCHENKO-I. I., BRIGGS-D. P., AND VALENTINE-J. (2014b). Dielectric meta-reflectarray for broadband linear polarization conversion and optical vortex generation, *Nano Letters*, **14**(3), pp. 1394–1399.

YI-H., QU-S.-W., NG-K.-B., CHAN-C. H., AND BAI-X. (2016). 3-D printed millimeter-wave and terahertz lenses with fixed and frequency scanned beam, *IEEE Transactions on Antennas and Propagation*, **64**(2), pp. 442–449.

YU-C., FAN-S., SUN-Y., AND PICKWELL-MACPHERSON-E. (2012). The potential of terahertz imaging for cancer diagnosis: A review of investigations to date, *Quantitative Imaging in Medicine and Surgery*, **2**(1), pp. 33–45.

YU-N., WANG-Q. J., KATS-M. A., FAN-J. A., KHANNA-S. P., LI-L., DAVIES-A. G., LINFIELD-E. H., AND CAPASSO-F. (2010). Designer spoof surface plasmon structures collimate terahertz laser beams, *Nature Materials*, **9**(9), pp. 730–735.

YU-X., ASIF-R., PIELS-M., ZIBAR-D., GALILI-M., MORIOKA-T., JEPSEN-P. U., AND OXENLØWE-L. K. (2016). 400-GHz wireless transmission of 60-Gb/s Nyquist-QPSK signals using UTC-PD and heterodyne mixer, *IEEE Transactions on Terahertz Science and Technology*, **6**, pp. 765–770.

ZEITLER-J. A., TADAY-P. F., NEWNHAM-D. A., PEPPER-M., GORDON-K. C., AND RADES-T. (2007). Terahertz pulsed spectroscopy and imaging in the pharmaceutical setting—a review, *Journal of Pharmacy and Pharmacology*, **59**(2), pp. 209–223.

ZHANG-C., ANZALONE-N. C., FARIA-R. P., AND PEARCE-J. M. (2013a). Open-source 3D-printable optics equipment, *PLoS One*, **8**(3), art. no. e59840.

ZHANG-X., TIAN-Z., YUE-W., GU-J., ZHANG-S., HAN-J., AND ZHANG-W. (2013b). Broadband terahertz wave deflection based on C-shape complex metamaterials with phase discontinuities, *Advanced Materials*, **25**(33), pp. 4567–4572.

ZHUANG-J.-X., HAO-Z.-C., AND HONG-W. (2015). Silicon micromachined terahertz bandpass filter with elliptic cavities, *IEEE Transactions on Terahertz Science and Technology*, **5**(6), pp. 1040–1047.

ZOU-L., ABBOTT-D., AND FUMEAUX-C. (2012). Omnidirectional cylindrical dielectric resonator antenna with dual polarization, *IEEE Antennas and Wireless Propagation Letters*, **11**, pp. 515–518.

ZOU-L., LÓPEZ-GARCÍA-M., WITHAYACHUMNANKUL-W., SHAH-C. M., MITCHELL-A., BHASKARAN-M., SRIRAM-S., OULTON-R., KLEMM-M., AND FUMEAUX-C. (2014a). Spectral and angular characteristics of dielectric resonator metasurface at optical frequencies, *Applied Physics Letters*, **105**(19), art. no. 191109.

ZOU-L., WITHAYACHUMNANKUL-W., SHAH-C., MITCHELL-A., KLEMM-M., BHASKARAN-M., SRIRAM-S., AND FUMEAUX-C. (2014b). Efficiency and scalability of dielectric resonator antennas at optical frequencies, *IEEE Photonics Journal*, **6**(4), art. no. 4600110.

ZOU-L., WITHAYACHUMNANKUL-W., SHAH-C. M., MITCHELL-A., BHASKARAN-M., SRIRAM-S., AND FUMEAUX-C. (2013). Dielectric resonator nanoantennas at visible frequencies, *Optics Express*, **21**(1), pp. 1344–1352.

Glossary

Mathematical and physical constants

A number of constants are utilised in this thesis, and they are detailed below.

Quantity	**Symbol**	**Value**
Archimedes' constant	π	3.141 592 653
Euler's number	e	2.718 281 828
Electrical permittivity of free space	ϵ_0	$8.854\,188 \times 10^{-12}$ F/m
Magnetic permeability of free space	μ_0	$4\pi \times 10^{-7}$ NA^{-1}
Speed of light in free space	c	299 792 458 ms^{-1}
Elementary charge	q	$1.602\,176\,621 \times 10^{-19}$ C

Symbols and concepts

That which follows is a list of basic terms, quantities, and principles that are made use of in the main text of this doctoral thesis. This also provides a summary of the symbolic conventions for algebraic terms used throughout.

Quantity or term	**Symbol** [SI unit]	**Definition**
Absorption coefficient	α [m^{-1}]	A measure of the degree to which a given medium is absorptive, in terms of the exponential decay of field magnitude over a unit distance that an electromagnetic wave experiences in that medium.
Alignment	–	The arrangement of a component or group of components in a given system, most likely a terahertz measurement system in the context of this thesis, such that power is delivered to a desired region of space.

Angle (general)	φ, ψ [radians or degrees]	This term is employed to denote an arbitrary angular quantity, which can be either a physical angle or the phase of a sinusoid or phasor.
Antenna aperture	–	A surface, near or on an antenna, on which it is convenient to make assumptions regarding the field values for the purpose of computing fields at external points (IEEE 1983). In general, a larger antenna aperture will produce higher gain.
Antenna gain	$G(\theta, \phi)$	In a given direction, that part of the radiation intensity corresponding to a given polarisation divided by the radiation intensity that would be obtained if the power accepted by the antenna were isotropically radiated (IEEE 1983).
Array element	–	In an array antenna, a single radiating element or a convenient grouping of radiating elements that have fixed relative excitations (IEEE 1983).
Array factor	$\mathrm{AF}(\theta, \phi)$	The radiation pattern of an array antenna when each array element is considered to radiate isotropically (IEEE 1983).
Bandwidth of an antenna	–	The range of frequencies within which the performance of the antenna conforms to a specified standard with respect to some characteristic (IEEE 1983).
Cartesian axes	(x, y, z), at times ξ and η [m]	Three orthogonal axes that jointly define three-dimensional space. Here, ξ and η are employed as integration variables corresponding to x and y respectively.
Complex amplitude	A	The combined magnitude and phase of a given excitation or field quantity, expressed as a complex number.

Density	ρ [kg/m^3 or C/m^3]	The quantity, for a given medium, of either mass or charge enclosed within a unit volume.
Dispersion	–	The capacity for some electromagnetic quantity to vary with respect to frequency. This can apply to the properties of a given medium (eg. refractive index), or to the characteristics of a device (eg. the focal length of a lensing device).
Distance (general)	d, D, l, L, h, or w [m]	These symbols are employed throughout this thesis to denote some arbitrary distance, length, width, or thickness.
Efficiency	–	The ratio of power expended to power delivered for some desired function. Detriments to efficiency can include dissipation, reflection, and diffraction.
Electric field	$\mathbf{E}$ [V/m]	This is a vector field that is typically associated with exerting electrostatic force upon free charges. In the context of this thesis, however, it is most often understood as one of the two vector field components of electromagnetic radiation, with the other being magnetic field.
Electromagnetic wave	–	A wave, composed of electric and magnetic vector field components, which is capable of propagating through a given medium without the need for free charges or externally-excited electric currents to sustain it. All phenomena and technologies associated with radio, terahertz waves, light, X-rays, and so on are essentially subsets of electromagnetic waves.
Focal length	F [m]	The distance, along the optical axis, which separates a given lensing device from its focal spot.

Frequency	f [Hz]	The rate, in cycles per second, at which a given quantity oscillates. In the context of this thesis, this is always associated with the periodic, sinusoidal fluctuation of electromagnetic fields.
Gaussian beam waist	w_0	For a given Gaussian beam, this represents the distance from the optical axis to the point at which field magnitude is equal to $\frac{1}{e}$ of its maximum value, for the thinnest part of the beam.
Huygens source radiator	–	An elementary radiator having the radiation properties of an infinitesimal area of a propagating electromagnetic wavefront (IEEE 1983).
Imaginary unit	j	Denotes the imaginary component of a given complex number, which satisfies the equation $j^2 = -1$.
Impedance	Z	Either the lumped impedance of a component, or the wave impedance of a medium, depending on the context. The former relates the potential difference across that component V, with the current passing through it, I, by $Z = \frac{V}{I}$. The latter relates electric field magnitude in the medium, E, with magnetic field magnitude, H, via $\frac{E}{H}$. In either case, the impedance can be complex, which indicates some value of phase between the two components.
Index of series	s, m, χ	Integer employed to denote a specific instance of a potentially-infinite series of integer values.

Isotropic radiator	–	A hypothetical, lossless antenna having equal radiation intensity in all directions. An isotropic radiator represents a convenient reference for expressing the directive properties of actual antennas (IEEE 1983). It is worth noting that such an antenna cannot be physically realised.
Lattice constant	a [m]	The spacing between adjacent elements in a two-dimensional periodic structure.
Limit of series	M or N	The final instance of some series of integers.
Loss tangent	$\tan\delta$	A quantification of the intrinsic loss of a dielectric medium, in terms of its complex relative permittivity.
Magnetic field	$\mathbf{H}$ [A m^{-1}]	A vector field that interacts with electric currents and magnetic materials. In the context of this thesis, it is most often understood as one of the two vector field components of electromagnetic radiation with the other being electric fields.
Mean	μ	The statistical average of a set of numerical data points, or alternatively, the central location of a given probability distribution (Kreyszig 2007).
Misalignment	–	When alignment is poor in a given system, this is referred to as misalignment. This condition results in power fades, aberrations of beam shape, and spurious spectral characteristics.
Optical axis	–	For a given propagating beam, this can be considered a vector in Cartesian space that is coaxial with the beam.
Permittivity	ϵ [Fm^{-1}]	A measure of the degree to which a given dielectric medium resists the formation of electric field.

Phasor	–	A means of expressing a sinusoid as a complex number, which makes use of Euler's identity $\cos\theta + j\sin\theta = \exp(j\theta)$. This allows for convenient representation and manipulation of the sinusoid in the complex plane. The actual value of the signal is extracted from the real component of the complex number.
Polar directionality	(θ, ϕ) [radians or degrees]	The directionality of a given vector that is oriented outward from the origin of the relevant coordinate system.
Poynting vector	$\mathbf{k}$ [W m^{-2}]	A vector that gives the intensity and directionality of a given electromagnetic wave, and is defined in terms of its electric and magnetic field components; $\mathbf{k} = \mathbf{E} \times \mathbf{H}$
Propagation	–	The capacity for waves to travel, and hence transmit power, without need of an external source of energy to sustain them.
Propagation constant	γ [m^{-1}]	A measure of both exponential decay of field amplitude and phase change as an electromagnetic wave propagates through a unit distance of a given medium.
Quality factor	Q	The ratio of stored energy to energy either dissipated in, or radiated from, a given resonator system.
Radiation pattern	–	The spatial distribution of a quantity that characterises the electromagnetic field generated by an antenna (IEEE 1983).
Radius	r [m]	Distance from the centre to the perimeter of a given circle.

Reciprocity	–	The notion that, for a given passive electromagnetic system, the propagation direction can be reversed (i.e. by reversing the polarity of the **E** or **H** vector), and there will be no alteration to beam shape or radiation pattern. This has relevance to antenna theory, in that a single radiation pattern characterises both the power that an antenna projects to a given direction, and the sensitivity when receiving fields from that direction.
Reference	–	In the context of THz-TDS, this describes a measurement that is taken in order to characterise the response of the relevant experimental system itself for normalisation purposes.
Reflection coefficient	Γ	The ratio of reflected to incident complex field amplitude a given interface or impedance boundary.
Refractive index	n	The ratio of the speed of light in free space to the speed at which light travels in the relevant medium.
Relative permittivity	ϵ	The ratio of the permittivity of a given medium to the permittivity of free space.
Sample	–	In the context of this thesis, this most often refers to some fabricated device or quantity of a given material, which is intended to be characterised in some way. In a broader sense, this may also refer to the acquisition of a given signal (i.e. as a verb; "to sample"), or specific data points of an acquired signal (i.e. sampling points).
Standard deviation	σ	A measure that characterises the spread of either a probability distribution or a set of sampled points (Kreyszig 2007).

Standing wave	–	A sinusoidal wave that is the sum of both forward and backward-propagating components, for which there is no apparent overall movement in the propagation direction due to interference. Rather, at certain points there is always destructive interference, and field magnitude is zero (nodes). At other points, there is maximum fluctuation of field due to constructive interference (antinode).
Time (general)	t or τ [s]	These symbols are employed in this thesis to denote some arbitrary span of time.
Transmission line	–	A form of guided-wave structure that employs two or more conductors.
Waveguide	–	A form of guided-wave structure that makes use of at most a single conductor.
Wavenumber	k [m^{-1}]	The number of wavelengths that fit in a unit distance for a given medium, $\frac{2\pi}{\lambda}$.

List of acronyms

The following is a list of acronyms that are made use of in this thesis, with definitions.

Acronym	**Expansion**	**Definition**
1D, 2D, and 3D	One, two, and three-dimensional	Describes the number of dimensions in a given coordinate system or device. It is noted that some objects are considered to be two-dimensional or one-dimensional for the purpose of design and analysis, but in actuality, all physical objects exist in three-dimensional space.

AMC	Artificial magnetic conductor	A device that exhibits reflective properties similar to those of a perfect magnetic conductor (i.e. no absorption, inversion of magnetic field vector) within a given frequency range.
CAD	Computer-aided design	A software tool that facilitates the design of physical objects and devices.
CMOS	Complementary metal-oxide semiconductor	A technology, of widespread use, for the development of high-density integrated circuits.
CST	Computer simulation technology	This is the name of a company that offers numerous tools for the numerical analysis of various structures and systems. In the context of this thesis, the particular tool that is made use of is known as CST Microwave Studio.
DC	Direct current	An electromagnetic quantity such as electric field, magnetic field, electric current, or electric voltage, which does not vary with respect to time.
DRA	Dielectric resonator antenna	A form of resonator, intended for interaction with free-space fields, for which the mode of resonance is of displacement current within a dielectric material of moderate-to-high relative permittivity.
DRIE	Deep reactive ion etching	A microfabrication technique that is suited towards deep penetration of etch depth.
EDX	Energy-dispersive X-ray spectroscopy	A form of X-ray spectroscopy in which a given material is excited with incident particles so as to evaluate the emission spectrum, with the aim of determining the constituent elements that make up the relevant material.

EIRP	Equivalent isotropically radiated power	In a given direction, the gain of a transmitting antenna multiplied by the net power accepted by the antenna from the connected transmitter (IEEE 1983).
FAST	Five-hundred-metre aperture spherical radio telescope	A Chinese telescope project intended for radio astronomy.
FIR	Far infrared	Frequencies in the infrared range spanning 3 to 20 THz, which exhibits some overlap with the terahertz range.
GDSII	Graphic databse system information exchange	A database file format typically associated with the CAD-based representation of integrated circuits and other microstructures.
GHz	Gigahertz	10^9 Hertz
GRIN	Gradient index	A device for which the refractive index, or effective refractive index, varies as a function of position.
HEM	Hybrid electromagnetic	Either a mode of resonance, or a guided-wave modem with non-zero components for both the electric and magnetic field components in the direction of propagation.
HR Si	High-resistivity float-zone intrinsic silicon	A form of intrinsic (i.e. un-doped) silicon that sees extensive use in this thesis due to its low loss, moderate refractive index, and low dispersion.
ICP	Inductively-coupled plasma	A method of generating plasma by means of time-varying magnetic fields.
IPKISS	–	Not technically an acronym, but rather this mask layout software is so-named after the fictional character Stanley Ipkiss, from the comic books *The Mask*. It is included in this section for clarity.

LED	Light-emitting diode	A form of diode that is intended to produce visible-range illumination when forwards-biased.
LTE	Long-term evolution	This refers to standards of mobile telephony systems that extend beyond the capabilities of standard 3G technology.
LPI	Low probability of intercept (communications)	Communications schemes that are engineered towards an exceptionally-high level of data security.
MRA	Metallic resonator antenna	A specific instance of a metallic resonator that is employed for comparison purposes in Chapter 6.
MHz	Megahertz	10^6 Hertz
MIMO	Multiple-input, multiple-output	A communications system in which both the transmitter and receiver are made up of multiple, distinct antenna elements, where each supplies a distinct channel.
PCA	Photoconductive antenna	A form of antenna, of widespread use in the terahertz range, for which the photoexcitation of free carriers in semiconductors is exploited to generate lower-frequency radiation.
PDMS	Polydimethylsiloxane	A silicon-based polymer of widespread use.
PEC	Perfect electrical conductor	A hypothetical substance for which tangential electric field is always equal to zero, regardless of the quantity of electric current that is flowing through it. Electromagnetic fields are not capable of penetrating such a substance.
PMC	Perfect magnetic conductor	A hypothetical substance for which tangential magnetic field is always equal to zero, regardless of electric field. Electromagnetic fields are not capable of penetrating such a substance.

PP	Polypropylene	A common thermoplastic polymer.
PTFE	Polytetrafluoroethylene	A synthetic polymer that is better-known by a particular commercial brand of PTFE-based formula, Teflon.
QCL	Quantum cascade laser	A particular form of laser that makes use of inter-subband transitions in a semiconductor. These lower-energy transitions can correspond to terahertz photons, and hence QCLs can operate in the terahertz frequencies, where conventional lasers cannot.
SEM	Scanning electron microscope	A microscope that makes use of a beam of electrons, rather than photons, in order to acquire images. The smaller de Brogile wavelength of the particles makes for higher-resolution imaging.
SLM	Selective laser melting	A 3D-printing technique that makes use of a high-intensity laser to selectively melt and fuse a given powder build material.
TE	Transverse-electric	In the context of free-space fields, this refers to an obliquely-incident wave in which the electric field vector is orthogonal to the plane made by the propagation and surface-normal vectors. For a guided-wave structure, this refers to a mode for which there is no electric field component in the direction of propagation. Similarly, as a resonant cavity can be viewed as a stub of a guided-wave structure that confines electromagnetic radiation, which propagates back and forth within the stub, a TE mode of resonance can be considered to have no electric field component in the propagation direction within the cavity.

TEM	Transverse-electromagnetic	In the context of free-space fields and guided waves, this refers to a wave that exhibits no electric or magnetic field vector components in the direction of propagation. Similarly, for a resonant cavity, a TEM mode of resonance exhibits no electric or magnetic field vector components in the direction of propagation within the cavity or at the cavity boundaries.
THz	Terahertz	10^{12} Hertz
THz-TDS	Terahertz time-domain spectroscopy	A method of terahertz spectroscopy that is made extensive use of in the context of this thesis.
TM	Transverse-magnetic	For free-space fields, this refers to an obliquely-incident wave in which the magnetic field vector is orthogonal to the plane made by the propagation and surface-normal vectors. For guided-wave structures, this refers to modes of resonance for which there is no magnetic field vector component in the direction of propagation. Likewise, for resonators, there is no magnetic field vector component in the direction of the back-and-forth motion of the confined wave.
TPX	Polymethylpentene	A rigid, terahertz-transparent polymer of widespread use.
UAV	Unmanned air vehicle	An aircraft that holds no crew, is controlled remotely, and is typically quite lightweight.
VLPI	Very low probability of intercept (communications)	A scheme, proposed in this thesis, whereby terahertz radiation is employed in order to further reduce the probability of decryption by a third party for a LPI system.

WiMAX	Worldwide interoperability for microwave access	Microwave-based telephony technology intended to provide a wireless alternative to high-volume cable and DSL services.

Index

Biography

Daniel Headland was born in Adelaide, Australia in 1991. He undertook tertiary-level education from 2009 to 2012 at The University of Adelaide, where he obtained a Bachelor of Engineering with first-class honours. During his undergraduate program, he obtained awards including four Dean's certificates of merit for outstanding achievement, the Sir William Goodman Scholarship for excellence in RF III, and the DSTO Surveillance systems prize. He commenced his doctoral program at The University of Adelaide immediately thereafter in 2013, having attained the George Fraser Scholarship, which is awarded to the highest-ranking PhD applicant for that year. During his PhD program he obtained a travel grant provided by an anonymous donor, which facilitated a period as a visiting scholar at the Los Alamos National Laboratory in New Mexico, USA, under Dr Hou-Tong Chen. He has since been awarded an Endeavour Postdoctoral Fellowship to undertake in Wuppertal, Germany, under the supervision of Prof. Ullrich Pfeiffer, which he will commence in 2017.

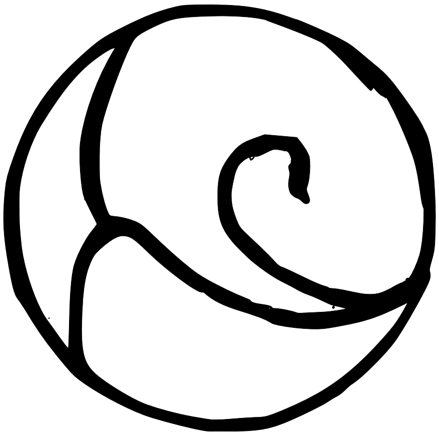

Scientific genealogy of

Daniel Headland

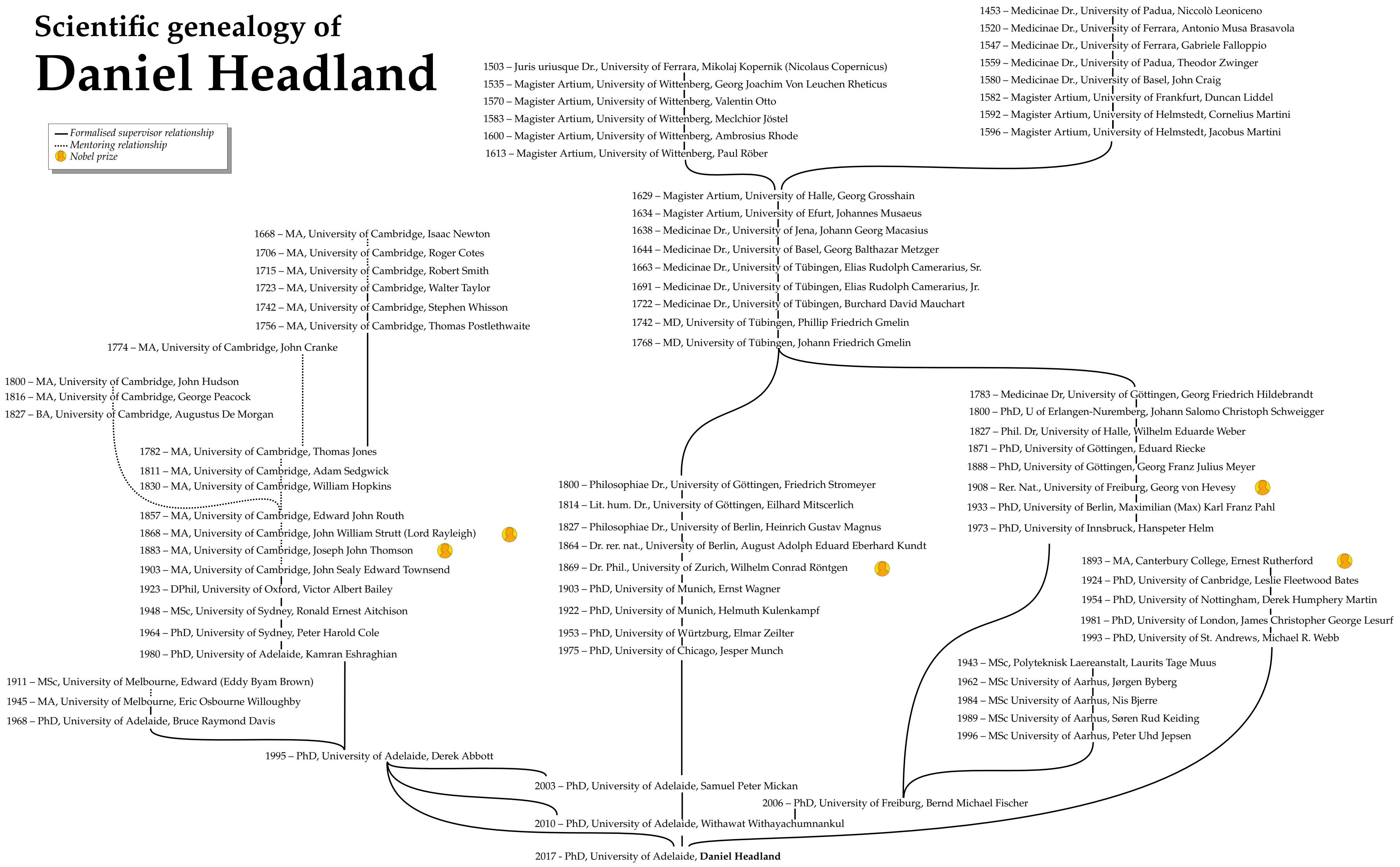

— *Formalised supervisor relationship*
···· *Mentoring relationship*
🏅 *Nobel prize*

1503 – Juris uriusque Dr., University of Ferrara, Mikolaj Kopernik (Nicolaus Copernicus)
1535 – Magister Artium, University of Wittenberg, Georg Joachim Von Leuchen Rheticus
1570 – Magister Artium, University of Wittenberg, Valentin Otto
1583 – Magister Artium, University of Wittenberg, Meclchior Jöstel
1600 – Magister Artium, University of Wittenberg, Ambrosius Rhode
1613 – Magister Artium, University of Wittenberg, Paul Röber

1453 – Medicinae Dr., University of Padua, Niccolò Leoniceno
1520 – Medicinae Dr., University of Ferrara, Antonio Musa Brasavola
1547 – Medicinae Dr., University of Ferrara, Gabriele Falloppio
1559 – Medicinae Dr., University of Padua, Theodor Zwinger
1580 – Medicinae Dr., University of Basel, John Craig
1582 – Magister Artium, University of Frankfurt, Duncan Liddel
1592 – Magister Artium, University of Helmstedt, Cornelius Martini
1596 – Magister Artium, University of Helmstedt, Jacobus Martini

1629 – Magister Artium, University of Halle, Georg Grosshain
1634 – Magister Artium, University of Efurt, Johannes Musaeus
1638 – Medicinae Dr., University of Jena, Johann Georg Macasius
1644 – Medicinae Dr., University of Basel, Georg Balthazar Metzger
1663 – Medicinae Dr., University of Tübingen, Elias Rudolph Camerarius, Sr.
1691 – Medicinae Dr., University of Tübingen, Elias Rudolph Camerarius, Jr.
1722 – Medicinae Dr., University of Tübingen, Burchard David Mauchart
1742 – MD, University of Tübingen, Phillip Friedrich Gmelin
1768 – MD, University of Tübingen, Johann Friedrich Gmelin

1668 – MA, University of Cambridge, Isaac Newton
1706 – MA, University of Cambridge, Roger Cotes
1715 – MA, University of Cambridge, Robert Smith
1723 – MA, University of Cambridge, Walter Taylor
1742 – MA, University of Cambridge, Stephen Whisson
1756 – MA, University of Cambridge, Thomas Postlethwaite

1774 – MA, University of Cambridge, John Cranke

1800 – MA, University of Cambridge, John Hudson
1816 – MA, University of Cambridge, George Peacock
1827 – BA, University of Cambridge, Augustus De Morgan

1782 – MA, University of Cambridge, Thomas Jones
1811 – MA, University of Cambridge, Adam Sedgwick
1830 – MA, University of Cambridge, William Hopkins
1857 – MA, University of Cambridge, Edward John Routh
1868 – MA, University of Cambridge, John William Strutt (Lord Rayleigh) 🏅
1883 – MA, University of Cambridge, Joseph John Thomson 🏅
1903 – MA, University of Cambridge, John Sealy Edward Townsend
1923 – DPhil, University of Oxford, Victor Albert Bailey
1948 – MSc, University of Sydney, Ronald Ernest Aitchison
1964 – PhD, University of Sydney, Peter Harold Cole
1980 – PhD, University of Adelaide, Kamran Eshraghian

1911 – MSc, University of Melbourne, Edward (Eddy Byam Brown)
1945 – MA, University of Melbourne, Eric Osbourne Willoughby
1968 – PhD, University of Adelaide, Bruce Raymond Davis

1995 – PhD, University of Adelaide, Derek Abbott

1800 – Philosophiae Dr., University of Göttingen, Friedrich Stromeyer
1814 – Lit. hum. Dr., University of Göttingen, Eilhard Mitscerlich
1827 – Philosophiae Dr., University of Berlin, Heinrich Gustav Magnus
1864 – Dr. rer. nat., University of Berlin, August Adolph Eduard Eberhard Kundt
1869 – Dr. Phil., University of Zurich, Wilhelm Conrad Röntgen 🏅
1903 – PhD, University of Munich, Ernst Wagner
1922 – PhD, University of Munich, Helmuth Kulenkampf
1953 – PhD, University of Würtzburg, Elmar Zeilter
1975 – PhD, University of Chicago, Jesper Munch

1783 – Medicinae Dr, University of Göttingen, Georg Friedrich Hildebrandt
1800 – PhD, U of Erlangen-Nuremberg, Johann Salomo Christoph Schweigger
1827 – Phil. Dr, University of Halle, Wilhelm Eduarde Weber
1871 – PhD, University of Göttingen, Eduard Riecke
1888 – PhD, University of Göttingen, Georg Franz Julius Meyer
1908 – Rer. Nat., University of Freiburg, Georg von Hevesy 🏅
1933 – PhD, University of Berlin, Maximilian (Max) Karl Franz Pahl
1973 – PhD, University of Innsbruck, Hanspeter Helm

1893 – MA, Canterbury College, Ernest Rutherford 🏅
1924 – PhD, University of Canbridge, Leslie Fleetwood Bates
1954 – PhD, University of Nottingham, Derek Humphery Martin
1981 – PhD, University of London, James Christopher George Lesurf
1993 – PhD, University of St. Andrews, Michael R. Webb

1943 – MSc, Polyteknisk Laereanstalt, Laurits Tage Muus
1962 – MSc University of Aarhus, Jørgen Byberg
1984 – MSc University of Aarhus, Nis Bjerre
1989 – MSc University of Aarhus, Søren Rud Keiding
1996 – MSc University of Aarhus, Peter Uhd Jepsen

2003 – PhD, University of Adelaide, Samuel Peter Mickan
2006 – PhD, University of Freiburg, Bernd Michael Fischer
2010 – PhD, University of Adelaide, Withawat Withayachumnankul

2017 - PhD, University of Adelaide, **Daniel Headland**